Cover Page

Author: Fedoseev, Gleb Sergeevich
Title: Atom addition reactions in interstellar ice - new pathways towards molecular complexity in space -
Issue Date: 2014-12-10

Atom Addition Reactions in Interstellar Ice

- new pathways towards molecular complexity in space -

Atom Addition Reactions in Interstellar Ice

- new pathways towards molecular complexity in space -

Proefschrift

ter verkrijging van
de graad van Doctor aan de Universiteit Leiden,
op gezag van de Rector Magnificus prof. mr. C. J. J. M. Stolker,
volgens besluit van het College voor Promoties
te verdedigen op woensdag 10 december 2014
klokke 12.30 uur

door

Gleb Sergeevich Fedoseev

Geboren te Kharkov, Voormalige Unie van Socialistische Sovjetrepublieken
in 1985

Promotiecommissie

Promotor: Prof. dr. H. V. J. Linnartz

Co-promotores: Dr. S. Ioppolo   Radboud University Nijmegen and
                                                  California Institute of Technology
                     Dr. H. M. Cuppen   Radboud University Nijmegen

Overige Leden: Prof. dr. H. J. A. Röttgering
                     Prof. dr. M. R. S. McCoustra   Heriot-Watt University
                     Dr. M. E. Palumbo   University of Catania
                     Prof. dr. E. F. van Dishoeck

Content

Any word on which three versed ones (intelligent ones) agree can be told anywhere; otherwise it must not be relied on. Do compare your word and the word of the others with the words of the versed ones (intelligent ones): if it will be in agreement you can say, otherwise there is no way to say.

Whoever lies with intention or through sorcery, or spies upon the behavior of others, or intervenes between the two arguing ones to help the one against the other is to be put to death.

Excerpts from Great Yassa of Genghis Khan

(An original list of the regulations legendarily declared by Genghis Khan on Kurultai in 1206 is not preserved. This text is based on reconstructions of Great Yassa by Rashid-al-Din Hamadani (1247 – 1318) and Al-Maqrizi (1364 – 1442) assembled by Erenzhen Khara-Davan in the work "Genghis Khan as a Warlord and His Heritage" (in Russian), Belgrade, 1929)

I

Introduction

To a young boy, who is trying to build for the first time his own cosmological picture of the Universe consisting of myriads of galaxies, the endless space between stars may seem to be just an empty barrier, a necessary "evil" that has to be passed before reaching the next island of matter – a star system similar to our own. To me, the concept of interstellar medium was for the first time introduced by Stanisław Lem's novel 'The Magellanic Cloud' (1955), where the first human expedition, which undertakes the venture of leaving our Solar system and travelling to a nearby star in search for a new World, had encountered an unexpected problem. Their spaceship was overheated for unknown reasons. It took a while before engineers on the ship had realized the cause: "The source of the heat rise could only be outside, but outside there was the emptiness. One cubic centimeter of this emptiness contains only few atoms, and that is why it could be considered as an absolute vacuum in comparison to the gas density under terrestrial conditions, where one cubic centimeter of gas has several trillions of molecules. However, "Gaia" moved with such velocity, that every square centimeter of its surface collided with 800 billions of atoms per second; this was enough for friction to take place and overheat the rocket". This was the first time when I looked at the interstellar medium as a system that has its own structure and life. However, it was difficult to me to imagine at that time that the chemistry of this "emptiness" would eventually become the subject of my thesis.

1.1 Star evolution

The interstellar medium (ISM) is an extremely dilute environment; nonetheless, it plays an important role in the evolution of our Galaxy. The ISM is the place where new stars and planets are formed from the remnants of stars that died in a former star cycles. A simplified scheme of this cycle of life and death is depicted in Fig. 1.1. The ISM is filled with gas (99% in mass) and dust (1% in mass). The gas is composed by hydrogen (H, 70%), helium (He, 28%), and a fraction of heavier elements; the dust comprises mainly silicate grains and carbonaceous material. Gas and dust are not distributed uniformly over the ISM. Therefore, there exist regions that are dominated by high densities and lower temperatures. With time, gravitational attraction or external shockwaves induce these cold regions to reach even higher densities (10^2-10^6 particles cm^{-3}). These values are still extremely low and can be considered as a perfect vacuum if compared to terrestrial standards. However, the size of these objects is so large (>10000 astronomical units) that the visual extinction by the dust grains does not allow visible light to pass through and therefore does not reach the observers, *i.e.*, us (Tielens 2005). This explains the name given to these objects, dark (molecular) clouds (see Barnard 68 in Fig. 1.1). When gravitational attraction induces further collapse of the cloud over a period that depends on the mass of the dark cloud (10^5-10^6 years for a cloud resulting in a Solar mass star), the innermost regions reach high enough density and temperature for a protostar (a future star) to be formed inside. For the conservation of the angular momentum, this process is accompanied by the formation of a protoplanetary disk and outflows (see DG Tau B in Fig. 1.1). This is not yet a star system, but also not a cloud anymore and therefore is called a young stellar object (YSO). It takes about 10 millions years before a star finally accretes most of the nearby material and reaches its final mass, while the protoplanatery disk is segregated and gives birth to future planets. A low-mass star with a planetary system similar to our own Solar system usually lasts for about 10^{10} years before most of the hydrogen fuel inside the star is consumed and it becomes a Red Giant, approaching the end of its life cycle. During all these stages, starting from YSO and ending with the Red Giant, the system releases gas and dust into the ISM that in turn provides material from which new stars are formed. Our own Sun belongs to the second-third generation of stars.
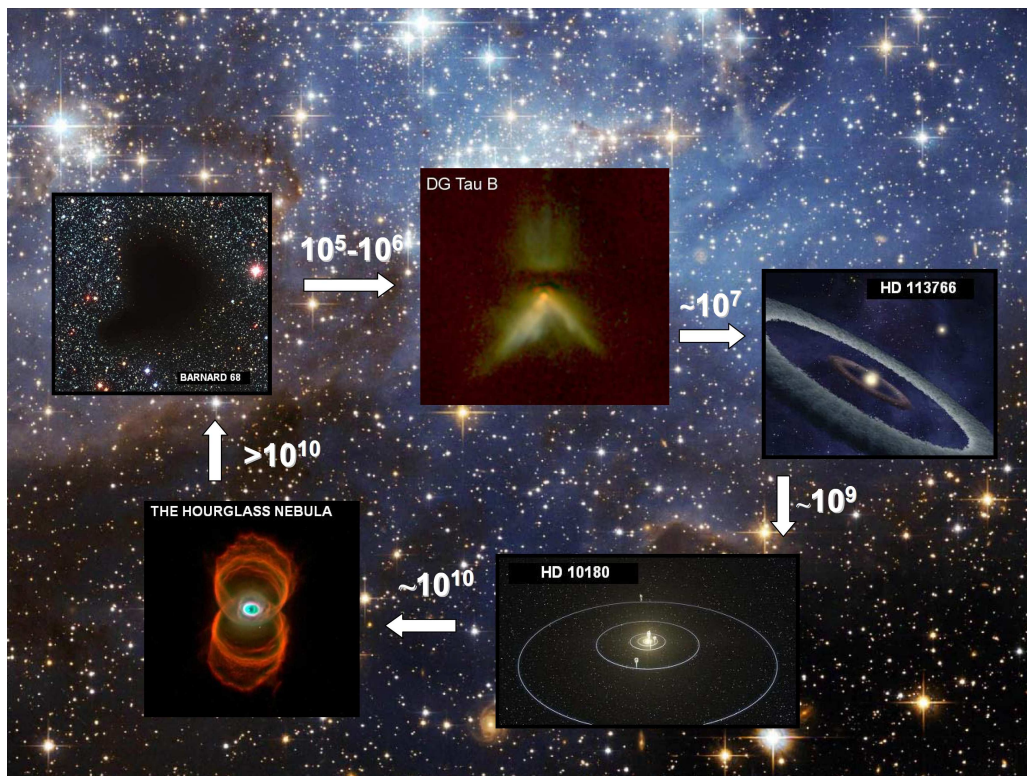
Figure 1.1. Artistic representation of a star formation cycle in the ISM. All objects are chosen to be close to the solar mass. Arrows indicate time in years. Pictures are taken from ESO and NASA web pages.

The study of every single stage of the star formation cycle involves different physical and chemical branches of science and faces many unresolved issues. This thesis mostly focusses on the very first steps of star formation, *i.e.*, the dark cloud stage and the formation of YSOs. This focus has two reasons: on one hand, infrared (IR) observations toward dark clouds show that these regions already possess a rich chemistry even before stars and planets are formed. On the other hand, an exact understanding of the chemical processes involved in the formation of interstellar species observed in these regions will help scientists to unlock the origin and fate of the organic molecules that are present on Earth and that at some point contributed to the formation of life.

1.2 Molecules in star forming regions

1.2.1 The role of dust and ice

More than 180 different molecules have been identified in the circumstellar and interstellar media (Woon 2014). These species comprise simple molecules, like H_2 or CO – two of the

most abundant molecules of the ISM – as well as about 50 molecules with 6 and more atoms, organic molecules, and structural isomers (Herbst & van Dishoeck 2009). This observed chemical complexity in space is the cumulative outcome of gas, dust, and gas-dust interactions. Many species can be formed in the gas-phase. However, gas-phase reactions alone cannot explain the observed abundances of many detected molecules, particularly the more complex organic species. Therefore, solid state processes become important. At low temperatures (~10 K), (sub)micrometer-sized dust grains act as small cryopumps onto which gas-phase molecules accrete. In dense cores (the innermost part of Molecular Clouds), the approximate timescale at which gas-phase species deplete onto grains is about 10^5 years, that is comparable to the lifetime of a dark cloud. Therefore, during the first stage of star formation, most of the species, with the exception of the lightest ones (H_2, He), are expected to be largely frozen-out onto interstellar grains. The resulting ice mantle provides a local molecule reservoir, which may be as thick as several tens of monolayers (ML, where 1 ML = 10^{15} molecules cm^{-2}). It also provides a 'third body' to which two reactive species can donate excess energy allowing formation of a stable molecule, a process that otherwise is impossible in two body gas-phase collisions. Although accretion rates on the surface of interstellar grains are extremely low, over thousands of years grains accumulate enough material for complex chemistry to take place. It is generally accepted nowadays that solid state astrochemistry plays an important role in the chemical enrichment of the ISM. Grains play here the same role of a solid-phase catalyst in gas-phase chemical synthesis.

1.2.2 Interstellar ice composition

The interstellar ice composition can be derived from mid-infrared observations of molecular clouds along the line of sight to a background star. Alternatively, a newly formed protostar embedded into a young stellar object can be used as a source of light. The ice absorption spectra are then obtained by subtracting the emission profile of a background star or embedded protostar from the observed spectra. The features leftover correspond to the absorbance of molecules in the line of sight between the emitting object and the observer. Observations in the mid-IR range from ground-based telescopes are limited to a few spectral windows, because of the presence of telluric lines in the Earth atmosphere. This limitation is overcome by airborne and space observations. Observations with the Infrared Space Observatory (ISO) (Whittet *et al*. 1996, Gibb *et al*. 2000, Gibb *et al*. 2004) and the Spitzer Space Telescope (, Boogert *et al*. 2008, Pontoppidan *et al*. 2008, Bottinelli *et al*. 2010 and Öberg *et al*. 2011) greatly improved our knowledge on interstellar ice composition by exploring wavelength ranges inaccessible from Earth. Some examples of ice spectra toward three chosen protostars are shown in Fig. 1.2.
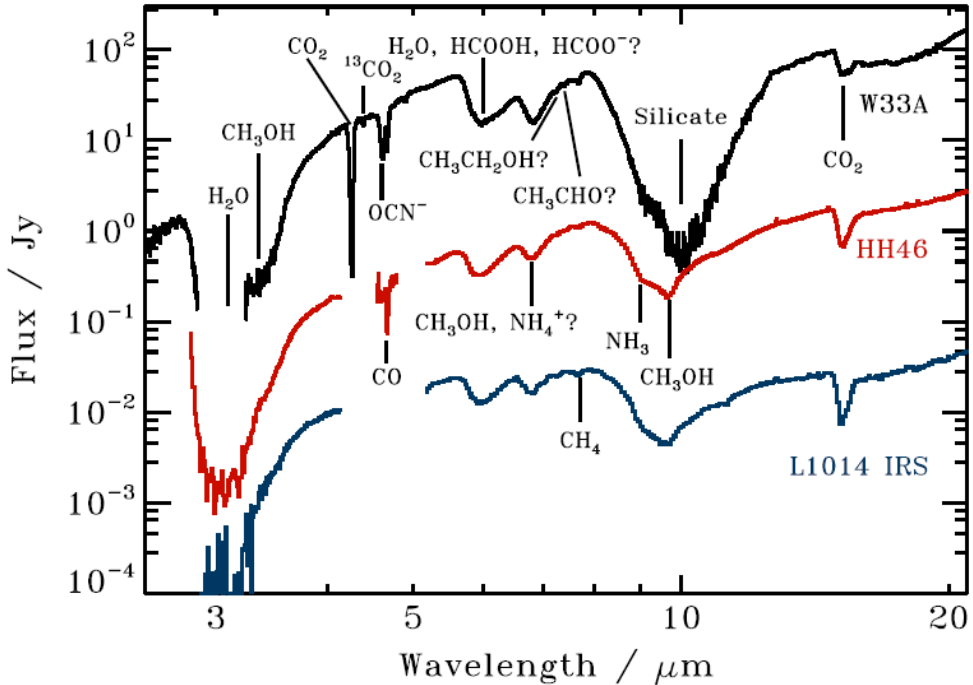
Figure 1.2. Ice spectra towards star forming regions W33A , HH46 and L1014 IRS with solar luminosities of 10^5, 12 and 0.09, respectively, obtained from ISO, Spitzer, and ground-based observations (Gibb *et al.* 2000, Boogert *et al.* 2004). The Figure is taken from Öberg *et al.* (2011).

Despite the different nature of the three objects reported in Fig. 1.2 (low-, high-mass YSO, and background star), similar spectral features are present in all these sources. A detailed and quantitative study of these bands, however, would not be possible without the use of laboratory ice spectroscopy (Hudgins *et al.* 1993, Gerakines *et al.* 1995, Baratta & Palumbo 1998, Cuppen *et al.* 2011). The systematic laboratory investigation of IR band profiles of pure and mixed ices (*i.e.*, containing two or more species) over a wide range of temperatures combined with the knowledge of all the absorption band strengths of each molecule allows for the identification of the components of the interstellar ice mantles. The main components of interstellar ices are reported in Table 1.1 and are – in order of decreasing abundance – H_2O, CO, CO_2, CH_3OH, NH_3, CH_4, and XCN. The latter is likely due to OCN^-. Moreover, from a comparison between laboratory work and observations, interstellar ices appear to be layered. The first layer is a H_2O-rich polar-ice with embedded CO_2, CH_4, and NH_3. The observed abundances of these species correlate with the abundance of solid H_2O. The second, top, layer is a non-polar CO-rich ice, which likely contains also most of the solid CH_3OH and OCN^- (Fuchs *et al.* 2009, Cuppen *et al.* 2011, Fedoseev *et al.* 2014). There is also evidence for the presence of more complex molecules,

like HCOOH, CH₃CHO, and C₂H₅OH (Schutte *et al*. 1998, Boudin *et al*. 1998). However, better constraints, *i.e.*, higher quality spectra, especially at 5-10 μm, are needed to unambiguously identify these species in the solid phase. Moreover, mid-IR observations are insensitive to homonuclear diatomic molecules, like O_2 and N_2. Although O_2 is not expected to be observed in the ice due to its chemical reactivity, N_2 may be in fact one of the most abundant ice components, because of its chemical inertness and stability.

Table 1.1. Abundance medians and lower and upper quartile values of ices and individual ice components with respect to H_2O ice. Taken from Öberg *et al*. (2011).

Ice Feature	Low Mass Protostar	High Mass Protostar	Background Star
H_2O	100	100	100
CO	38^{61}_{20} (29)	13^{19}_{7}	31
CO_2	29^{35}_{22}	13^{22}_{12}	38^{41}_{32}
CH_3OH	7^{12}_{5} (3)	8^{16}_{8} (4)	8^{10}_{7} (4)
NH_3	5^{6}_{4}	16^{17}_{10} (5)	-
CH_4	5^{7}_{4}	4^{4}_{2} (2)	-
XCN	$0.6^{0.8}_{0.2}$ (0.3)	$0.8^{1.4}_{0.4}$ (0.6)	-
CO (pure)	21^{36}_{7}	3^{6}_{2}	-
CO in H_2O	13^{19}_{7}	10^{12}_{5}	-
CO in CO_2	2^{3}_{1}	$1.3^{1.6}_{0.4}$ (0.3)	-
CO_2 (pure)	$2^{4}_{0.3}$	2^{2}_{1}	-
CO_2 in H_2O	20^{23}_{15}	9^{15}_{6}	24
CO_2 in CO	5^{7}_{4}	5^{6}_{2}	6
OCN^-	$0.4^{0.4}_{0.3}$ (0.2)	$0.6^{1.4}_{0.4}$	-

1.3 Interstellar ice evolution and chemistry

To date, it is generally accepted that a substantial part of the stable and complex species identified so far, is formed on icy dust grains *via* non-energetic atom addition induced reaction schemes. Since solid-state radical-radical and radical-molecule reactions often do not require any activation energy, they can occur even at extremely low temperature (10 K): *i.e.*, in the innermost part of molecular clouds, where newly formed molecules are largely shielded from radiation by dust particles. These regions are part of collapsing envelopes that feed new stars - young stellar objects - and provide the original material from which comets and ultimately planets are made.

Grain surface chemistry is governed by the accretion rate of gas-phase species onto the grains, the surface migration rate which sets the reaction network, and the desorption rate. Therefore, it also depends on a number of physical parameters, such as cloud density,

ice temperature, and chemical composition of the grain surface. Figure 1.3 shows a schematic representation of ice evolution starting from the prestellar stage (dark cloud) through the collapsing envelope resulting in the formation of a protoplanetary disk around the protostar. In short, a less-volatile water-rich ice is formed on top of bare grains. Then, with increasing densities to 10^4-10^5 cm^{-3}, CO freeze-out occurs and CO-rich ice mantles are formed on top of the water-rich ice. This newly formed CO-rich ice is hydrogenated to form most of the interstellar CH$_3$OH observed in space. Molecules formed on the surface of dust grains can in turn desorb to the gas phase. At low temperature, this can be achieved by the interaction of the ice with cosmic rays, cosmic ray induced UV-photons, or as the result of grain collisions. When the core collapses and a protostar is formed, ice will further experience heat, UV- and cosmic rays induced reactions in the region close to the newly formed protostar. At this stage, volatile species desorb, while less-volatile species undergo a "warm" ice chemistry, and, as a result, more complex (organic) species are formed in the ice mantles. When the temperature reaches values of 100 K and higher, water ice and other less-volatile species trapped in the ice start to sublimate. Alternatively, some of the icy grains will flow into the mid-plane of protoplanetary disk, where they are shielded from heat and UV irradiation caused by the newly formed protostar and from the external UV-field. In this region, planets and comets are formed. Therefore, understanding formation mechanisms and delivery processes of complex and even prebiotic molecules to planets is fundamental for a better understanding of the early composition of Earth, and its primordial oceans.
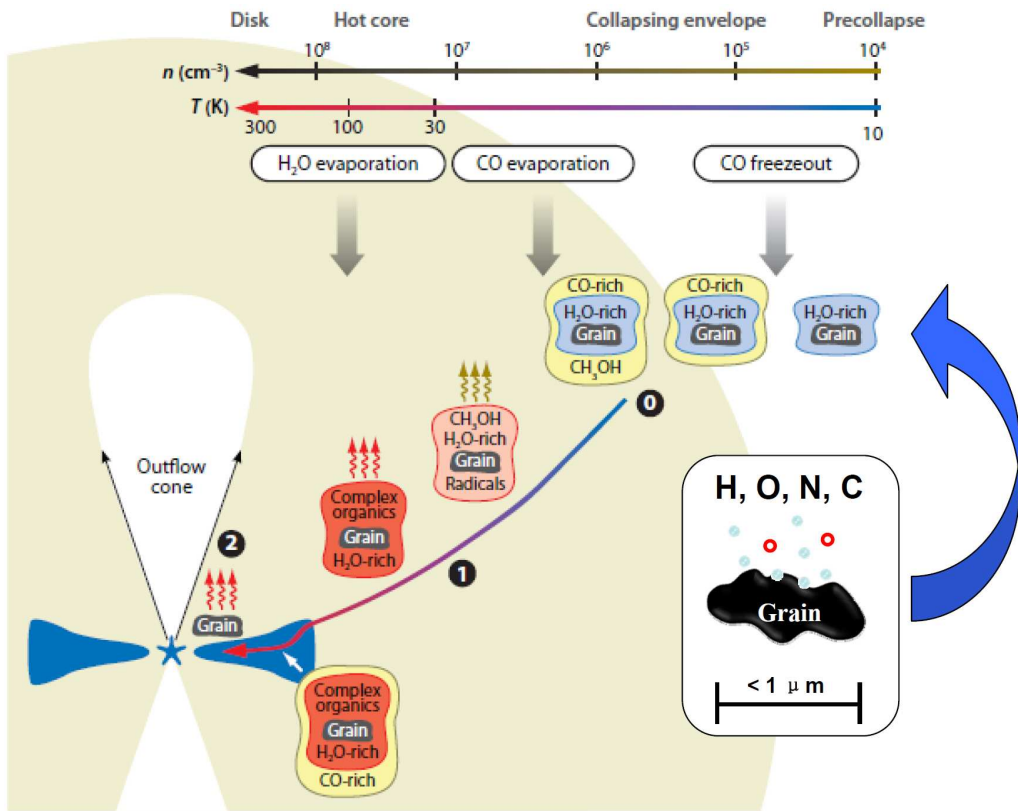
Figure 1.3. Evolution of the ice composition starting from the prestellar stage through the collapsing envelope, and into a protoplanetary disk. Adapted from a figure by van Dishoeck & Visser (Herbst & van Dishoeck 2009).

Some of the most important mechanisms that rule the interstellar ice chemistry are discussed below:

1) *Atom and radical addition reactions*. Among all the possible atom addition reactions (*e.g.*, H, O, N, and C) occurring in space, the most important one is the hydrogenation of the ice. This is not surprising since hydrogen is the most abundant element in the Universe. Some of the species formed through hydrogenation reactions on the surface of dust grains are H_2 (through H + H), H_2O (through hydrogenation of $O/O_2/O_3$), NH_3 (through hydrogenation of N atoms), CH_3OH (through hydrogenation of CO), and possibly CH_4 (through the hydrogenation of C atoms). CO_2 can be formed through atom and radical addition reactions: CO+O and CO+OH. Radical-radical and radical-molecule reactions often do not require any activation energy and therefore can easily proceed even at low temperature (10 K). Three of the most relevant reaction mechanisms on the grain surface are the Langmuir-Hinshelwood (L-H), Eley-Rideal (E-R), and hot-atom mechanisms (see Figure 1.4). In the case of the

Langmuir-Hinshelwood mechanism, two reactants are adsorbed on different surface spots of an interstellar grain and reach thermal equilibrium with the surface before one or both of them diffuse to find each other and react. In the Eley-Rideal mechanism, one of the reactive species directly lands on top of the other and the reaction immediately occurs before thermal equilibrium is reached. The hot-atom mechanism is a combination of both: one species is located on the surface in thermal equilibrium, while the second one lands on the nearby surface spot; migration and reaction occur before the thermal equilibrium is reached.
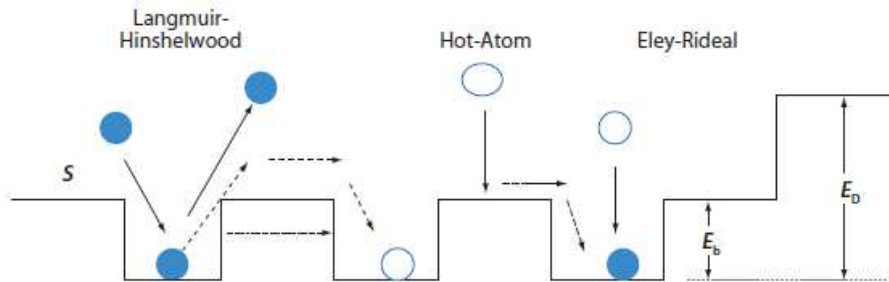
Figure 1.4. Three mechanisms for surface reaction on the grain surface. E_d is the desorption activation barrier; E_b is an activation barrier of the diffusion from a surface spot to another. The figure is taken from van Dishoeck & Herbst (2009).

Distinguishing between Langmuir-Hinshelwood, Eley-Rideal, and Harris-Kasemo ("hot-atom") mechanisms is of great importance when the temperature of the adsorbing species is significantly higher than the temperature of the surface. For the Eley-Rideal and the hot-atom mechanisms, the high energy of the incoming species helps to overcome the activation barrier of the reaction. This is not the case if the Langmuir-Hinshelwood mechanism takes place, where both the reactants are in thermal equilibrium with the ice surface. In cold dark molecular clouds, the difference in temperature between the accreting species and the ice surface is not large. Furthermore, the Langmuir-Hinshelwood mechanism is the most important mechanism in non-energetic surface reactions, because of the extremely low accretion rates even in the densest regions of molecular clouds. However, under laboratory conditions, the temperature of the exposing atom beams is often equal or higher than the room temperature. This deviation from the conditions found in space has to be taken into account during the interpretation of laboratory data. Monte Carlo (MC) simulations (Cuppen *et al*. 2013) can be used to simulate and reproduce laboratory results to investigate qualitatively and quantitatively all the mechanisms at play in the solid phase (*e.g.*, deposition, diffusion, segregation, reaction, and desorption). Results from these models can then be included into astrochemical MC models to extend laboratory

results to interstellar timescales and fluxes (Fuchs *et al*. 2009, Cuppen *et al*. 2009, Vasyunin & Herbst 2013). The experimental investigation of non-energetic reaction routes is the main subject of this thesis.

2) *UV-induced reaction routes*. As opposed to the neutral-neutral, atom, and radical addition surface reactions discussed above, UV processing of ices provides an energetic input that leads to the excitation of molecules and dissociation of molecular bonds followed by the formation of "hot" fragments, *i.e.*, radicals, atoms, and ions with high internal energy. These "hot" fragments can in turn react with the surrounding molecules and easily overcome activation barriers, desorb from the ice surface, or diffuse into the bulk of the ice and even eject other molecules from the surface (Arasa *et al*. 2010). A complete analysis of the UV-induced reaction network is often challenging without the knowledge of photodissociation and photoionisation cross sections for all the molecules involved in the UV photolysis process. Furthermore, these cross-sections and photodissociation branching ratios are wavelength dependent and, therefore, significant variations in the final outcome may occur, depending on the energy of the UV-photon applied. Secondary processes, like photodesorption, and structural changes in the ice morphology should also be taken into account. UV-photon induced chemistry can efficiently lead to the formation of complex organic species in the ice mantles. Therefore, UV-photolysis significantly increases complexity in the ice (see Öberg *et al*. 2009). At high doses and high enough thickness of the ice, a complex polymeric refractory residue can be formed as well (D'Hendecourt *et al*. 1996, Allamandola *et al*. 1988, Greenberg *et al*. 1995, Herbst & van Dishoeck 2009).

3) *Cosmic rays*. The chemical composition of the ices can be further modified by ion and electron bombardment. For example, the energy released by a highly energetic ion passing through a material causes the dissociation of hundreds of molecules along their path. These fragments can then recombine. As a result of the interaction between a cosmic ray and the ice, hundreds of new molecules including both simple and more complex molecules are formed. Moreover, the impact of a cosmic ray with the ice surface causes the release of some of the ice material into the gas phase through sputtering and local heating. In this respect, cosmic ion irradiation is a more complex mechanism than UV-photolysis that involves only a single-photon event (Baratta *et al*. 2002).

4) *Thermal processing*. During their evolution, star-forming regions are exposed to thermal processing. Most of the chemistry in interstellar ices takes place within the range of temperatures 10-100 K. Thermal processes can induce sublimation of ice

material, changes in the ice morphology, segregation of species in the ice, neutral-neutral reactions – such as deuterium-exchange reactions – and charge transfer within the ice (Ratajczak *et al* 2009, Novozamsky *et al*. 2001 and Theule *et al*. 2011).

The aforementioned mechanisms may dominate in different regions of the ISM or at different evolutionary stages in star-forming regions, but all mechanisms have in common that they contribute to a higher molecular complexity in space.

1.4 Chemistry of interstellar ices in the laboratory

1.4.1 Experimental setups

SURFRESIDE

Atom and radical addition reactions in interstellar ice analogues are here studied using SURFRESIDE, an ultrahigh vacuum (UHV) setup, and its more recent upgrade SURFRESIDE^2, operational since 2012. SURFRESIDE^2 is an extended version of the former system and comprises a second atom line to allow the simultaneous use of two atom-beams together with regular molecular dosing lines. Details of both setups are available from Fuchs *et al*. (2009) and Ioppolo *et al*. (2013) (Chapter 2 of this thesis). The use of an UHV setup (base pressure ~10^{-10} mbar of mainly H_2) allows us to grow ices with submonolayer precision. Extremely low background gas deposition rates provide enough time to perform selected atom-bombardment experiments under fully controlled laboratory conditions (*i.e.*, the exposure of background gas H_2O, N_2, and CO_2 to a cold sample at 10^{-10} mbar requires almost 4 hours to obtain 1 ML surface coverage).

Ices are deposited with controllable deposition rates on a gold substrate at a selected temperature. Deposition with a variable incident angle is possible. The substrate is mounted on the tip of a cold head of a He close-cycle cryostat and a temperature regulation is realized by means of a heating wire. The absolute temperature precision is ~2 K while the relative precision is as high as 0.5 K

The setup comprises two molecular deposition lines and two atom-beam lines. In order to provide diversity in the way atoms beam are generated two different atom sources are used: (*i*) a Hydrogen Atom Beam Source (HABS, Dr. Eberl MBE-Komponenten GmbH, see Tschersich 2000) that produces H or D atoms through thermal cracking of H_2 or D_2; (*ii*) a Microwave Atom Source (MWAS, Oxford Scientific Ltd, see Anton *et al*. 2000) that generates H, D, O, and N atoms as well as OH, NH, and NH_2 radicals by using a microwave discharge (125-300 W at 2.45 GHz). In the following chapters of this thesis, various parent molecules are used to generate atom beams: $H_2(D_2)$ for H(D) atoms, O_2 and

N$_2$O for O atoms, N$_2$ and NH$_3$ for N atoms, H$_2$O for OH radicals, and NH$_3$ and even mixtures of two gases N$_2$ and H$_2$ for NH and NH$_2$ radicals. A nose-shaped quartz pipe is placed along the path of each of the atom beams to efficiently quench the excited electronic and ro-vibrational states of the formed atoms and non-dissociated molecules through collisions with the walls of the pipe before they reach the ice sample. Furthermore, the experimental results on hydrogenation (deuteration) of interstellar ice analogues can be repeated sequentially by using the thermal cracking source and then the microwave discharge to increase the "confidence" level of the obtained results.

Two molecular deposition lines that allow for separate depositions of stable molecules are used to simulate different molecular environments as typical for different evolutionary stages of interstellar ices (*i.e.*, polar, H$_2$O-rich, or non-polar, CO-rich, interstellar ice analogues) In this way, it becomes possible to co-deposit a number of various atoms and molecules together, simulating selected astrophysical conditions. Furthermore, experiments performed in a H$_2$O or CO environment have the advantage that reactive species can donate their excess energy to the surface (H$_2$O or CO) before they participate into reactions through the Langmuir-Hinshelwood mechanism. Thus, reactants are most likely thermalized to the surface temperature and their kinetic energy should not affect the final results. Another advantage of using H$_2$O and CO matrices is to make sure that the reactive atoms participating in the selected reaction routes are deposited isolated and not as dimers, trimers, or even larger oligomers.

Two different experimental procedures are here regularly applied. In "pre-deposition" experiments, ices are first deposited on the sample and are subsequently exposed to a thermal atom-beam. In this case, the formation and consequent destruction of the intermediate products followed by the formation of final products can be monitored. This allows us to obtain kinetic curves that then can be fitted by a system of differential equations in order to obtain formation rates. However, this technique has considerable drawbacks. Limited penetration depth of atoms into the pre-deposited ice causes low final yields of the products. Furthermore, unstable intermediate radicals are rapidly converted to the stable species and consequently hard to identify. These drawbacks can be overcome by using a "co-deposition" technique. In the latter case, molecules and atoms are deposited simultaneously with specified rates. Varying the ratio with which reactive species are deposited, formation of only first intermediate products without further conversion into the stable final products or, on the contrary, a thick ice of only final products can be obtained. These two techniques fully complement each other.

CRYOPAD

Several UV photolysis experiments shown in this thesis are performed by using the

CRYOgenic Photoproducts Analysis Device (CRYOPAD), which is described in details by Öberg *et al*. (2009) and references therein. As for SURFRESIDE, the rotatable gold-coated substrate in CRYOPAD is mounted on the tip of a cold head of a He close-cycle cryostat in the centre of a stainless steel UHV chamber. The temperature of the substrate is controlled between 15 and 300 K by means of a heater and a temperature controller. Ice deposition proceeds through a molecular dosing line by injecting either pure gases or preliminarily prepared gas mixtures. After deposition of an ice, the film is irradiated by UV light from a broadband hydrogen microwave discharge, which peaks at Ly-α (121 nm) and around 160 nm. The experiments discussed in chapter 4 are performed sequentially, but the system also allows the simultaneous molecular deposition and UV irradiation of the growing ice.

1.4.2 Measuring techniques

In both SURFRESIDE[2] and CRYOPAD, ice composition is monitored *in situ* by means of Reflection Absorption Infrared Spectroscopy (RAIRS) using a FTIR spectrometer, which covers the range between 4000 and 700 cm^{-1}. While 1 cm^{-1} is the typical spectral resolution used in the chapters of this thesis, spectral resolution can be varied between 0.5 and 4 cm^{-1}. The main advantage of the RAIRS technique is the ability to detect products of the reactions investigated in the solid phase at the sample temperature and to monitor the amount of products over time, *i.e*., to obtain kinetic curves. The choice of RAIRS over transmission infrared spectroscopy is due to the higher sensitivity of the RAIR technique: the glancing angle of an infrared beam (*e.g*., 8° to the substrate plane) results in enhancement of the *p*-polarized electric field at the surface and, therefore, to a gain in sensitivity. Furthermore, this effect is further enhanced by the increase in the path length of the beam through the deposited ice film and by the fact that the beam has to pass through the ice film twice, once before reaching the sample (gold-coated mirror) and a second time after reflecting from the sample. Such geometry improves the minimal detection limits of the infrared technique. Another great advantage of the RAIR technique is that only the ice deposited on one side of the substrate is probed. This is because the substrate is a gold-coated piece of copper, which reflects IR light. In the case of transmission spectroscopy, an infrared transparent material is used as a substrate window. Therefore, molecules are deposited on both sides of the window through direct or background deposition, as the result the final IR spectrum is a combination of the two ices. This can potentially be an issue during data analysis when only one of the two sides of the substrate window is processed to induce chemistry.
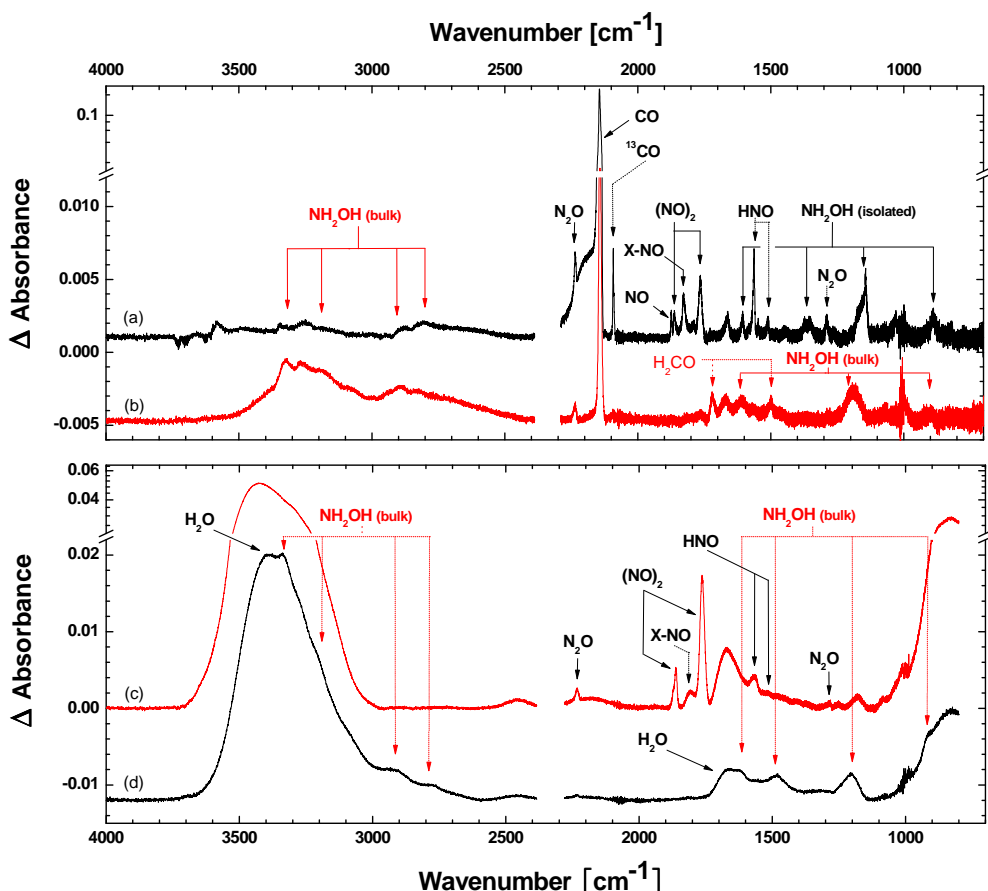
Figure 1.5. RAIR spectra of NO hydrogenation experiments taken from chapter 4. The upper panel shows co-deposition spectra of NO, CO and H atoms with NO:CO:H = 1:6:15 (a) and 1:1:20 (b). On the lower panel co-deposition spectra of NO and H_2O with H atoms for NO:H_2O:H = 1:6:3.5 (c) and 1:6:15 (d) are shown. All spectra are acquired at 15 K.

Species in the ice are identified according to their specific frequency fingerprint at which infrared light is absorbed. These specific frequencies, in turn, can be the same for few different species that share same functional groups or can shift for the very same species according to the specific molecular environment that surrounds them (polar vs. non-polar ice). For example, in Figure 1.5, one can see that the absorbance features of H_2O overlap with the NH_2OH bands. Moreover, the NH_2OH absorption features in Fig. 1.5(b) are shifted compared to those of NH_2OH in Fig. 1.5(a), where 6 times more CO is co-deposited and the formed NH_2OH molecules are in a way more isolated from each other. In addition, hydrogen bonds formed between polar species significantly broaden their absorption features making their exact assignments and quantification harder. The band broadening effect is illustrated in Fig. 1.5, where hydroxylamine (NH_2OH) absorbance

features are significantly wider in presence of water (lower panel of Fig. 1.5), and narrower when NH_2OH is mixed with CO (upper panel of Fig. 1.5). Low amounts of products formed in the experiments may significantly affect a correct assignment of the formed species and a quantitative analysis of the results. Furthermore, diatomic homonuclear molecules (*e.g.*, N_2, O_2, and H_2) are infrared inactive and their detection is not trivial if only infrared techniques are used. Therefore, a second analytical technique is routinely used to constrain the obtained IR results. This is Quadrupole Mass Spectrometry (QMS) in combination with Temperature Programmed Desorption (TPD) experiments.

In a TPD experiment a deposited ice sample is heated linearly with a selected rate (normally 1-10 K/min), molecules eventually desorb and their gas-phase signal is monitored by means of the QMS. Every chemical species has a specific desorption temperature, depending on its binding energy to the surface spot it occupies. When the temperature of the ice sample reaches the desorption temperature of a constituent, the latter evaporates into the gas phase, where it can be ionized in the ion source of the QMS. Ionization is realized through the impact with electrons that are produced by a hot filament. When ions are produced, they undergo a selection process that takes place in the quadrupole mass filter in a way that only the ions with a selected mass-to-charge (m/z) ratio can reach the detector at any given time. The detected signal is proportional to the density of the produced ions of a given m/z ratio. Up to twelve m/z signals can be recorded in series over time. As a result, a three dimensional plot of temperature *vs*. m/z *vs*. intensity of the signal can be obtained. However, the analysis of such plots is not trivial. The temperatures at which different species desorb can be close or even overlap. Furthermore, for the very same species the desorption temperature depends on the binding energy to the surface and therefore on the chemical composition of the surface (*e.g.*, H_2O ice, CO ice, amorphous carbon, and amorphous silicates) and even for the same type of surface, the binding energy can vary a lot because the surface is usually not uniform and different adsorption spots can have different binding energies. Moreover, TPD experiments of mixed ices are even harder to analyze because, for instance, volatile species can react or be trapped in a matrix of non-volatile species during a TPD. This way, they can only desorb at higher temperatures, together with the non-volatile species. The full picture is further complicated by the fact that species are fragmented upon electron impact in the ion source of the QMS, and a number of charged fragments are produced with a certain ratio (depending on the electron energy), forming a unique pattern for each species. This is illustrated in Fig. 1.6.
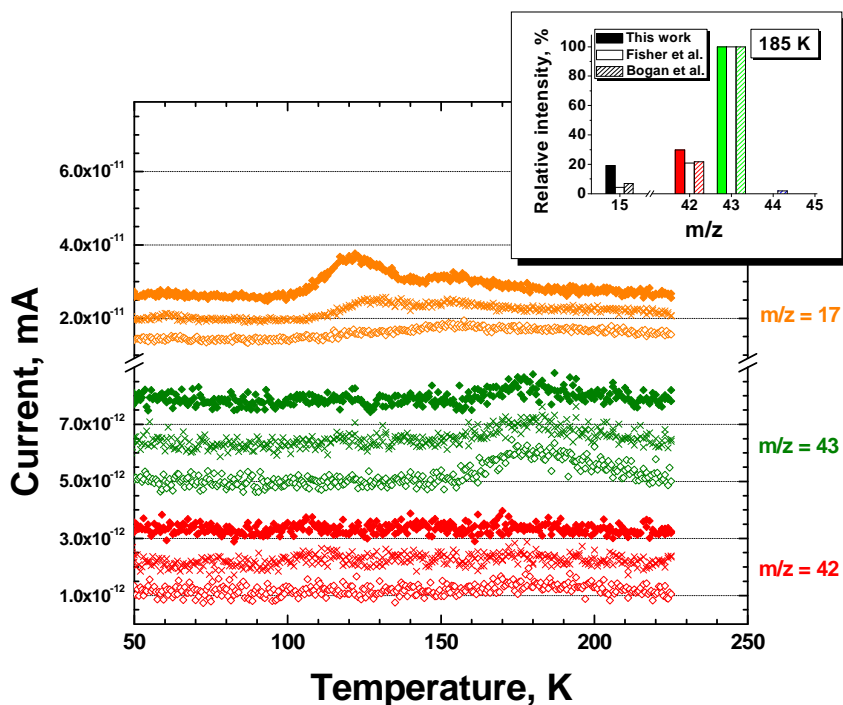
Figure 1.6. TPD spectra of three distinct experiments (this figure is taken from chapter 6 of this thesis). Three curves for each of the m/z values are shown. These curves from top to bottom correspond to smaller amounts of NH_3 formed in the ice (peak starting at 100 K for m/z = 17) and higher amounts of HNCO formed (peak starting at 160 K for m/z = 43). In the inset in the right top corner of the figure, a comparison between fragmentation pattern taken from the literature and fragmentation pattern obtained in our experiment is given.

Figure 1.6 shows that the desorption peak of NH_3 is slightly shifted toward higher temperatures when smaller amounts of NH_3 are formed. This can be explained as follow: when a smaller amount of NH_3 is adsorbed on the surface of the sample, it mainly occupies the "best" surface spots, *i.e.*, with high binding energy, while for a higher amount of NH_3, also spots with low energy are occupied and as a consequence the desorption peak shifts toward lower temperatures. The fragmentation pattern of HNCO (inset in the Fig. 1.6) is quite similar to the one reported in literature. In return, this greatly enhances the level of confidence of this assignment. In this thesis, care has been taken always to analyze more than one m/z value for the same chemical species in order to achieve reliable results.

TPD experiments can also be performed by using RAIRS as an analytical tool. In this case, RAIR difference spectra monitor the chemical composition of the ice that is not desorbed yet. In this thesis, the same experiment is often repeated twice to use both techniques, or both RAIR and QMS spectra are recordered simultaneously during a single

experiment. This procedure allows making unambiguous identifications of several surface reaction products (see next chapters). Finally, it is important to note that, although QMS is a more sensitive technique than RAIRS, QMS data of a TPD experiment do not provide *in situ* information. Therefore, RAIR spectroscopy at low temperatures is considered the primary analytical tool in all the following chapters.

1.5 This thesis

This thesis presents detailed laboratory based research on solid-state atom and radical addition reactions aimed to increase our understanding of the chemistry that occurs in interstellar ices. The focus here is on the chemistry of nitrogen-bearing species as well as on the formation of molecules of astrobiological importance. An attempt to provide a link between the formation of the simplest nitrogen-bearing molecules and simplest amino acids is made. In addition to amino-acid formation routes, the simplest representatives of two other classes of prebiotic compounds - aldoses (polyhydroxy aldehydes) and polyols - with their corresponding formation routes are presented. The main conclusions for each chapter are linked to Fig. 1.3 and in particular to the corresponding stages of interstellar ice evolution. Here, a brief description of every chapter is made.

Chapter 2 presents the new setup SURFace Reaction SImulation DEvice (SURFRESIDE^2) that allows a systematic investigation of solid-state reaction pathways resulting in the formation of molecules of astrophysical interest. This ultrahigh vacuum setup focuses on studying atom and radical addition reactions in interstellar ice analogues at astronomically relevant cryogenic temperatures. The implementation of two atom-beam lines along with two molecular beam deposition lines makes it possible to expose deposited ice molecules to different atoms and/or radicals sequentially or at the same time. Special efforts are made for precise atom flux determinations, in order to quantitatively characterize different reaction channels. In addition, we demonstrate the performance of the new setup on the example of carbon dioxide formation by comparing the efficiency of two different solid-state formation routes of CO_2 ($CO + OH = CO_2 + H$ and $CO + O = CO_2$). We find that under the same experimental conditions formation of CO_2 through the reaction $CO+OH$ takes place more efficiently than through the reaction $CO+O$. We further discuss the potential of SURFRESIDE^2 to study complex molecule formation, including nitrogen-containing (and even prebiotic) compounds. This is indeed the focus of the next chapters.

Chapters 3 and **4** investigate in detail the surface hydrogenation of NO molecules in polar (water-rich) and non-polar (carbon monoxide rich) interstellar ice analogues. A complex

reaction network involving both final (N_2O, NH_2OH) and intermediate (HNO, $NHOH/NH_2O\cdot$) products is discussed. We demonstrate that hydroxylamine formation takes place efficiently *via* a fast mechanism and it is found to be even more abundantly formed in a water-rich environment at lower temperatures. In parallel, we experimentally verified the non-formation of hydroxylamine upon UV photolysis of NO containing ices at cryogenic temperatures as well as the non-detection of NC- and NCO-bond bearing species after UV processing of NO in carbon monoxide-rich ices. Our results are implemented into an astrochemical reaction model, which shows that NH_2OH is supposed to be abundant in the solid phase under dark molecular cloud conditions. The assumed abundant presence of NH_2OH in interstellar ices adds a new perspective to the way molecules of biological importance may form in space. For instance, once NH_2OH desorbs from the ice grains, it becomes available to form more complex species (*e.g.*, glycine and β-alanine) in gas-phase reaction schemes. The possible formation scheme of these two molecules of astrobiological importance is discussed.

In **Chapter 5** a full reaction network involving nitrogen oxides (NO, NO_2, N_2O) and H, O, and N atoms is described. Here we show that NO_2 is efficiently formed in the reaction of NO with O atoms, and then rapidly destroyed in NO_2 + H/O/N reactions, which proceed in a barrierless way or with a very low barrier. The surface destruction of solid NO_2 leads to the formation of a series of nitrogen oxides of which the most important ones are NO, N_2O, as well as to the formation of HNO, NH_2OH, and H_2O. It is shown that the final stable products of the joint NO+H/O/N and NO_2+H/O/N reaction network are NH_2OH, H_2O, N_2, and N_2O. When NO_2 is mixed with an interstellar more relevant CO-rich ice, solid CO_2 and HCOOH are also formed due to interactions between the investigated reaction routes and CO-molecules. The astrophysical implications of the full reaction network are discussed.

Chapter 6 further expands the full nitrogen and oxygen reaction network as derived in chapters 3-5 by experimentally investigating the formation of NH_3 and HNCO through non-energetic surface reactions in interstellar ice analogues. It is shown that NH_3 is efficiently formed by three consecutive H-atom additions to N atoms. Furthermore, we show that in CO-rich interstellar ice analogues the formation of NH_3 is inhibited due to the surface formation of solid HNCO through the interaction of CO molecules with NH radicals – one of the intermediates in the formation of solid NH_3. This is an important experimental conclusion, since it shows that, in general, surface reaction routes cannot be treated independently. Moreover, possible reactions of intermediate products with different lattice molecules should always be taken into account. The surface formation route of HNCO is an important step to explain the observation of XCN spectral bands: HNCO can easily yield OCN^- in various thermally induced acid-base reactions. Finally, we discuss the

implications of HNCO in astrobiology, and suggest a new possible solid-state formation route of peptides and their fragments.

In **Chapter 7**, the deuterium enrichment of species produced on the surface of interstellar grains is investigated. In Chapter 6, NH_3 was for the first time detected *in situ* through the N+H reaction route. This allows us to further expand this study and to perform the simultaneous addition of hydrogen and deuterium atoms to nitrogen atoms in CO-rich interstellar ice analogues in order to study the exact fractionation of the formed NH_3, NH_2D, NHD_2, and ND_3 isotopologues at low temperatures (<15 K). The experiments yield a deviation from a statistical distribution in favour of deuterium-enriched species. Deuteration events are estimated to have a 1.7 times higher probability to take place compared to a regular hydrogenation event. It is suggested that the most likely explanation for this laboratory result is a higher sticking coefficient of D atoms over H atoms to the surface of the ice. This results in a higher surface D-atom density and a preferred formation of deuterium enriched ammonia isotopologues.

Chapter 8 focuses on the formation of two molecules of astrobiological importance - glycolaldehyde ($HC(O)CH_2OH$) and ethylene glycol ($H_2C(OH)CH_2OH$) - by surface hydrogenation of CO molecules. This laboratory-based research is aimed to simulate the CO freeze-out stage in interstellar dark cloud regions, well before thermal and energetic processing become predominant. It is shown that along with the formation of H_2CO and CH_3OH – two well-established products of CO hydrogenation – side products containing more than one carbon atom are formed. The laboratory investigated reaction pathways are then implemented into a continuous-time random-walk Monte Carlo model to study their impact on the solid-state abundances of glycolaldehyde and ethylene glycol in space. This work is particularly important because glycolaldehyde and ethylene glycol are the two simplest components of two classes of prebiotic compounds - aldoses (among which the most important are sacharides) and polyols (with best-known representative glycerine – a basic compound of fats).

References

Allamandola L. J., Sandford S. A., Valero G. J., 1988, Icarus, 76, 225

Anton R., Wiegner T., Naumann W., Liebmann M., Klein Chr., Bradley C., 2000, RSI, 71, 1177

Arasa C., Andersson S., Cuppen H. M., van Dishoeck E. F., Kroes G.-J., 2010, JCP, 132, 184510

Baratta G. A., Leto G., Palumbo M. E., 2002, A&A, 384, 343

Baratta G. A., Palumbo M. E., 1998, J. Opt. Soc. Am. A, 15, 3076

Boogert A. C. A. *et al*., 2008, ApJ, 678, 985

Bottinelli S., Boogert A. C. A., Bouwman J., Beckwith M., van Dishoeck E. F.; Öberg K. I., Pontoppidan K. M., Linnartz H., Blake G. A.; Evans N. J., II; Lahuis F., 2010, ApJ, 718, 1100

Bottinelli S., Boogert A. C. A., van Dishoeck E. F., Beckwith M., Bouwman J., Linnartz H., Öberg K. I., 2008, Proceedings of the International Astronomical Union, IAU Symposium, 251, 105

Boudin N., Schutte W., Greenberg J. M., 1998, A&A, 331, 749

Cuppen H. M., Karssemeijer L. J., Lamberts T., 2013, Chem. Rev., 113, 8840

Cuppen H. M., Penteado E. M., Isokoski K., van der Marel N., Linnartz H., MNRAS, 2011, 417, 2809

Cuppen H. M., van Dishoeck E. F., Herbst E., Tielens A. G. G. M., 2009, A&A, 508, 275

D'Hendecourt L. B., Allamandola L. J., Grim R. J. A., Greenberg J. M., 1986, A&A, 158, 119

Fedoseev G., Ioppolo S., Zhao D., Lamberts T., Linnartz H., 2014, submitted to MNRAS

Fuchs G. W., Cuppen H. M., Ioppolo S., Bisschop S. E., Andersson S., van Dishoeck E. F., Linnartz H., 2009, A&A, 505, 629

Gerakines P. A., Schutte W. A., Greenberg J. M., van Dishoeck E. F., 1995, A&A, 296, 810

Gibb E. L. *et al*., ApJ, 536, 347

Gibb E. L., Whittet D. C. B., Boogert A. C. A., Tielens A. G. G. M., 2004, ApJS, 151, 35

Greenberg M. J., Li A., Mendoza-Gomez C. X., Schutte W. A., Gerakines P. A., de Groot M., 1995, ApJL, 455, L177

Herbst E. & van Dishoeck E. F., 2009, Annu. Rev. Astron. Astrophys., 47, 427

Hudgins D. M., Sandford S. A., Allamandola L. J., Tielens A. G. G. M., 1993, ApJS, 86, 713

Ioppolo S., Fedoseev G., Lamberts T., Romanzin C., Linnartz H., 2013, Rev. Sci. Instrum., 84, 073112

Öberg K. I. *et al*., 2011, ApJ, 740, 109

Öberg K. I., Garrod R. T., van Dishoeck E. F., Linnartz H., 2009, A&A, 504, 891

Pontoppidan K. M., Boogert A. C. A., Fraser H. J., van Dishoeck E. F., Blake G. A., Lahuis F., Öberg K. I., Evans II N. J., Salyk C., 2008, ApJ, 678, 1005

Schutte W. A., Greenberg J. M., van Dishoeck E. F., Tielens A. G. G. M., Boogert A. C. A., Whittet D. C. B., 1997, Astrophys. Space Sci., 255, 61

Tielens A. G. G. M., 2005, The Physics and Chemistry of the Interstellar Medium, Cambridge University Press, Cambridge, UK

Tschersich K. G., 2000, J. Applied Phys., 87, 2565

Vasyunin A. I., Herbst E., 2013, ApJ, 762, 86

Whittet D. C. B., Schutte W. A., Tielens A. G. G. M., Boogert A. C. A., de Graauw T., Ehrenfreund P., Gerakines P. A., Helmich F. P., Prusti T., van Dishoeck E. F., 1996, A&A, 315, L357

Woon D. E., Interstellar & Curcumstellar Molecules, The Astrochemist, retrieved from http://www.astrochymist.org/astrochymist_ism.html

II

SURFRESIDE^2: An Ultrahigh Vacuum System for the Investigation of Surface Reaction Routes of Interstellar Interest

A new ultrahigh vacuum experiment is described to study atom and radical addition reactions in interstellar ice analogues for astronomically relevant temperatures. The new setup - SURFRESIDE^2 - allows a systematic investigation of solid state pathways resulting in the formation of molecules of astrophysical interest. The implementation of a double beam line makes it possible to expose deposited ice molecules to different atoms and/or radicals sequentially or at the same time. Special efforts are made to perform experiments under fully controlled laboratory conditions, including precise atom flux determinations, in order to characterize reaction channels quantitatively. In this way we can compare and combine different surface reaction channels with the aim to unravel the solid state processes at play in space. Results are constrained in situ by means of a Fourier transform infrared spectrometer and a quadrupole mass spectrometer using RAIRS and TPD, respectively. The performance of the new setup is demonstrated on the example of carbon dioxide formation by comparing the efficiency through two different solid state channels ($CO + OH \rightarrow CO_2 + H$ and $CO + O \rightarrow CO_2$) for which different addition products are needed. The potential of SURFRESIDE^2 to study complex molecule formation, including nitrogen containing (prebiotic) compounds, is discussed.

2.1 Introduction

More than 180 different molecules, not including isotopes, have been identified in the space around and in between stars, *i.e.*, the circum- and interstellar medium. It is commonly accepted that this chemical diversity is the outcome of a complex interplay between reactions in the gas phase and on icy dust grains. The latter have been identified in space and are currently topic of dedicated laboratory simulations. During the last decade, the introduction of ultrahigh vacuum systems has improved our understanding of molecule formation in the solid state for astronomically relevant temperatures, introducing a new research field: solid state astrochemistry. Fully controlled laboratory experiments have shown that new molecules form in and on the ices upon thermal processing; energetic processing induced by vacuum UV light, X-rays, cosmic rays, and electrons; and non-energetic processing like atom bombardment. Meanwhile it has been confirmed that, except for CO that is efficiently formed in the gas phase, the bulk of interstellar ices (*i.e.*, water, carbon dioxide, methanol, formaldehyde, formic acid, ammonia) is formed in the solid phase through surface reactions (Hiraoka *et al*. 1994, Watanabe & Kouchi 2002a, Fuchs *et al.* 2009, Miyauchi *et al.* 2008, Ioppolo *et al.* 2008, Matar *et al.* 2008, Dulieu *et al*. 2010, Oba *et al*. 2010a, Ioppolo *et al*. 2011a, Noble *et al*. 2011, Ioppolo *et al*. 2011b, Loeffler *et al*. 2005, Ioppolo *et al*. 2009, Raut & Baragiola 2011, Fulvio *et al*. 2012, Linnartz *et al*. 2011). The focus in this paper is on a new UHV setup able to study atom and radical addition reactions in interstellar ices. In recent years, the formation of a number of molecules was proven upon CO, O_2, and O_3 hydrogenation, yielding H_2CO, CH_3OH, H_2O_2, and most importantly H_2O (Watanabe & Kouchi 2002a, Fuchs *et al*. 2009, Miyauchi *et al*. 2008, Ioppolo *et al*. 2008, Matar *et al*. 2008, Ioppolo *et al*. 2010, Cuppen *et al*. 2010, Mokrane *et al*. 2009, Romanzin *et al*. 2011). Also more complex species such as ethanol (CH_3CH_2OH) upon ethanal hydrogenation (Bisschop *et al*. 2007a) and hydroxylamine (NH_2OH) following NO hydrogenation (Congiu *et al*. 2012a, Congiu *et al*. 2012b, Fedoseev *et al*. 2012) have been shown to form in the solid state. The latter is a potentially important prebiotic precursor of glycine and β-alanine (Blagojevic *et al*. 2003). Not only reaction products have been determined in this way, but also the underlying reaction schemes have been characterized as well as their dependence on a number of variable parameters, such as temperature, H-atom flux, ice morphology (mixing ratio, thickness, and structure). It is found that the chemical processes involved are far from trivial and this only gets more complicated when ice mixtures are studied (Ioppolo *et al*. 2009a, Ioppolo *et al*. 2009b, Fedoseev *et al*. 2012).

The majority of these experiments have been realized using setups in which a single atom/radical source is available for ice processing. This comes with restrictions, as reactions are limited to one specific impacting species. A second beam line offers much

additional potential, *i.e.*, the simultaneous or sequential bombardment of an ice with different constituents, for example H- and D-atoms to study isotopic effects, or H- and O-atoms or H- and N-atoms to combine hydrogenation with oxygenation or nitrogenation reactions, in order to grow more and more complex molecules. The new SURFace REaction SImulation DEvice allows ice deposition using two deposition lines and comprises two separate atom beam lines for ice processing. In the following, the setup is denoted as SURFRESIDE[2]. This next generation UHV setup has been constructed with the specific aim to "unlock the chemistry of the heavens", by studying molecular complexity in interstellar ice analogues upon atom/radical addition reactions.

The focus here is on a quantitative characterization of the experimental properties of SURFRESIDE[2], using a new approach to fully characterize atom fluxes. Its performance is demonstrated through different reactions in the ice resulting in CO_2 formation. Solid carbon dioxide is found in relatively large abundances w.r.t. water ice, typically at the level of 13–29% towards high- and low-mass stars, see Oberg *et al*. (2011). Consequently, it offers an excellent tracer to characterize the chemical history of the interstellar medium, provided that its formation scheme is well understood.

2.2 System description

SURFRESIDE[2] consists of three distinct UHV chambers (Fig. 2.1). In the main chamber, ices are deposited with monolayer precision and processed at astronomically relevant temperatures. Reflection-Absorption Infrared Spectroscopy (RAIRS) and Temperature Programmed Desorption (TPD) are used as analytical tools to characterize the ice composition. In the other chambers different atom sources are mounted for the controlled production of well-characterized atom (molecular) beams. Shutters separate the beam line chambers from the main chamber and allow an independent operation of the individual beam lines.

SURFRESIDE²

1 - MAIN CHAMBER
2 - GOLD SUBSTRATE (12-300 K)
3 - QMS
4 - FTIR SPECTROMETER
5 - FTIR EXTERNAL OPTICS
6 - PURGE BOXES
7 - MCT DETECTOR
8 - ATOM LINE I
9 - HABS
10 - DOSING LINE HABS
11 - DOSING LINE MAIN CHAMBER
12 - ATOM LINE II
13 - MWAS
14 - DOSING LINE MWAS
15 - MICROWAVE CAVITY
* - UHV GAUGES
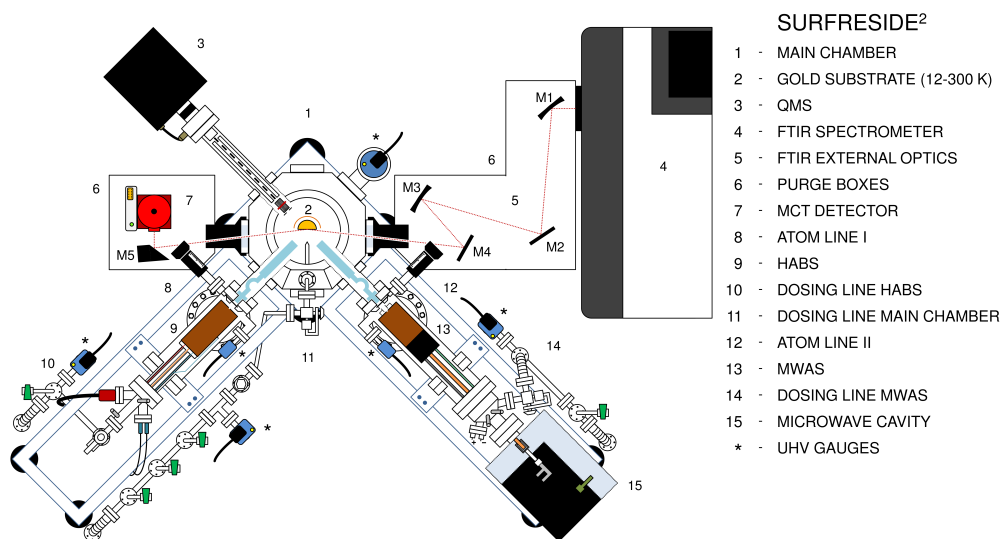
Figure 2.1. A schematic top-view of the experimental apparatus.

2.2.1 Main chamber

The custom-made ultrahigh vacuum 304 stainless steel main chamber has a diameter of 30 cm and is provided with eight lateral CF 35, two lateral CF 16, one top CF 63 and one bottom CF 200 flange connections (#1 in Fig. 2.1). A gate valve connects the bottom-flange with a 260 l/s (for N_2) turbomolecular pump (Pfeiffer Vacuum, TMU 261P). The CF 35 lateral flanges are used to connect the main chamber to the two atom lines (#8 and #12 in Fig. 2.1), an active cold cathode transmitter (Pfeiffer Vacuum, IKR270) for pressure readings in the $5 \cdot 10^{-11}$ - 0.01 mbar range, and a quadrupole mass spectrometer (QMS; Spectra - Microvision Plus; #3 in Fig. 2.1). Two CF 35 windows are used for in- and out-going light from a Fourier transform infrared spectrometer (FTIR; Agilent Technologies Cary 600 Series; #4 in Fig. 2.1). The two CF 16 flanges are used as inlet for a double ice deposition dosing line (#11 in Fig. 2.1), while a differentially-pumped (Leybold Vacuum, TW 300) ϑ rotatable stage (0°-360°) connects the top-flange to a helium closed-cycle refrigerator (ASR Inc.; #2 in Fig. 2.1).

The room temperature base pressure of the main chamber is in the low 10^{-10} mbar regime. An optically-flat gold-coated copper substrate (2.5 x 2.5 cm²) is placed in the center of the main chamber and is in thermal contact with the cold finger of the helium closed-cycle cryostat. The gold surface is not representative for interstellar grain surfaces, but it is an effective heat conductor, highly reflective in the mid-infrared, and chemically

inert, *i.e.*, the substrate plays no role in catalyzing chemical reactions or processes at the substrate surface. Moreover, ice thicknesses are typically more than ten monolayers, reducing the role of the substrate. Therefore, it is well suited to study interstellar relevant reaction routes that occur on and in ice samples. The substrate temperature is varied between 12 and 300 K with a relative precision of 0.5 K through a cryogenic temperature controller (LakeShore model 340). To achieve temperatures as low as 12 K an aluminum thermal shield kept at ~77 K surrounds the cold finger and the back-side of the sample. The temperature of the sample is changed and monitored by means of heating wires and thermocouples, respectively. The heating wires are mounted around the cold finger close to the substrate, while the two KP-type thermocouples are connected above and below the gold substrate. The absolute temperature accuracy is better than 2 K. This is checked by monitoring the well known desorption temperature of volatile species like for instance CO, N_2, and O_2 (Acharyya *et al.* 2007).

An all metal high-vacuum stainless steel ice deposition dosing line is used to prepare, store and introduce gas mixtures into the main chamber. The pressure in the deposition dosing line is monitored mass independently by means of an active capacitance transmitter (Pfeiffer Vacuum, CMR361) in the range between 0.1 and 1100 mbar. Lower pressures are monitored with an active Pirani transmitter (Pfeiffer Vacuum, TPR280) ($5 \cdot 10^{-4}$ to 1000 mbar). The deposition dosing line is first pre-pumped with a diaphragm pump (ABM, VDE 0530) and then with a 180 l/s (for N_2) turbomolecular pump (Pfeiffer Vacuum, TPH 180H) to reach low pressures ($<5 \cdot 10^{-4}$ mbar). Gaseous species are admitted into the main chamber through a dosing line comprising of two separate all-metal leak valves connected to gas reservoirs. Therefore, different gases can be prepared and stored in two different sections of the dosing line and then deposited separately or simultaneously onto the gold substrate. Deposition proceeds under an angle of 90° and 68°, respectively, and with a controllable flow between 10^{-8} and 10^{-7} mbar s^{-1}, where $1.3 \cdot 10^{-6}$ mbar s^{-1} corresponds to 1 Langmuir (L). Gas-phase species are monitored during deposition mass spectrometrically by means of the QMS, which is placed behind the substrate and mounted opposite to one of the two atom lines.

2.2.2 Analytical tools

Ices are monitored *in situ* by means of RAIRS using the FTIR, which covers the range between 4000 and 700 cm−1 (2.5–14 μm). A spectral resolution between 1 and 4 cm^{-1} is generally used and between 128 and 512 scans are co-added. The infrared beam coming from the FTIR is slowly diverging. Therefore, a series of $\lambda/4$ precision gold-coated mirrors (Edmund Optics and Thorlabs) is used to focus the beam onto the gold substrate (#5 in Fig. 2.1). The first one (M1) is a spherical mirror with a diameter of 76.2 mm and an effective

focal length (EFL) of 762 mm. This mirror is used to gently converge the beam. The second (M2) and the fourth mirror (M4) are flat mirrors, while the third one (M3) is a spherical mirror with a diameter of 75.0 mm and an EFL of 500 mm. The latter focusses the beam onto the substrate with a glancing angle of ~8°. The main chamber mounts two Zinc Selenide (ZnSe) CF 35 view ports that act as a vacuum seal and allow the IR beam to enter and leave the chamber with a transmission >95% in the range between $4-20$ μm. The out-going beam is then focussed into a narrow band and LN2 cooled Mercury Cadmium Telluride (MCT; #7 in Fig. 2.1) detector by means of a 90° off-axis parabolic gold-coated mirror (M5) with a diameter of 50.8 mm and a reflected EFL of 50.8 mm. The external optics and the detector are mounted in metal boxes (#6 in Fig. 2.1). These boxes as well as the FTIR are purged with dry-air to minimize atmospheric absorptions.

Two different experimental procedures are applied when using the FTIR. During pre-deposition experiments, ices are first deposited onto the gold substrate and subsequently exposed to atoms. To detect newly formed stable solid species, RAIR difference spectra are acquired during atom exposure with respect to a background spectrum of the initial deposited ice. In co-deposition experiments, molecules and atoms are simultaneously deposited onto the substrate. The formation of intermediate species and final products is controlled by changing the deposited molecule/atom ratio. In this case, RAIR difference spectra are acquired during co-deposition with respect to a background spectrum of the bare gold substrate.

At the end of the atom exposure a TPD experiment can be performed: the sample is heated linearly (*i.e.*, with a constant rate between 0.1 and 10 K/min) till the ice is fully desorbed. The thermal desorption can be followed spectroscopically by using the FTIR. Alternatively, the sample can be turned 135° to face the QMS. In this way, gas-phase species thermally desorbed from the ice are monitored mass spectrometrically. The desorbed species are recorded as a function of temperature by the QMS, which produces a signal proportional to the number of incoming molecules as a function of their mass to charge ratio (m/z). The incoming molecules first enter the ion source of the QMS, where they are ionized through electron bombardment by electrons released from a hot filament. The resulting ions are then focussed, selected and directed onto a Faraday detector, which collects the ions directly, allowing the ion current to be monitored. Alternatively, for higher sensitivity, a Channel Electron Multiplier (CEM) can be used. This type of detector is a Secondary Electron Multiplier (SEM) in which a large negative potential (~2000 V) is used to attract the ions into the channel entrance. The channel is coated with a material that readily releases secondary electrons upon ion/electron impact. This produces a cascade of electrons down to the channel which can be detected, either as an electron current, or as a series of pulses.

TPD combined with a QMS is a sensitive technique, but it has several disadvantages: surface reaction products that remain in the solid phase cannot be probed *in situ*; additional surface reactions during the TPD (*i.e.*, during the linear heating of the ice and before complete desorption of the species) cannot be excluded; quantifying the desorbing species is not trivial as some of the interesting species have equal (*i.e.*, undistinguishable) masses and the analysis of the fractionated components of species upon electronic bombardment is not always straightforward. Finally, a TPD experiment inherently involves the destruction of the ice. Therefore, QMS data are mainly used here to constrain RAIRS data acquired during atom exposure of the ice.

2.2.3 Data analysis

After fitting the infrared spectra with connected straight baseline segments, the column densities (molecules cm^{-2}) of newly formed species can be determined from the integrated intensity of their infrared bands using a modified Lambert-Beer equation (Bennett *et al.* 2004):

$$N_X = \frac{\int A(v)dv}{S_X},\qquad(2.1)$$

where $A(v)$ is the integrated absorbance and S_X is the corresponding band strength. This equation can, however, only be used for thin ice layers. Teolis *et al.* (2007) showed that the proportionality between the optical depth and the ice abundance breaks down for thicker layers (~20 ML onwards); the integrated band area oscillates as a function of the layer thickness due to optical interference that is caused by the reflection at both the film-vacuum and film-substrate interfaces.

Since literature values of transmission band strengths cannot be used directly in reflectance measurements (Greenler 1966), an apparent absorption strength of stable species has to be calculated from calibration experiments. The determination of this apparent absorption strength is setup dependent. Therefore we performed a series of isothermal desorption experiments for the new apparatus introduced here to derive these values. Briefly, a layer of the selected ice is deposited at a temperature lower than its desorption temperature. The sample is then linearly heated to a temperature close to its desorption value. Infrared spectra are acquired regularly until the desorption of the ice is complete. The transition from zeroth-order to first-order desorption is assumed to occur at the onset to the submonolayer regime and appears in the desorption curve as a sudden change in slope (see Fig. 2.2). The apparent absorption strength in cm^{-1} ML^{-1} is then calculated by relating the observed integrated area to 1 ML in the modified Lambert-Beer

equation. We estimate the uncertainty of band strengths determined in this way to be large but within 50% (also see Fuchs *et al.* 2009, Ioppolo *et al.* 2011, Fraser *et al.* 2001).

The determination of the band strength allows for a quantitative study of stable species formed upon atom exposure of the ice. This is mostly the case in pre-deposited experiments. Isothermal desorption experiments of unstable intermediate species cannot be performed and therefore their band strengths cannot be derived. Thus, a qualitative study is generally performed in co-deposition experiments where unstable species are frozen in ice matrices and then detected in the infrared. In this case, formation trends of detected species are followed by integrating the corresponding band area as a function of time, *i.e.*, without calculating column densities. As a consequence, only formation trends of the same species obtained under different experimental conditions (*e.g.*, ice temperature, atom flux, ice composition) can be compared, but this still allows to derive valuable information on the involved reaction network.
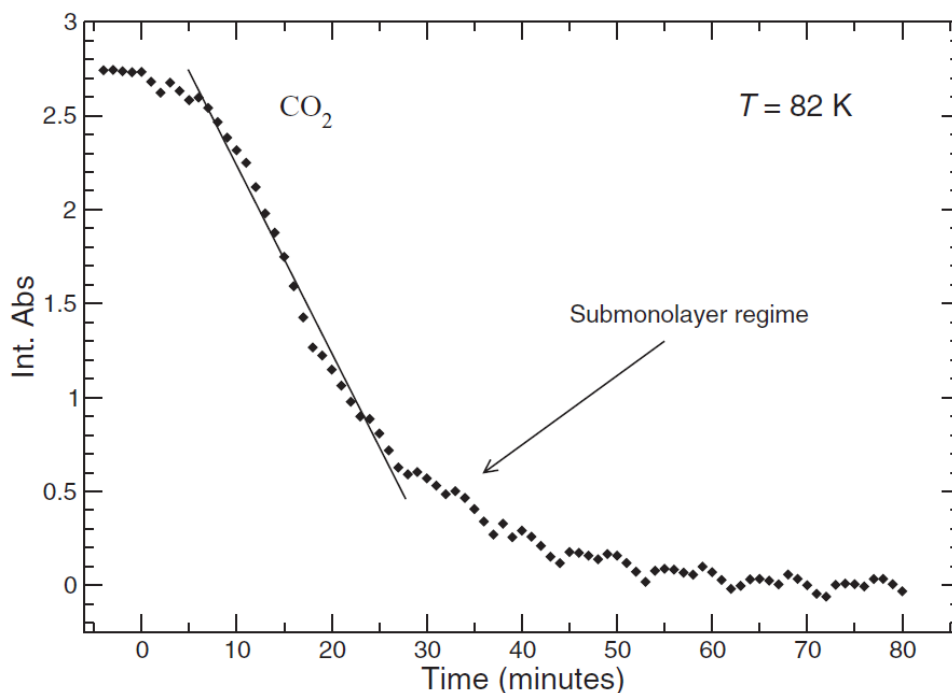
Figure 2.2. The decrease in integrated absorbance of CO_2 following desorption at a constant temperature of 82 K. The arrow indicates the transition point from the multi- to sub-monolayer regime.

2.2.4 Atom beam lines

Two different atom sources are used, one (HABS) based on thermal cracking, and the other (MWAS) using a microwave discharge (#9 and #13 in Fig. 2.1). The two custom-made

atom line chambers present identical geometrical characteristics (see Figs. 2.3 and 2.4): they are both pumped by 180 l/s (for N_2) turbomolecular pumps (Varian, TV 301 NAV); their room temperature base pressure is in the high 10^{-10} mbar regime (micro ion gauges, Granville-Phillips); they both are situated under an angle of 45° with respect to the substrate, both during single or simultaneous operation; a shutter is used to separate the lines from the main chamber; and a quartz pipe is placed after the shutter and along the path of the dissociated beam. The nose-shaped form of the pipe is designed to efficiently quench the excited electronic and ro-vibrational states of species through collisions with the walls of the pipe before they reach the ice sample. The geometry is designed in such a way that this is realized through at least four wall collisions of the atoms before leaving the pipe. In this way, "hot" species cannot reach the ice directly.

Two separate all metal dosing lines are used to prepare and inlet pure gasses and mixtures into each of the atom sources (#10 and #14 in Fig. 2.1). The dosing lines are pre-pumped with the same diaphragm pump that is used for evacuating the deposition dosing line. Each of the atom lines is then pumped with a 70 l/s (for N_2) turbomolecular pump (Pfeiffer Vacuum, TMU 071P). The room temperature base pressure of these lines is $< 1 \cdot 10^{-5}$ mbar and is monitored by means of a compact process ion gauge for each line (Pfeiffer Vacuum, IMR 265).

2.2.4.1 HABS

An all metal precision leak valve is used to admit H_2/D_2 molecules (99.8% purity, Praxair) from the all metal dosing line into the capillary of a well characterized and commercially available thermal cracking source, a Hydrogen Atom Beam Source (HABS, Dr. Eberl MBE-Komponenten GmbH), see Tschersich & von Bonin (1998), Tschersich (2000), Tschersich et al. (2008), which is used to hydrogenate/deuterate the sample through heating the capillary from 300 to a maximum of 2250 K by a surrounding tungsten filament (see top-box in Fig. 2.3). During experiments the $H + H_2$ ($D + D_2$) flow through the capillary and the temperature of the tungsten filament are controlled and kept constant by adjusting the all metal valve position and the voltage of the power supply of the HABS (Delta Elektronika, SM 7020-D). The temperature of the filament is monitored by means of a C-type thermocouple placed close to the filament and inside the internal thermal shield. To prevent melting of components a water cooling system is implemented into the source, in thermal contact with an external copper thermal shield. The temperature of this shield is controlled with a second C-type thermocouple. The HABS is used in horizontal mode.

A wide range of atom beam fluxes is accessible with this source by changing the pressure in the capillary pipe and/or the temperature of the filament. Typically values cover a range from 10^{11} to 10^{13} atoms cm^{-2} s^{-1}. Atom fluxes are measured at the sample position

in the main chamber, following a procedure described in section 2.2.5.1 (also see Bergh *et al.* 1999, Hidaka *et al.* 2004, Ioppolo *et al.* 2010).

As aforementioned, a quartz pipe is placed along the path of the beam (*i.e.*, after the shutter and before the sample in the main chamber) to cool the beam to room temperature. Previous experiments with liquid nitrogen cooled atom beams did not show any H/D-atom temperature dependence in CO hydrogenation reaction processes compared to experiments at room temperature (Watanabe & Kouchi 2002a). It is important to note that the relatively high temperature of 300 K of the incident H/D atoms in our experiments does not affect the experimental results, since H/D atoms are thermally adjusted to the surface temperature before they can react with other species through Langmuir-Hinshelwood mechanism, as shown in Fuchs *et al.* (2009), Hidaka *et al.* (2007), Watanabe *et al.* (2006).
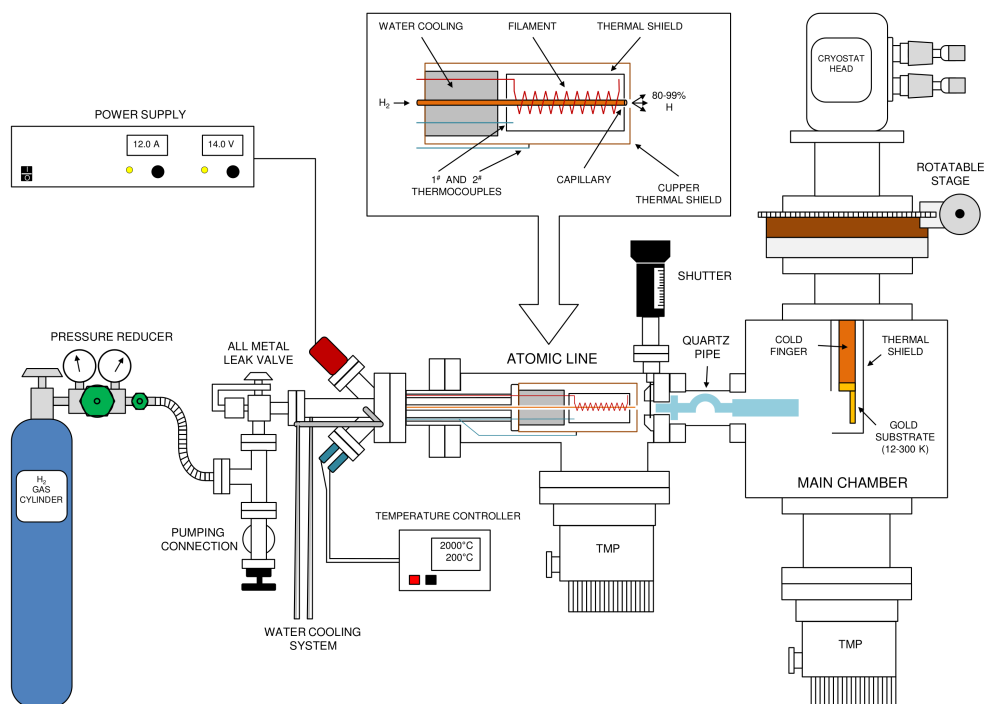
Figure 2.3. A schematic side-view of the atom line (HABS) with the thermal cracking H/D atom source and the main chamber

2.2.4.2   MWAS

A Microwave Atom Source (MWAS, Oxford Scientific Ltd) is included in the second atom line to produce beams of different atoms and radicals (*e.g.*, H, D, O, OH, OD, N). Figure

2.4 shows a schematic diagram of the MWAS. A 2.45 GHz microwave power supply (Sairem) produces up to 300 W that are coupled into a microwave cavity. Along this path a circulator is placed to avoid that the back-reflected power enters the power supply. A custom-made double tuner is placed after the circulator and before the microwave cavity to minimize the back-reflected power that ultimately is dissipated in a resistor. Part of the back-reflected signal is monitored by means of an oscilloscope (Tektronix, TDS 2012) connected to an attenuator and a crystal detector (Aertech Industries). An antenna (coaxial transmission line) connects the microwave cavity to a boron nitrite chamber in which gasses enter through the all metal precision leak valve of the dosing line (see top-box in Fig. 2.4). A plasma is created in a coaxial waveguide by coupling a radially symmetric 2.45 GHz microwave field to ions on the 86 mT surface of a multi-polar magnetic array (permanent magnets). The plasma is enhanced by the electron cyclotron resonance (ECR) effect. A water cooling system keeps the source and particularly the antenna close to room temperature. Moreover, the absence of a hot filament permits operation with most gases including reactive gases such as oxygen and nitrogen.

A specially designed alumina aperture plate allows reactive neutrals to escape from the plasma. The addition of an ion-trap (*i.e.*, two metal plates charged by a Oxford Scientific DC power supplier) can deflect the residual ion content from the beam, preventing ion exposure of the sample. All the electronically and ro-vibrationally excited species coming from the source are quenched through multiple collisions on passing through a quartz pipe before they reach the sample. Different plasma cavity pressures and/or different plasma power values give access to a wide range of atom fluxes, typically between 10^{10} and 10^{13} atoms cm^{-2} s^{-1}. These numbers depend on the dissociated species (see next section).
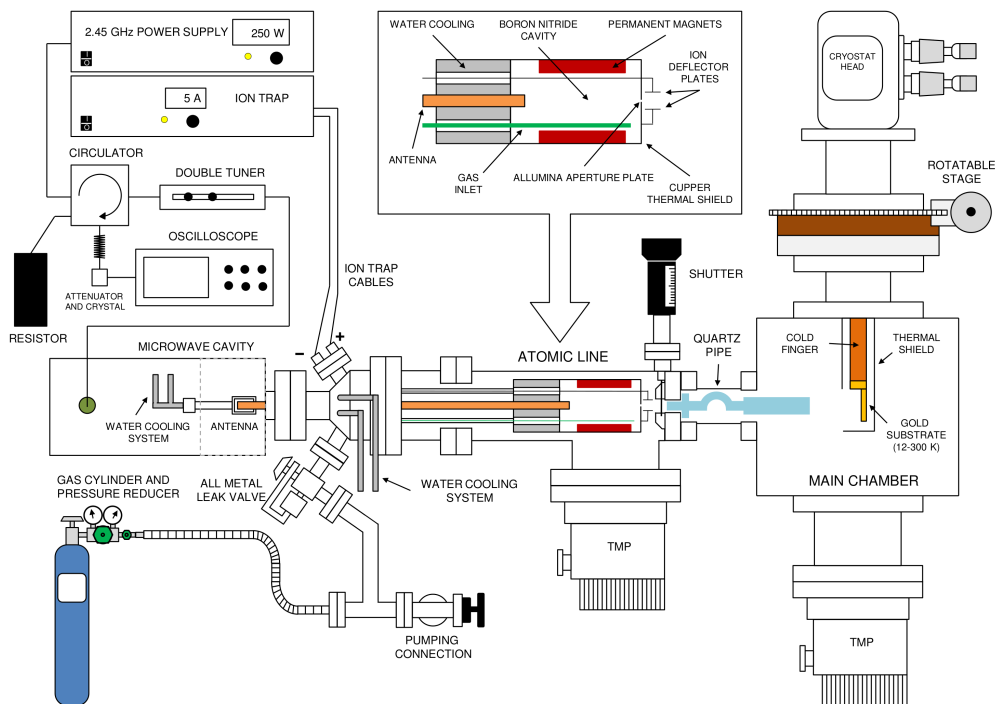
Figure 2.4. A schematic side-view of the atom line (MWAS) with the microwave plasma atom source and the main chamber.

2.2.5 Beam flux determinations

In order to measure the absolute D-atom fluxes for HABS and MWAS in the main chamber, the gold substrate is removed and the inlet of the QMS is placed at the center of the chamber facing the two atom lines, exactly at the same position and with the same angle that the substrate has when the ice is deposited and exposed to atom beam bombardment (see also Hidaka *et al*. 2007, Ioppolo *et al*. 2010). Since the sensitivity of the standard 1–200 amu QMS does not allow an accurate measurement at mass 1 amu, we measure the absolute D-atom fluxes instead of the H-atom fluxes for HABS and MWAS by following the aforementioned procedure. H-atom fluxes are then derived from the H/D ratio as obtained in selected experiments discussed in section 2.2.5.1.

The other MWAS absolute atom fluxes (*e.g.*, oxygen and nitrogen) cannot be measured mass spectrometrically because the background signal from the fractionated molecular species coming from the molecular component of the beam and the residual gas in the main chamber interferes with the signal coming straight from the atom beam. Therefore, effective O/N-atom fluxes are derived at the ice surface by using a new calibration method

described here for the first time and based on measuring the formation yield of final products of barrierless surface reactions (see sections 2.2.5.2 and 2.2.5.3).

2.2.5.1 H/D-atom beam fluxes

The D-atom and D_2 molecule fluxes for both HABS and MWAS are measured by monitoring masses 2 and 4 amu, respectively. Once the source is turned on, an increase in intensity of the D atoms is monitored with the QMS. The QMS measurements do not directly give the D-atom flux values. However, the increase in intensity of the QMS signal, ΔQ_D, is proportional to the increase in pressure in the main chamber, ΔP_D:

$$\Delta P_D = a\Delta Q_D. \tag{2.2}$$

The setup specific proportionality factor a is measured from eq. (2.2) by introducing in the main chamber D_2 molecules instead of D atoms. The choice of D_2 is given by the fact that the factor a is independent of gas species, and that the D-atom beam contains a significant amount of undissociated D_2 molecules. Therefore, an exact measurement of ΔP_D is not trivial, while ΔP_{D_2} can be easily measured. The absolute D-atom fluxes are subsequently obtained from the following expression:

$$f_D = \frac{c_D \Delta P_D \langle v \rangle}{4k_B T} = \frac{c_D a \Delta Q_D \langle v \rangle}{4k_B T}, \tag{2.3}$$

where cD is the calibration factor for the pressure gauge for D atoms taken from the specifications, $\langle v \rangle$ is the thermal velocity of the D atoms at 300 K, k_B is the Boltzmann constant, and T is the D-atom temperature. Different D-atom fluxes are obtained by varying the filament temperature and/or the D_2 inlet flow with the HABS, and by changing the plasma cavity pressure and/or plasma power with the MWAS. Figure 2.5 shows the D-atom flux values produced by the HABS (left panel) and by the MWAS (right panel), as measured at the substrate site for different parameter settings. The relative error for D-atom fluxes (HABS and MWAS) is within 10%. The absolute error is within 50%. These errors may seem large, but it should be noticed that here atom fluxes at the ice surface are actually determined experimentally, whereas in previous studies these numbers are generally only estimated.

Since an absolute H-atom flux cannot be directly measured, the comparison between H- and D-atom fluxes is difficult. We compared the H_2O_2 and D_2O_2 formation rate upon O_2 hydrogenation and deuteration, which is flux dependent, in two identical 25 K experiments for both the HABS and the MWAS. The H_2O_2 formation rate was found to be a factor of

~2 higher than the D_2O_2 formation rate for both sources. This value confirms our previous finding in Ioppolo *et al.* (2010) and is used here to scale H-atom fluxes with an uncertainty of 50%. This simplistic way of measuring a scaling factor between H- and D-atom fluxes does not however take into account that H and D atoms can differ by (i) sticking probability onto the surface, (ii) hopping rate, (iii) HO_2 + H (DO_2 + D) branching ratio and reaction barrier, (iv) desorption probability, and (v) recombination probability with other H/D atoms. Therefore, a new method for the determination of the H-atom fluxes, based on trapping H and D atoms inside an O_2 ice matrix, is used in a future work to determine the effective H/D-atom fluxes at the ice surface. In brief, the reaction H + $O_2 \rightarrow HO_2$ is barrierless under certain incoming angles in the gas phase. During co-deposition experiments, the angle dependence has a negligible physical importance since the oxygen beam provides O_2 molecules with a range of different orientations at the surface before they can align Lamberts *et al.* (2013). Therefore, the amount of HO_2 (DO_2) formed in the ice is proportional to the H- (D)-atom flux, and gives us an estimate of the effective fluxes at the cold surface. Preliminary results show that the trends found in Fig. 2.5 for the D-atom fluxes are reproduced for the H-atom fluxes as well, but an exact ratio between the H/D fluxes is still to be determined and will not be discussed here.
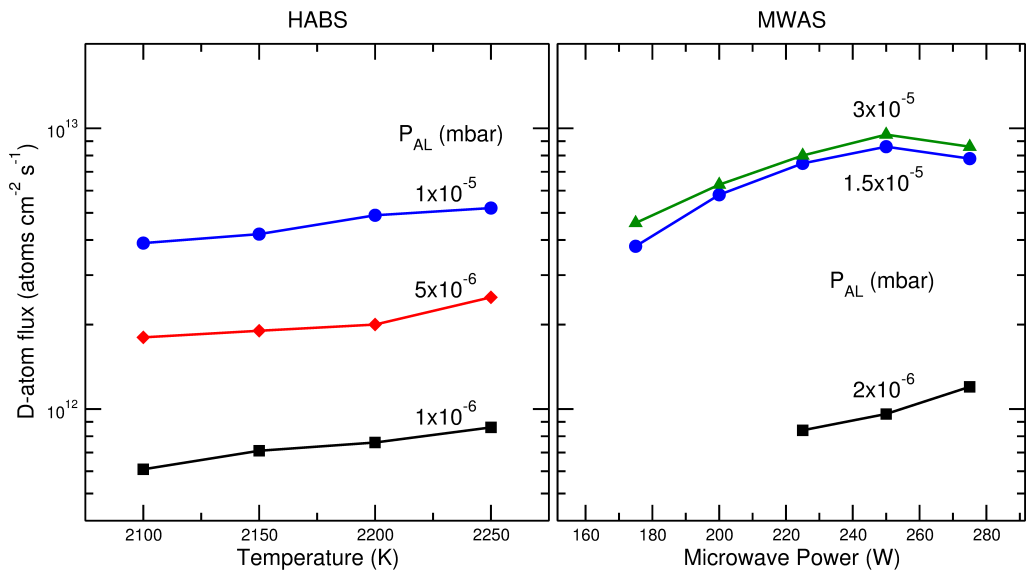
Figure 2.5. D-atom flux values as measured for the HABS (left panel) and the MWAS (right panel) at the substrate place for different parameter settings.

2.2.5.2 O-atom beam fluxes

The effective MWAS O-atom fluxes (*i.e.*, oxygen atoms directly involved in surface reactions) are derived by measuring the final column density of newly formed ozone ice after co-deposition of ^{16}O atoms and $^{18}O_2$ molecules at 15 K. The reaction $O_2 + O \rightarrow O_3$ is barrierless (Campbell & Gray 1973, Lin & Leu 1982), and therefore, we can safely assume that most of the oxygen atoms available for reaction on the surface will recombine to form ozone ice. Co-deposition experiments are used in order to avoid limitations in penetration depth of oxygen atoms into molecular oxygen ice.

Final fluxes are calculated from the knowledge of the duration of O-atom exposure, the number of monolayers of O_3 formed upon reaction, and assuming 1 ML = 10^{15} molecules cm^{-2}:

$$f_X = \frac{N_{X'} \times 10^{15}}{\text{exposure time}}, \qquad (4.4)$$

where f_X is the O-atom flux, and $N_{X'} = N_{O_3} = {}^{16}O^{18}O^{18}O + {}^{16}O^{16}O^{16}O$ in monolayers. We do not count the $^{16}O_3$ contribution three times because solid $^{16}O_3$ is not likely to be formed through the sequential merging of ^{16}O atoms on the surface of the ice. Most of the $^{16}O_2$ can indeed form in the quartz pipe through recombination of ^{16}O atoms (see section 2.2.4.2), or it originates from a not fully dissociated beam, mainly in the case that ^{16}O atoms form through dissociation of $^{16}O_2$ gas molecules. The overall contribution of $^{16}O_2$ originating from the atom line is considerably smaller when N_2O is used instead of $^{16}O_2$ as a precursor gas to produce ^{16}O atoms. This can be checked by comparing the amount of $^{16}O_3$ formed in the ice in co-deposition experiments of ^{16}O (from $^{16}O_2$) + $^{18}O_2$ at 15 K with the amount of $^{16}O_3$ formed in similar co-deposition experiments with ^{16}O from N_2O. Moreover, the amount of $^{16}O_3$ can be controlled by changing the ratio $^{16}O/^{18}O_2$. An over-abundance of $^{18}O_2$ minimizes the amount of $^{16}O_3$ formed in the ice because ^{16}O atoms react mostly with $^{18}O_2$. A negligible amount of $^{16}O_3$ in the co-deposition experiments gives $N_{O_3} \approx {}^{16}O^{18}O^{18}O$, and therefore a more direct and accurate O-atom flux value. This is true, especially when ^{16}O atoms are obtained from N_2O. Finally, the non-detection of the other ozone isotopologues (*e.g.*, $^{18}O^{16}O^{16}O$, $^{18}O^{16}O^{18}O$, or $^{18}O^{18}O^{18}O$) in our experiments indicates that isotopic exchange induced by surface destruction reactions, like $O_3 + O \rightarrow 2\,O_2$, is under the detection limit. Therefore, our method can be safely used to characterize the O-atom beam fluxes produced by the MWAS.

To quantify the amount of ozone produced in the oxygen flux-determination experiments, we derived the absorption band strength of ozone in two different ways: (i) performing an isothermal desorption experiment as described in section 2.2.3 (see left

panel of Fig. 2.6); (ii) measuring the consumption of ozone through hydrogenation reactions and assuming that hydrogen can penetrate only up to 2 ML of ozone ice. In the first case, in order to determine one monolayer of ozone, we first produce $^{16}O^{18}O^{18}O$ during 3 hrs of co-deposition of ^{16}O and $^{18}O_2$ at 35 K. Subsequently, an isothermal desorption experiment is performed at 58.5 K. From the offset between zeroth-order and first-order desorption we estimate the band strength of $^{16}O^{18}O^{18}O$. In the second case, a co-deposition of ^{16}O and $^{18}O_2$ at 15 K is performed for 3 hrs to form again $^{16}O^{18}O^{18}O$. The ice is then annealed to 50 K in order to remove the molecular oxygen and to realize a pure ozone ice. The $^{16}O^{18}O^{18}O$ ice is then exposed to H atoms at 15 K to monitor the destruction of the ozone layer. Assuming that only ~2 ML of ozone ice are fully hydrogenated, Romanzin *et al*. 2011 derive the number of ozone molecules destroyed upon hydrogenation per monolayer, which gives us back the apparent band strength for $^{16}O^{18}O^{18}O$. The final band strength for ozone is confirmed within 30% of uncertainty by the two different methods.

To verify that 1 ML of ozone is destroyed by 1 ML of H or D atoms (following reaction $O_3 + H/D \rightarrow O_2 + OH/OD$), and that our calibration methods used here to determine the D/H/O/N atom fluxes lead to coherent results, we performed a control experiment. A new co-deposition of ^{16}O and $^{18}O_2$ at 35 K is performed for 40 minutes to form ~2 ML of $^{16}O^{18}O^{18}O$ ice. The ice is then heated up to 50 K in order to have a layer of pure ozone ice. The $^{16}O^{18}O^{18}O$ ice is then exposed to D atoms at the same temperature to monitor the destruction of the ozone layer versus the time of exposure. We use D atoms instead of H atoms, because the deuterium flux is more accurately determined, as described before. Moreover, at 50 K secondary reaction products, like O_2, will desorb without reacting with D atoms and therefore leaving mainly O_3 on the surface to be processed. The right panel of Fig. 2.6 shows three infrared spectra of ozone ice at different thickness in the range of the v_3 mode (see Table 2.2). These spectra are acquired during the deuteration of the ~2 ML of $^{16}O^{18}O^{18}O$ ice. The central panel of Fig. 2.6 shows the integrated absorbance of $^{16}O^{18}O^{18}O$ versus the D-atom fluence. The left panel shows the aforementioned isothermal desorption experiment of O_3 ice at 58.5 K used to identify the integrated absorbance of solid O_3 that corresponds to 1 ML of thickness. From the knowledge of the ozone apparent band strength and the data shown in the central panel of Fig. 2.6, we derive that 1 ML of O_3 is consumed by ~1.5 ML of D atoms, which is within the experimental uncertainties of apparent band strength and D-atom flux determination.

The $^{16}O_3$ apparent band strength is obtained from the available data for $^{16}O^{18}O^{18}O$ for our setup and the ratio between the transmission band strengths for $^{16}O_3$ and $^{16}O^{18}O^{18}O$ (for the transmission band strength values see Sivaraman *et al*. (2011). According to eq. 4 standard O-atom fluxes span in the range between 10^{11} and 10^{12} atoms cm^{-2} s^{-1}. The O-atom flux values shown in Table 2.1 have to be considered as lower limits because (i) fluxes are derived indirectly (effective fluxes), (ii) some of the ^{16}O can recombine on the

surface of the ice, and (iii) $^{16}O_2$ can potentially not be further oxygenated to form ozone because it is trapped into the $^{18}O_2$ matrix. The dissociation rates shown in Table 1 are obtained by comparing the undissociated molecular component of the beam (*i.e.*, N_2O, O_2, N_2) measured mass spectrometrically (*i.e.*, with the atom source on and the QMS placed at the center of the main chamber) with the O- and N-atom flux values as derived in sections 2.2.5.2 and 2.2.5.3, respectively.
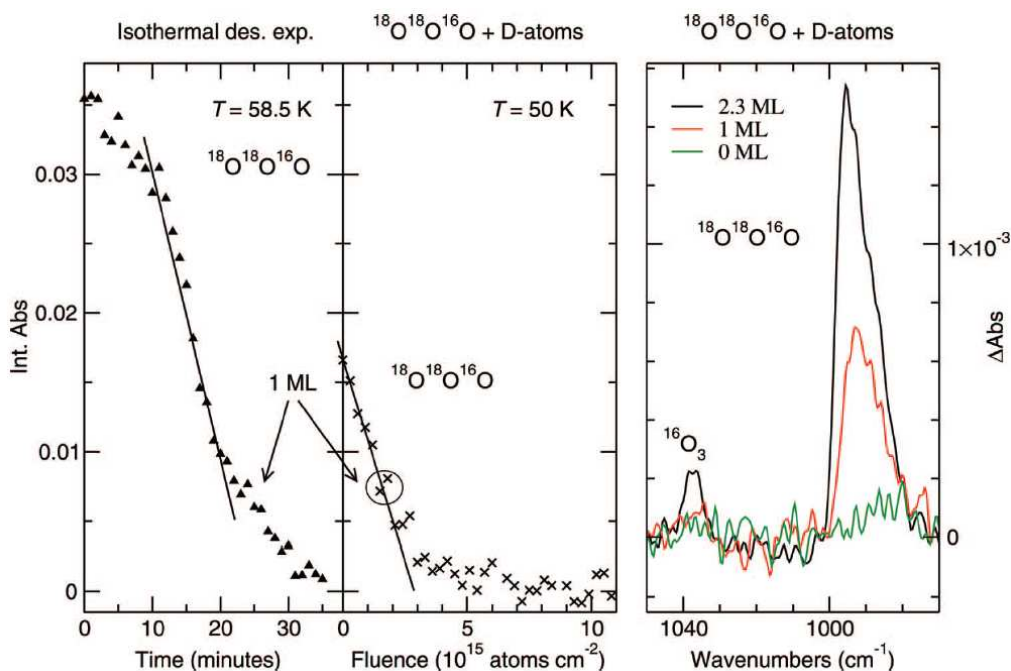
Figure 2.6. The left panel shows the isothermal desorption experiment of O_3 ice at 58.5 K. The central pannel shows the destruction of ~2 ML thick O_3 ice versus the D-atom fluence at 50 K. In both left and center panel, the lines and the circle are used to guide the eye. The right panel shows selected infrared spectra of ozone deuteration at 50 K for different ice thicknesses in the spectral range of the v_3 mode.

2.2.5.3 N-atom beam fluxes

As for the MWAS O-atom fluxes, the determination of effective nitrogen-atom fluxes is obtained indirectly by measuring the final column density of newly formed dinitrogen trioxide (N_2O_3) ice after co-deposition of ^{15}N atoms and NO molecules at 15 K. In this particular experiment, a sequence of barrierless (or very low barrier) surface reactions is involved in the formation of N_2O_3 (Campbell & Gray 1973, Schieferstein *et al*. 1983, Markwalder *et al*. 1993): $N + NO \rightarrow N_2 + O$, $NO + O \rightarrow NO_2$, and $NO_2 + NO \rightarrow N_2O_3$. Therefore in this specific case, N-atom fluxes are directly proportional to the amount of

N_2O_3 formed in the ice, and are determined by using eq. (2.4), where f_X is the N-atom flux, and $N_{X'} = N_{N_2O_3}$ which is the amount of monolayers of N_2O_3 formed in the ice after a certain time of N-atom exposure.

As in section 2.2.5.2, we use two different methods to obtain the apparent N_2O_3 band strength. In particular, two new co-deposition experiments of NO and O_2 are performed at 15 K. Also in this case N_2O_3 is formed through surface reactions. The ice obtained from these two experiments is in both cases heated up to remove the NO trapped in the ice. In one of the two experiments, the ice temperature is then kept at 121 K to monitor the desorption of N_2O_3 (isothermal desorption experiment). From this experiment we obtain the band strength for N_2O_3, as discussed in the latter sections. In the second experiment, the ice is cooled down again to 15 K and subsequently hydrogenated to see the destruction of N_2O_3. The penetration depth of hydrogen into N_2O_3 ice is expected to involve only a few monolayers, as for O_3, CO, and NO ice (Romanzin *et al*. 2011, Fuchs *et al*. 2009, Fedoseev *et al*. 2012). Therefore, assuming that only ~2 ML of N_2O_3 are consumed by the surface hydrogenation of the ice, we can estimate the band strength of N_2O_3 which is found to be consistent with the value obtained from the isothermal desorption experiment within 40% of uncertainty.

The N-atom flux values are roughly one order of magnitude lower than the O-atom values (see Table 2.1). As explained in section 2.5.2, these values are all lower limits, because of the way the fluxes are derived. In the specific case of nitrogen fluxes, the formation of N_2O_3 is a three step reaction, and therefore the single reactant can further react with the others to form N_2O_3, or alternatively desorb, or be trapped in a NO matrix. Therefore, we expect the O- and N-atom absolute fluxes to be higher than reported in Table 2.1.

Table 2.1. The effective O- and N-atom fluxes as derived from the formation yields of solid species in the ice upon barrierless reactions (see eq. 4.4).

Effective atom flux	High (atoms cm^{-2} s^{-1})	Dissociation rate (%)	Low (atoms cm^{-2} s^{-1})	Dissociation rate (%)
^{16}O from O_2	$9 \cdot 10^{11}$	8	$2 \cdot 10^{11}$	12
^{16}O from N_2O	$7 \cdot 10^{11}$	19	$1 \cdot 10^{11}$	10
^{15}N from $^{15}N_2$	$9 \cdot 10^{10}$	0.4	—	—
^{14}N from $^{14}N_2$	$8 \cdot 10^{10}$	0.4	—	—

2.3 Experimental results

In this section we present the first science results obtained with SURFRESIDE[2] in order to demonstrate its performance and to illustrate the potential of the experimental setup. Figure

2.7 shows the IR spectrum of ^{13}CO co-deposited with oxygen and hydrogen atoms on a 13.5 K gold substrate ($^{13}CO + O + H$). This spectrum is compared to co-deposition spectra of ^{13}CO and oxygen atoms ($^{13}CO + O$); ^{13}CO and hydrogen atoms ($^{13}CO + H$); and oxygen atoms and hydrogen atoms ($O + H$). In all four experiments, oxygen atoms are produced by the MWAS, while hydrogen atoms are formed by the HABS. The ^{13}CO deposition rate (0.0075 ML s^{-1}) as well as O- and H-atom fluxes ($1 \cdot 10^{11}$ and $1 \cdot 10^{13}$ atoms cm^{-2} s^{-1}, respectively) are kept the same in all the experiments and the spectra shown in Fig. 2.7 are all acquired after 45 minutes of co-deposition. As discussed in section 2.2.5, the O-atom flux value is an effective flux at the ice surface, while the H-atom flux is scaled from the absolute D-atom flux value which is probably higher than the effective flux at the cold surface. Therefore for instance, the H/O ratio presented below has to be considered as an upper limit for H atoms. Oxygen atoms are obtained by dissociating N_2O in the microwave atom source. This explains the presence of nitrogen-bearing species in the ice when the O-atom beam line is used (see Fig. 2.7 and Table 2.2).

The aforementioned experiments demonstrate the advantage of having a double atom beam line when investigating surface atom addition reactions. The choice of using one or both atom lines allows us to select, investigate, compare, and combine different reaction channels. For instance, in order to better interpret results from the simultaneous hydrogenation and oxygenation of solid CO, it is necessary to first distinguish the single contributions of the different reaction channels, *i.e.*, O + H, CO + H, and CO + O:

• The O + H spectrum in Fig. 2.7 shows the presence of N_2O from the not fully (N_2O) dissociated O-atom beam. The amount of water formed in this experiment is around the detection limit, while H_2O_2 is below the detection limit. The limiting factor on the production of water ice is the number of O atoms available to react with the H atoms on the cold surface (H/O ~ 100). After 45 minutes of co-addition of O and H atoms, only 0.2 ML of water can be formed assuming that all the oxygen available will react to form water. Surface formation of water ice through the hydrogenation of $O/O_2/O_3$ has been the object of many recent physical-chemical and astrochemical relevant studies (Dulieu *et al.* 2010, Miyauchi *et al.* 2008, Ioppolo *et al.* 2008, Matar *et al.* 2008, Ioppolo *et al.* 2010, Cuppen *et al.* 2010, Lamberts *et al.* 2013, Mokrane *et al.* 2009, Romanzin *et al.* 2011) and is not extensively discussed in this paper again.

• Formaldehyde is clearly present in the $^{13}CO + H$ spectrum (Fig. 2.7), whereas methanol is not. As previously shown Watanabe & Kouchi (2002a), Fuchs *et al.* (2009), formaldehyde and methanol are the main final products of solid CO hydrogenation. However, methanol is under the detection limit in the experiment shown in Fig. 2.7 because of the low penetration depth (~ 4 ML) of hydrogen atoms into a CO ice Fuchs *et al.* (2009), as well as a comparable abundance of CO with respect to hydrogen atoms (CO/H ~ 0.75). The amount of hydrogen atoms available to react with CO molecules is

further lowered by the molecular hydrogen recombination on the surface. Therefore, the newly formed H_2CO ice is not further hydrogenated under these experimental conditions. For other conditions (see Fuchs *et al.* 2009) it does.

- The ^{13}CO + O spectrum in Fig. 2.7 is the richest in absorption features due to N-bearing molecules, like N_2O, NO_2, N_2O_3, $(NO)_2$ dimer, and NO monomer. These species are either coming from the not fully dissociated O-atom beam or are formed through surface oxygenation of other N-bearing species. Alternatively, O atoms recombine in the ice with each other to form O_2 and O_3, or react with CO to form carbon dioxide.

- The surface reaction products present in the ^{13}CO + O + H spectrum (Fig. 2.7) come from the single isolated aforementioned reaction routes as well as from the interaction of different reaction products with each other. Ozone, methanol, and hydrogen peroxide are under the detection limit, while water ice is slightly above it. Formaldehyde and mostly carbon dioxide are visible in the spectrum. The only nitrogen-bearing species clearly present in the ice is N_2O. In the ^{13}CO + O + H experiment the final column density of solid $^{13}CO_2$ is ten times higher than in the case of the ^{13}CO + O experiment (see inset in Fig. 2.7).
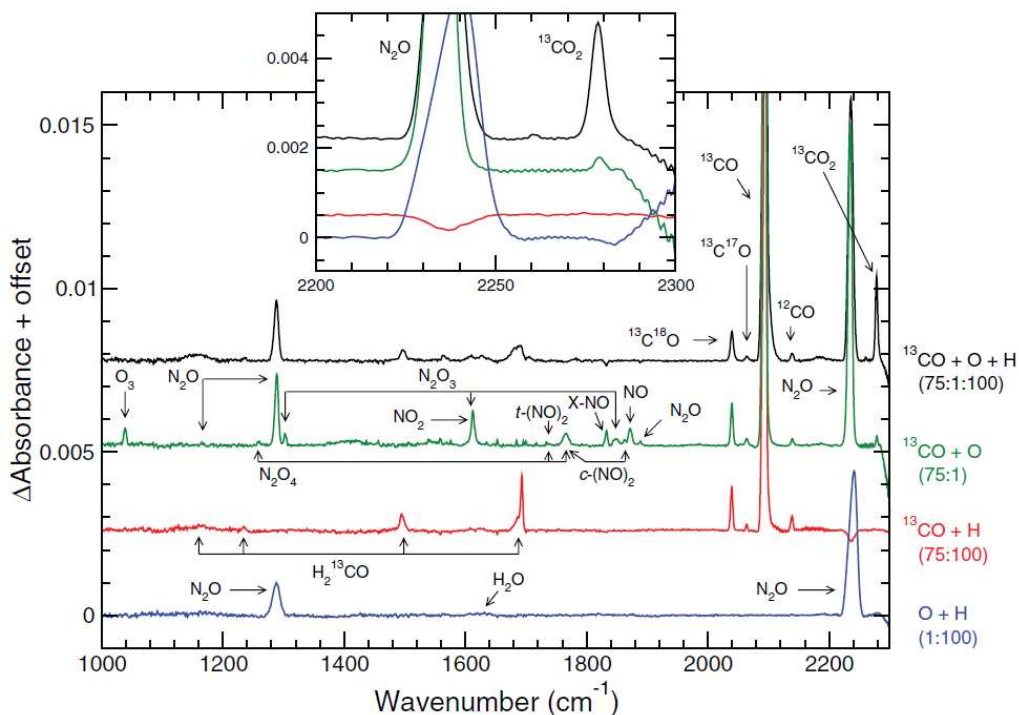
Figure 2.7. RAIR co-deposition spectra of ^{13}CO, O- and H-atoms on a 13.5 K gold substrate (top-spectrum in main panel, ^{13}CO + O + H); ^{13}CO and O-atoms (second spectrum from the top, ^{13}CO + O); ^{13}CO and H-atoms (third spectrum from the top, ^{13}CO + H); and O- and H-atoms (bottom-spectrum, O + H). The inset figure shows the $^{13}CO_2$ stretching mode region for all four experiments.

The focus of the following section is on the formation of solid carbon dioxide at low temperatures through surface reactions induced by non-energetic processing. The chemical origin of solid CO_2 as observed in our experiments is subsequently discussed and placed in an astronomical context.

Table 2.2. Assigned infrared features with their corresponding references.

Position, cm^{-1}	Species	Mode	Reference
1040	O_3	v_3	Brosset *et al.* (1993), Chaabouni *et al.* (2000), Bennett & Kaiser (2005)
1162	$H_2^{13}CO$	v_4	Wohar & Jagodzinski (1991)
1167	N_2O	$2v_2$	Dows (1957), Łapiński *et al.* (2001)
1240	$H_2^{13}CO$	v_6	Wohar & Jagodzinski (1991)
1260	N_2O_4	v_{11}	Holland & Maier II (1983)
1289	N_2O	v_1	Jamieson *et al.* (2005), Dows (1957), Łapiński *et al.* (2001)
1304	N_2O_3	v_3	Fateley *et al.* (1959), Nour *et al.* (1983)
1497	$H_2^{13}CO$	v_3	Wohar & Jagodzinski (1991)
1612	NO_2/N_2O_3	v_3/v_2	Fateley *et al.* (1959), Jamieson *et al.* (2005) / Fateley *et al.* (1959), Nour *et al.* (1983)
1630	H_2O	v_2	Hagen & Tielens (1981)
1694	$H_2^{13}CO$	v_2	Wohar & Jagodzinski (1991)
1737	t-$(NO)_2/N_2O_4$	v_1/v_9	Fateley *et al.* (1959) / Holland & Maier II (1983)
1766	c-$(NO)_2/N_2O_4$	v_5/v_9	Fateley *et al.* (1959), Nour et. al. (1984) / Holland & Maier II (1983)
1833	X-NO		Fedoseev *et al.* (2012)
1850	N_2O_3	v_1	Fateley *et al.* (1959), Nour *et al.* (1983)
1864	c-$(NO)_2$	v_1	Fateley *et al.* (1959), Nour *et al.* (1984)
1872	NO (monomer)	v_1	Fateley *et al.* (1959), Nour *et al.* (1984), Holland & Maier II (1983)
1888	N_2O	v_1+v_2	Dows (1957), Łapiński *et al.* (2001)
2039	$^{13}C^{18}O$	v_1	Loeffler *et al.* (2005)
2066	$^{13}C^{17}O$	v_1	Loeffler *et al.* (2005)
2096	^{13}CO	v_1	Ewing & Pimentel (1961)
2139	CO	v_1	Sandford *et al.* (1988)
2235	N_2O	v_3	Dows (1957), Łapiński *et al.* (2001), Jamieson *et al.* (2005)
2278	$^{13}CO_2$	v_3	Berney & Eggers (1964)

2.3.1 Astrochemical implications

It is generally accepted that due to its low gas-phase abundance ($CO_2^{gas}/CO_2^{ice} \ll 1$) carbon dioxide is formed in the solid phase in the interstellar medium on the surface of icy dust grains (10–20 K) through surface reactions involving energetic (*e.g.*, UV photolysis, cosmic rays irradiation, thermal processing) and non-energetic processing (*e.g.*, atom bombardment), see van Dishoeck *et al.* (1996), Boonman *et al.* (2003). Solid CO is the CO_2 precursor that has been mostly studied in literature. The most cited surface reaction routes involving solid CO are:

$$CO + O \rightarrow CO_2, \tag{2.5}$$
$$HCO + O \rightarrow CO_2 + H, \tag{2.6}$$
$$CO + OH \rightarrow CO_2 + H. \tag{2.7}$$
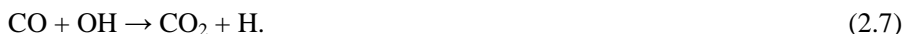
These reaction routes can be activated by both energetic and non-energetic processing. For instance, solid CO_2 can form from the interaction of energetic photons/ions and pure CO molecules or CO-bearing mixtures (Garozzo *et al.* 2011, Ioppolo *et al.* 2013, Moore *et al.* 1991, Gerakines *et al.* 1996, Ehrenfreund *et al.* 1997, Palumbo *et al.* 1998, Satorre *et al.* 2000, Watanabe *et al.* 2002b, Loeffler *et al.* 2005, Ioppolo *et al.* 2009). Solid CO_2 can, however, also be formed through photolysis/radiolysis of amorphous carbon capped with a layer of water or oxygen ice (Mennella *et al.* 2004, Mennella *et al.* 2006, Gomis & Strazzulla 2005, Raut *et al.* 2012, Fulvio *et al.* 2012).

In space, thermal atom-addition induced chemistry is more dominant in quiescent cold interstellar regions, where newly formed species are protected from radiation to a great extent by dust particles. In these regions, solid CO_2 can form through reactions (2.5)-(2.7). Reaction (2.5) has been investigated experimentally in Roser *et al.* (2001), Madzunkov *et al.* (2006), Raut *et al.* (2012). Raut & Baragiola (2011) showed that CO_2 forms in small quantities during co-deposition of CO and cooled O atoms and O_2 molecules into thin films at 20 K. The reason for the low CO_2 yield is that O atoms react preferentialy with O to form O_2, and with O_2 to form O_3. The latter experimental findings, also supported by theoretical studies (Talbi *et al.* 2006), indicate that the surface reaction (2.5) has a barrier of ~2000 K in the gas phase (Slanger *et al.* 1972). Moreover, Goumans & Andersson (2010) showed that although tunnelling increases the surface reaction rate for reaction $O(^3P) + CO$ at low temperatures, the onset of tunnelling is at too low temperatures for the reaction to significantly contribute to the formation of solid CO_2 under interstellar conditions. Therefore, reaction (2.5) is not an efficient CO_2 formation pathway unless energetic processing is involved. Our laboratory results from the CO + O experiment (Fig. 2.7) show

indeed a more efficient production of ozone compared to carbon dioxide at 13.5 K, and are consistent with previous findings.

Solid CO_2 can also form through reaction (2.6) (Ruffle & Herbst 2001), which is experimentally challenging to investigate in the solid phase because other CO_2 formation reaction routes will compete. Moreover, when the H/O ratio is in favor of H atoms, the hydrogenation of CO ice will convert most of the HCO in formaldehyde and methanol. Therefore, this route is negligible under our experimental conditions, and we will further not consider it in our discussion.

Alternatively, solid CO_2 can be formed through reaction (2.7), which yields a HOCO intermediate. This complex can directly dissociate, forming solid CO_2 and leaving a H atom, or can be stabilized by intramolecular energy transfer to the ice surface and eventually react with an incoming H atom in a barrierless manner to form CO_2 and H_2 or other products with a purely statistical branching ratio as theoretically shown by Goumans et al. (2008). Recently, several independent experimental studies showed that reaction (2.7) is an efficient surface CO_2 formation channel without need for an energetic input (Oba et al. 2010a, Ioppolo et al. 2011a, Noble et al. 2011. In earlier work (Ioppolo et al. 2011a), we demonstrated with a one beam line system the formation of CO_2 at low temperatures through reaction (2.7) by hydrogenation of a $CO:O_2$ binary ice mixture. In that case, we used a single H-atom beam line. Here, we are able to compare reactions (2.5) and (2.7) under the same experimental conditions by using two atom beam lines.

Reactions (2.5)-(2.7) have never been experimentally compared with each other before under the same laboratory conditions. So far, only theoretical work investigated these surface reactions within a larger astrochemical reaction network. For instance, Garrod & Pauly (2011) studied in their three-phase (gas/surface/mantle) astrochemical model the formation and evolution of interstellar dust-grain ices under dark-cloud conditions, with a particular emphasis on CO_2. By including reactions (2.5)-(2.7) in their reaction network, they were able to reproduce the observed behavior of CO_2, CO, and water ice in the interstellar medium. Furthermore, reaction (2.7) was found to be efficient enough to account for the observed CO_2 ice production in dark clouds.

Our experimental results confirm the conclusions found in Garrod & Pauly (2011). The $^{13}CO_2$ formed in the $^{13}CO + O + H$ experiment is ten times more abundant than the $^{13}CO_2$ formed in the $^{13}CO + O$ experiment. In the $^{13}CO + O + H$ experiment, solid $^{13}CO_2$ is mainly formed through the HOCO intermediate. Under these experimental conditions, all the O atoms will indeed react in a barrierless way with H atoms to form hydroxyl radicals that will either react with another H atom to form H_2O, or will react with ^{13}CO to form $^{13}CO_2$. The non-detection of ozone and other N-bearing products formed in the ice is due to the overabundance of H atoms, and confirms that O atoms are all used-up to form OH radicals. Moreover, the presence of formaldehyde in the ice indicates that H atoms are over

abundant with respect to O atoms. Solid HCOOH and H_2CO_3 are under the detection limit. The non-detection of these two species that are formed through the hydrogenation of the HOCO complex and the reaction of the latter with the hydroxyl radical, respectively, Ioppolo *et al*. (2011b) and Oba *et al*. (2010b) indicate that the HOCO complex is efficiently dissociated in CO_2 + H under our experimental conditions.

The fact that the $^{13}CO_2$ formed in the ^{13}CO + O + H experiment is ten times more abundant than the $^{13}CO_2$ formed in the ^{13}CO + O experiment indicates that reaction (2.7) has a lower activation barrier and is faster than reaction (2.5). Chang & Herbst (2012) investigated the surface reaction CO + O + H among others by means of a unified microscopic-macroscopic Monte Carlo simulation of gas-grain chemistry in cold interstellar clouds in which both the gas-phase and the grain-surface chemistry are simulated by a stochastic technique. In their model, solid CO_2 is produced mainly by reaction (2.7), which occurs by a so-called "chain reaction mechanism", in which an H atom first combines with an O atom lying above a CO molecule, so that the OH does not need to undergo horizontal diffusion to react with CO. Their CO_2 calculated abundances are in good agreement with observations (Oberg *et al*. 2011). Moreover, this scenario is not far from our experimental conditions, where O and H atoms meet to form OH radicals that then further react with neighboring CO molecules to form CO_2. This shows that SURFRESIDE^2 is suited to investigate astrochemical relevant surface reaction networks. Chang & Herbst (2012) finally suggested that the solid CO formed in early cold cloud stages via accretion and surface reactions is mainly converted into CO_2 through reaction (2.7). This makes reaction (2.7) to be most likely the main non-energetic CO_2 formation route under early cold cloud conditions, where H atoms are orders of magnitude more abundant than O atoms (Dupuis *et al*. 2009). Chang & Herbst (2012) also suggested that the conversion of CO into CO_2 becomes inefficient at later times, where, for the low-mass YSO case, there can be a high abundance of almost pure CO, with some conversion to formaldehyde and methanol. Under these conditions, solid CO_2 can still be formed via energetic processing (Ioppolo *et al*. 2013).

2.4 Conclusions

We have presented a novel and versatile UHV setup designed for the quantitative investigation of interstellar relevant surface processes under fully controlled conditions. The system implements a main chamber and two atom beam lines. Molecules are deposited in the main chamber onto a cold gold substrate, able to reproduce interstellar dense cloud temperatures and ice thicknesses. The ice is monitored with a FTIR spectrometer, while gas phase species present in the chamber are monitored with a QMS. As for interstellar ices in dense cloud conditions, laboratory ices are exposed to (H/D/O/N) atom beam fluxes. These

are accurately determined using a chemical calibration procedure. The choice of using one or both atom lines sequentially or at the same time allows us to characterize interstellar relevant reaction channels in a bottom-up approach. In particular, the design of the system is suited for the isolation of single surface reaction channels and the comparison of their efficiency with those of other surface reactions that lead to the same final products. Here we demonstrate the potential of the system by studying the efficiency of solid CO_2 formation through surface reactions induced by atom addition. We find that under the same experimental conditions CO_2 is formed through the reaction $CO + OH$ more efficiently than through the reaction $CO + O$. Our results are in good agreement with the most recent astrochemical models and observations (Chang & Herbst 2012, Oberg *et al*. 2011), and therefore show that SURFRESIDE[2] has the potential to solve important questions within the field of astrochemistry.

The results that we present here illustrate only one of the possible applications of SURFRESIDE[2]. This system will indeed shine light on several other unresolved topics in astrochemistry, such as the competition between hydrogenation and deuteration of interstellar relevant species linking planetary H/D abundances to interstellar processes. SURFRESIDE[2] is ultimately designed to study the surface formation of complex organic molecules (COMs), sugars, and amino-acids under interstellar relevant conditions by sequential or co-addition of the different reactive components of those species onto the cold substrate. The use of a double beam line system is essential to achieve this aim. The future implementation of these and similar experimental results into astrochemical models that take into account astronomical fluxes and timescales as well as energetic and non-energetic processes is needed to understand the pathways that lead to molecular complexity in space.

References

Acharyya K., Fuchs G. W., Fraser H. J., van Dishoeck E. F., Linnartz H., 2007, A&A, 466, 1005

Bennett C. J., Jamieson C., Mebel A. M., Kaiser R. I., 2004, PCCP, 6, 735

Bennett C. J., Kaiser R. I., 2005, ApJ, 635, 1362

Bergh H. S., Gergen B., Nienhaus H., Majumdar A., Weinberg W. H., McFarland E. W., 1999, Rev. Sci. Instrum., 70, 2087

Berney C. V., Eggers D. F., Jr., 1964, JCP, 40, 990

Bisschop S. E., Fuchs G. W., van Dishoeck E. F., Linnartz H., 2007, A&A, 474, 1061

Blagojevic V., Petrie S., Bohme D. K., 2003, MNRAS, 339, L7

Boonman A. M. S., van Dishoeck E. F., Lahuis F., Doty S. D., 2003, A&A, 399, 1063

Brosset P., Dahoo R., Gauthierroy B., Abouafmarguin L., Lakhlifi A., 1993, Chem. Phys., 172, 315

Campbell I. M., Gray C. N., 1973, Chem. Phys. Lett., 18, 607

Chaabouni H., Schriver-Mazzuoli L., Schriver A., 2000, Low Temp. Phys., 26, 712

Chang Q., Herbst E., 2012, ApJ, 759, 147

Congiu E. *et al*., 2012a, ApJL, 750, L12

Congiu E., Chaabouni H., Laffon C., Parent P., Baouche S., Dulieu F., 2012b, JCP, 137, 054713

Cuppen H. M., Ioppolo S., Romanzin C., Linnartz H., 2010, PCCP, 12, 12077

Dows D. A., 1957, JCP, 26, 745

Dulieu F., Amiaud L., Congiu E., Fillion J., Matar E., Momeni A., Pirronello V., Lemaire J. L., 2010, A&A, 512, A30

Dupuis J., Oliveira C. M., Hebrard G. H., Moos H. W., Sonnentrucker P., 2009, ApJ, 690, 1045

Ehrenfreund P., Boogert A. C. A., Gerakines P. A., Tielens A. G. G. M., van Dishoeck E. F., 1997, A&A, 328, 649

Ewing G. E., Pimentel G. C., 1961, JCP, 35, 925

Fateley W. G., Bent H. A., Crawford B., Jr., 1959, JCP, 31, 204

Fedoseev G., Ioppolo S., Lamberts T., Zhen J. F., Cuppen H. M., Linnartz H., 2012, JCP, 137, 054714

Fraser H. J., Collings M. P., McCoustra M. R. S., Williams D. A., 2001, MNRAS, 327, 1165

Fuchs G.W., Cuppen H. M., Ioppolo S., Bisschop S. E., Andersson S., van Dishoeck E. F., Linnartz H., 2009, A&A, 505, 629

Fulvio D., Raut U., Baragiola R. A., 2012, ApJL, 752, L33

Garozzo M., La Rosa L., Kanuchova Z., Ioppolo S., Baratta G. A., Palumbo M. E., Strazzulla G., 2011, A&A, 528, 118

Garrod R. T., Pauly T., 2011, ApJ, 735, 15

Gerakines P. A., Schutte W. A., Ehrenfreund P., 1996, A&A, 312, 289

Gomis O., Strazzulla G., 2005, Icarus, 177, 570

Goumans T. P. M., Andersson S., 2010, MNRAS, 406, 2213

Goumans T. P. M., Uppal M. A., Brown W. A., 2008, MNRAS, 384, 1158

Greenler R. G., 1966, JCP, 44, 310

Hagen W., Tielens A. G. G. M., JCP, 75, 4198

Hidaka H., Kouchi A., Watanabe N., 2007, JCP, 126, 204707

Hidaka H., Watanabe N., Shiraki T., Nagaoka A., Kouchi A., 2004, ApJ, 614, 1124

Hiraoka K., Ohashi N., Kihara Y., Yamamoto K., Sato T., Yamashita A., 1994, Chem. Phys. Lett., 229, 408

Holland R. F., Maier II W. B., 1983, JCP, 78, 2928

Ioppolo S., Cuppen H. M., Romanzin C., van Dishoeck E. F., Linnartz H., 2008, ApJ, 686, 1474

Ioppolo S., Cuppen H. M., Romanzin C., van Dishoeck E. F., Linnartz H., 2010, PCCP, 12, 12065

Ioppolo S., Cuppen H. M., van Dishoeck E. F., Linnartz H., 2011b, MNRAS, 410, 1089

Ioppolo S., Palumbo M. E., Baratta G. A., Mennella V., 2009, A&A, 493, 1017

Ioppolo S., Sangiorgio I., Baratta G. A., Palumbo M. E., 2013, A&A, 554, A34

Ioppolo S., van Boheemen Y., Cuppen H. M., van Dishoeck E. F., Linnartz H., 2011a, MNRAS, 413, 2281

Jamieson C. S., Bennett C. J., Mebel A. M., Kaiser R. I., 2005, ApJ, 624, 436

Lamberts T., Cuppen H. M., Ioppolo S., Linnartz H., 2013, PCCP, 15, 8287

Łapiński A., Spanget-Larsen J., Waluk J., Radziszewski J. G., 2001, JCP, 115, 1757

Lin C. L., Leu M. T., 1982, Int. J. Chem. Kinet., 14, 417

Linnartz H. *et al.*, 2011, in IAU Symposium, edited by J. Cernicharo and R. Bachiller (2011), 280, 390

Loeffler M. J., Baratta G. A., Palumbo M. E., Strazzulla G., Baragiola R. A., 2005, A&A, 435, 587

Madzunkov S., Shortt B. J., Macaskill J. A., Darrach M. R., Chutjian A., 2006, Phys. Rev. A, 73, 020901

Markwalder B., Gozel P., van den Bergh H., 1993, JCP, 97, 5260

Matar E., Congiu E., Dulieu F., Momeni A., Lemaire J. L., 2008, A&A, 492, L17

Mennella V., Baratta G. A., Palumbo M. E., Bergin E. A., 2006, ApJ, 643, 923

Mennella V., Palumbo M. E., Baratta G. A., 2004, ApJ, 615, 1073

Miyauchi N., Hidaka H., Chigai T., Nagaoka A., Watanabe N., Kouchi A., 2008, Chem. Phys. Lett., 456, 27

Mokrane H., Chaabouni H., Accolla M., Congiu E., Dulieu F., Chehrouri M., Lemaire J. L., 2009, ApJL, 705, L195

Moore M. H., Khanna R., Donn B., 1991, J. Geophys. Res., 96, 17541

Noble J. A., Dulieu F., Congiu E., Fraser H. J., 2011, ApJ, 735, 121

Nour E. M., Chen L. H., Laane J., 1983, J. Phys. Chem., 87, 1113

Nour E. M., Chen L. H., Strube M. M., Laane J., 1984, J. Phys. Chem., 88, 756

Oba Y., Watanabe N., Kouchi A., Hama T., Pirronello V., 2010a, ApJL, 712, L174

Oba Y., Watanabe N., Kouchi A., Hama T., Pirronello V., 2010b, ApJ, 722, 1598

Öberg K. I., Boogert A. C. A., Pontoppidan K. M., van den Broek S., van Dishoeck E. F., Bottinelli S., Blake G. A., Evans II N. J., 2011, ApJ, 740, 109

Palumbo M. E., Baratta G. A., Brucato J. R., Castorina A. C., Satorre M. A., Strazzulla G., 1998, A&A, 334, 247

Raut U., Baragiola R. A., 2011, ApJL, 737, L14

Raut U., D. Fulvio, M. J. Loeffler, R. A. Baragiola, 2012, ApJ, 752, 159

Romanzin C., Ioppolo S., Cuppen H. M., van Dishoeck E. F., Linnartz H., 2011, JCP, 134, 084504

Roser J. E., Vidali G., Manrico G., Pirronello V., 2001, ApJ, 555, L61

Ruffle D. P., Herbst E., 2001, MNRAS, 324, 1054

Sandford S. A., Allamandola L. J., Tielens A. G. G. M., Valero G. J., 1988, ApJ, 329, 498

Satorre M. A., Palumbo M. E., Strazzulla G., 2000, Astrophys. & Space Sci., 274, 643

Schieferstein M., Kohse-Höinghaus K., Stuhl F., 1983, Ber. Bunsenges. Phys. Chem., 87, 361

Sivaraman B., Mebel A. M., Mason N. J., Babikov D., Kaiser R. I., 2011, PCCP (Incorporating Faraday Transactions), 13, 421

Slanger T. G., Wood B. J., Black G., 1972, JCP, 57, 233

Talbi D., Chandler G. S., Rohl A. L., 2006, Chem. Phys., 320, 214

Teolis B. D., Loeffler M. J., Raut U., Fama M., Baragiola R. A., 2007, Icarus, 190, 274

Tschersich K. G., 2000, J. Appl. Phys., 87, 2565

Tschersich K. G., Fleischhauer J. P., Schuler H., 2008, J. Appl. Phys., 104, 034908

Tschersich K. G., von Bonin V., 1998, J. Appl. Phys., 84, 4065

van Dishoeck E. F. *et al*., 1996, A&A, 315, L349

Watanabe N., Hidaka H., Kouchi A., 2006, in Astrochemistry - From Laboratory Studies to Astronomical Observations, edited by R. I. Kaiser, P. Bernath, Y. Osamura, S. Petrie, and A. M. Mebel, vol. 855 of AIP Conf. Ser., pp. 122–127.

Watanabe N., Kouchi A., 2002a, ApJL, 571, L173

Watanabe N., Kouchi A., 2002b, ApJ, 567, 651

Wohar M. M., Jagodzinski P. W., 1991, J. Molec. Spectrosc., 148, 13

III

Surface NO Hydrogenation: A Solid Pathway to NH$_2$OH Formation in Space

Icy dust grains in space act as catalytic surfaces on which complex molecules form. These molecules are synthesized through exothermic reactions from precursor radicals and, mostly, hydrogen atom additions. Among the resulting products are species of biological relevance, such as hydroxylamine - NH$_2$OH - a precursor molecule in the formation of amino acids. In this Letter, laboratory experiments are described that demonstrate NH$_2$OH formation in interstellar ice analogs for astronomically relevant temperatures via successive hydrogenation reactions of solid nitric oxide (NO). Inclusion of the experimental results in an astrochemical gas–grain model proves the importance of a solid-state NO + H reaction channel as a starting point for prebiotic species in dark interstellar clouds and adds a new perspective to the way molecules of biological importance may form in space.

3.1 Introduction

Molecular astrophysicists explain the chemical diversity and complexity in space as the cumulative outcome of gas, grain, and gas–grain interactions in dense interstellar clouds, the birth sites of stars and planets (Wakelam *et al*. 2010; Herbst & van Dishoeck 2009). More than 180 species have been unambiguously identified so far, and icy dust grains are the template where stable species like acetonitrile, a precursor molecule for the simplest amino-acid glycine, are formed (Codella *et al*. 2009, Hudson *et al*. 2008). In quiescent dark clouds, cold grains indeed provide micrometer-sized surfaces onto which gas-phase species accrete, meet, and react (van Dishoeck 2004, Öberg *et al*. 2011). Particularly, hydrogenation of interstellar ices, *i.e*., H-atom additions, can induce the formation of species in the solid phase and, therefore, it has been the topic of recent laboratory-based studies. The efficient surface formation of the bulk of interstellar ices, *i.e*., water, methanol, carbon dioxide, formaldehyde, and formic acid has been demonstrated through H-atom additions of CO- and/or O_2-ices under interstellar relevant conditions (Watanabe *et al*. 2006, Fuchs *et al*. 2009, Cuppen *et al*. 2010, Noble *et al*. 2011). In space, thermal atom-addition induced chemistry occurs mostly at low temperatures ($\sim$ 10 K), *i.e*., in the innermost part of the clouds where newly formed species are protected from radiation to a great extent by dust particles. These regions are part of collapsing envelopes that feed young stellar objects and that provide the original material from which comets and ultimately planets are made (Sandford *et al*. 2006). The solid-state formation of organic material is therefore of considerable interest, as efficient surface reaction routes provide a general recipe to form prebiotic species in star and planet-forming regions (Charnley *et al*. 2001). The focus in this Letter is on hydroxylamine, NH_2OH, that has been proposed as an important precursor species in the formation of amino acids (Blagojevic *et al*. 2003, Barrientos *et al*. 2012). Inter- and circumstellar nitrogen chemistry is rather poorly understood as well as the mechanisms leading to the inclusion of interstellar nitrogen into a refractory aminated species. Charnley *et al*. (2001) suggested that hydroxylamine can be formed through hydrogenation of NO ice under quiescent cloud conditions:

$$NO \xrightarrow{H} HNO \xrightarrow{H} H_2NO \xrightarrow{H} NH_2OH. \tag{3.1}$$

However, to date there has been no experimental evidence that this reaction indeed proceeds. Here, we present a successful attempt to form hydroxylamine under fully controlled laboratory conditions via the non-energetic route NO + H on crystalline H_2O ice and on amorphous silicate, two very realistic analogs of grain surface materials in the interstellar medium, and on a bare gold substrate through subsequent hydrogenation reactions.

3.2 Experimental

The experiments are performed using two different setups: FORMOLISM located at the University of Cergy-Pontoise (FR; Accolla *et al*. 2011) and SURFRESIDE at the Sackler Laboratory for Astrophysics in Leiden (NL; Ioppolo *et al*. 2010). Both setups comprise a central ultrahigh vacuum chamber with a base pressure of $\sim 10^{-10}$ mbar in which a sample holder is mounted in thermal contact with the cold finger of a closed-cycle He cryostat. We have studied the reaction NO + H (NO + D) at low temperatures (10–15 K) by exposing the substrate surface to a molecular beam of NO and H- (D-) atoms generated in state-of-the-art atom beam lines. Atoms are cooled and instantaneously thermalized upon surface impact. In Cergy, NO hydrogenation is studied with sequential deposition of NO and H- (D-) atoms in the low surface coverage regime not exceeding one monolayer of NO on the 10 K silicate or water-ice substrate. In Leiden, co-depositions of NO and H- or D-atoms are studied for lower ($\sim 7 \cdot 10^{12}$ atoms cm^{-2} s^{-1}) and higher ($\sim 3 \cdot 10^{13}$ atoms cm^{-2} s^{-1}) H- and D-atom fluxes in the high surface coverage regime (>50 monolayers) on the 15 K cold gold substrate. Newly formed species upon H- or D-atom addition are monitored in the solid phase by means of Fourier transform Reflection-Absorption Infrared Spectroscopy (RAIRS; Greenler 1966) using vibrational fingerprint spectra in the 4000–700 cm^{-1} region and in the gas phase by means of Quadrupole Mass Spectrometry (QMS) upon temperature programmed desorption (TPD) by steadily heating the ice and monitoring evaporated species. Special efforts have been made to exclude contaminants in the ultrahigh vacuum chambers and on the ice surface, the actual reaction site. A series of control experiments is performed to assure that the final key product is indeed only due to successive hydrogenation of solid NO (Equation (3.1)).

3.3 Results

In the two setups, hydroxylamine is produced at comparable rates on all surfaces regardless of the hydrogen isotope used, H or D. Moreover, the NO ice is almost completely consumed by an equivalent amount of hydrogen atoms, suggesting a NO + H (NO + D) reaction with an efficiency close to one and able to proceed with no appreciable barrier even at 10 K. Figure 3.1 displays RAIR spectra at 15 K after simultaneous deposition of NO during low- and high-hydrogen atom flux (Figure 3.1(a) with H/NO = 0.2 and Figure 3.1(b) with H/NO = 4, respectively). Spectral features appearing upon solid NO hydrogenation are assigned to bulk NH$_2$OH (3317, 3261, 3194, 2899, 2716, 1608, 1514, 1203, 919 cm^{-1}), isolated NH$_2$OH (1175, 1359, 1144 cm^{-1}), HNO (1561, 1507 cm^{-1}), and N$_2$O (2235, 1286 cm^{-1}; Nightingale & Wagner 1954, Jacox & Milligan 1973, Sivaraman *et al*. 2008). The simultaneous detection of NH$_2$OH and HNO is consistent with the reaction

scheme given in Equation (3.1).

At lower H-atom flux the NO is not completely consumed by hydrogen atoms, and the strongest bands (1865, 1776 cm^{-1}) correspond to NO-dimer transitions (Fateley *et al.* 1959). However, also under these conditions HNO is formed, and isolated bands of NH$_2$OH molecules are visible. This indicates that even at the lower H-atom flux the addition process proceeds fast. In the higher H-atom flux experiment NO-dimer bands are barely visible.

In both the low- and high-hydrogen atom flux experiments nitrous oxide (N$_2$O) is found, likely formed via

$$NO + HNO \rightarrow N_2O + OH \text{ and} \qquad\qquad (3.2)$$
$$(NO)_2 + H \rightarrow N_2O + OH. \qquad\qquad (3.3)$$

Figure 3.2 shows TPD spectra of NH$_2$OH (m/z = 33, peak at ~188 K) produced after six cycles of H-atom exposure of one monolayer coverage (10^{15} molecules cm^{-2}) of NO on a silicate surface. This procedure ensures that the reaction NO + H occurs for each cycle on the surface of the ice, until all NO molecules have been consumed. The repetition of several cycles enhances the signal-to-noise ratio of the QMS ion count upon ice sublimation. In the figure, signals are recorded at m/z = 33 (NH$_2$OH) as well as 30 (NO), 17 (OH), and 16 (NH$_2$), reflecting partial fragmentation upon NH$_2$OH ionization in the QMS head (Kutina *et al.* 1982).

All signals have a common peak at T ~ 188 K, confirming NH$_2$OH fragmentation upon ionization. The 150 K temperature peaks for m/z = 30 and 17, included here for the sake of completeness, are due to co-desorption of NO molecules and OH fragments from thermal desorption at T ~ 150 K of the newly formed water ice through reaction of H + OH (Dulieu *et al.* 2010).
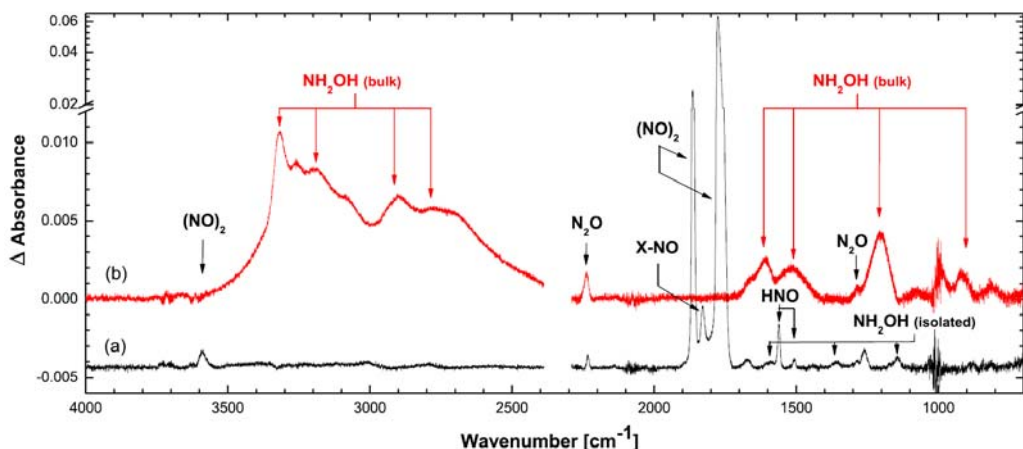
Figure 3.1. RAIR spectra of solid NO deposited on the gold substrate at 15 K upon H-atom exposure. Diagram (a) shows the resulting spectrum for a co-deposition experiment during 60 minutes and H-atom flux of $7 \cdot 10^{12}$ atoms cm^{-2} s^{-1} (H/NO = 0.2). Diagram (b) shows the spectrum for a deposition time of 120 minutes and an H-atom flux of $3 \cdot 10^{13}$ atoms cm^{-2} s^{-1} (H/NO = 4). Spectra are offset for clarity.
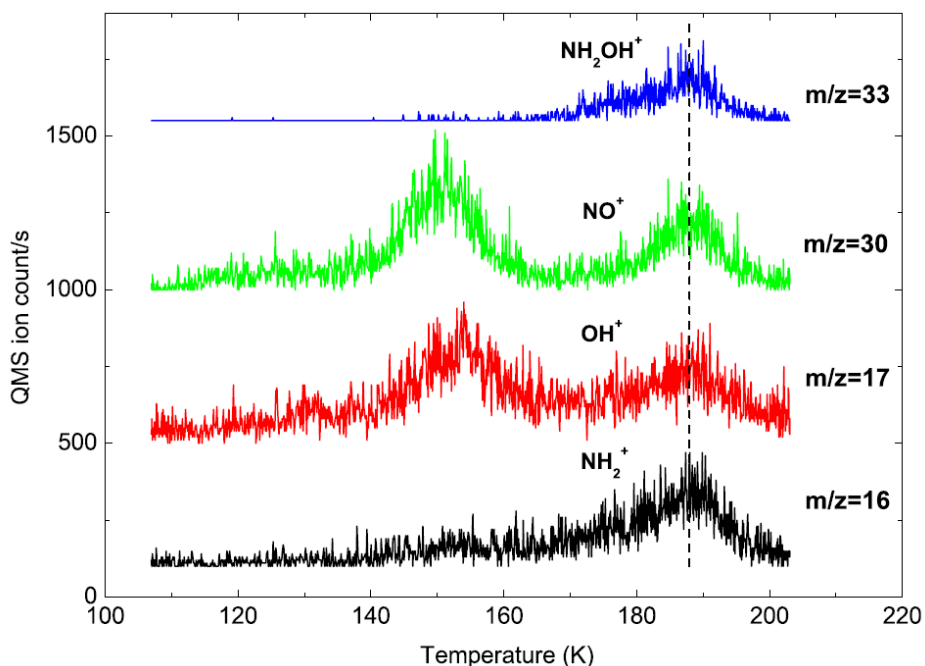
Figure 3.2. Quadrupole mass spectrometer signal as a function of temperature during a TPD experiment after six sequential depositions of ~1 ML of NO and H-atoms on a bare silicate surface at 10 K. The peak at T ~ 188 K indicates desorption of hydroxylamine (NH_2OH, mass = 33 amu). NH_2OH fragmentation is induced in the mass spectrometer head upon ionization, resulting in NO^+, OH^+, and NH_2^+ fragments. Low temperature peaks for mass = 30 and 17 amu are due to co-desorption of NO molecules and OH fragments with water at T ~ 150 K. The traces are offset for clarity.

3.4 Discussion

The present study proves NH_2OH formation upon NO hydrogenation at low temperatures and without external energetic input. It therefore provides a likely pathway for an efficient formation in quiescent cold dense clouds where energetic processing is not likely to be efficient. Two previous experimental studies showed the formation of NH_2OH by irradiating a mixture of NH_3 and H_2O ices with UV photons (Nishi *et al*. 1984) and electrons (Zheng & Kaiser 2010). The experimental conditions used there are not fully representative for quiescent cold dense clouds, regions where NH_2OH is assumed to be already present in the ice as indicated by our results. The astronomical relevance of NO + H is discussed below. Interstellar temperatures and substrates can be rather well reproduced in the laboratory, but experiments are not fully representative of dark cloud conditions, especially in terms of timescale and ice inhomogeneity. To prove that the presented reaction scheme facilitates NH_2OH formation in dense cores, a gas–grain model (Hasegawa *et al*. 1992, Hassel *et al*. 2008) is used that comprises a full gas and grain chemical network. Conditions are chosen as in the prototypical dense cloud "TMC 1" (Semenov *et al*. 2010). The resulting predictions are shown in Figure 3.3. The reaction between H and HNO in the current chemical networks (dashed lines in Figure 3.3) leads to H_2 and NO and NH_2OH is usually formed through NH_2 + OH. Along this reaction pathway, no NH_2OH is formed under dark cloud conditions and NO is mostly converted into HNO or N_2O. This is in agreement with Garrod *et al*. (2008) who performed chemical models of star formation and found that NH_2OH is only abundantly formed in the "hot core" phase when the grain is lukewarm and NH_2 and OH become mobile. On the other hand, with a model including the NO hydrogenation reactions experimentally proven in this paper (the solid lines in Figure 3.3), NH_2OH is found to be abundantly present in both the solid and the gas phase. The hydroxylamine abundance peaks at 10^5 years, with relative values with respect to gas phase H_2 of at least $7 \cdot 10^{-9}$ on the grain surface and $3 \cdot 10^{-11}$ in the gas phase at the end of the lifetime of a dense cold cloud (1–10 Myr), *i.e.*, before the core collapse. This finding is particularly relevant for a better understanding of the molecular evolution of the universe. This work indeed shows that the hydroxylamine locked up on the grains at the beginning of the core collapse becomes available for further reactions at later stages, when a protostar forms and UV irradiation and thermal processing start. So far, positive identifications of NH_2OH in molecular clouds have not yet been reported, but upper limits have been derived for a number of sources (Pulliam *et al*. 2012). These correspond to fractional abundances of $<10^{-11}$. This is around the same order of magnitude as the gas-phase model predictions for dense clouds, concluded here. Gas-phase abundances in the model are upper limits since destruction routes that lead to the formation of more complex species are not included.

Snow *et al.* (2007) showed that gas phase NH_2OH can react with CH_5^+ to form NH_3OH^+ that in turn reacts with different carboxylic acids to form protonated amino acids. These reactions are not included in the available chemical networks and therefore can not be traced. The left panel of Figure 3.3, however, shows that CH_5^+ and H_3^+ - both able to protonate hydroxylamine - are available in the gas phase The present work and a previous study (Zheng & Kaiser 2010) show that NH_2OH desorbs at relatively high temperatures (>175 K under laboratory conditions) from the ice. Therefore, abundances may be high enough for gas-phase detection only in those parts of the cloud that experienced a dramatic heating phase. In fact, NH_2OH provides a solid-state nitrogen reservoir along the whole evolutionary process of interstellar ices from dark clouds to planets. We expect that in the nearby future the faint radio hum from NH_2OH molecules will be recorded by the receivers of ALMA that will investigate the inner parts of protoplanetary disks and hot cores with high temperatures (Herbst 2008). ALMA will also come with a hugely improved sensitivity that, added to a high angular resolution, will allow perhaps detection of NH_2OH in cold starless cores and pre-stellar cores as well. The present laboratory study illustrating that possible precursor molecules of amino acids are efficiently formed on the surface of dust grains along with an astronomical detection of NH_2OH in space will confirm that the building blocks of life are omnipresent in the universe.
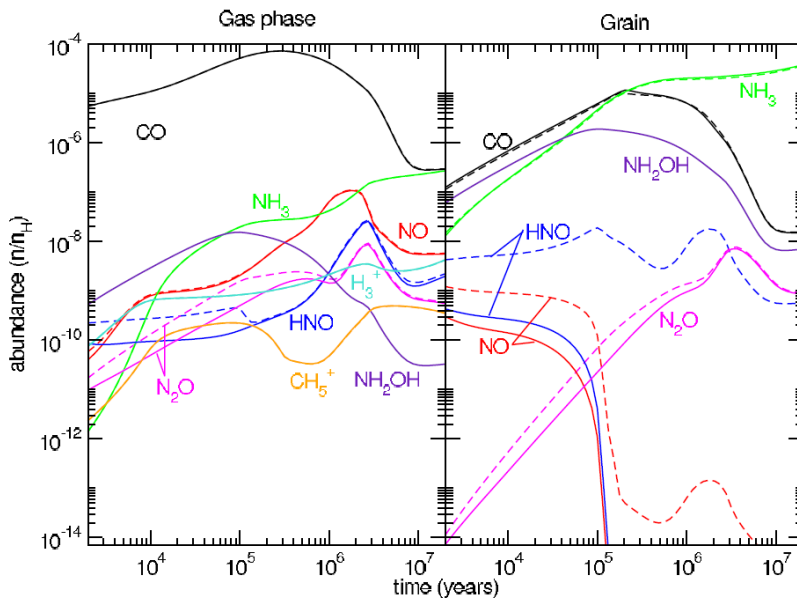
Figure 3.3. Fractional abundance of species involved in nitrogen chemistry for an astrochemical model in which the effect of an NO hydrogenation channel is shown. Solid lines are with NO + H and dashed lines do not take this surface reaction into account. The left panel indicates gas-phase species; the right panel shows the grain-surface abundance with respect to the gas-phase density of H nuclei ($nH = n(H) + 2n(H_2)$).

References

Accolla M., Congiu E., Dulieu F. *et al.*, 2011, PCCP, 13, 8037

Barrientos C., Redondo P., Largo L., Rayón V. M., Largo A., 2012, ApJ, 748, 99

Blagojevic V., Petrie S., Bohme D. K., 2003, MNRAS, 339, L7

Charnley S. B., Rodgers S. D., Ehrenfreund P., 2001, A&A, 378, 1024

Codella C., Benedettini M., Beltrán M. T. *et al.*, 2009, A&A, 507, L25

Cuppen H. M., Ioppolo S., Romanzin C., Linnartz H., 2010, PCCP, 12, 12077

Dulieu F., Amiaud L., Congiu E. *et al.*, 2010, A&A, 512, 30

Fateley W. G., Bent H. A., Crawford B., Jr., 1959, JCP, 31, 204

Fuchs G. W., Cuppen H. M., Ioppolo S. *et al.*, 2009, A&A, 505, 629

Garrod R. T., Widicus Weaver S. L., Herbst E., 2008, ApJ, 682, 283

Greenler R. G., 1966, JCP, 44, 310

Hasegawa T. I., Herbst E., Leung C. M., 1992, ApJS, 82, 167

Hassel G. E., Herbst E., Garrod R. T., 2008, ApJ, 681, 1385

Herbst E., 2008, Ap&SS, 313, 129

Herbst E., van Dishoeck E. F., 2009, ARA&A, 47, 427

Hudson R. L., Moore M. H., Dworkin J. P., Martin M. P., Pozun Z. D., 2008, Astrobiology, 8, 771

Ioppolo S., Cuppen H. M., Romanzin C., van Dishoeck E. F., Linnartz H., 2010, PCCP, 12, 12065

Jacox M. E., Milligan D. E., 1973, J. Mol. Spec., 48, 536

Kutina R. E., Goodman G. L., Berkowitz J., 1982, JCP, 77, 1664

Nightingale R. E., Wagner E. L., 1954, JCP, 22, 203

Nishi N., Shinohara H., Okuyama T., 1984, JCP, 80, 3898

Noble J. A., Dulieu F., Congiu E., Fraser H. J., 2011, ApJ, 735, 121

Öberg K. I., Boogert A. C. A., Pontoppidan K. M. *et al.*, 2011, ApJ, 740, 109

Pulliam R. L., McGuire B. A., Remijan A. J., 2012, ApJ, 751, 1

Sandford S. A., Aléon J., A., Conel M. O. D. *et al.*, 2006, Science, 314, 1720

Semenov D., Hersant F., Wakelam V. *et al.*, 2010, A&A, 522, A42

Sivaraman B., Ptasinska S., Jheeta N. J., Mason N. J., 2008, Chem. Phys. Lett., 460, 108

Snow J. L., Orlova G., Blagojevic V., Bohme D. K., 2007, J. Am. Chem. Soc., 129, 9910

van Dishoeck E. F., 2004, ARA&A, 42, 119

Wakelam V., Smith I. W. M., Herbst E. *et al.*, 2010, Space Sci. Rev., 156, 13

Watanabe N., Nagaoka A., Hidaka H. *et al.*, 2006, Planet. Space Sci., 54, 1107

Zheng W., Kaiser R. I., 2010, J. Phys. Chem. A, 114, 5251

IV

Surface NO Hydrogenation: The Multilayer Regime in Interstellar Relevant Ices

Hydroxylamine (NH_2OH) is one of the potential precursors of complex pre-biotic species in space. Here we present a detailed experimental study of hydroxylamine formation through nitric oxide (NO) surface hydrogenation for astronomically relevant conditions. The aim of this work is to investigate hydroxylamine formation efficiencies in polar (water-rich) and non-polar (carbon monoxide-rich) interstellar ice analogues. A complex reaction network involving both final (N_2O, NH_2OH) and intermediate (HNO, $NH_2O\cdot$, *etc*.) products is discussed. The main conclusion is that hydroxylamine formation takes place *via* a fast and barrierless mechanism and it is found to be even more abundantly formed in a water-rich environment at lower temperatures. In parallel, we experimentally verify the non-formation of hydroxylamine upon UV photolysis of NO ice at cryogenic temperatures as well as the non-detection of NC- and NCO-bond bearing species after UV processing of NO in carbon monoxide-rich ices. Our results are implemented into an astrochemical reaction model, which shows that NH_2OH is abundant in the solid phase under dark molecular cloud conditions. Once NH_2OH desorbs from the ice grains, it becomes available to form more complex species (*e.g.*, glycine and β-alanine) in gas phase reaction schemes.

4.1 Introduction

The observed chemical complexity in space results from the cumulative outcome of gas, grain and gas-grain interactions. Recent studies indicate that a substantial part of the stable and complex species identified so far, form on icy dust grains (Herbst & van Dishoeck 2009, Wakelam *et al.* 2010). Interstellar grains, indeed, act as micrometer-sized cryo-pumps providing surfaces onto which gas-phase species can accrete, meet and react. During the last decade several independent laboratory studies showed the relevance of such astrochemical solid-state reactions. Meanwhile, the surface formation of the bulk of the identified interstellar ices (*i.e.*, water, methanol, carbon dioxide, formaldehyde, and formic acid) has been confirmed through subsequent H-atom addition reactions to simple species, like CO- and/or O_2-ices (Watanabe & Kouchi 2002, Fuchs *et al.* 2009, Miyachi *et al.* 2008, Ioppolo *et al.* 2008, Matar *et al.* 2008, Oba *et al.* 2010, Ioppolo *et al.* 2011, Noble *et al.* 2011).

In space, non-energetic atom addition induced solid state chemistry occurs mostly at low temperatures (~10 K), *i.e.*, in the innermost part of circumstellar clouds where newly formed molecules are, to a great extent, shielded from radiation by dust particles. These regions are part of collapsing envelopes feeding new stars - young stellar objects (YSOs) - and provide the original material from which comets and ultimately planets are made (Sandford *et al.* 2006). Since solid-state neutral-neutral reactions often do not require activation energy (Herbst & van Dishoeck 2009, Wakelam *et al.* 2010), they play a key role in the chemistry of dark interstellar clouds. In the final stages of star formation energetic processing - like UV photolysis, cosmic ray irradiation and thermal processing - also contributes to surface reaction schemes by adding external energy into the ice. It has indeed been demonstrated that complex organic molecules and even amino acids are formed after energetic processing of interstellar ice analogues (Öberg *et al.* 2010, Muñoz Caro *et al.* 2002). Therefore, laboratory-based studies of the solid-state formation of organic material is of considerable interest, since efficient reaction routes provide a recipe to form pre-biotic species in star- and planet-forming regions (Charnley *et al.* 2001).

Hydroxylamine (NH_2OH) is an important precursor species in the formation of amino acids (Blagojevic *et al.* 2003). Several formation schemes of hydroxylamine have been proposed in the past. Blagojevic *et al.* (2003) describe NH_2OH formation through UV photolysis of NH_3 + H_2O and/or "NO + 3H" ices. Charnley *et al.* (2001) suggested that hydroxylamine is formed through non-energetic hydrogenation of NO ice under dark cloud conditions. Nitric oxide has been detected in the gas phase towards many dark and warm clouds with relative abundances of $1 \cdot 10^{-8}$ - $1 \cdot 10^{-7}$ with respect to H_2 (Liszt & Turner 1978, Pwa & Pottasch 1986, McGonagle *et al.* 1990, Gerin *et al.* 1992). Detailed astrochemical models (Charnley *et al.* 2001, Gerin *et al.* 1992, Herbst & Klemperer 1973) indicate that the main formation route for NO in the gas-phase is a neutral-neutral reaction N + OH → NO +

H, while the main gas-phase destruction channel is NO + N → N_2 + O. Under dense cloud conditions, gas-phase NO can accrete, like CO, on the surface of dust grains and is, therefore, expected to participate in the solid-state chemical network leading to the formation of N- and NO-bearing species. Moreover, solid NO may also be formed through surface reactions in the early stages of quiescent dark clouds.

Although NO has the potential to be one of the main precursors of complex molecules in space, solid state reaction schemes involving NO-bearing ices have not yet been studied in detailed experiments. Recently, we presented for the first time hydroxylamine formation *via* a non-energetic solid-phase route - pure NO + H on crystalline H_2O ice as well as on other different substrates (Congiu *et al*. 2012a) – and we showed the astrochemical impact of that scheme. In the present paper, the focus is on the investigation of the underlying physical-chemical processes that lead to surface hydroxylamine formation in the multilayer regime. Thus, experiments are extended to more realistic and interstellar relevant polar (NO:H_2O + H/D) and non-polar (NO:CO + H/D) environments. In the following sections we investigate the effect of temperature, ice composition and H-atom flux on the NH_2OH and HNO formation efficiencies. We also discuss experiments in which NO, NO:H_2O and NO:CO ices are UV irradiated with Ly-α light. The astrophysical implications of this work are briefly discussed. In an accompanying and complementary paper (Congiu *et al*. 2012b, published back-to-back with the present chapter) NO hydrogenation reactions are studied with the focus on the submonolayer regime using interstellar relevant substrates, *i.e.*, amorphous silicate and crystalline H_2O ice.

4.2 Experimental details and data reduction

4.2.1 Experimental procedure

The experiments are performed using two similar ultra-high vacuum (UHV) setups: a SURFace REaction SImulation DEvice (SURFRESIDE), optimized to study H-atom addition reactions, and a CRYOgenic Photoproduct Analysis Device (CRYOPAD), designed for UV photolysis experiments of interstellar ice analogues.

4.2.1.1 SURFRESIDE

Thermal H/D-atom addition reactions are investigated using SURFRESIDE which consists of a stainless steel UHV main chamber and an atomic line. Details are available in Fuchs *et al*. (2009), Ioppolo *et al*. (2008), Ioppolo *et al*. (2011). A rotatable gold-coated copper substrate is placed in the centre of an UHV chamber. The room temperature base pressure in the main chamber is <3.5·10^{-10} mbar. The substrate temperature is controlled from 12 to 300 K using a He closed-cycle cryostat. Ice deposition proceeds under an angle of 45º, with

controllable rates from 0.5 to 2.5 Langmuir per minute (L/min, where 1 L $=$ $1.3 \cdot 10^{-6}$ mbar s^{-1}). A quadrupole mass spectrometer (QMS) placed behind the substrate is used to monitor the main-chamber gas composition. The atomic line faces the sample and comprises a well-characterized hydrogen thermal cracking source (Tschersich 2002) used to produce non-energetic H/D atoms from H_2/D_2 molecules. Hydrogen/deuterium molecules are cracked by passing through a capillary pipe surrounded by a heated tungsten filament. Dissociation of molecules occurs through collisions with the hot (1850 ºC) walls of the capillary pipe with a degree of dissociation >35% (Tschersich 2002). A nose-shaped quartz pipe is placed along the path of the beam and is used to thermalize both H/D atoms and non-dissociated H_2/D_2 molecules to room temperature before they reach the surface of the ice sample. H/D-atom fluxes are measured quantitatively by placing the QMS at the substrate position and are controlled between $7 \cdot 10^{12}$ and $3 \cdot 10^{13}$ atoms cm^{-2} s^{-1}. This procedure has been described in detail in Ioppolo *et al*. (2010).

A high vacuum glass manifold with a base pressure $<5 \cdot 10^{-5}$ mbar is used for gas mixture preparation. To avoid water contamination the glass line is connected to a liquid nitrogen trap and is flushed well by mixture components. A new mixture is prepared for each experiment. After preparation, the mixture is introduced to a pre-pumped stainless steel dosing line ($<1 \cdot 10^{-5}$ mbar). The metal line is typically filled with a gas pressure of 30 mbar and is kept isolated for the duration of the experiment. The deposition rate is controlled by a precise all-metal leak valve. The gases used in this work are: NO (Linde 99.5 %), CO (Linde 99.997%), N_2O (Praxair 99.5%), NO_2 (Linde 99%) and a Milli-Q water sample degassed under high vacuum conditions.

The ice composition is monitored *in situ* by means of Reflection Absorption InfraRed Spectroscopy (RAIRS) in the range: $700 - 4000$ cm^{-1} ($14 - 2.5$ μm) with a spectral resolution of 0.5 cm^{-1} using a Fourier transform infrared spectrometer. Two different experimental procedures are applied here. In "pre-deposition" experiments, ices are first deposited on a gold surface and are subsequently exposed to a thermal H/D-atom beam. In this case RAIR difference spectra are acquired during hydrogenation/deuteration of the sample with respect to a background spectrum of the initial deposited ice at low temperature. In the case of "co-deposition" experiments, nitrogen oxide bearing ices are continuously deposited simultaneously with H/D atoms. The formation of intermediate species and final products is monitored in the ice by changing ice deposition rates and H/D-atom fluxes, as discussed in Cuppen *et al*. (2010). In this case RAIR difference spectra are acquired during co-deposition with respect to a background spectrum of the bare gold substrate at a low temperature.

At the end of every H/D-atom exposure a temperature programmed desorption (TPD) experiment is performed. Because the QMS is placed behind the substrate, RAIR spectra and QMS data cannot be taken simultaneously during the heating phase, and crucial

experiments are performed twice in order to interpret TPD results using both RAIRS and QMS techniques. In the first experiment, the sample is rotated 180º to face the QMS and it is heated linearly at a rate of 1 K/min. Desorbed species are subsequently detected as a function of sample temperature using the QMS. In the second experiment, the sample is not rotated and RAIR spectra of the ice are acquired every 5 K while heating at a rate of 1 K/min. In this way infrared spectroscopic and mass spectrometric information can be combined. It should be noted that a TPD experiment implicitly leads to the morphological modification and eventual destruction of the ice. Therefore TPD data are mainly used in our experiments as an additional tool to constrain the low temperature RAIR results.

4.2.1.2 CRYOPAD

UV photolysis experiments are performed using CRYOPAD which is described in detail in Öberg *et al*. (2009) and references therein. Similarly to SURFRESIDE, the rotatable gold-coated substrate in CRYOPAD is connected to a He close-cycle cryostat and placed in the centre of a stainless steel UHV chamber. The room temperature base pressure of the system is $<2.5 \cdot 10^{-9}$ mbar and the temperature of the substrate is controlled between 15 and 200 K. Ice deposition proceeds at an angle of 90º and a rate of 1.5 L/min. After deposition, the ice film is irradiated by UV light from a broadband hydrogen microwave discharge, which peaks at 121 nm (Ly-α) and covers the range from 115 – 170 nm (7 – 10.5 eV) with an incidence angle of 45º. Photolysis products upon UV irradiation are monitored by means of the same FTIR spectrometer that is used for SURFRESIDE, covering 700 – 4000 cm^{-1} with 0.5 cm^{-1} resolution. A QMS is incorporated into the setup in order to monitor molecules in the gas phase and specifically photodesorption products. At the end of a UV irradiation experiment, a TPD experiment is routinely performed. The setup is constructed such that the QMS already faces the sample, and consequently it is possible to monitor ice constituents both spectroscopically and mass spectrometrically during a TPD. The heating rate used for these experiments is the same used for SURFRESIDE (1 K/min)**.** The UV flux is measured indirectly by calibration *via* the previously studied photodesorption rate of a pure CO ice: carbon monoxide ice is exposed to Ly-α light and the number of photodesorbed CO molecules is then determined using the RAIR difference spectra. The UV flux is then derived, assuming that the CO photodesorption rates obtained here and previously in Öberg *et al*. (2007) are identical. Typical UV fluxes amount to $1.5 \cdot 10^{14}$ photons cm^{-2} s^{-1}.

Gas mixtures used during experiments with CRYOPAD are prepared separately in the same glass manifold as described above. The mixtures are then introduced into a pre-pumped stainless steel dosing line ($<1 \cdot 10^{-4}$ mbar) that is always filled twice in order to avoid the decomposition of gas mixture components on the metal walls during the

preparation hours: a first time (at the beginning of the experiment) to select at room temperature the desired deposition rate by adjusting a precise all-metal leak valve and monitoring the increase in pressure in the main chamber; and a second time (right before deposition) using the same pressure used the first time to fill the dosing line. When not in use, the deposition line is kept under high vacuum. This allows for a highly reproducible deposition rate.

The experiments at SURFRESIDE and CRYOPAD focus on selected surface reactions involving the hydrogenation and UV irradiation of pure NO ices and mixtures of NO with CO, H_2O and N_2 over a wide range of laboratory conditions including different atomic fluxes, ice temperatures, co-deposition rates and mixture ratios. A number of control experiments are performed to prove that newly detected species are formed upon H/D-atom exposure or UV photolysis on top of or in the ice sample, and that they are not the result of contamination or background gas-phase reactions. All experiments are summarized in Table 4.1. Moreover, in order to unambiguously identify absorption bands of possible reaction products we have performed separate experiments to acquire spectra of pure N_2O as well as $NO:N_2O_3$ and $NO_2:N_2O_4$ ice mixtures (see Table 4.2) to make direct comparisons possible.

Table 4.1. List of performed experiments.

Depositing ice composition	Type	Temperature (K)	Deposition rate, (L/min)	H/D flux (atom·cm^{-2}·s^{-1})	H$_2$/D$_2$ flux (mol·cm^{-2}·s^{-1})	UV flux (ph·cm^{-2}·s^{-1})	Time (min)
Co-deposition:[a]							
NO	+H	15	0.5	$3\cdot10^{13}$	$3.5\cdot10^{15}$	-	200
-//-	+H$_2$	15	0.5	0	$3.5\cdot10^{15}$		40
-//-	+H	15	2.5	$7\cdot10^{12}$	$2.5\cdot10^{14}$	-	120
-//-	+H	25	2.5	$7\cdot10^{12}$	$2.5\cdot10^{14}$	-	100
-//-	+D	15	0.5	$3\cdot10^{13}$	$3.5\cdot10^{15}$	-	120
-//-	+D	15	2.5	$7\cdot10^{12}$	$2.5\cdot10^{14}$	-	120
NO:N$_2$ (1:5)	+H	15	0.5	$3\cdot10^{13}$	$3.5\cdot10^{15}$	-	100
-//-	+H$_2$	15	2.5	0	$3.5\cdot10^{15}$	-	30
NO:CO (1:1)	+H	15	0.5	$3\cdot10^{13}$	$3.5\cdot10^{15}$	-	200
-//-	+H	15	2.5	$7\cdot10^{12}$	$2.5\cdot10^{14}$	-	120
-//-	+D	15	0.5	$3\cdot10^{13}$	$3.5\cdot10^{15}$	-	200
-//-	+D	15	2.5	$7\cdot10^{12}$	$2.5\cdot10^{14}$	-	120
NO:CO (1:6)	+H	15	0.5	$3\cdot10^{13}$	$3.5\cdot10^{15}$	-	420
-//-	+H	15	2.5	$3\cdot10^{13}$	$3.5\cdot10^{15}$	-	120
-//-	+H	15	2.5	$7\cdot10^{12}$	$2.5\cdot10^{14}$	-	120
-//-	+H	25	0.5	$3\cdot10^{13}$	$3.5\cdot10^{15}$	-	120
-//-	+D	15	2.5	$3\cdot10^{13}$	$3.5\cdot10^{15}$		120
NO:H$_2$O (1:6)	+H	15	2.5	$7\cdot10^{12}$	$2.5\cdot10^{14}$	-	150
-//-	+H	15	2.5	$3\cdot10^{13}$	$3.5\cdot10^{15}$	-	60
Pre-deposition:[b]							
NO	+H	15	2.5 (50 L)	$3\cdot10^{13}$	$3.5\cdot10^{15}$		150
NO:CO:N$_2$ (1:1:5)	+H	15	2.5 (100 L)	$3\cdot10^{13}$	$3.5\cdot10^{15}$		60
Nitrogen oxides deposition:[c]							
N$_2$O		30	2.5 (100 L)	-	-	-	-
N$_2$O	+H	15	0.5	$3\cdot10^{13}$	$3.5\cdot10^{15}$	-	120
NO$_2$[d]		15	2.5 (30 L)	-	-	-	-
NO$_2$[d]	+H	15	2.5	$7\cdot10^{12}$	$2.5\cdot10^{14}$	-	40
NO$_2$:NO (1:2)[e]		15	2.5 (60 L)	-	-	--	-
Pre-deposition (UV-photolysis):							
NO	+hυ	15	1.0 (40 L)	-		$1.5\cdot10^{14}$	130
NO:CO (1:1)	+hυ	15	1.0 (40 L)	-	-	$1.5\cdot10^{14}$	75
NO:CO (1:6)	+hυ	15	1.0 (40 L)	-	-	$1.5\cdot10^{14}$	150
NO:H$_2$O (1:6)	+hυ	15	1.0 (40 L)	-	-	$1.5\cdot10^{14}$	120
NO:H$_2$O:CO (1:1:1)	+hυ	15	2.5 (80 L)	-	-	$1.5\cdot10^{14}$	160
NO:H$_2$O:CO (1:6:6)	+hυ	15	2.5 (80 L)	-	-	$1.5\cdot10^{14}$	140
NO:CH$_4$ (1:1)	+hυ	15	2.5 (80 L)	-	-	$1.5\cdot10^{14}$	120

[a]Co-deposition is an experiment in which NO containing ices are deposited during H/D flux exposure.

[b]Pre-deposition is an experiment in which NO containing ices are first deposited and subsequently exposed to H/D atom or UV fluxes.

[c]This is a set of experiments in which the spectra of different nitrogen oxides were obtained and then monitored for stability upon H-atom flux exposure.

[d]NO$_2$ gas contained considerable NO admixture; formation of N$_2$O$_3$ (ON-NO$_2$) along with N$_2$O$_4$ (O$_2$N-NO$_2$) is observed upon deposition.

[e]Mixture of N$_2$O$_3$ (ON-NO$_2$) and *cis*-(NO)$_2$ is formed upon deposition.

4.2.2 Data analysis

Straight baseline segments are subtracted from all acquired spectra. Subsequently, the areas of bands corresponding to species present in the ice are integrated. As previously discussed in Fuchs *et al.* (2009) and Ioppolo *et al.* (2008) transmission band strengths cannot be used directly to derive column densities of species in reflection experiments. Moreover, isothermal desorption experiments, which provide us with absorbance per monolayer, cannot be performed for the unstable intermediates that are detected during co-deposition experiments. Therefore, we refrain from deriving column densities and instead follow the formation trends of the detected species only by integrating the corresponding band areas as a function of time (see Results and Discussion). As a consequence, a full quantitative characterization is not directly possible. However, we can compare formation trends of the same species from different experiments and thereby derive information on temperature dependence, ice composition effects and the reaction network. All the assigned absorption features that correspond to nitrogen-bearing species and present in our experiments are summarized in Table 4.2. The asterisk in Table 4.2 marks the spectral features used for integration and relative quantification.

All absorbance features chosen for data analysis have a good signal-to-noise ratio and do not overlap with other absorbance features. The range of integration is set manually for each species and kept the same for all the spectra acquired during a single experiment. The error bars that are indicated in the figures listed in the Results and Discussion section are estimated as follows: several blank spectra, *i.e.*, without deposited ice but with a cold substrate, are acquired before each experiment. The corresponding baseline segments are subtracted from the blank data. The noise area in the blank spectra is integrated over the same frequency range that is used for band integration of the selected species. The uncertainties are then derived by averaging the values of the measured blank area for each selected range. Although these error bars do not include deviations in the baseline subtraction procedure, they provide lower limits for the detectable signal.

Table 4.2. List of assigned nitrogen-bearing species.

Mode	Regular species	Frequency (cm^{-1})	Deuterated species	Frequency (cm^{-1})	Reference
υ_5 [*]	cis-(NO)$_2$	1776			I, II
υ_1	cis-(NO)$_2$	1865			I, II
	trans-(NO)$_2$	1741			I
	NO(monomer)	1875			I, II
υ_6	NH$_2$OH	889	ND$_2$OD	825	III, IV
υ_6	NH$_2$OH (bulk)	919	ND$_2$OD (bulk)	878	V
υ_5 [a]	NH$_2$OH	1144	ND$_2$OD	920	III, IV
υ_5 [a]	NH$_2$OH (bulk)	1203	ND$_2$OD (bulk)	946	V
υ_4	NH$_2$OH	1359	ND$_2$OD	1026	III, IV
υ_4	NH$_2$OH (bulk)	1514	ND$_2$OD (bulk)	1126	V
υ_3	NH$_2$OH	1592	ND$_2$OD	1175	III, IV
υ_3	NH$_2$OH (bulk)	1608	ND$_2$OD (bulk)	1185	V
	NH$_2$OH (bulk)	2716	ND$_2$OD (bulk)	2045	V
υ_2	NH$_2$OH (bulk)	2899	ND$_2$OD (bulk)	2184	V
υ_2	NH$_2$OH (bulk)	3194	ND$_2$OD (bulk)	2393	V
υ_7	NH$_2$OH (bulk)	3261			V
υ_1	NH$_2$OH (bulk)	3317	ND$_2$OD (bulk)	2482	V
υ_3	N$_2$O	1286			VI
υ_1 [a]	N$_2$O	2235			VI
υ_2	HNO	1507	DNO	1156	VII
υ_3 [a]	HNO	1561	DNO	1546	VII
	X-NO	1829	X-NO	1823	-
υ_1	N$_2$O$_3$	1851			I, VIII
υ_2	N$_2$O$_3$	1614			I, VIII
υ_3	N$_2$O$_3$	1302			I, VIII
υ_4	N$_2$O$_3$	782			I, VIII

[a]Spectral features used for integration and relative quantification.

I – Fateley *et al.* (1959); II – Noir *et al.* (1984); III – Withnall & Andrews (1988); IV – Yeo & Ford (1990); V – Nightingale & Wagner (1954); VI – Jamieson *et al.* (2005), VII – Jacox & Milligan (1973), VIII – Sluyts & Van der Veken (1994).

4.3 Results and discussion

4.3.1 Hydrogenation of pure NO ice

Figure 4.1(a) shows RAIR difference spectra recorded with SURFRESIDE of a pre-deposited NO ice after exposure to a thermal H-atom beam at 15 K. The negative peaks around 1776 and 1865 cm^{-1} correspond to cis-(NO)$_2$ (Fateley *et al.* 1959, Noir *et al.* 1984) used up during hydrogenation of the ice. Due to the small exothermicity of NO dimerization (14 kJ per mol, see Sluyts & Van der Veken 1994) and a fast radical-radical recombination reaction rate, nitric oxide forms solid cis-(NO)$_2$ immediately after deposition. Therefore, NO monomers are detected in the ice by means of RAIRS only when NO is trapped in an ice matrix of other species (see below). Thus,

hydrogenation/deuteration of a pure NO ice involves as a first step the hydrogenation/deuteration of $(NO)_2$ dimers. The positive peaks in Fig. 4.1(a) indicate the presence of newly formed species in the ice. However, their identification is not clear *a priori* because of their low signal to noise ratio. A possible reason for this low coverage of processed ice can be found in the structure of the ice. Crystalline $(NO)_2$ has a compact monoclinic unit cell with a space group $P2_1/a$ (Dulmage *et al*. 1953), which is more comparable to a CO than an O_2 ice structure (Barrett & Meyer 1967, Cromer *et al*. 1983). Although our deposited ice is not necessarily crystalline, the local structure of $(NO)_2$ agglomerates is probably close to crystalline. As shown in Fuchs *et al*. (2009) and Ioppolo *et al*. (2011) a compact ice structure prevents H/D atoms from penetrating deep into the bulk of the ice. As a consequence, in a pre-deposition experiment only the first few monolayers are actively involved in surface reactions, the final yield of H/D atom addition products is low and no intermediate products are detected.

Figures 4.1(b) and (c) show NO/H-atom co-deposition experiments at 15 K. The main advantage of co-deposition experiments is the ability to change the NO/H(D) ratio in order to: 1) trap non-fully hydrogenated products inside the growing ice by using a high NO flow with a low H(D)-atom flux (Fig. 4.1(c) and (e)); or 2) deposit a fully hydrogenated thick ice by using a low NO flow with a high H(D)-atom flux (Fig. 4.1(b) and (d)). Growing a thick hydrogenated ice during co-deposition experiments increases the column densities of the reaction products and allows their unambiguous identification *in situ* and at low temperatures by means of RAIRS. Although QMS is more sensitive than RAIRS, it allows for the detection of species only above their desorption temperatures. For the species studied here, this is higher than 15 K, *i.e.*, >75 K for N_2O and >140 K for NH_2OH.

Several positive absorption features, *e.g.*, at 1608 cm^{-1} (NH_2 scissoring), 1514 cm^{-1} (HON bending), 1203 cm^{-1} (NH_2 wagging), and 919 cm^{-1} (ON stretching) (see Yeo & Ford 1990), present in Fig. 4.1(b) clearly show that the main hydrogenation product of a pure NO ice at low temperature is solid hydroxylamine. The NH_2OH formed during the co-deposition experiment shown in Fig 4.1(b) is bulk hydroxylamine, bound with four different types of hydrogen bonds, such as OH…H, OH…N, NH…O, NH…N, and with different strengths. The hydroxylamine OH and NH stretching modes are in the range from 2600 to 3400 cm^{-1} and overlap with each other. There are two groups of broad bands in this region, at 3317, 3261 and 3194 cm^{-1} and at 2899 and 2716 cm^{-1}. The first group can be assigned to the symmetric and asymmetric N-H stretches, and the O-H…O stretch, while the second group is due to a hydrogen bonded OH…N stretch (Yeo & Ford 1990, Bertie & Shehata 1985). The formation of hydroxylamine in our pre-deposition experiments is confirmed by comparing all the hydroxylamine peaks present in Fig. 4.1(b) with those shown in Fig. 4.1(a).

Figure 4.1(c) presents several features due to the $(NO)_2$ dimer, N_2O, and isolated NH_2OH, and reveals several new features: two narrow bands at 1561 and 1507 cm^{-1} that can be assigned to HNO, and another two at 1829 cm^{-1} and 1680 cm^{-1} with an unclear origin. The feature at 1829 cm^{-1} overlaps with the NO stretching mode which may indicate that this species contains weakly bound NO molecules. In the following sections we will refer to this unknown component as X-NO. A broad peak at 1680 cm^{-1} is present in almost every spectrum and demonstrates similar behaviour under various experimental conditions, thus interpretation of this feature is uncertain. To verify our assignments we repeated the same co-deposition experiments discussed above using D atoms instead of H atoms (Figs. 4.1(d) and (e)).

TPD experiments further constrain the formation of NH_2OH and N_2O. Under our experimental conditions the desorption of NH_2OH starts at 140 K and peaks at 175 K (TPD rate 1 K/min). The NH_2OH desorption peak is reported at 188 K in Congiu *et al.* (2012b). There a desorption energy of 54.2 kJ mol^{-1} is calculated for pure NH_2OH from a surface of amorphous silicate. The difference in desorption temperature between the present work and Congiu *et al.* (2012b) is not surprising, as we study ices in the multilayer regime. Here desorption of NH_2OH takes place from the surface of the ice itself. Therefore, under this regime molecules from a layer of NH_2OH are weakly bound to other molecules (like NH_2OH, or NH_2OH mixed with CO and/or H_2O, see sections 4.3.2 and 4.3.3). This leads to a low temperature desorption peak. In Congiu *et al.* (2012b) at most one monolayer of NH_2OH is deposited onto an amorphous silicate surface. In that case NH_2OH molecules are bound to the silicate surface and not to another layer of ice. The resulting binding energy is higher, leading to a higher temperature desorption peak.

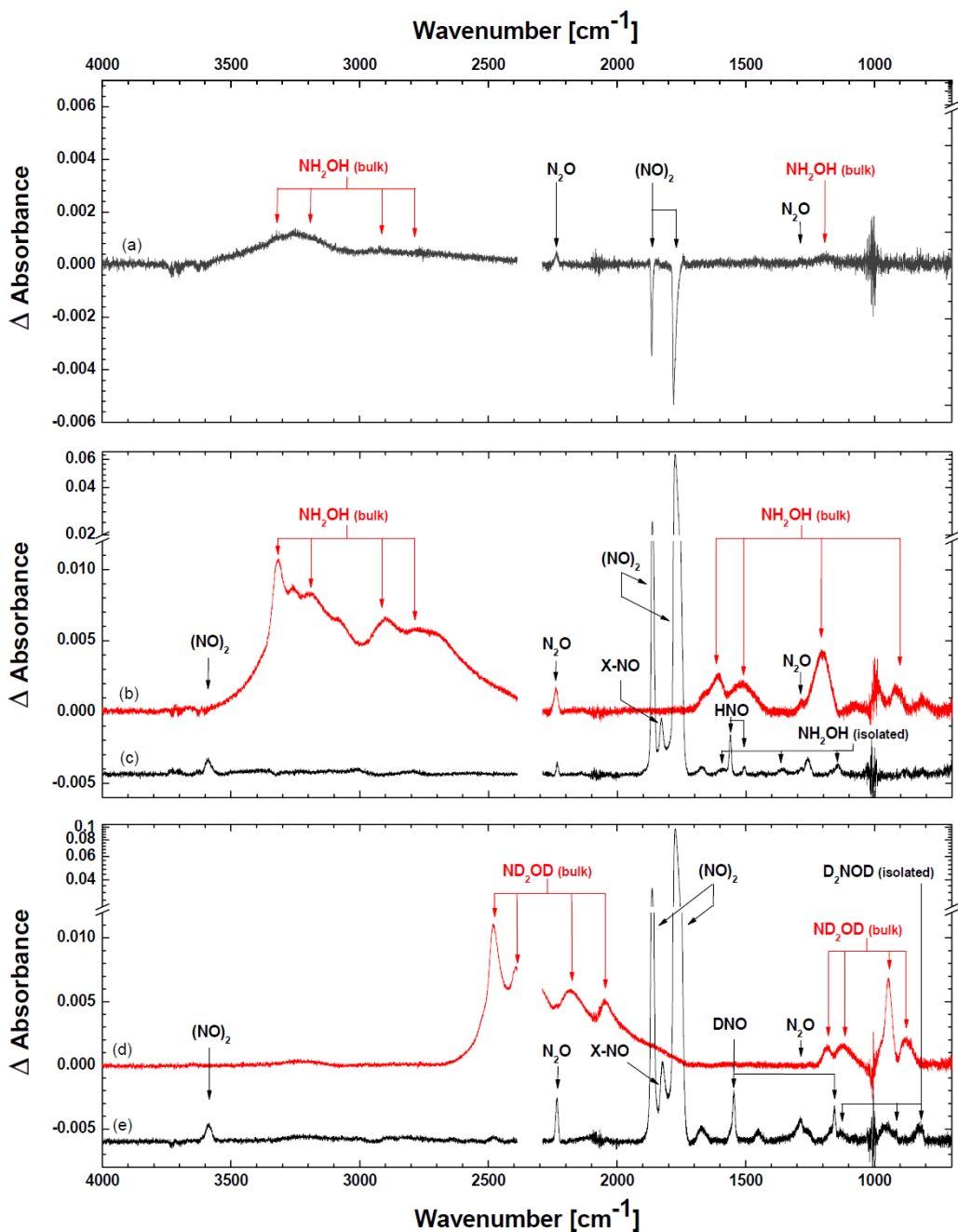**Figure 4.1.** RAIR difference spectra of H/D atom addition to a pure NO ice for a sample temperature of 15 K. The upper panel (a) shows a spectrum of a pre-deposited NO (50 L) after exposure to an H-atom beam. The middle panel shows co-deposition of NO and H atoms with NO:H = 1:10 (b) and 2:1 (c). In the lower panel two spectra recorded upon co-deposition of NO and D atoms with NO:D = 1:10 (d) and 2:1 (e) are presented.

4.3.2 Hydrogenation of NO in non-polar CO surroundings

We performed a series of experiments aimed at studying the effect of NO dilution in CO and N_2 (non-polar) matrices on the hydrogenation pathways. These experiments simulate the formation of hydroxylamine under dense and cold interstellar cloud conditions, when gas-phase CO freezes out. Figure 4.2 shows several examples of RAIR spectra of NO:CO co-deposition experiments with different ice mixtures (1:1, 1:6) and H/D-atom ratios.

All bands observed in a pure NO co-deposition experiment (Figs. 4.1(b) and (c)) are present here, and in addition, new features appear. In Figure 4.2(a) the NO monomer feature peaks at 1875 cm^{-1} (Fateley *et al*. 1959, Noir *et al*. 1984), while the *trans*-$(NO)_2$ absorbance band is centred around 1745 cm^{-1} (Fateley *et al*. 1959). The presence of the NO monomer in the ice mixture indicates that the NO mobility is limited in a CO lattice at 15 K. The remaining absorption features belong to the products of H/D-atom addition to CO, such as H_2CO (1720, 1499 cm^{-1}) and CH_3OH (1060 cm^{-1}). These reactions have been examined extensively in previous studies (Watanabe & Kouchi 2002, Fuchs *et al*. 2009). In the case of D-atom exposure traces of D_2CO are detected at 1674 and 2092 cm^{-1} but deuterated methanol is not found. It should be noted that formaldehyde is detected only in the experiments where all NO is converted into its final hydrogenation products (Figs. 4.2(b) and (d)). In the experiments where nitric oxide is still present in the ice, no products of H/D-atom addition to CO ice are found. This observation will be addressed in the following sections. Furthermore, no absorption features that can be assigned to N-C bond bearing species, like ·NCO radicals, HNCO or NH_2CHO, are found by RAIRS or by QMS. Unstable intermediates like HCO and HNOH are not detected either. Note that due to the abundance of the ^{13}CO isotope in the CO gas cylinder (1.1 %), a clear ^{13}CO absorbance feature at 2092 cm^{-1} is also observed.

Unlike CO ice, N_2 ice is inert to H-atom addition. The hydrogenation of nitric oxide in a nitrogen matrix with a ratio of NO:N_2 = 1:5 shows qualitatively that the final products from NO + H addition are the same as in a pure NO hydrogenation co-deposition experiment (Fig. 4.1(c)) with the difference that this time a small feature around 1875 cm^{-1} can be assigned to the NO monomer (as in Fig. 4.2). Here N_2O seems to be formed more efficiently compared to the NO hydrogenation experiment in a CO matrix.

Figure 4.2. RAIR difference spectra of H/D atom additions to NO in non-polar CO ice for a sample temperature of 15 K. The upper panel shows co-deposition spectra of NO, CO and H atoms with NO:CO:H = 1:6:15 (a) and 1:1:20 (b). The lower panel shows two spectra for the co-deposition of NO, CO and D atoms with a ratio of 1:6:15 (c) and 1:1:20 (d).

4.3.3 Polar H_2O surroundings

Water is the most abundant species detected in interstellar ices towards dark clouds, low-mass and high-mass YSOs. It is generally accepted that water ice is formed mainly during the early stages of a translucent and quiescent cloud (Herbst & van Dishoeck 2009, Charnley *et al.* 2001). Gas-grain chemical models predict that the NO abundance peaks later during CO freeze out (Charnley *et al.* 2001). Solid hydroxylamine can be formed during the same early stages in star forming regions from accreted NO or from NO formed on the surface of grains. Therefore, we studied the hydrogenation of NO in a water (polar) matrix (NO:H_2O = 1:6). H_2O molecules are inert to H-atom addition, but provide hydrogen

bonds that may interact with NO molecules as well as possible reaction products upon NO hydrogenation, *i.e.*, HNO and NH$_2$OH. Here, an NO:H$_2$O (1:6) ratio is used for comparison with the aforementioned non-polar mixtures.

Water ice deposited at 15 K forms an amorphous bulk with several very broad bands: the OH stretching modes between 3000 and 3700 cm^{-1}, the HOH bending mode in the 1400 – 1700 cm^{-1} range and the libration mode between 700 and 1000 cm^{-1}. All these bands are present in our spectra (see Fig. 4.3). As opposed to NO:CO ices, no nitric oxide monomer and *trans*-(NO)$_2$ are detected in the ice, which can be explained by a different mobility of NO in water ice compared to NO in a CO matrix. Although most of the NH$_2$OH absorption features overlap with the water OH stretching and HOH bending modes, all of them can be found in Fig. 4.3(b), where the H-atom flux is high enough to efficiently convert all NO to hydroxylamine. Figure 4.3(a) shows a RAIR spectrum after co-deposition of NO:H$_2$O with a low H-atom flux. Here unlike for Fig. 4.3(b), HNO, X-NO and N$_2$O features can be observed in the ice.
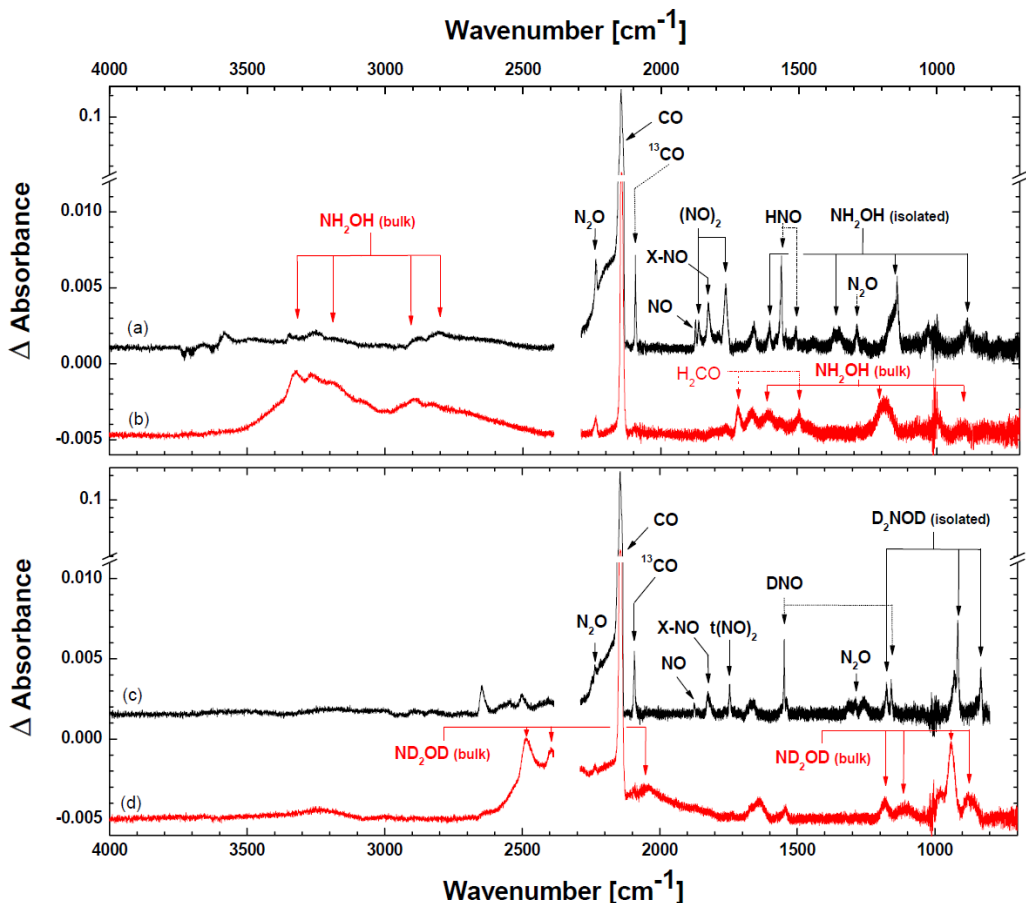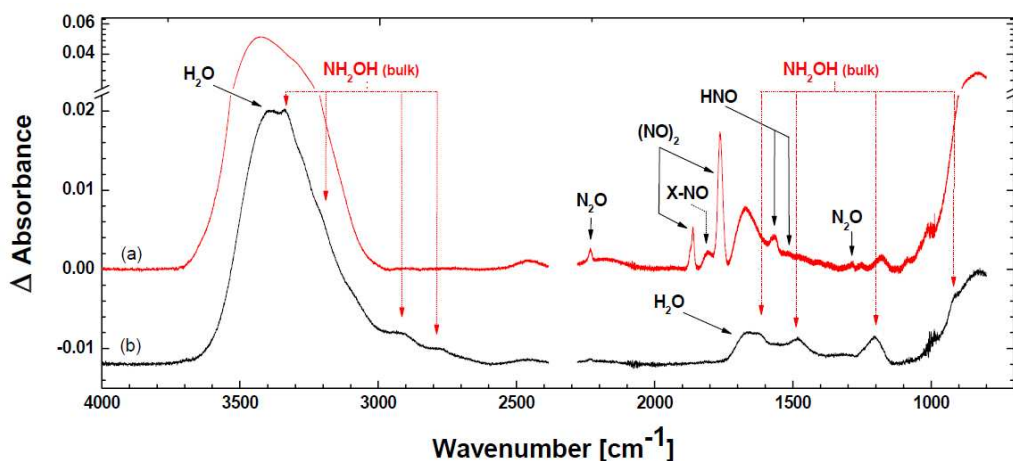

Figure 4.3. RAIR difference spectra of H-atom additions to NO in a polar H$_2$O ice for a sample temperature of 15 K. Co-deposition results of NO and H$_2$O with H atoms for NO:H$_2$O:H = 1:6:3.5 (a) and 1:6:15 (b) are shown.

4.3.4 UV photolysis of NO containing ices

Several pre-deposition experiments were performed with CRYOPAD to study the UV photon-induced chemistry in pure NO ice and in ice mixtures containing nitric oxide in water or carbon monoxide. In addition, tertiary ice mixtures NO:CO:H$_2$O with ratios 1:1:1 and 1:6:6 were exposed to UV photons.

As discussed in the previous sections, pure NO converts efficiently into *cis*-(NO)$_2$ ice upon deposition (Fig. 4.4(b)). Several positive bands appear after UV processing of

cis-(NO)$_2$ ice: the features at 2235 and 1286 cm^{-1} already observed in the NO hydrogenation experiments are assigned to N$_2$O. New bands with maxima at 1602, 1299, 779 cm^{-1} and, although not well resolved, 1850 cm^{-1} appear only in the UV photolysis experiments. These can be assigned to N$_2$O$_3$ (see Fig. 4.4(a)) (Fateley *et al*. 1959, Sluyts & Van der Veken 1994, Noir *et al*. 1983). The dilution of NO molecules in a CO matrix does not seem to influence this outcome substantially. As for Figure 4.4(a), all the absorption features assigned to *cis*-(NO)$_2$, N$_2$O and N$_2$O$_3$ are present in the RAIR spectra after exposure of NO:CO = 1:6 ice to UV photons (see Fig. 4.4(c)). In addition, the NO monomer is clearly detected because of the low mobility of NO in a CO lattice before and after UV photolysis of the ice sample. Moreover, the NO monomer abundance increases upon UV irradiation.

Two more carbon bearing species, apart from ^{12}CO and ^{13}CO are detected in an NO:CO ice upon UV photolysis: carbon dioxide and its ^{13}C isotope analogue. Since the solid carbon dioxide IR absorption feature overlaps with atmospheric gas-phase CO$_2$ present outside the UHV chamber and along the line of the FTIR beam, the formation of carbon dioxide in the ice upon UV photolysis is constrained by QMS data.

Figures 4.4(e-f) show the resulting spectra upon UV photolysis of an NO:H$_2$O (1:6) ice mixture. Also in this case, two species are present in the ice upon deposition: *cis*-(NO)$_2$ and H$_2$O. UV processing of the sample induces formation of several products: N$_2$O and monomeric NO, hydrogen peroxide (H$_2$O$_2$) and traces of HNO (right shoulder at 1565 cm^{-1}). Absorption features at 1607 and 1303 cm^{-1} may be due to N$_2$O$_3$ or NO$_2$. The absence of an absorption feature at 1850 cm^{-1} makes the NO$_2$ assignment more likely, but due to the low final yield this is not conclusive.

The UV processing of the tertiary NO:CO:H$_2$O ice mixtures reveals the formation of the same species formed in the aforementioned NO:CO and NO:H$_2$O ice photolysis experiments. Here the same features are assigned to H$_2$CO with peaks at 1715 and 1500 cm^{-1} and tentatively assigned to the NO stretching mode of HNO$_2$ peaking at 1640 cm^{-1}. It should be noted that the final yield of solid CO$_2$ is higher than in the case of UV irradiated NO:CO experiments. The addition of water ice to the NO:CO ice mixture increases the carbon dioxide formation. This can be explained by the presence of free OH radicals in the ice after UV irradiation that can react with CO to form CO$_2$ (more in the 'UV processing' section).

As can be concluded from Fig. 4.4, NCO radicals, NC$^-$ and NCO$^-$ anions as well as their hydrogenated analogues HNC and HNCO (Moore & Hudson *et al*. 2003, Pettersson *et al*. 1999, Bondybey *et al*. 1982, Hudson *et al*. 2005) are not present in any of our RAIR spectra. Another main result here is that NH$_2$OH is not formed upon UV photolysis of water rich ices. The straightforward conclusion is that surface H-atom addition reactions

are needed to provide a pathway for the formation of NH_2OH in simple interstellar ice analogues. We will address these points in the following sections.
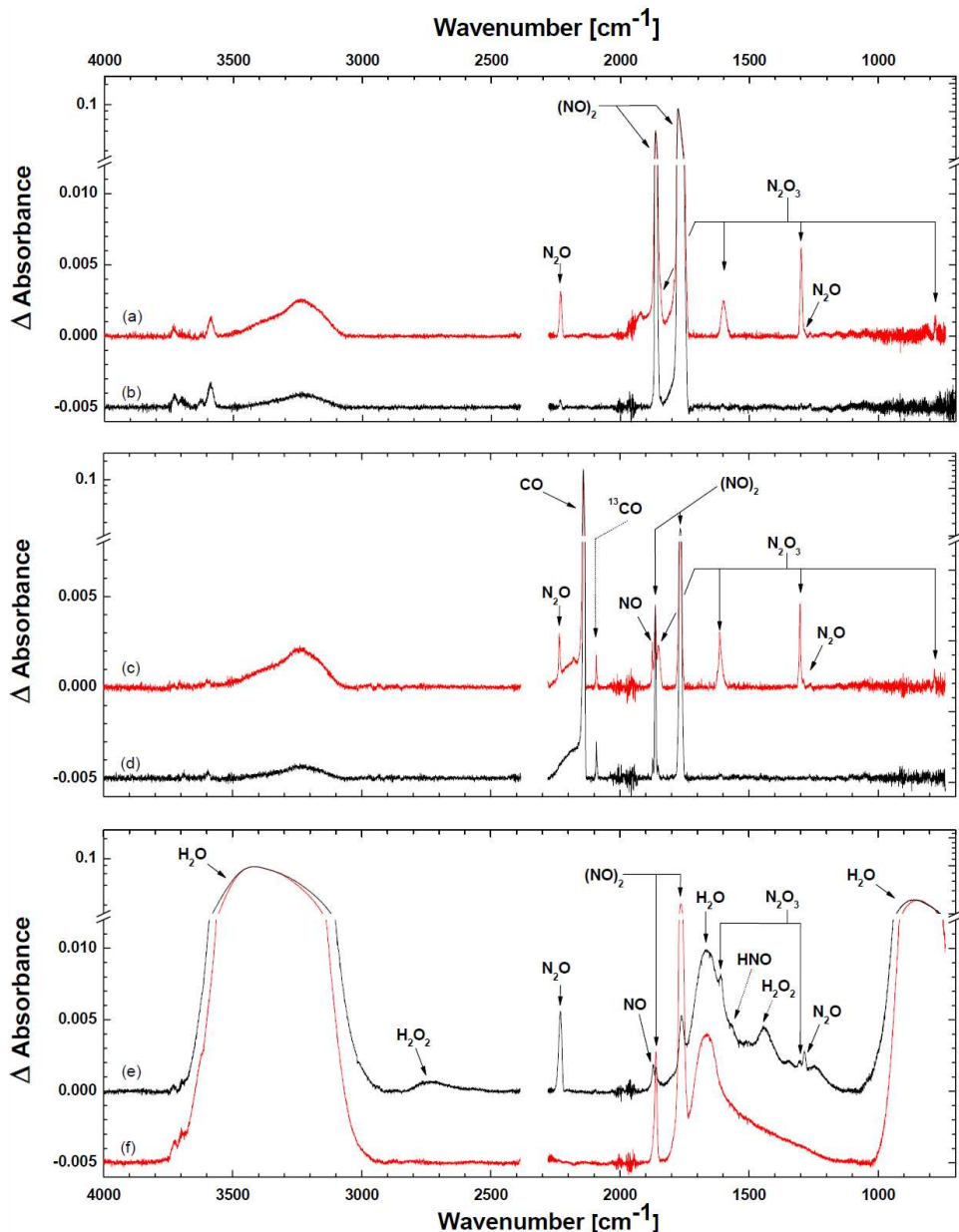
Figure 4.4. RAIR difference spectra obtained after UV photolysis of pre-deposited NO containing ices for a sample temperature of 15 K. The upper panel shows spectra of pure NO ice after deposition (b) and after exposure to $1 \cdot 10^{18}$ photons cm^{-2} (a). The middle panel shows similar spectra of NO in non-polar CO ice for NO:CO = 1:6 before (d) and after exposure to $1 \cdot 10^{18}$ photons cm^{-2} (c). The lower panel shows spectra of NO in polar H_2O ice after exposure to a fluence of $1 \cdot 10^{18}$ photons cm^{-2} (e) and after deposition (f) for comparison.

4.3.5 Temperature dependence

Temperature effects on reaction mechanisms can be rather complex and reflect the cumulative outcome of different temperature dependent processes. First of all, a higher ice temperature means more thermal energy that can help to overcome activation barriers. This has a direct effect on the final yields of the formed species and, therefore, on the formation trends. Secondly, a higher temperature can have an effect on the structure of the ice leading to molecular reorganization. For instance, it has been shown that different deposition temperatures result in different ice structures, *e.g.*, amorphous water ice *versus* crystalline water ice (Yabushita *et al*. 2008, Bossa *et al*. 2012). This affects the penetration depth of H atoms in the ice and more generally diffusion processes. Then, the hopping and swapping rates of molecules in the ice increase with temperature, while the residence lifetime of a species on the ice surface decreases.

The temperature dependence of selected surface formation reaction pathways is studied here by repeating the same experiments for two different and astronomically relevant temperatures, *i.e.*, 15 and 25 K. Since the thermal desorption temperatures of CO and N_2 are around this value, higher temperatures have not been studied. The top panel of Fig. 4.5 shows the formation trends of HNO and NH_2OH at 15 and 25 K as a function of the H-atom fluence for a co-deposition experiment of pure NO and H atoms. Here the integrated absorption of the formed species presents a linear trend because of the constant co-deposition of the parent species. The bottom left-side panel of Fig. 5.5 shows NH_2OH, HNO and N_2O final yields from the aforementioned pure NO + H experiments, while the bottom right-side panel shows NH_2OH, HNO and N_2O final yields for two NO:CO/H co-deposition experiments at 15 and 25 K. All these experiments present lower final product yields at higher temperatures. Moreover, as shown in both bottom panels, the ratios between HNO and NH_2OH final yields at 15 and 25 K are roughly constant and are 1.5 and 3.5 for the pure NO + H and the NO:CO + H experiments, respectively. This indicates that the formation of HNO and NH_2OH are linked and are most likely temperature independent, *i.e.*, reactions take place without an activation barrier. The lower final yields at higher temperature can be explained by the lifetime of H atoms on the ice surface that, for instance, is 10^3 times shorter at 25 K than at 15 K on water ice (Cuppen & Herbst 2007). In this way H atoms have less time to react with NO molecules leading to a decrease in the hydrogenation final yields. All final yields in the bottom right panel are lower than their counterparts in the bottom left panel. This can be explained by a lower abundance of NO molecules in the ice and the presence of solid CO. For the pure NO + H experiments, the final yield of solid N_2O is the same at different temperatures within the experimental uncertainties, while it decreases for higher temperatures in the NO:CO + H experiments.

This indicates that the formation of N_2O requires a temperature dependent reaction scheme and a more complex ice composition.
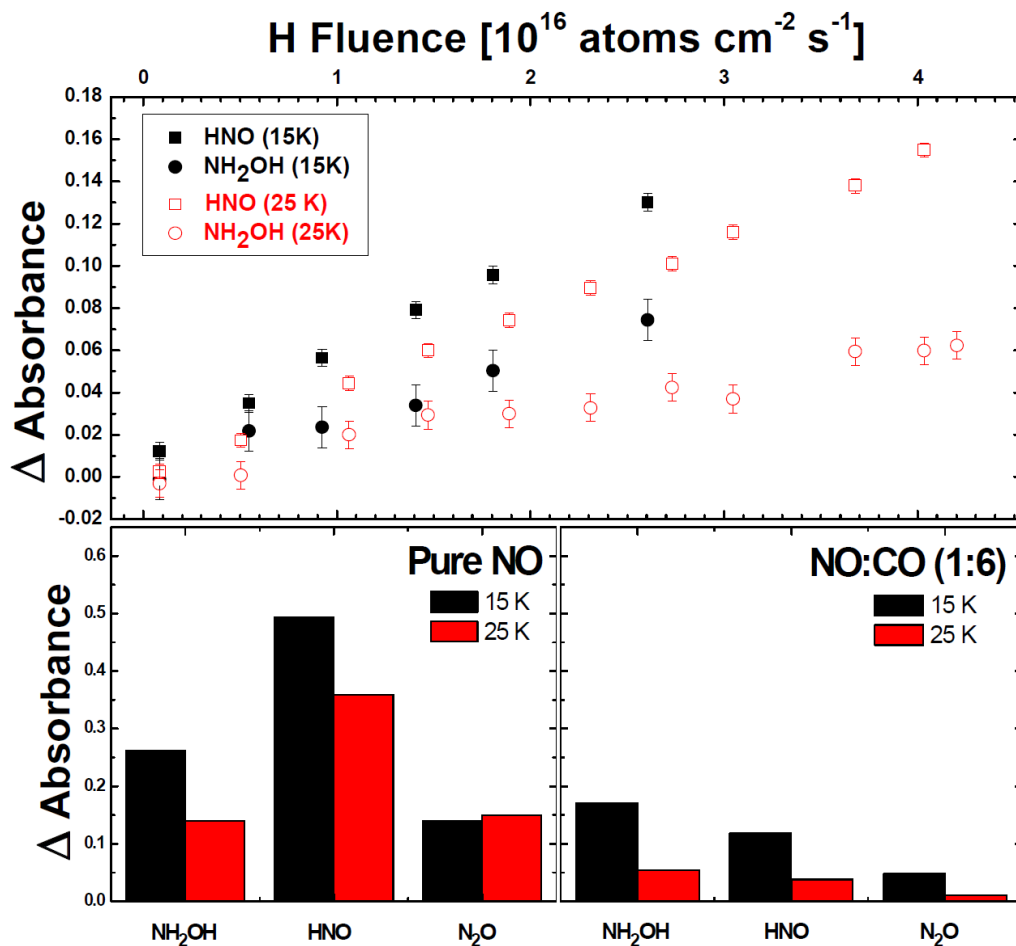
Figure 4.5. The top panel shows the temperature dependence of HNO and NH_2OH abundances *versus* the H-atom fluence for NO:H (2:1) co-deposition experiments at 15 and 25 K. The lower panels show the final yields of N_2O, HNO and NH_2OH for an NO:H (2:1) co-deposition experiment (bottom left) and an NO:CO:H (1:6:15) co-deposition experiment (bottom right). The left panel final yields are extrapolated from experimental data at the same H-atom fluence used for the final yields shown in the right panel.

4.3.6 Matrix effects

The dilution of NO in polar (water-rich ice) and non-polar (water-poor ice) matrices has a number of important effects on the hydrogenation pathways: 1) NO hydrogenation products can react with components of the mixture other than hydrogen atoms leading to a more complex reaction scheme; 2) the other molecules present in the deposited matrix (like

CO) can participate in H-atom addition reactions, effectively influencing reaction rates through additional H-atom consumption. Their reaction products may interact with NO and NO hydrogenation reaction products; 3) other species in the ice can trap NO molecules in the bulk of the ice hiding them from the impinging H atoms; 4) H-bonding can improve coupling and heat dissipation through the ice, promoting the stabilization of intermediate products and changing reaction branching ratios.

In order to investigate non-polar ices we have compared the results from the hydrogenation of pure NO ice with those from the hydrogenation of NO:CO ice mixtures with ratios of 1:1 and 1:6. The choice of these ratios is not random: if NO hydrogenation products interact with those from CO hydrogenation, then the 1:1 ratio should provide the highest yield of the final products; on the other hand, for an NO:CO = 1:6 ratio a single NO molecule is surrounded on average by an octahedron of six CO molecules (the NO dimer is surrounded by 12 CO molecules). Therefore, this is a good approach to see whether NO and CO interact with each other upon hydrogenation of the ice. Moreover, since CO is highly abundant in quiescent dark clouds compared to NO (Liszt & Turner 1978, Pwa & Pottasch 1986, McGonagle *et al*. 1990, Gerin *et al*. 1992), A 1:6 ratio is astrochemically more relevant. We furthermore investigated the two NO:CO 1:1 and 1:6 mixtures for two different H-atom fluxes of $7 \cdot 10^{12}$ and $3 \cdot 10^{13}$ atom$\cdot$cm$^{-2} \cdot$s^{-1}. During these co-deposition experiments the ratio between H atoms and the sum of NO and CO molecules is kept constant. Figure 4.6 plots the integrated intensities of NO hydrogenation products as a function of the H-atom fluence for pure NO and NO:CO mixtures with ratios 1:1 and 1:6 co-deposited with H atoms.

The upper panels of Fig. 4.6 show the integrated intensities of NH_2OH, HNO and N_2O *versus* the H-atom fluence for three co-deposition experiments (NO/H = 1/10, NO:CO/H = 1:1/20, 1:6/70) where the H-atom flux is high in order to efficiently convert nitric and carbon oxides into their hydrogenation products. The abundance of NH_2OH in the ice is proportional to the abundance of NO in the mixture, while the HNO abundance is inversely proportional to that of NO. The N_2O ice abundance is strongly affected by the presence of CO in the ice, however it does not seem to depend on the mixture ratios used here. In addition, and as mentioned before, NO absorption features (from both the dimer and monomer) are not present in the RAIR spectra of pure NO + H and NO:CO = 1:1 + H (see Fig. 4.1(b) and Fig. 4.2(b)) but only in the NO:CO = 1:6 hydrogenation experiment (Fig. 4.2(a)). The presence of NO in the ice after hydrogenation can be explained by the trapping effect of NO inside a CO lattice and the consequent blocking effect of H atoms in a CO ice (Fuchs *et al*. 2009, Ioppolo *et al*. 2011). Consequently, the gradual decrease of the hydroxylamine yield with increasing CO content in the ice can be explained by a decrease in the absolute amount of NO available for hydrogenation reactions. This conclusion is further constrained by the nitroxyl final yield, which is inversely proportional to the

hydroxylamine yield: HNO is only observed in the ice when some NO remains unconverted into NH_2OH. This confirms that the formation paths of nitroxyl and hydroxylamine are linked.

The lower panels of Fig. 4.6 show the RAIR integrated absorbances of NH_2OH, HNO and N_2O *versus* the H-atom fluence for three co-deposition experiments (NO/H = 1/0.5, NO:CO/H = 1:1/1, 1:6/3.5) but now the H-atom flux is low in order to detect the not-fully-hydrogenated species in the ice. All plots show very similar abundances of N_2O and HNO and slightly higher yields for NH_2OH in a pure NO hydrogenation experiment compared to the hydrogenation of NO:CO mixtures. The products of H-atom addition to CO molecules (H_2CO, CH_3OH) are not detected in any of these experiments. This leads to an important conclusion: the hydrogenation of NO ice is more efficient than the hydrogenation of CO ice and is most likely barrierless as concluded here and in (Congiu *et al*. 2012a). It was shown before that the intermediate CO + H and H_2CO + H reaction steps have an activation barrier, while HCO + H and H_3CO + H take place without an activation barrier (Watanabe & Kouchi 2002, Fuchs *et al*. 2009). Thus, if the subsequent hydrogenation of nitric oxide (NO + H, HNO + H, H_2NO + H) proceeds with no activation barrier, then the NH_2OH final yield depends only on the amount of NO molecules and H atoms available for reaction. This is fully consistent with the observation that all infrared NH_2OH, HNO and N_2O integrated band intensities shown in the lower panels of Fig. 4.6 present a similar final yield. Minor differences among the formation trends may be due to the presence of CO molecules.

The dipole moments of CO, NO and the *cis*-$(NO)_2$ are all small and comparable (Smyth & McAlpine 1933, Rawlins *et al*. 1998, Western *et al*. 1980), and the ice structures are also quite similar (Dulmage *et al*. 1953, Cromer *et al*. 1983). This explains why dilution of NO in a CO matrix does not substantially influence the reaction network and, consequently, the formation trends of the final products. In contrast, water molecules have a strong dipole moment and form strong hydrogen bonds in the ice with other species, such as NH_2OH, $NH_2O\cdot$ and $\cdot NHOH$ radicals, and H_2O itself. We performed several experiments co-depositing NO:H_2O binary mixtures and H atoms using similar experimental conditions to those adopted for the non-polar ice investigation. The results are summarized in Fig. 4.7. In this case we compared results for an NO:H_2O = 1:6 ratio co-deposition experiment with low and high H-atom fluxes. For a high H-atom flux the water matrix significantly increases the hydroxylamine final yield, while it decreases both nitroxyl and nitrous oxide final yields. For low H-atom flux only hydroxylamine exhibits a higher yield in a water lattice compared to a similar experiment with NO:CO = 1:6.

The NHOH and NH_2O intermediates, as well as final product NH_2OH, form strong hydrogen bonds with a water lattice. HNO also forms this kind of bond, but less efficiently. Such hydrogen bonds help HNO and NH_2OH molecules to dissipate excess energy quickly

upon formation and make the hydrogenation of NO and HNO kinetically favourable compared to the case of NO + H in a CO lattice in which these kinds of bonds are not formed. It should be noted that a water matrix significantly decreases the N_2O final yield for high H-atom flux, but increases it for low flux. Moreover, hydrogenation of NO in an N_2 matrix (NO:N_2 = 1:5) for high H-atom flux gives an N_2O yield that is three times higher than that obtained in an NO:CO hydrogenation experiment. The interpretation of this result is not straightforward and the influence of different lattice types on the N_2O formation route is therefore uncertain.
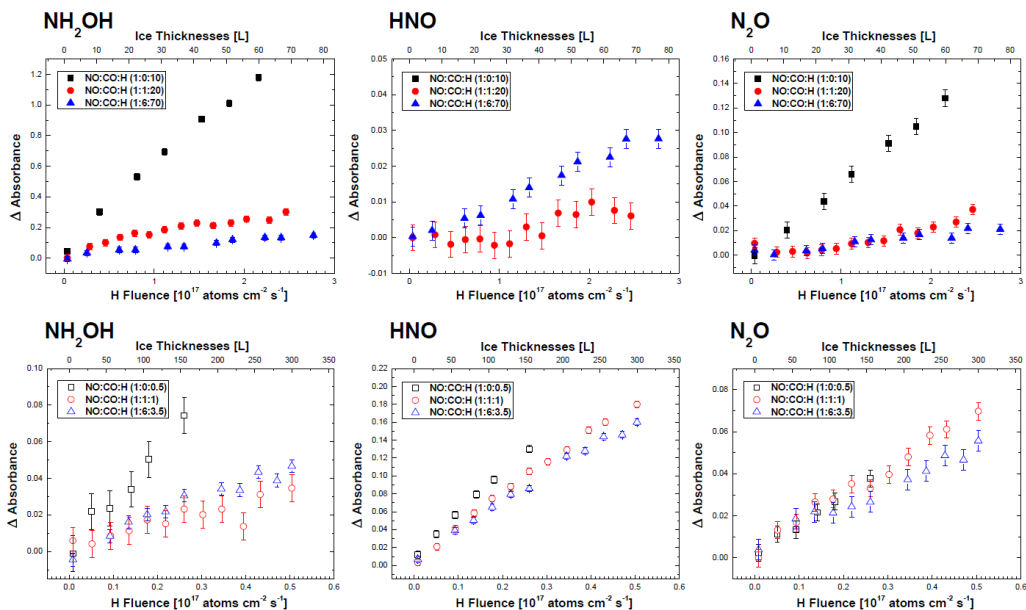
Figure 4.6. RAIR integrated intensities of hydroxylamine (left-side panels), nitroxyl (centre panels) and nitrous oxide (right-side panels) *versus* H-atom fluence for several co-deposition experiments using high H-atom flux (top panels) and low H-atom flux (bottom panels). Every panel shows three curves: one for H atoms co-deposited with pure NO (black squares), another for H atoms co-deposited with NO:CO = 1:1 mixture (red circles) and one for co-deposition of H atoms co-deposited with NO:CO = 1:6 mixture (blue triangles). A missing curve indicates that the product is not detected during the experiment.
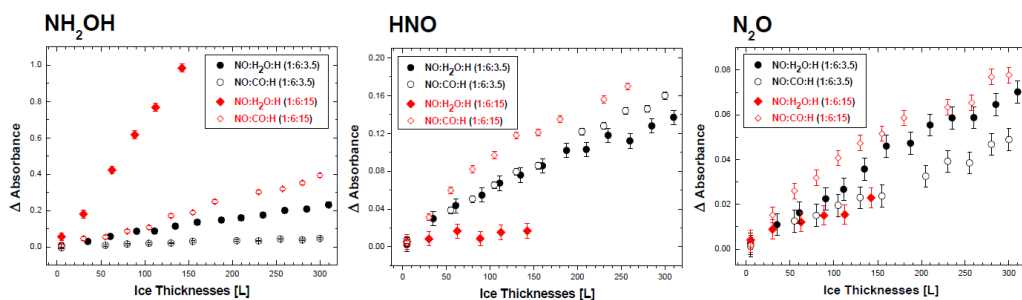
Figure 4.7. RAIR integrated intensities of hydroxylamine (left-side panel), nitroxyl (centre panel) and nitrous oxide (right-side panel) formed upon H-atom exposure *versus* the ice thickness in a co-deposition experiment of NO:CO(1:6) + H and NO:H$_2$O(1:6) + H. Each panel shows four curves: low H-atom flux co-deposited with NO:H$_2$O = 1:6 mixture (full black circles); low H-atom flux co-deposited with NO:CO = 1:6 mixture (empty black circles); high H-atom flux co-deposited with NO:H$_2$O = 1:6 mixture (full red diamonds); low H-atom flux co-deposited with NO:CO = 1:6 mixture (empty red diamonds).

4.3.7 Possible reaction pathways

4.3.7.1 NO hydrogenation network

Figure 4.8 shows the NH$_2$OH formation reaction scheme as investigated in this work. The solid lines indicate reaction pathways that take place without an activation barrier or with a very small activation barrier and are therefore efficient at cryogenic temperatures, *e.g.*, in dense cold quiescent clouds. The dashed lines represent the reactions that proceed with an activation barrier.

In Fig. 4.8, three subsequent H-atom addition reactions to form NH$_2$OH from a single NO molecule are highlighted in red double-bordered boxes.

$$NO + H \rightarrow HNO, \tag{4.1a}$$
$$HNO + H \rightarrow H_2NO, \tag{4.1b}$$
$$H_2NO + H \rightarrow H_2NOH. \tag{4.1c}$$

These three reactions represent the simplest and most efficient formation route of hydroxylamine. In reactions (4.1a) and (4.1b), the H atoms are subsequently added to the N atom of the NO molecule, while the last H atom in reaction (4.1c) is added to the oxygen. The reactions

$$NO + H \rightarrow NOH, \tag{4.2a}$$
$$HNO + H \rightarrow HNOH, \tag{4.2b}$$

where the addition of H atoms takes place on the oxygen atom side of the NO molecule, are expected to be less efficient. Matrix isolation experiments (Jacox & Milligan 1973) and *ab initio* calculations (Page & Soto 1993) indeed indicate that these reactions have high activation barriers (>4000 K and >10000 K, respectively, see Page & Soto 1993) and are, therefore, less efficient compared to the barrierless reactions (4.1a) and (4.1b). However, for the reaction

$$HNO + H \rightarrow NO + H_2, \tag{4.3a}$$

gas-phase *ab initio* calculations (Page & Soto 1993) show that the rate of hydrogen atom abstraction is higher than the rate of hydrogen atom addition at all temperatures (*e.g.*, by a factor of 20 at 300 K). This is not consistent with our experimental results where hydroxylamine is formed even at very low H-atom fluxes. This discrepancy, however, is likely due to differences between solid-state and gas-phase reactions. Reactions (4.1b) and (4.3a) are both exothermic. Reaction (4.3a) provides two final products and in this case the excess energy of the reaction can be efficiently distributed over two bodies to be translationally dissipated both in the gas phase and in the solid state. For reaction (4.1b) this excess energy must be distributed only over the vibrational- and in the gas phase also rotational-levels of a single hydrogenation product (unless photon emission with required energy is allowed)**,** and will be much less efficient in the gas phase than in the solid state where the surrounding molecules play the role of an absorbing third body. Therefore, the presence of a third body can efficiently change the branching ratio between H-atom addition and H-atom subtraction reactions, leading, for instance, to the efficient surface formation of NH_2OH ice. As in reaction (4.3a), the hydrogen abstraction reaction

$$H_2NO + H \rightarrow HNO + H_2, \tag{4.3b}$$

is also barrierless (Diau *et al*. 1995, Page & Soto 1993) and should compete with the hydrogen addition reaction (4.1c). However, as discussed above, the formation of hydroxylamine has a higher effective branching ratio than reaction (4.3b) in the solid state.

The hydrogenation of NO monomers through reactions (4.1a) – (4.1c) takes place only in NO:CO and NO:H_2O hydrogenation experiments where the CO or H_2O lattice can keep a fraction of the NO monomers isolated and can prevent their dimerization through reactions (4.4a) and (4.4b):

$$NO + NO \rightarrow cis\text{-}(NO)_2, \tag{4.4a}$$
$$NO + NO \rightarrow trans\text{-}(NO)_2. \tag{4.4b}$$

Formation of *cis*-(NO)$_2$ is the preferred reaction pathway and is confirmed by NO matrix isolation experiments (Fateley *et al.* 1959, Sluyts & Van der Veken 1994). Under our experimental conditions *trans*-(NO)$_2$ is observed only in an NO:CO:H = 1:6:70 co-deposition experiment where it is trapped by the CO lattice and the products of NO hydrogenation.

Due to a lack of gas-phase kinetic data the hydrogenation reaction scheme for (NO)$_2$ has so far been unclear. Here we experimentally show several reaction routes involving the hydrogenation of (NO)$_2$. First, the nitric oxide dimer reacts with an H atom to form HNO and NO,

$$(NO)_2 + H \rightarrow HNO + NO, \tag{4.5a}$$
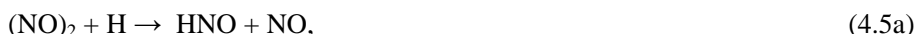
or produces an HNO·NO associated complex. The existence of this complex has already been suggested by several groups (Lin *et al.* 1992, Cheskis *et al.* 1981, Seddon *et al.* 1973, Chakraborty *et al.* 1988),

$$(NO)_2 + H \rightarrow HNO \cdot NO. \tag{4.5b}$$

The addition of another H atom to a nitrogen atom of this associated complex leads to the formation of H$_2$NO, HNO and NO:

$$HNO \cdot NO + H \rightarrow H_2NO + NO, \tag{4.6a}$$
$$HNO \cdot NO + H \rightarrow HNO + HNO. \tag{4.6b}$$

All these reactions lead to the formation of hydroxylamine precursors as shown by reactions (4.1a) – (4.3b). Our experiments confirm that hydroxylamine will eventually be formed upon hydrogenation of these species.

There is another final product of NO hydrogenation reactions which is always observed in our experiments: N$_2$O ice. The reaction pathway to form N$_2$O is not yet clear, since all known possible mechanisms involve a high activation barrier.

A possible mechanism to form N$_2$O is through HNO dimerization and the subsequent dissociation of the formed hyponitrous acid (Diau *et al.* 1995, Lin *et al.* 1992, Cheskis *et al.* 1981),

$$HNO + HNO \rightarrow H_2N_2O_2 \; (OHN=NHO), \tag{4.7}$$
$$H_2N_2O_2 \; (OHN=NHO) \rightarrow isomerisation \rightarrow N_2O + H_2O. \tag{4.8}$$
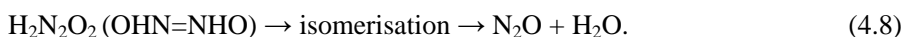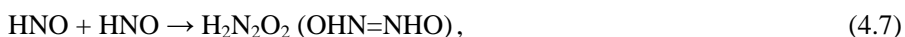
This mechanism is rather unlikely to occur at cryogenic temperatures, because reaction (4.8) involves at least one H-atom migration from a nitrogen atom to an oxygen atom of an OHN=NHO molecule leading to the formation of the intermediate HON(NO)H or HON=NOH which will then dissociate to form nitrous oxide and water (Diau *et al*. 1995, Lin *et al*. 1992). Both dissociation and H-atom migration involve activation barriers as well as the HNO dimerization itself (reaction 4.7). However, several of these activation barriers can be overcome by the following mechanism. First, an H atom is added to an N atom of the HNO·NO associated complex. This reaction is exothermic and takes place without an activation barrier. The excess energy of this reaction can then help to overcome the $H_2N_2O_2$ dissociation barrier leading to the formation of nitrous acid by a mechanism similar to reactions (4.7) and (4.8):

$$HNO \cdot NO + H \rightarrow H_2N_2O_2(\text{"hot"}) \rightarrow \text{isomerisation} \rightarrow N_2O + H_2O. \qquad (4.9)$$
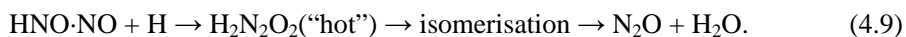
The weak point of both suggested mechanisms is the high activation barrier in the last step of reactions (4.8) and (4.9). Because of this barrier $H_2N_2O_2$ (OHN=NHO) should be detectable in our spectra under our experimental conditions together with N_2O. Moreover, the infrared spectrum of $H_2N_2O_2$ and its deuterated analogue have strong absorption features, *i.e.*, two close bands around 1000 cm^{-1} which are not present in our RAIR spectra (see Figs. 4.1(c, e), Figs. 4.2(a, c)) (McGraw *et al*. 1967). The absence of $H_2N_2O_2$ absorption features indicates that another reaction pathway is likely responsible for the N_2O formation.

One of these possible formation mechanisms for N_2O was suggested earlier in Cooper *et al*. 1970 and Bonner *et al*. 1978, where reduction of NO with alkaline hydroxylamine was studied:

$$HNOH + NO \rightarrow HON(NO)H, \qquad (4.10)$$
$$HON(NO)H \rightarrow N_2O + H_2O. \qquad (4.11)$$

Reaction (4.10) is exothermic (Diau *et al*. 1995) and, as other radical-radical reactions, should proceed without an activation barrier. The product of reaction (4.10) may be formed with enough internal energy to overcome its dissociation barrier and to produce nitrous oxide and water (reaction 4.11). However, the formation of HNOH (reaction 4.2b) is thermodynamically unfavourable (Diau *et al*. 1995). Therefore another formation mechanism is proposed here, *i.e.*, the direct addition of an H atom to the oxygen atom of an (NO)$_2$ dimer followedy the dissociation of the unstable radical:

$$ONNO + H \rightarrow (ONNOH) \rightarrow N_2O + OH. \qquad (4.12)$$
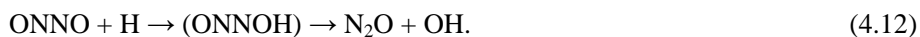
This reaction pathway is exothermic, and according to BAC – MP4 calculations (Diau *et al*. 1995) the second step is barrierless (or at least has a very small barrier). The first step of this reaction is similar to reaction (4.2a) and, therefore, presents an activation barrier (dashed arrow in Fig. 4.8). Although our experimental data are not conclusive on the efficiency of the N_2O formation mechanisms, reaction (4.12) is likely the most efficient pathway because of its simplicity and because we do not detect the intermediates formed according to reactions (4.7) – (4.11).

In Congiu *et al* (2012b), two reaction pathways are suggested for the formation of N_2O ice in a low surface coverage regime (<1 monolayer) on silicate surfaces. The first one is reaction (4.12) as discussed above. A different formation route is:

$$HNO + NO \rightarrow N_2O + OH. \tag{4.13a}$$

BAC-MP4 calculations (Diau *et al*. 1995) show that this formation mechanism involves at a certain stage the migration of one H atom from a nitrogen to an oxygen atom:

$$HNO + NO \rightarrow HN(O)NO \rightarrow ONNOH \rightarrow N_2O + OH. \tag{4.13b}$$
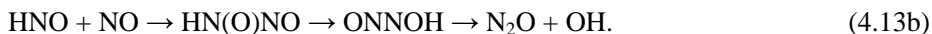
This migration process has a very high activation barrier (122 kJ mol^{-1}) and is endothermic (Diau *et al*. 1995). A possible way to overcome this activation barrier under our experimental conditions is through the participation of a "hot" HNO molecule formed from reaction (4.1a) before the HNO dissipates its excess energy (203 kJ mol^{-1}, see Diau *et al*. 1995) into the bulk of the ice. However this reaction is unlikely to occur in a high surface coverage regime, when HNO is always surrounded by other species. Moreover, reaction (4.13) requires at the same time the presence of NO monomer, which is detected in a high surface coverage regime only if NO is diluted into a CO matrix (see Fig 4.2a). Therefore, reaction (4.13) is unlikely to be efficient under our experimental conditions.

The unidentified absorption feature in our IR spectra, here named X-NO, appears at 1829 cm^{-1}. Further experimental constraints are needed to assign this feature to the HNO·NO complex or to the HON(NO)H intermediate.

The produced OH radicals from reaction (4.12) can react with H atoms and NO molecules to form:

$$OH + H \rightarrow H_2O, \tag{4.14a}$$
$$OH + NO \rightarrow HNO_2. \tag{4.14b}$$

Recently another solid-state reaction pathway involving the OH radical was extensively investigated at cryogenic temperatures in (Romanzin et al. 2011, Oba et al. 2012):

$$OH + H_2 \rightarrow H_2O + H. \tag{4.14c}$$

The identification of H_2O and HNO_2 is not trivial due to the low final yield of these species and the overlap of their absorption features with other molecules present in the ice. Newly formed H_2O molecules are reported in the gas phase upon desorption from the ice in Congiu et al (2012b). The amount of water ice formed at the end of the experiments described there is estimated to be a fraction of a monolayer ($\sim$ 0.5 ML). Moreover, all the suggested formation routes of H_2O ice have N_2O as an accompanying product. Since N_2O is present only in low abundances in our experiments, the formation of H_2O in the present study is expected to be inefficient.

As previously mentioned H_2CO is not formed during low H-atom flux experiments, but it is present in the ice only if all NO is converted to its hydrogenation products. Both gas-phase experimental work (Butkovskaya et al. 1997) and calculations (Diau et al. 1995) show that the following reaction:

$$HCO + NO \rightarrow HNO + CO, \tag{4.15}$$

is exothermic and likely barrierless. If reaction (4.15) takes place under our experimental conditions, the presence of NO in the ice can efficiently reduce the final H_2CO yield in favour of the NH_2OH formation. This is consistent with our experimental results. However, there is no direct evidence for this reaction pathway in our experiments. In particular, the low efficiency of H_2CO formation may also be explained by a short residence time of the H atoms on the ice surface combined with the competition between the CO + H reaction, which has a barrier, and the barrierless NO + H reaction (4.1a).
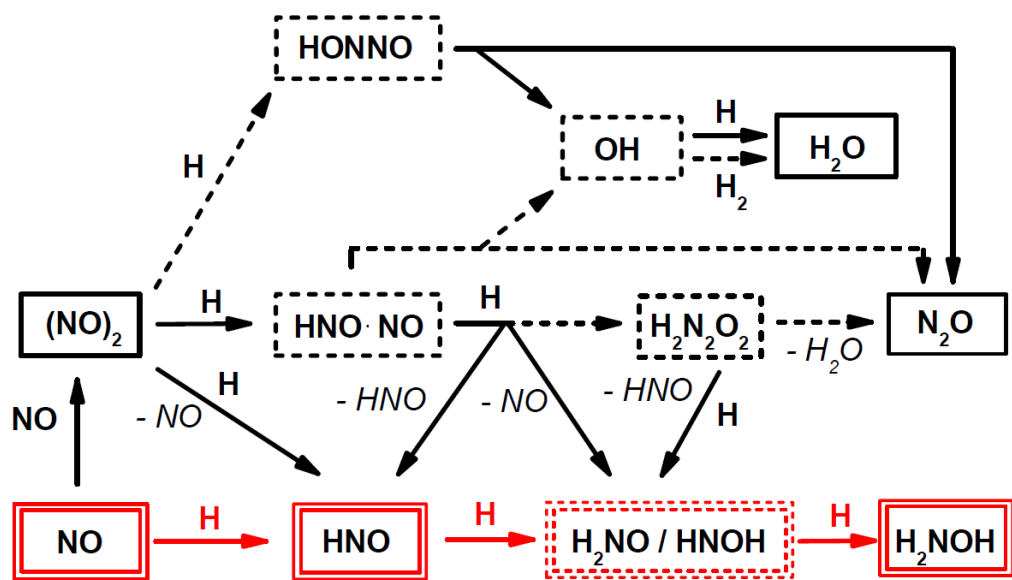
Figure 4.8. A schematic representation of the solid state NO + H reaction network, summarizing the conclusions from this work and Congiu *et al.* (2012b). Solid squares indicate species that are detected in the ice while dashed squares indicate intermediate products that are not detected but may be formed in the ice. Solid arrows represent efficient and/or barrierless reactions. Dashed arrows represent reaction pathways with an activation barrier. Only atom and radical addition reactions are presented here (*e.g.*, hydrogen abstraction reactions are omitted for simplicity).

4.3.7.2. UV processing of the ice

As opposed to the neutral-neutral non-energetic surface reactions discussed in the previous section, UV processing of ices provides an energetic input that leads to the dissociation of molecular bonds and the formation of "hot" fragments, *i.e.*, radicals, atoms and ions. These "hot" fragments can in turn react with the surrounding molecules and easily overcome activation barriers, desorb from the ice surface or diffuse into the bulk of the ice and kick other molecules out (Öberg at al. 2007, Öberg at al. 2009, Öberg at al. 2010). Here we focus on the UV photolysis of pure solid NO and NO mixed with CO and H_2O ices. Although a detailed quantitative analysis of the UV-induced reaction network is challenging without knowing photodissociation and photoionisation cross-sections for all the molecules present and/or formed in the ice upon UV photolysis, we can still draw important conclusions on the efficiency of several reaction pathways.

UV processing of pure NO ice gives two final products: N_2O and N_2O_3. These species can be formed through the following reaction:

$$2(NO)_2 + h\nu \rightarrow N_2O + N_2O_3. \tag{4.16}$$

First, a N-O bond from a *cis*-$(NO)_2$ is broken upon UV photolysis (reaction 4.17a). Then, the free oxygen atom recombines with a nearby nitrogen atom of another $(NO)_2$ dimer to form dinitrogen trioxide (reaction 4.17b):

$$(NO)_2 + h\nu \rightarrow N_2O + \cdot O, \tag{4.17a}$$
$$(NO)_2 + \cdot O \rightarrow N_2O_3. \tag{4.17b}$$

This result is consistent with Hawkins & Downs (1984) where the photolysis of *cis*-$(NO)_2$ is studied at 13 K in an Ar matrix. The formation of nitrous oxide *via* direct photodissociation of nitric oxide and the consequent N-atom addition reaction to an NO dimer:

$$(NO)_2 + h\nu \rightarrow NO + \cdot N + \cdot O, \tag{4.18a}$$
$$(NO)_2 + N \rightarrow N_2O + NO. \tag{4.18b}$$

is unlikely to occur since gas-phase chemical data show (Diau *et al.* 1995, Lin *et al.* 1992) that the nitrogen atom addition to NO forms molecular nitrogen rather than nitrous oxide. Moreover, the non-detection of the $\cdot$NCO radical in NO:CO photolysis experiments constrains the low efficiency of reaction (4.18a):

$$CO + N \rightarrow \cdot NCO. \tag{4.19}$$

UV processing of NO:CO ice mixtures yields two additional products: NO monomers and CO_2. The formation of NO monomers can be explained by the reaction:

$$(NO)_2 + h\nu \rightarrow NO + NO^*, \tag{4.20}$$

and the subsequent isolation and relaxation of "hot" (electronically or vibrationally excited) monomers in a CO lattice.

The other product is CO_2 ice that can be formed through "hot" oxygen atom addition to carbon monoxide:

$$CO + \cdot O \rightarrow CO_2. \tag{4.21}$$

This reaction pathway is discussed in several experimental studies (Raut & Baragiola 2011). According to Raut & Baragiola (2011), reaction (4.21) takes place even at cryogenic

temperatures, although it has a significant activation barrier. The transfer of O atoms from cis-$(NO)_2$ molecules is also observed in Hawkins & Downs (1984) after the exposure of Ar/NO/CO samples to photons at $\lambda = 220 - 330$ nm.

Our experiments show that photolysis of nitric oxide in a matrix of carbon monoxide and water produces an even larger amount of CO_2. As recently shown in independent laboratory experiments (Oba *et al*. 2010, Ioppolo *et al*. 2011, Noble *et al*. 2011), CO_2 can be efficiently formed through the reactions:

$$H_2O + h\nu \rightarrow \cdot OH + \cdot H, \tag{4.22}$$
$$CO + \cdot OH \rightarrow HOCO \rightarrow CO_2 + H, \tag{4.23}$$

where direct dissociation of the HOCO complex leads to the formation of CO_2 ice.

Photodissociation of water ice (reaction 4.22) can also explain the formation of the final products only detected when an $NO:H_2O$ ice was exposed to UV photons: H_2O_2 by recombination of two OH radicals, HNO by H-atom addition to NO (reaction 4.1a), and possibly HNO_2 by recombination of nitric oxide with a hydroxyl radical:

$$NO + \cdot OH \rightarrow HONO. \tag{4.24}$$

Additionally, water can react with a "hot" (electronically excited) oxygen atom to form hydrogen peroxide:

$$H_2O + \cdot O \rightarrow \cdot OH + \cdot OH \rightarrow H_2O_2. \tag{4.25}$$

This reaction pathway competes with the formation of N_2O_3 in water-rich matrices (reactions 4.17a – 4.18a) by consuming free O atoms and may be the cause of the low final yield of N_2O_3 detected in water-rich ices (see Fig. 4.4).

The newly formed products may themselves participate in UV-induced chemistry. For example, UV photodissociation of CO_2 and N_2O leads to the formation of free O atoms:

$$CO_2 + h\nu \rightarrow CO + \cdot O, \tag{4.26}$$
$$N_2O + h\nu \rightarrow N_2 + \cdot O. \tag{4.27}$$

These reactions can play a role in oxygen transfer, but become important only after a long photolysis period with a total UV exposure of at least 10^{17} photons cm^{-2}. This flux corresponds to more than hundred incident UV photons per adsorption spot.

The low ionisation potential of cis-$(NO)_2$ can lead to the formation of NO^+ and $(NO)_2^+$ in the ice upon absorption of Ly-α radiation (Levchenko *et al*. 2006). However, it is not

clear from our experimental data to what extent ion chemistry is involved in the O atom transfer and the subsequent formation of N_2O_3 and CO_2.

The non-detection of NH_2OH in the $NO:H_2O$ ice photolysis experiments indicates that there is a lack of free H atoms in the bulk of the ice. Therefore, reaction (4.22) has a low efficiency and/or recombination of hydrogen atoms is an efficient mechanism under our experimental conditions. Another mechanism which could reduce the final NH_2OH yield is the efficient photodissociation of the intermediate HNO. Recently, we tried to form NH_2OH by UV photolysis of $NH_3:H_2O$ and $NH_3:O_2$ ice mixtures. These experiments show that the formation of NH_2OH in the bulk of $NH_3:H_2O$ ice is not efficient either, while UV photolysis of $NH_3:O_2$ ice mixtures gives uncertain results.

4.4 Astrochemical implications

In quiescent dark clouds, grains provide surfaces on which species can accrete, meet and react and to which excess reaction energy can be donated. Grain surface chemistry is governed by the accretion rate of the gas-phase species and the surface migration rate. The timescale at which gas-phase species deplete onto grains is about 10^5 years in dense clouds with lifetimes of dense cores between 10^5 and 10^6 years. Early during dense cloud formation an H_2O-rich (polar) ice containing mainly CO_2 and traces of CH_4 and NH_3 forms. Under these conditions NO can be also formed through surface reactions. In prestellar cores, where densities are as high as 10^5 cm^{-3} and temperatures are $10 - 20$ K, gas-phase CO molecules freeze out onto the water ice layer forming a non-polar ice which is the site for additional and more complex reaction pathways. Under these conditions gas-phase formed NO can also deposit onto icy grains and species like N_2O, HNO and NO itself can be formed through surface reactions involving H-, N- and O-atoms. These species are, therefore, expected to be present in both polar and non-polar ices during the prestellar core-phase. In a recent astronomical study (Congiu *et al*. 2012a) we discussed the efficiency of the formation of hydroxylamine starting from the hydrogenation of a pure NO ice. In this work, by studying the hydrogenation of NO in H_2O-, CO-, and N_2- ice mantles, a full reaction scheme in polar and non-polar environments has been derived.

Due to the low abundance of interstellar solid NO compared to water ice the upper part of the chemical network presented in Fig. 4.8 is not likely to be astronomically relevant. The formation of an $(NO)_2$ dimer in space is indeed not favourable. However, the hydrogenation of NO molecules and the subsequent formation of NH_2OH is efficient (through a barrierless mechanism) at cryogenic temperatures (15 K) in both water- and carbon monoxide-rich ices. Therefore, according to our experimental results we expect that in quiescent dark clouds NO is efficiently converted to hydroxylamine. However, special

care is needed to extrapolate the laboratory data to astronomical timescales and fluxes, as our experiments, for obvious reasons, are not fully representative for interstellar conditions.

To show that the presented reaction scheme (Fig. 4.8) can indeed lead to the formation of NH_2OH in dense cores, we have performed a gas-grain model using a full gas and grain chemical network of more than 6000 reactions between 460 species of which 195 are involved in both gas-phase and grain-surface reactions (Congiu *et al*. 2012a). For this we used the OSU gas-grain code, first described by Hasegawa *et al*. (1992) with some recent modifications, which are described in Hassel *et al*. (2008). The initial abundances and chemical network are taken from a benchmark study of chemical codes (Semenov *et al*. 2010). The physical conditions are chosen similar to their "TMC 1" model which represents a prototypical dense cloud. A fraction of the formed surface species is allowed to desorb into the gas phase according to the Rice-Ramsperger-Kessel (RRK) theory (Holbrook *et al*. 1996, Garrod *et al*. 2007) with an efficiency of $\alpha = 0.01$.

Most surface reactions in chemical networks are based on chemical intuition or are included by analogy to gas-phase reactions. The reaction between H and HNO in standard chemical networks leads to H_2 and NO, while NH_2OH is usually formed through $NH_2 + OH$. Therefore, in standard chemical networks, no NH_2OH is formed and NO ice is mostly converted into HNO or N_2O under dark cloud conditions. This is in agreement with Garrod *et al*. (2007) who performed chemical models of star formation and who found that NH_2OH is only abundantly formed in the "hot-core" phase when the grain is lukewarm and NH_2 and OH become mobile.

Since in cold dense clouds the visual extinction is around 10 mag and photodissociation events are rare, the surface abundance of radical species like OH and NH_2 is low. The low grain-surface temperature of 10 K reduces the mobility of these species, while hydrogen atoms are already mobile at this temperature. Moreover, UV photolysis experiments show that hydroxylamine is not formed by irradiating $NO:CO:H_2O$ nor $NH_3:H_2O$ ice mixtures at low temperatures. The NO hydrogenation scheme as experimentally investigated in the present study is, therefore, much more promising as an NH_2OH formation reaction route. In our model, that includes the NO hydrogenation scheme, NH_2OH is indeed abundantly present in both the solid and the gas phase. The hydroxylamine abundance peaks at 10^5 years. Photodissociation into OH and NH_2, of which the latter converts into NH_3 upon hydrogenation, starts to become important at this time. Snow *et al*. (2007) showed that gas-phase NH_2OH can react with CH_5^+ to form NH_3OH^+ that can in turn react with different carboxylic acids to form protonated amino acids. These reactions are not included in the networks used. Our model (Congiu *et al*. 2012a), however, predicts that hydroxylamine has a relative abundance of at least $7 \cdot 10^{-9}$ n_H on the grain surface and $3 \cdot 10^{-11}$ n_H in the gas phase at the end of the lifetime of a dense cold cloud (1-10 Myr), before the core collapses.

To date, and to the best of our knowledge, interstellar hydroxylamine has not been observed in space, and only upper limits have been found for a number of sources (Pulliam *et al* 2012). These correspond to fractional abundances of $<10^{-11}$ in the gas phase. This is around the same order of magnitude as our gas-phase model predictions for dense clouds. We therefore expect that in the near future the faint radio signal from NH_2OH gas-phase molecules will be recorded by the receivers of ALMA that will investigate the inner parts of proto-planetary disks and hot-cores with relatively high temperatures (Herbst 2008). The hydroxylamine locked onto the grains at the beginning of the core collapse becomes accessible for further reaction at later stages when a protostar forms and UV irradiation and thermal processing start. The astrobiological implications of our study are constrained by the results of Blagojevic *et al*. (2003). They proposed a route for the synthesis of amino acids in interstellar environments starting from desorption of NH_2OH. In their study NH_2OH is formed through energetic processing at a late stage of star formation. Here we have shown how NH_2OH is already formed in the solid phase though a non-energetic route in the early stages of star formation. Figure 4.9 shows the link between the updated solid-phase NH_2OH formation scheme and the gas-phase formation routes of amino acids in space. Here the key stage of this suggested mechanism is that in which reactions between protonated hydroxylamine and carboxylic acids occur. Although these reaction pathways were already proved experimentally to be efficient at room temperature (Blagojevic *et al*. 2003), recent calculations show that they may involve activation barriers (Barrientos *et al*. 2012) and, therefore, that they may not be efficient under astronomically relevant conditions. Thus, there is now great demand for experimental verification of the latter results.

Finally, acetic acid, another main component of this reaction network, has already been detected towards several astronomical objects (mainly hot-cores), see Mehringer *et al*. (1997) and Remijan *et al*. (2003). Bennett & Kaiser (2007) showed successfully the laboratory synthesis of acetic acid by UV photolysis of $CO_2:CH_4$ ices under UHV conditions and cryogenic temperatures.
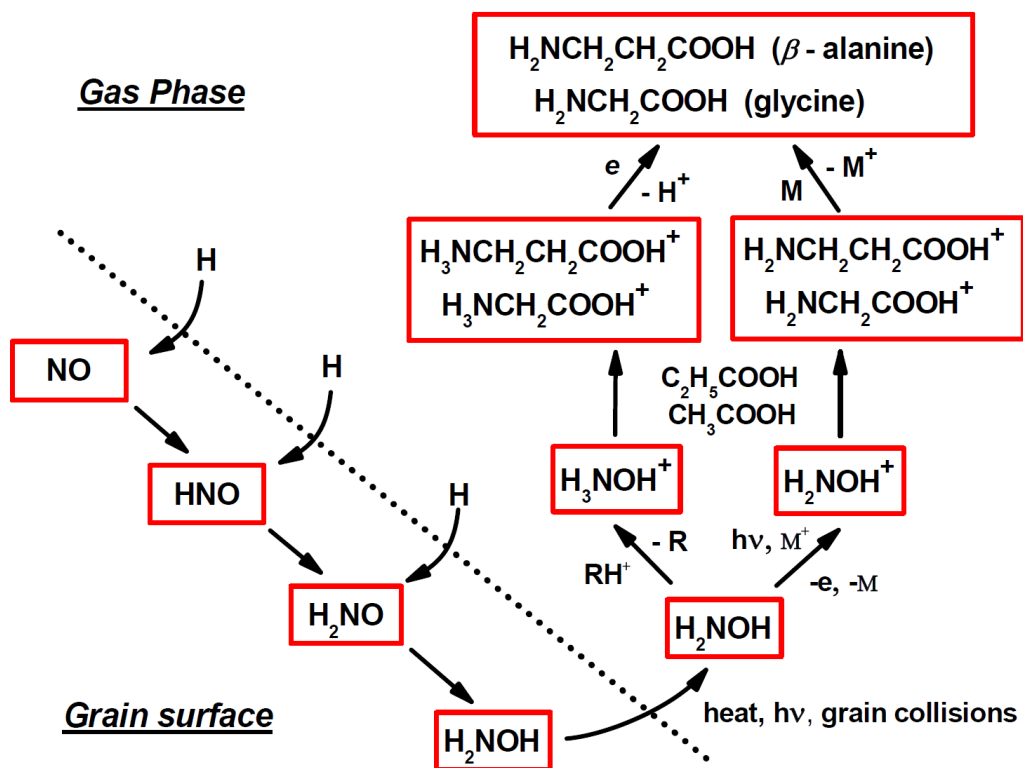
Figure 4.9. Proposed formation route of amino acids in star-forming regions based on the hydroxylamine surface formation route investigated in the present study combined with the experimental work of Blagojevic *et al.* (2003).

4.5 Conclusions

A systematic study of NO hydrogenation pathways under UHV conditions and for cryogenic temperatures is presented. In particular, the influence of sample temperature, NO deposition rate, H-atom flux and UV photolysis on the formation of different hydrogenation products is studied. Special attention is given to the hydrogenation of NO in CO- and H_2O-rich ices and the astronomical implications of our results are also discussed. The main conclusions of this work are listed below:

1. In CO- and H_2O-rich interstellar ice analogues NO is efficiently converted to hydroxylamine upon exposure to thermal H atoms.
2. The formation of hydroxylamine takes place through a fast and barrierless mechanism by subsequent addition of three H atoms to a single NO molecule.
3. HNO is an intermediate product of hydroxylamine formation and is observed in our experiments only under low H atom flux conditions.

4. The final HNO and NH_2OH formation yield is higher at 15 K than at 25 K.

5. In water-rich interstellar ice analogues the final NH_2OH formation yield is higher than in CO-rich ices.

6. In CO-rich ices hydroxylamine is formed well before CO molecules are hydrogenated to form formaldehyde and methanol.

7. N_2O is a side product of the NO hydrogenation reaction scheme.

8. Solid NH_2OH is not formed upon UV photolysis of $NO:CO:H_2O$ ices. The end products are N_2O, N_2O_3 (or NO_2), HNO, H_2O_2 and CO_2 ice.

9. According to our laboratory and modelling results we expect that NH_2OH is already present in the solid phase in dark molecular clouds and mainly in the gas phase in protostar regions. We therefore expect that in the near future gas-phase NH_2OH will be detected by ALMA.

10. Hydroxylamine formed efficiently in the solid phase provides a gas-phase reservoir upon desorption as a starting point in the formation of glycine and β-alanine.

References

Barrett C. S. & Meyer L., 1967, Phys. Rev., 160, 694

Barrientos C., Redondo P., Largo L., Rayon V. M., Largo A., 2012, ApJ, 748, 99

Bennett C. J. & Kaiser R. I., 2007, ApJ, 660, 1289

Bertie J. E. & Shehata M. R., 1985, JCP, 83, 1449

Blagojevic V., Petrie S., Bohme D. K., 2003, MNRAS, 339, L7

Bondybey V. E., English J. H., Weldon Mathews C., Contolini R. J., 1982, J. Molec. Spectrosc., 92, 431

Bonner F. T., Dzelzkalns L. S., Bonucci J. A., 1978, Inorg. Chem., 17. 2487

Bossa J. B., Isokoski K., de Valois M., Linnartz H., 2012, A&A, 545, A82

Butkovskaya N. I., Muravyov A. A., Setser D. W., 1997, Chem. Phys. Lett., 266, 223

Chakraborty D., Hsu C.-C., Lin M. C., 1998, JCP, 109, 8887

Charnley S. B., Rodgers S. D., Ehrenfreund P., 2001, A&A, 378, 1024

Cheskis S. G., Nadtochenko V. A., Sarkisov O. M., 1981, Int. J. Chem. Kin., 13, 1041

Congiu E., Chaabouni H., Laffon C., Parent P., Baouche S., Dulieu F., 2012b, JCP, 137, 054713

Congiu E., Fedoseev G., Ioppolo S., Dulieu F., Chaabouni H., Baouche S., Lemaire J. L., Laffon C., Parent P., Lamberts T., Cuppen H. M., Linnartz H., 2012a, ApJL, 750, L12

Cooper J. N., Chilton J. E., Powell R. E., 1970, Inorg. Chem., 9, 2303

Cromer D. T., Schiferl D., LeSar R., Mills R. L., 1983, Acta Cryst., C39, 1146

Cuppen H. M. & Herbst E., 2007, ApJ, 668, 294

Cuppen H. M., Ioppolo S., Romanzin C., Linnartz H., 2010, PCCP, 12, 12077

Diau E. W. G., Lin M. C., He Y., Melius C. F., 1995, Prog. Energy Combust. Sci., 21, 1

Dulmage W. J., Meyers E. A., Lipscomb W. N., 1953, Acta Cryst., 6, 760

Fateley W. G., Bent H. A., Crawford B., 1959, JCP, 31, 204

Fuchs G. W., Cuppen H. M., Ioppolo S., Romanzin C., Bisschop S. E., Andersson S., van Dishoeck E. F., Linnartz H., 2009, A&A, 505, 629

Garrod R. T., Wakelam V., Herbst E., 2007, A&A, 467, 1103

Garrod R. T., Widicus Weaver S. L., Herbst E., 2008, ApJ, 682, 283

Gerin M., Viala Y., Pauzat F., Ellinger Y., 1992, A&A, 266, 463

Hasegawa T. I., Herbst E., Leung C. M., 1992, ApJS, 82, 167

Hassel G. E., Herbst E., Garrod R. T., 2008, ApJ, 681, 1385

Hawkins M. & Downs A. J., 1984, J. Phys. Chem., 88, 1527

Herbst E. & Klemperer W., 1973, 185, 505

Herbst E. & van Dishoeck E. F., 2009, Annu. Rev. Astro. Astrophys., 47, 427-480

Herbst E., 2008, Astrophys. Space Sci., 313, 129

Holbrook K. A., Pilling M. J., Robertson S. H., 1996, Unimolecular reactions, Wiley, Second Edition, New York

Hudson R. L., Khanna R. K., Moore M. H., 2005, J. Suppl. Ser., 159, 277

Ioppolo S., Cuppen H. M., Romanzin C., van Dishoeck E. F., Linnartz H., 2008, ApJ, 686, 1474

Ioppolo S., Cuppen H. M., Romanzin C., van Dishoeck E. F., Linnartz H., 2010, PCCP, 12, 12065

Ioppolo S., van Boheemen Y., Cuppen H. M., van Dishoeck E. F., Linnartz H., 2011, MNRAS, 413, 2281

Jacox M. E. & Milligan D. E., 1973, J. Molec. Spectrosc., 48, 536

Jamieson C. S., Bennett C. J., Mebel A. M., Kaiser R. I., 2005, ApJ, 624, 436

Levchenko S. V., Reiser H., Krylov A. I., Gessner O., Stolow A., Shi H., East A. L. L., 2006, JCP, 125, 084301

Lin M. C., He Y., Melius C. F., 1992, Int. J. Chem. Kin., 24, 489

Liszt H. S. & Turner B. E., 1978, ApJ, 224, L73

Matar E., Congiu E., Dulieu F., Momeni A., Lemaire J. L., 2008, A&A, 492, L17

McGonagle D., Ziurys L. M., Irvine W. M., Minh Y. C., 1990, ApJ, 359, 121

McGraw G. E., Bernitt D. L., Hisatsune I. C., 1967, Spectrochim. Acta, 23A, 25

Mehringer D. M., Snyder L. E., Miao Y., Lovas F. J., 1997, ApJ, 480, L71

Miyauchi N., Hidaka H., Chigai T., Nagaoka A., Watanabe N., Kouchi A., 2008, Chem. Phys. Lett., 456, 27

Moore M. H. & Hudson R. L., 2003, Icarus, 161, 486

Muñoz Caro G. M., Meierhenrich U. J., Schutte W. A., Barbier B., Arcones Segovia A., Rosenbauer H., Thiemann W. H.-P., Brack A, Greenberg J. M., 2002, Nature, 416, 403

Nightingale R. E. & Wagner E. L., 1954, JCP, 22, 203

Noble J. A., Dulieu F., Congiu E., Fraser H. J., 2011, ApJ, 735, 121

Noir E. M., Chen L. H, Laane J., 1983, J. Phys. Chem., 87, 1113

Noir E. M., Chen L. H., Strube M. M., Laane J., 1984, J. Phys. Chem., 88, 756

Oba Y., Watanabe N., Hama T., Kuwahata K., Hidaka H., Kouchi A., 2012, ApJ, 749, 67

Oba Y., Watanabe N., Kouchi A., Hama T., Pirronello V., 2010, ApJ, 712, L174

Öberg K. I., Bottinelli S., Jørgensen J. K., van Dishoeck E. F., 2010, ApJ, 716, 825

Öberg K. I., Garrod R. T., van Dishoeck E. F., Linnartz H., 2009, A&A, 504, 891

Öberg K. I., Fuchs G. W., Awad Z., Fraser H. J., Schlemmer S., van Dishoeck E. F., Linnartz H., 2007, ApJ, 662, L23

Page M. & Soto M. R., 1993, JCP, 99, 7709

Pettersson M., Khriachtchev L., Jolkkonen S., Räsänen M., 1999, J. Phys. Chem. A., 103, 9154

Pulliam R. L., McGuire B. A., Remijan A. J., 2012, ApJ, 751, 1

Pwa T. H., Pottasch S. R., 1986, ApJ, 164, 116

Raut U. & Baragiola R. A., 2011, ApJL, 737, L14

Rawlins W. T., Person J. C., Fraser M. E., Miller S. M., Blumberg W. A. M., 1998, JCP, 109, 3409

Remijan A., Snyder L. E., Friedel D. N., Liu S.-Y., Shah R. Y., 2003, ApJ, 590, 314

Romanzin C., Ioppolo S., Cuppen H. M., van Dishoeck E. F., Linnartz H., 2011, JCP, 134, 084504

Sandford S. A. *et al.*, 2006, Science, 314, 1720

Seddon W. A., Fletcher J. W., Sopchyshyn F. C., 1973, Can. J. Chem., 51, 1123

Semenov D., Hersant F., Wakelam V., Dutrey A., Chapillon E., Guilloteau St., Henning T., Launhardt R., Pietu V., Schreyer K., 2010, A&A, 522, A42

Sluyts E. J. & Van der Veken B. J., 1994, J. Molec. Struct., 320, 249

Smyth C. P. & McAlpine K. B., 1933, JCP, 1, 60

Snow J. L., Orlova G., Blagojevic V., Bohme D. K., 2007, J. Am. Chem. Soc., 129, 9910

Tschersich K. G., 2000, J. Appl. Phys., 87, 2565

Wakelam V., Smith I. V. M., Herbst E., Troe J., Geppert W., Linnartz H., Öberg K., Roueff E., Agúndez M., Pernot P., Cuppen H. M., Loison J. C., Talbi D., 2010, Space Sci. Rev., 156, 13

Watanabe N. & Kouchi A., 2002, ApJ, 571, 173

Western C. M., Langridge-Smith P. R. R., Howard B. J., 1980-1989, OSU international symposium on molecular spectroscopy, 1980-TF-7

Withnall R. & Andrews L., 1988, J. Phys. Chem., 92, 2155

Yabushita A., Hama T., Iida D., Kawanaka N., Kawasaki M., Watanabe N., Ashfold M. N. R., Loock H.-P., 2008, JCP, 129, 044501

Yeo G. A. & Ford T. A., 1990, J. Molec. Struct., 217, 307

V

Solid State Chemistry of Nitrogen Oxides：
Completing the Full Network

Nitrogen oxides are considered to be important astrochemical precursors of complex species and prebiotics. However, apart from the hydrogenation of solid NO that leads to the surface formation of hydroxylamine, little is known about the full solid state reaction network involving both nitrogen and oxygen. Our study is divided into two papers, hereby called Part I and Part II. In the accompanying paper published back-to-back to this chapter, we investigate the surface reactions NO + $O/O_2/O_3$ and NO + N with a focus on the formation of NO_2 ice. Here, we complement this study by measurements of the surface destruction of solid NO_2, *e.g*., NO_2 + H/O/N. Experiments are performed in two separate ultra-high vacuum setups and therefore under different experimental conditions to better constrain the experimental results. Surface reaction products are monitored by means of Fourier Transform Reflection Absorption Infrared pectroscopy (FT-RAIRS) and Temperature Programmed Desorption (TPD) techniques using mass spectrometry. The surface destruction of solid NO2 leads to the formation of a series of nitrogen oxides such as NO, N_2O, N_2O_3, and N_2O_4 as well as HNO, NH_2OH, and H_2O. When NO_2 is mixed with an interstellar more relevant apolar (*i.e*., CO) ice, solid CO_2 and HCOOH are also formed due to interactions between different reaction routes. The astrophysical implications of the full nitrogen and oxygen reaction network derived from Parts I and II are discussed.

5.1 Introduction

Ice-covered dust grains play a key role in the chemistry of the interstellar medium. The cumulative outcome of recent observations, laboratory studies, and astrochemical models indicates that there is a strong interplay between the gas and the solid phase throughout the formation process of molecules in space (Herbst & van Dishoeck 2009, Garrod 2013). Surface reaction mechanisms on cold dust grains initiate molecular chemistry starting with the formation of H_2, and dominate the formation of complex organic molecules (COMs) in space. Indeed, interstellar grains provide surfaces on which gas-phase species can accrete, meet, and react, and to which they can donate the excess energy. Therefore, in dense cold clouds, icy dust grains act both as a molecular reservoir and as sites for catalysis.

Complex grain surface chemistry is also triggered by photon-induced cosmic ray irradiation and particle bombardment, *e.g.*, free atoms, electrons, and cosmic rays (Herbst & van Dishoeck 2009, van Dishoeck & Blake 1998). During later stages of star formation, condensed-phase molecules can be thermally processed to form more complex species (Theulé *et al*. 2013). Ultimately, ices may desorb from the dust grains and participate in second generation gas-phase reaction schemes (Charnley *et al*. 1992). Some of this material can re-condense in the inner part of the protoplanetary disk, according to their snow-lines, and then be eventually delivered to icy planetesimals and planets (Qi *et al*. 2013).

Nitrogen-containing molecules are essential for life on Earth. Therefore, understanding the nitrogen and oxygen chemistry in space is an important step to link the formation of interstellar COMs to the origin of life. However, to date, surface nitrogen chemistry is poorly understood. Laboratory studies showed that ion irradiation of interstellar relevant ices containing N_2 (*e.g.*, $H_2O:N_2$ + 60 keV of Ar^{2+}, $CO:N_2$ + 200 keV of H^+) leads to the formation of some nitrogen oxides, such as NO, N_2O, and NO_2. When carbon-bearing species are present in the ice and are irradiated in a mixture with N_2, also OCN^- is formed (Boduch *et al*. 2012, Sicilia *et al*. 2012). Laboratory studies of non-energetic surface processing showed that, for instance, ammonia (NH_3), hydroxylamine (NH_2OH), nitrogen dioxide (NO_2), dinitrogen trioxide (N_2O_3), nitrous acid (HNO_2), and nitric acid (HNO_3) are efficiently formed at low temperatures through hydrogenation of N-atoms, NO+H, $NO+O_2$, $NO+NO_2$, NO+OH, and NO_2+OH reactions, respectively (Hiraoka *et al*. 1995, Hidaka *et al*. 2011, Congiu *et al*. 2012a, Congiu *et al*. 2012b, Fedoseev *et al*. 2012, Minissale *et al*. 2013, Ioppolo *et al*. 2013, Joshi *et al*. 2012).

In the accompanying paper, hereafter referred to as Part I (Minissale *et al*. 2014), we investigate the oxygenation of solid NO ($NO+O/O_2/O_3$) at low temperature, on different substrates (silicate, graphite, compact amorphous solid water - ASW, and gold), and in different environments (pure NO, polar ice - $NO:H_2O$, and apolar ice - NO:CO). Solid NO_2

is shown to be efficiently formed in all cases indicating that the reaction NO+O is barrierless or has a small barrier. Despite these findings, interstellar NO_2 has not been observed yet. According to the UMIST database, NO_2 has an estimated abundance of $\sim 10^{-11}$ wrt molecular hydrogen in the early stage of an interstellar cloud, and $\sim 2 \cdot 10^{-10}$ later at steady state (McElroy *et al*. 2013). The non-detection of NO_2 can be explained by efficient photodissociation and/or a non-energetic surface consumption pathway. The latter is the topic of the present study that shows the laboratory destruction of NO_2 through surface reactions (NO_2+H/O/N).

It should be noted that *pure* NO and NO_2 ice are not expected to exist in space, however interstellar NO and NO_2 should be present in the solid phase mixed with more abundant species. The astrophysical relevance of the work presented here aims at characterizing selected surface reaction processes, such as NO+H/O/N and NO_2+H/O/N, that occur in interstellar ices and that can explain the formation of more complex species in space (*e.g.*, NH_2OH). In order to achieve this goal, a systematic study is presented that starts from the simplest case of pure ices and also includes interstellar more relevant environments. In Part I, we studied the formation of NO_2 in both polar and apolar ices. Figure 3 of Part I shows that all the infrared features from N-bearing species present in a water-rich ice are broadened, shifted, and overlap with the strong OH bending mode of water ice. Thus, the unambiguous identification of species consumed or formed in the ice upon atom exposure is not trivial in a polar environment. On the other hand, Figure 4 of Part I shows that a CO-rich ice is a better environment to study surface reactions of N-bearing species, because all the spectral features are sharp and do not overlap with the CO modes. Therefore, only the results for pure and interstellar relevant apolar ices are presented here.

5.2 Experimental

As for Part I, experiments are performed in two different setups: SURFRESIDE[2] at the Sackler Laboratory for Astrophysics, Leiden University, The Netherlands, and FORMOLISM at the University of Cergy-Pontoise, France. Here follows a brief description of the setups and the experimental methods, since both systems are discussed in detail elsewhere (Congiu *et al*. 2012b, Ioppolo *et al*. 2013). The use of two ultrahigh vacuum (UHV) systems allows for complementary studies of selected interstellar relevant surface reactions. Therefore, a combination of experiments performed in these setups gives information on surface reactions occurring under different surface coverage (sub-monolayer vs multilayer regime), different substrates (gold, silicates, graphite, and ASW ice), and different matrix environments (pure NO and NO_2, NO in polar ice, and NO and NO_2 in apolar ice).

5.2.1 SURFRESIDE^2 setup

SURFRESIDE^2 consists of three distinct UHV chambers. In the main chamber, ices are deposited with monolayer precision (where 1 ML is assumed to be 10^{15} molecules cm^{-2}) and processed at astronomically relevant temperatures (13–300 K) on a gold substrate. Reflection Absorption Infrared Spectroscopy (RAIRS) and Temperature Programmed Desorption (TPD) are used as analytical tools to characterize the ice composition. In the other chambers different atom sources are mounted for the controlled production of well characterized atom (molecular) beams. Two different atom sources are used, one Hydrogen Atom Beam Source (HABS, Dr. Eberl MBE-Komponenten GmbH, see Tschersich & von Bonin 1998, Tschersich 2000, Tschersich *et al*. 2008) based on thermal cracking, and a Microwave Atom Source (MWAS, Oxford Scientific Ltd, see Shmidt *et al*. 1996, Anton *et al*. 2000) that implements a microwave discharge (300 W at 2.50 GHz). The HABS is used to hydrogenate/deuterate the sample, while the MWAS can produce beams of different atoms and radicals (*e.g.*, H, D, O, OH, OD, and N).

The two custom-made atom line chambers present identical geometrical characteristics. Shutters separate the beam lines from the main chamber and allow for an independent operation of the individual atom beam lines. A quartz pipe is placed after each shutter and along the path of the dissociated beam. The nose-shaped form of the pipe is designed to efficiently quench the excited electronic and ro-vibrational states of species through collisions with the walls of the pipe before they reach the ice sample. The geometry is designed in such a way that this is realized through at least four wall collisions of the atoms before leaving the pipe. In this way, "hot" species cannot reach the ice directly. All atom fluxes are in the range between 10^{11} and 10^{13} atoms cm^{-2} s^{-1} and the calibration procedures are described in Ioppolo *et al*. 2013.

The system is designed to investigate selected surface reactions in the multilayer regime, on an optically flat gold substrate, in pure, polar, and apolar ices, and for different atom fluxes. As described in Part I, co-deposition and sequential deposition experiments can be performed with this system under fully controlled conditions. Since ices are studied in the multilayer regime, RAIR spectra are used to test the reaction routes *in situ*, while QMS data are used as a complementary technique to constrain the RAIR results.

5.2.2 FORMOLISM setup

FORMOLISM consists of an UHV main chamber and two triply differentially pumped atom lines. The main chamber contains a silicate (or graphite) substrate that can be cooled down to 6.5 K. As for SURFRESIDE^2, ices are studied *in situ* by a Fourier Transform

Infrared (FTIR) spectrometer in RAIR mode, and a quadrupole mass spectrometer (QMS). Diversly from SURFRESIDE[2] that mounts the QMS on the back-side of the rotatable gold substrate, the substrate in FORMOLISM can be linearly translated in front of the rotatable QMS. In several experiments, compact ASW is deposited at 110 K on the substrate prior to the deposition of any reactants to study the substrate effect on thin ices (*i.e.*, sub-monolayer regime). The two atom sources are both microwave driven dissociation sources (300 W at 2.50 GHz). The atom fluxes are characterized in Part I and elsewhere (Congiu *et al*. 2012b, Amiaud *et al*. 2006). FORMOLISM uses TPD and QMS data as main techniques to investigate surface reaction schemes. Due to the lower signal-to-noise ratio of the RAIR data acquired in the sub-monolayer regime, RAIR spectra are usually used to constrain the results from the more sensitive, however, non-*in situ* QMS technique.

SURFRESIDE[2] and FORMOLISM are two complementary and unique systems that combined investigate interstellar relevant surface reaction schemes under an extensive physical and chemical range of conditions. Table I lists the experiments performed by the two systems to study the destruction of NO_2 molecules for astronomically relevant temperatures. In the next section, we show the results of the experiments listed in Table 5.1. The possible destruction routes are presented in the discussion section. The paper completes with astrophysical implications and conclusions.

Table 5.1. List of experiments performed by SURFRESIDE^2 and FORMOLISM.

Experiment	Method	Ratio	R_{dep} (L/min)	T_{dep} (K)	$T_{atom-add}$ (K)	P_{AL} (10^{-6} mbar)	T_{AL} (K)	MWP (W)	Atom-fluence (10^{16} atoms/cm^2)	t (min)	RAIRS	TPD
SURFRESIDE^2			NO_2						(H from H_2)			(10 K/min)
30 ML NO_2:H^a	seq-dep	–	1.2	80	15	1	2150	–	0.6	60	Y	–
30 ML NO_2:H^a	seq-dep	–	1.2	80	15	10	2150	–	1.5	25	Y	QMS
NO_2:H	co-dep	1:0.5	1.2	80	80	10	2150	–	1.5	25	Y	–
NO_2:H	co-dep	1:0.5	1.2	50	50	10	2150	–	1.5	25	Y	–
NO_2:H	co-dep	1:0.5	1.2	35	35	10	2150	–	1.5	25	Y	–
NO_2:H	co-dep	1:0.5	1.2	15	15	10	2150	–	1.5	25	Y	–
NO_2:H	co-dep	1:0.1	1.2	15	15	1	2150	–	0.3	30	Y	–
NO_2:H	co-dep	1:10	0.05	15	15	10	2150	–	3.0	50	Y	QMS
30 ML NO_2	dep	–	1.2	15	–	–	–	–	–	–	Y	QMS
30 ML NO_2	dep	–	1.2	15	–	–	–	–	–	–	Y	IR
			NO_2, ^{13}CO						(H from H_2)			(1 K/min)
NO_2:^{13}CO:H	co-dep	1:25:2	0.05, 1.25	15	15	1	2150	–	0.2	27	Y	–
NO_2:^{13}CO:H	co-dep	1:50:10	0.05, 2.5	15	15	10	2150	–	3.0	50	Y	–
NO_2:^{13}CO	co-dep	1:50	0.05, 2.5	15	–	–	–	–	–	–	Y	IR+QMS
^{13}CO:H	co-dep	1:1.5	–, 0.50	15	15	10	2150	–	3.0	50	Y	–
			NO_2, ^{13}CO						(O from N_2O)			
NO_2:^{13}CO:O:N_2O	co-dep	1:50:0.1:1	0.05, 2.5	15	15	2	–	275	0.02	29	Y	–
NO_2:^{13}CO	co-dep	1:50	0.05, 2.5	15	–	–	–	–	–	–	Y	–
^{13}CO:O:N_2O	co-dep	50:0.1:1	–, 2.5	15	15	2	–	275	0.02	29	Y	–
			NO_2						(N from N_2)			
NO_2:N:N_2	co-dep	1:0.1:10	0.05	15	15	8	–	300	0.01	25	Y	–
NO_2:N_2	co-dep	1:10	0.05	15	15	8	–	0	–	25	Y	–
N:N_2	dep	0.1:10	–	–	15	8	–	300	0.01	25	Y	–
			NO_2, ^{13}CO						(N from N_2)			
NO_2:^{13}CO:N:N_2	co-dep	1:50:0.1:10	0.05, 2.5	15	15	8	–	300	0.02	50	Y	–
NO_2:^{13}CO:N_2	co-dep	1:50:10	0.05, 2.5	15	15	8	–	0	–	57	Y	–
^{13}CO:N:N_2	co-dep	50:0.1:10	–, 2.5	15	15	8	–	300	0.02	50	Y	–

Table 5.1. (continued)

Experiment	Method	Thickness (ML)	R_{dep} (L/min)	T_{dep} (K)	$T_{atom\text{-}add}$ (K)	P_{AL} (10^{-10} mbar)	MWP (W)	Atom-fluence (10^{16} atoms/cm^2)	t (min)	RAIRS	TPD
FORMOLISM				NO_2				(H from H_2)			
$NO_2 + H + H_2$	seq-dep	1.5	0.12	15	15	2.8	85	0.6	32	N	QMS
$NO_2 + H + H_2$	seq-dep	2	0.12	15	15	2.8	105	1	50	Y	QMS
$NO_2 + H + H_2$	seq-dep	0.5	0.12	15	15	2.8	105	0.15	8	N	QMS
$NO_2 + H + H_2$	co-dep	2	0.12	15	15	2.8	105	0.55	30	N	QMS
$H + NO_2$	seq-dep	1	0.12	10	10	2.8	105	0.2	10	N	QMS
$NO_2 + H_2$	seq-dep	1	0.12	10	10	2.8	105	–	–	N	QMS
			H_2O, NO_2								
$H_2O + NO_2 + H$	seq-dep	50:1	2.4, 0.08	15	15	2.8	100	0.9	40	Y	QMS
			NO_2					(O from O_2)			
$NO_2 + O + O_2$	seq-dep	2	0.12	60	60	1.9	90	0.7	25	Y	QMS
$NO_2 + O + O_2$	co-dep	1	0.12	15	15	1.9	90	0.28	10	N	QMS
$NO_2 + O_2$	co-dep	1	0.12	10	10	1.9	90	–	–	N	QMS
$O_3 + NO_2$	seq-dep	1	0.12	10	10	1.9	90	–	–	N	QMS
			H_2O, NO_2								
$H_2O + NO_2 + O$	seq-dep	50:1	2.4, 0.08	15	15	1.9	90	0.7	25	N	QMS
			NO_2					(N from N_2)			
$NO_2 + N + N_2$	seq-dep	3.2	0.12	60	60	2	110	1	72	Y	QMS
$NO_2 + N + N_2$	seq-dep	1	0.12	15	15	2	110	0.75	55	N	QMS
$NO_2 + N + N_2$	co-dep	0.5	0.12	60	60	2	110	0.15	10	N	QMS
$NO_2 + N_2$	co-dep	1	0.12	10	10	2	110	–	–	N	QMS
$N + N_2 + NO_2$	seq-dep	1	0.12	10	10	2	110	0.15	10	N	QMS
			H_2O, NO_2								
$H_2O + NO_2 + N + N_2$	seq-dep	50:0.5	2.4, 0.08	15	15	2	110	0.15	10	N	QMS

Sequential deposition (seq-dep), co-deposition (co-dep), and deposition of single species (dep) are performed under different laboratory conditions. The thickness is expressed in monolayers (ML); R_{dep} is the deposition rate of a selected molecule expressed in Langmuir (L) min^{-1}, where $1\,L = 1.3 \cdot 10^{-6}$ mbar s^{-1}; T_{dep} is the substrate temperature during deposition; $T_{atom\text{-}add}$ is the substrate temperature during atom addition; P_{AL} is the atomic line pressure during atom exposure; T_{AL} is the tungsten filament temperature of the HABS; MWP is the microwave power used in the experiments; atom-fluence is the total fluence at the end of the experiment; t is the total time of atom addition; RAIRS is the acquisition of RAIR spectra during seq-dep, co-dep, or dep of selected species; TPD is the temperature programmed desorption experiment performed afterward.

[a]These two experiments are from the hydrogenation of the same ice, *i.e.*, first with low and then with high H-atom flux.

5.3 Results

5.3.1 $NO_2 + H$

Figure 5.1 shows the TPD curves of NO_2 (mass 46, left panel), H_2O (mass 18, central panel), and NH_2OH (mass 33, right panel) for two different sequential deposition experiments: 2.5 ML of NO_2 (black line) and 2.5 ML of NO_2 + 10 ML of H atoms (red line). A graphite plate held at 10 K is used as a substrate. To have similar background water contributions to the total water observed in both experiments (central panel), TPD experiments were started in both cases 50 minutes after the ice was deposited. Therefore, for the first experiment (2.5 ML of NO_2) the ice was left at 10 K for 50 minutes before the TPD started, while for the second experiment (2.5 ML of NO_2 + 10 ML of H) the ice was exposed to 50 minutes of H atoms with a H-flux of $3.3 \cdot 10^{12}$ atoms cm^{-1} s^{-1} and the TPD was started afterward.

Figure 5.1 shows the destruction of NO_2 upon hydrogenation of the ice, and the formation of new molecules. In particular, the NO_2 desorption peak is attenuated and shifted toward higher temperatures in the hydrogenation experiment (red curve) compared to the deposition of pure NO_2 (black curve), indicating that new species are formed in the ice. In our experiments, the desorption temperatures of NO_2, H_2O, and NH_2OH are between 110 and 140 K, 140 and 170 K, and 225 and 265 K, respectively. Congiu *et al.* (2012b) showed that NH_2OH desorbs between 180 and 200 K under UHV conditions. The higher desorption temperature of NH_2OH reported here indicates that either mass 33 is due to NH_2OH trapped by a less volatile unidentified species formed in the ice, or mass 33 is actually caused by an unidentified species that desorb at higher temperatures than NH_2OH but fractionates via a NH_2OH channel in the QMS.

A comparison between infrared spectra for pure NO_2, H_2O, and NH_2OH depositions, and co-deposition of $NO_2 + H$ with a ratio ~1:10 confirms the TPD results shown in Fig. 5.1 (see Figure 5.2). In particular, spectrum (a) shows the dimerization of solid NO_2, while spectrum (b) presents all the absorption peaks due to H_2O and NH_2OH as confirmed in spectra (c) and (d). Table 5.2 lists all the absorption features visible in Figure 5.2. The results shown in Figures 5.1 and 5.2 are obtained under different experimental conditions: Fig. 5.1 - silicon substrate and sequential deposition; Fig. 5.2 - gold substrate and co-deposition. The ice thickness is similar for both experiments (~ 3 ML), while the analysis techniques are different: TPD with QMS (Fig. 5.1) and insitu FT-RAIR measurements (Fig. 5.2). Since both experiments use a high H-atom coverage, the final result in both experiments is the formation of saturated species, such as water and hydroxylamine. This indicates that independent of these experimental settings, the reaction $NO_2 + H \rightarrow NO + OH$ is efficient in the solid phase.
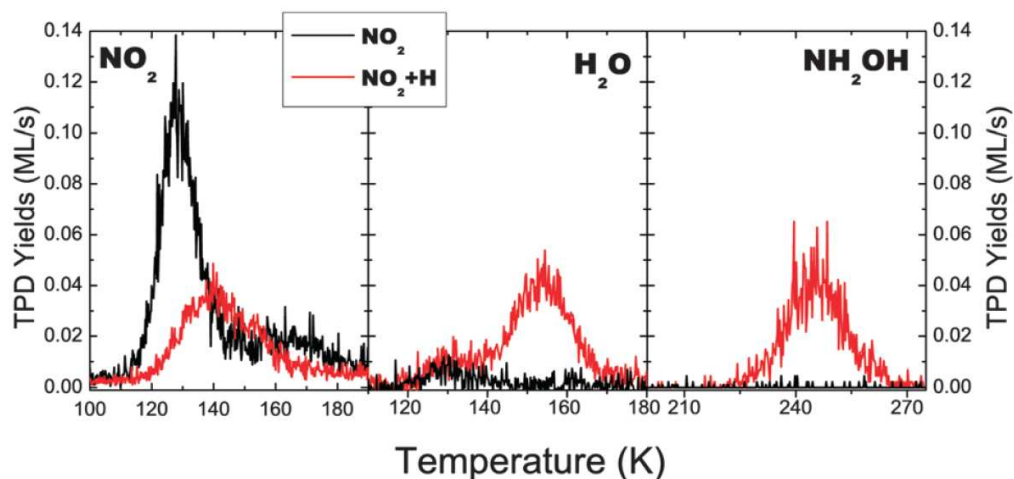
Figure 5.1. TPD curves of NO_2 (m/z=46, left panel), H_2O (m/z=18, central panel), and NH_2OH (m/z=33, right panel) for two different co-deposition experiments at 10 K: 2.5 ML of NO_2 (black line) and 2.5 ML of NO_2 + 10 ML of H atoms (red line).
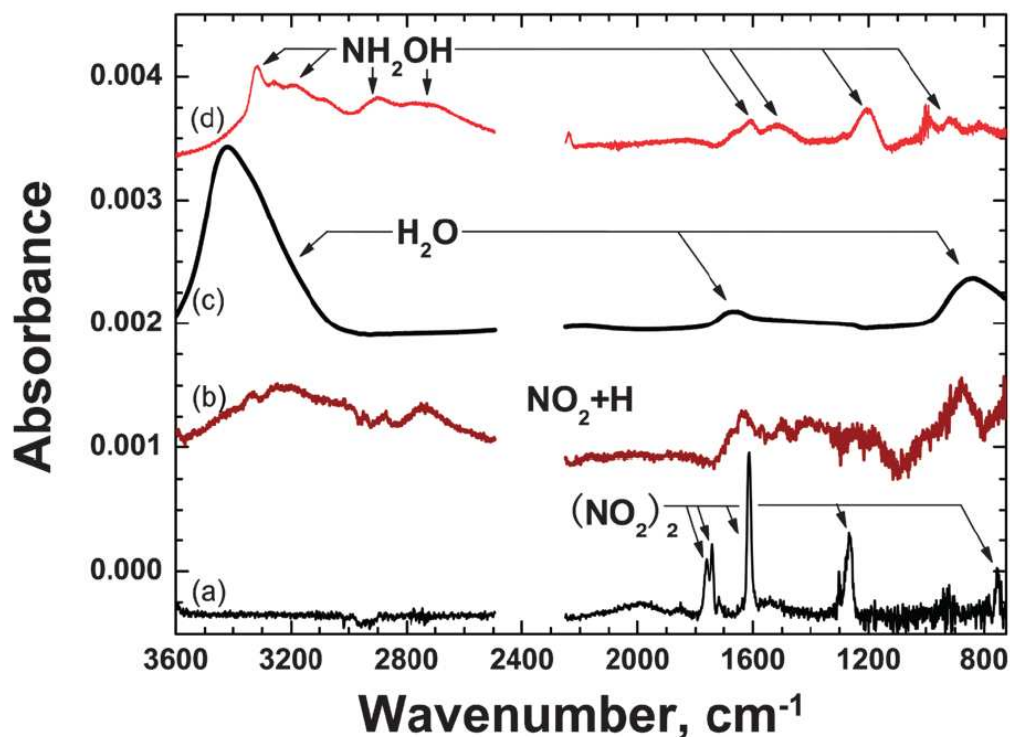
Figure 5.2. Four RAIR spectra at 15 K of: (a) 3 ML of NO_2; (b) NO_2 co-deposited with H atoms with a ratio of ~1:10 and a H-atom flux of $1 \cdot 10^{13}$ atoms cm^{-2} s^{-1}; (c) a spectrum of pure H_2O ice; and (d) pure NH_2OH ice obtained by co-depositing NO molecules and H atoms with a ratio of 1:10 (see Congiu *et al.* 2012b, Fedoseev *et al.* 2012).

Table 5.2. Assigned infrared features with their corresponding references.

| Frequency/cm^{-1}	Species	Mode	Reference
751	N_2O_4/NO_2	ν_{12}/ν_2	Fateley *et al.* (1959)
781	N_2O_3	ν_4	Fateley *et al.* (1959)
870	NH_2OH	ν_6	Withnall & Andrews (1988), Yeo & Ford (1990)
1041	O_3	ν_3	Brosset *et al.* (1993), Chaabouni *et al.* (2000), Bennet & Kaiser (2005)
1117	$H^{13}COOH$	ν_6	Milligan & Jacox (1971)
1143	NH_2OH	ν_5	Withnall & Andrews (1988), Yeo & Ford (1990)
1167	N_2O	$2\nu_2$	Dows (1957), Łapiński *et al.* (2001)
1260	N_2O_4	ν_{11}	Holland & Maier II (1983), Fateley *et al.* (1959)
1290	N_2O	ν_1	Jamieson *et al.* (2005), Dows (1957), Łapiński *et al.* (2001)
1303	N_2O_3/NO_2	ν_3/ν_1	Fateley *et al.* (1959) / Nour *et al.* (1983)
1494	$H_2^{13}CO$	ν_3	Milligan & Jacox (1971) / Wohar & Jagodzinski (1991)
1571	HNO	ν_3	Jacox & Milligan (1973)
1602	NH_2OH	ν_3	Withnall & Andrews (1988), Yeo & Ford (1990)
1615	NO_2/N_2O_3	ν_3/ν_2	Fateley *et al.* (1959), Jamieson *et al.* (2005) / Fateley *et al.* (1959), Nour *et al.* (1983)
1693	$H_2^{13}CO$	ν_2	Milligan & Jacox (1971) / Wohar & Jagodzinski (1991)
1712	$H^{13}COOH$	ν_3	Milligan & Jacox (1971)
1737	$t\text{-}(NO)_2/N_2O_4$	ν_1/ν_9	Fateley *et al.* (1959) / Holland & Maier II (1983)
1754	$c\text{-}HO^{13}CO$	ν_2	Milligan & Jacox (1971)
1766	$c\text{-}(NO)_2/N_2O_4$	ν_5/ν_9	Fateley *et al.* (1959), Nour *et al.* (1984) / Holland & Maier II (1983)
1786	$t\text{-}HO^{13}CO$	ν_2	Milligan & Jacox (1971)
1833-1848[a]	N_2O_3	ν_1	Fateley *et al.* (1959)
1850	N_2O_3	ν_1	Fateley *et al.* (1959) / Nour *et al.* (1983)
1875	NO (monomer)	ν_1	Fateley *et al.* (1959), Nour *et al.* (1984), Holland & Maier II (1983)
2039	$^{13}C^{18}O$	ν_1	Loeffler *et al.* (2005)
2066	$^{13}C^{17}O$	ν_1	Loeffler *et al.* (2005)
2096	^{13}CO	ν_1	Ewing & Pimentel (1961)
2139	CO	ν_1	Sandford *et al.* (1988a)
2235	N_2O	ν_3	Jamieson *et al.* (2005), Dows (1957), Łapiński *et al.* (2001)
2280	$^{13}CO_2$	ν_3	Berney & Eggers (1964)

[a]N_2O_3 peak position shifts in different environments (see Figs. 5.5 and 5.7).

5.3.1.1 $NO_2 + H$ in an apolar ice

The $NO_2 + H$ reaction is studied in an apolar ice by co-depositing NO_2, [13]CO, and H atoms onto a gold substrate at 15 K. The choice of an astrochemically relevant CO ice matrix allows for the study of different reactants formed through hydrogenation of the ice and, therefore, a better understanding of the full reaction scheme. Figure 5.3 shows the co-deposition spectrum of [13]CO + H = 1:1.5 at 13.5 K (a) compared to the co-deposition of NO_2 + [13]CO = 1:50 (b) and the co-deposition of NO_2 + [13]CO + H = 1:50:10 (c), both at 15 K. All these experiments have the same H-atom fluence ($1.5 \cdot 10^{16}$ atoms cm^{-2}) as well as the same NO_2 and [13]CO deposition rates (0.05 and 2.5 L min^{-1}) when deposited together. Therefore, a comparison of these spectra gives a qualitative picture of the destruction of solid NO_2 and allows for the identification of new species formed through the hydrogenation of the ice. In particular, spectrum (a) confirms the formation of formaldehyde after hydrogenation of [13]CO ice (Hiraoka *et al*. 1994, Watanabe & Kouchi 2002, Fuchs *et al*. 2009); spectrum (b) clearly shows all the carbon monoxide isotopologues, as well as the NO_2 monomer, N_2O_3 and N_2O_4. The strong NO_2 feature seen in spectrum (b) at 1612 cm^{-1} almost disappears in spectrum (c) where new features due to [13]CO_2, HO[13]CO, H[13]COOH, HNO, and NH_2OH show up. The presence of HNO in the ice can be explained by the nature of the co-deposition experiments, where the continuous deposition of new molecules on the cold ice surface causes some of the formed HNO to get trapped in the ice matrix, where it is not further converted into NH_2OH as shown in Congiu *et al*. (2012a), Congiu *et al*. (2012b), Fedoseev *et al*. (2012). The formation of species not previously detected during the hydrogenation of pure NO_2 or pure CO indicates that the interaction of the two reaction pathways leads toward a higher degree of chemical complexity in the ice. The full reaction scheme leading to the formation of the aforementioned species is presented in the discussion section, while a list of spectral features and their assignments is shown in Table 5.2.

Although NO_2 is mixed in a [13]CO matrix (NO_2 << [13]CO), the only hydrogenation products observed in spectrum (c) of Fig. 5.3 are due to the hydrogenation of NO_2: *i.e*., the hydrogenation products of solid [13]CO (H_2[13]CO and [13]CH_3OH) are under the detection limit. HO[13]CO, [13]CO_2, and H[13]COOH are all products of the reaction OH + [13]CO as is discussed in Section 5.4. Thus, the reaction $NO_2 + H$ is more efficient than reaction [13]CO + H for the experimental settings studied here, and proceeds most likely barrierless or with a small barrier in the solid phase.
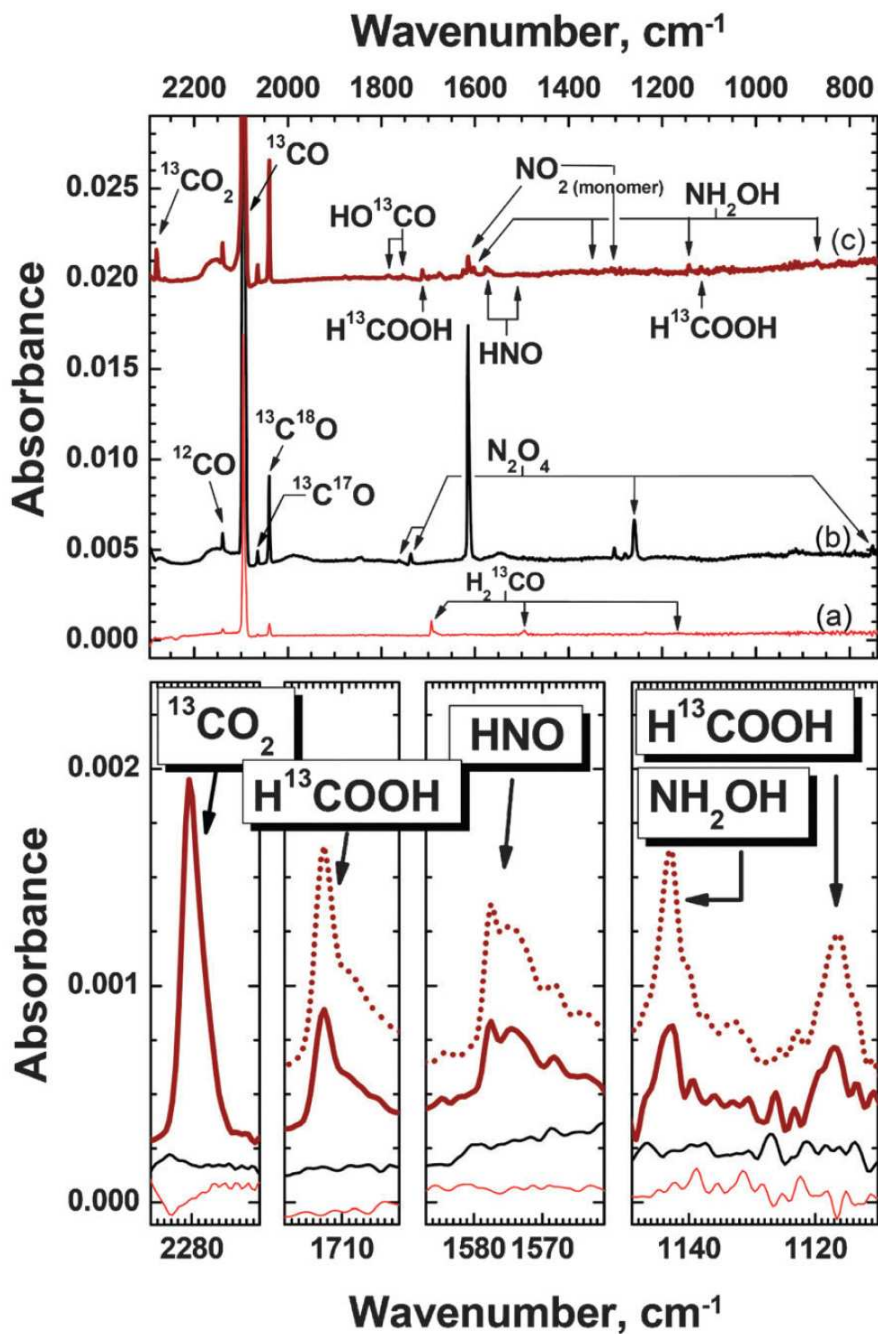
Figure 5.3. Top panel: three RAIR co-deposition spectra at 15 K of: (a) ^{13}CO molecules and hydrogen atoms (HABS) with a ratio of 1:1.5 and a H-atom fluence of $1.5 \cdot 10^{16}$ atoms cm^{-2}; (b) NO_2 and ^{13}CO with a ratio of 1:50; (c) NO_2, ^{13}CO, and H atoms with a ratio of 1:50:10 and the same H-atom fluence as for spectrum (a). The insets show absorption features of solid $^{13}CO_2$, $H^{13}COOH$, HNO, and NH_2OH. The dotted spectrum shown in the insets is from the same experiment shown in spectrum (c) at higher H-atom fluence - *i.e.*, twice the co-deposition time shown in spectrum (c).
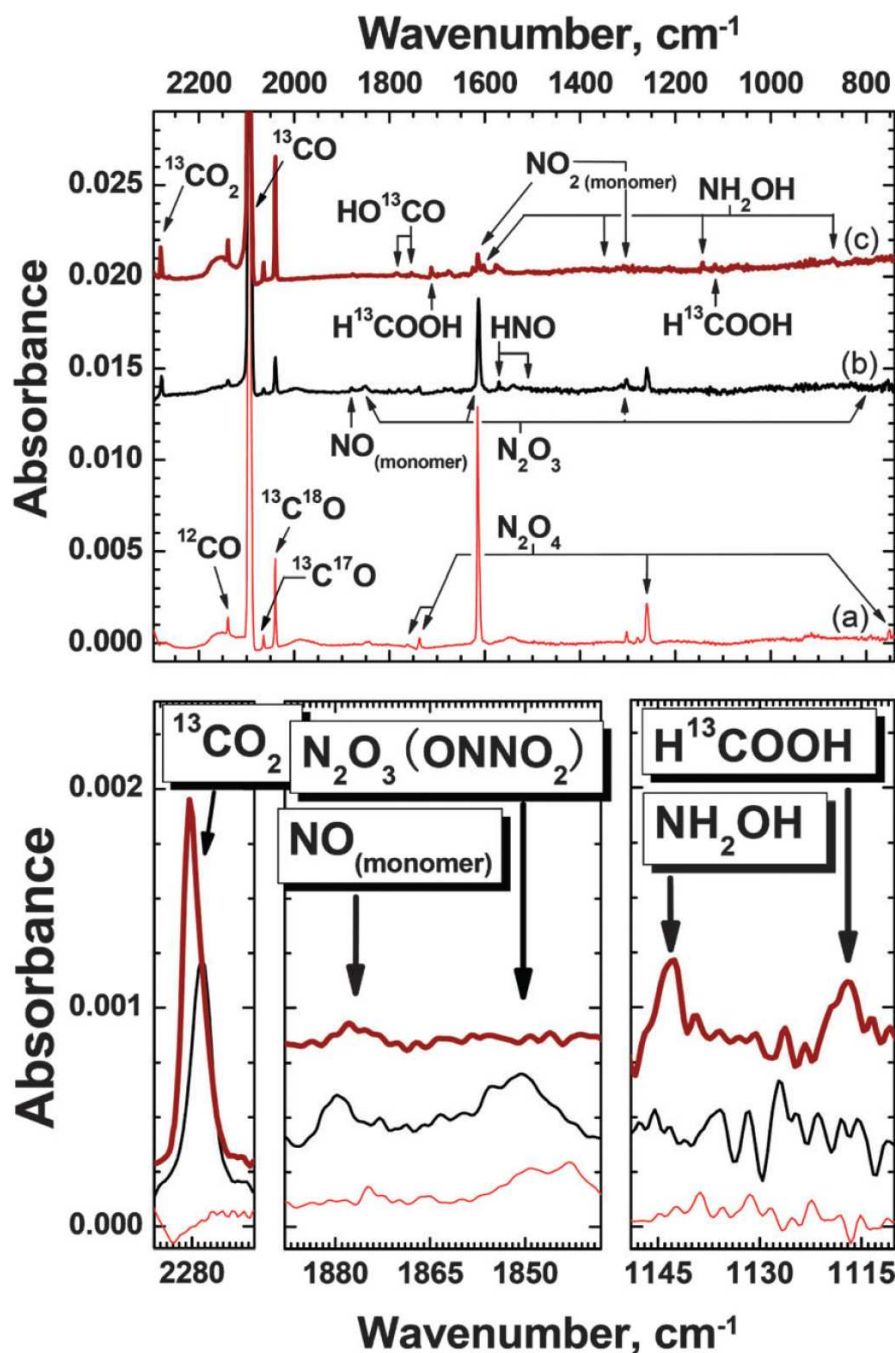
Figure 5.4. Top panel: three RAIR co-deposition spectra at 15 K of: (a) NO_2 and ^{13}CO molecules with a ratio of 1:50; (b) NO_2, ^{13}CO, and hydrogen atoms (HABS) with a ratio of 1:25:2 and an H-atom fluence of $0.2 \cdot 10^{16}$ atoms cm^{-2} (low H-atom flux); (c) NO_2, ^{13}CO, and hydrogen atoms (HABS) with a ratio of 1:50:10 and an H-atom fluence of $1.5 \cdot 10^{16}$ atoms cm^{-2} (high H-atom flux). The insets show absorption features of solid $^{13}CO_2$, N_2O_3 ($ONNO_2$), NO monomer, $H^{13}COOH$, and NH_2OH.

5.3.1.2 H-atom flux dependence

Figure 5.4 shows NO_2:^{13}CO hydrogenation experiments for different H-atom fluxes: spectrum (a) is a co-deposition of NO_2:^{13}CO = 1:50 at 15 K used for comparison with spectrum (b), that is the low H-atom flux co-deposition experiment (NO_2:^{13}CO:H = 1:25:2), and with spectrum (c), that is the high H-atom flux co-deposition experiment (NO_2:^{13}CO:H=1:50:10). NO_2 monomer, N_2O_4, and all the isotopologues of ^{13}CO are present in spectrum (a). Spectrum (b) shows that NO_2 monomer is consumed by the low H-atom flux to form NO monomer, HNO, and $^{13}CO_2$. At high H-atom fluences and for a high H-atom flux, the NO_2 concentration is further reduced, most of the formed NO is converted into NH_2OH, also the $HO^{13}CO$ complex is above the detection limit as well as $H^{13}COOH$, and the $^{13}CO_2$ signal is further increased. The use of different H-atom fluxes in co-deposition experiments allows for the identification of the single steps of the reaction routes involved in the experiments as extensively discussed in Cuppen *et al.* (2011), and thus helps understanding the formation pathway of second generation molecules such as NH_2OH.

5.3.2 NO_2 + O

As for the hydrogenation of NO_2, NO_2 + O is studied in an apolar astrochemically relevant CO ice at 15 K. Figure 5.5 shows the co-deposition spectrum of ^{13}CO+O = 50:0.1 with the O-atom beam arising from N_2O plasma dissociation (O:N_2O=0.1:1) (a), compared to the co-deposition of NO_2 + ^{13}CO = 1:50 (b), and the co-deposition of NO_2 + ^{13}CO + O = 1:50:0.1 (c). All these experiments have the same O-atom fluence ($1.5 \cdot 10^{14}$ atoms cm^{-2}) as well as the same NO_2 and ^{13}CO deposition rates (0.05 and 2.5 L min^{-1}). Since O atoms are produced in a N_2O plasma in the MWAS, spectrum (a) of Fig. 5.5 shows features due to N_2O, in addition to all the isotopologues of ^{13}CO, and the newly formed O_3 and $^{13}CO_2$. Spectrum (b) of Fig. 5.5 is very similar to spectrum (b) in Fig. 5.5 showing features from the ^{13}CO isotopologues, NO_2 monomer, N_2O_3, and N_2O_4. A comparison between spectrum (b) and (c) reveals that NO_2 is destroyed during O-atom bombardment, while NO monomer and N_2O_3 are formed in this process (see Table 5.2).

A comparison between spectra (a) and (c) of Fig. 5.5 shows that less O_3 (and $^{13}CO_2$) is formed when NO_2 is present in the ice. Since the formation of ozone through the oxygenation of molecular oxygen is efficient, reaction NO_2 + O has to be also fast (barrierless or with a small barrier) in the solid phase (Mokrane *et al.* 2009, Romanzin *et al.* 2011).

Figure 5.5. Top panel: three RAIR co-deposition spectra at 15 K of: (a) ^{13}CO molecules and oxygen atoms (MWAS) with a ratio of 50:01 and an O-atom fluence of $1.5 \cdot 10^{14}$ atoms cm^{-2}; (b) NO_2 and ^{13}CO with a ratio of 1:50; (c) NO_2, ^{13}CO, and O atoms with a ratio of 1:50:0.1 and the same O-atom fluence as for spectrum (a). The insets show absorption features of solid $^{13}CO_2$, N_2O_3 ($ONNO_2$), NO monomer, and O_3.

5.3.3 $NO_2 + N$

Figure 5.6 shows the TPD curves of N_2O (mass 44, left panel), and NO_2 (mass 46, right panel) for three different sequential deposition experiments: 10 ML of N atoms (green line), 1 ML of NO_2 (black line), and 1 ML of NO_2 + 10 ML of N atoms (red line). A graphite substrate held at 60 K is used as a substrate. Figure 5.6 shows the destruction of NO_2 and the formation of N_2O upon N-atom exposure of the ice. The NO_2 desorption peak is slightly attenuated while the N_2O peak shows up between 70 and 80 K when N_2O is exposed to N atoms, confirming that new species are formed in the ice upon N-atom exposure.

Here, $NO_2 + N$ is also studied in an apolar astrochemically relevant CO ice at 15 K. Figure 5.7 shows the spectrum of a $^{13}CO + N = 50:0.1$ with the N-atom beam generated from N_2 plasma dissociation ($N:N_2 = 0.1:25$) (a) compared to the co-deposition of $NO_2 + {}^{13}CO + N_2 = 1:50:10$ (b), and the co-deposition of $NO_2 + {}^{13}CO + N = 1:50:0.1$ (c). All these experiments have the same N-atom fluence ($1.2 \cdot 10^{14}$ atoms cm^{-2}) as well as the same NO_2 and ^{13}CO deposition rates (0.05 and 2.5 L min^{-1}). Spectrum (b) of Fig. 5.7 is very similar to the spectra (b) from Figs. 5.3 and 5.5 showing features from the ^{13}CO isotopologues, NO_2 monomer, N_2O_3, and N_2O_4. A comparison between spectrum (b) and (c) reveals that NO_2 is destroyed during N-atom bombardment, while N_2O, the NO monomer, and N_2O_3 are formed (see Table 5.2).

In the next section, a comparison between the efficiency of $NO_2 + N$ and $NO_2 + O$ is discussed. Since the H-atom flux is order of magnitudes higher than the O- and N-atom fluxes (as in space), such a comparison cannot be easily made for the hydrogenation experiments.
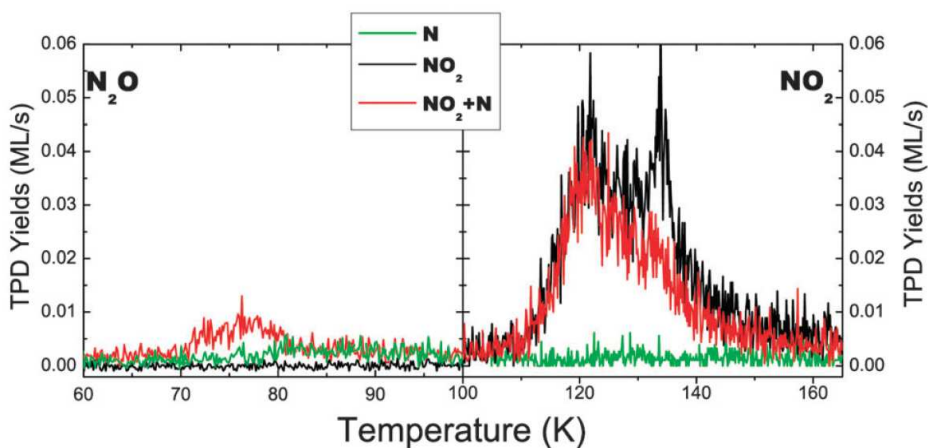
Figure 5.6. TPD curves of N_2O (left panel) and NO_2 (right panel) for three different experiments at 60 K: 10 ML of N atoms (green line), 1 ML of NO_2 (black line), and 1 ML of NO_2 + 10 ML of N atoms (red line).
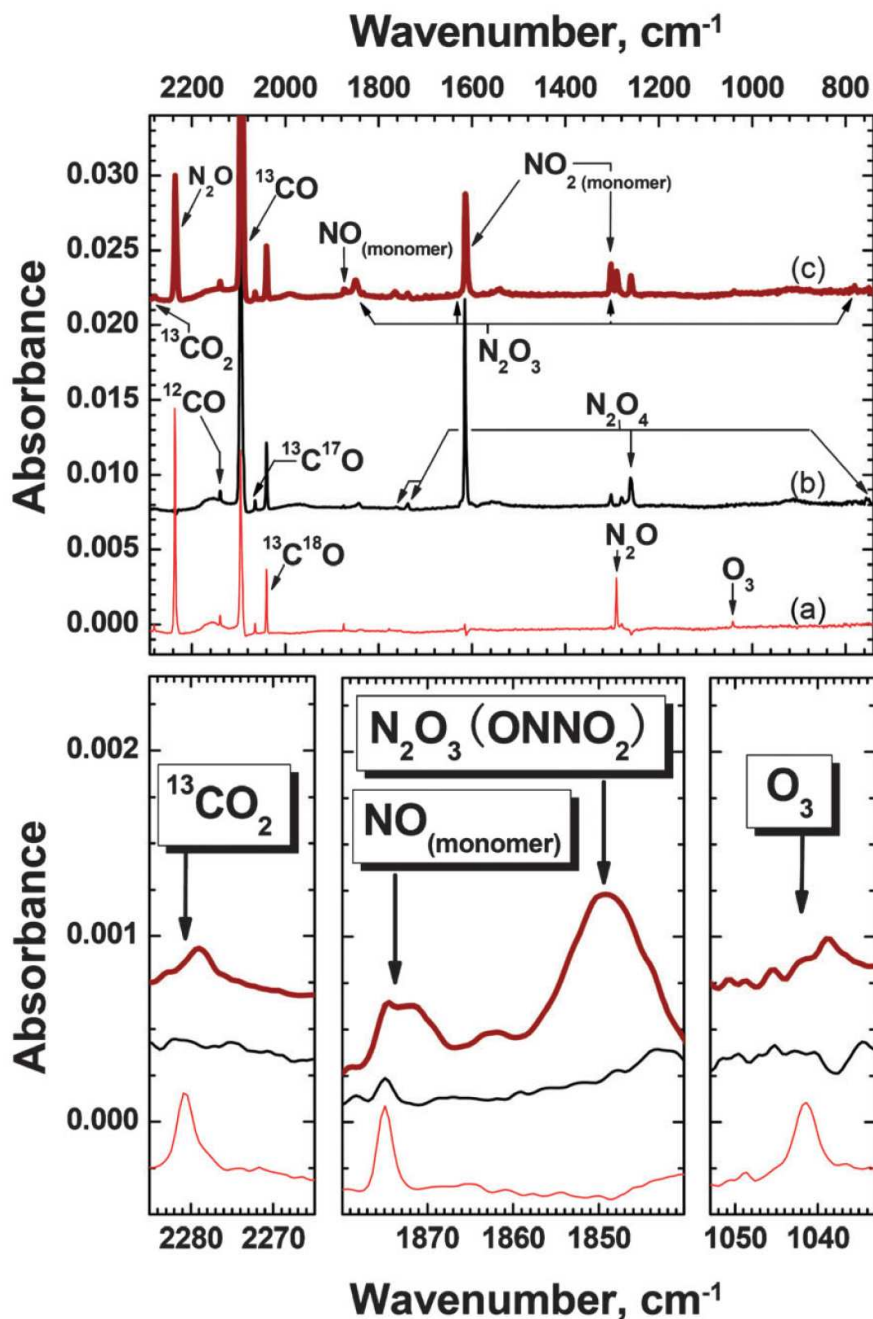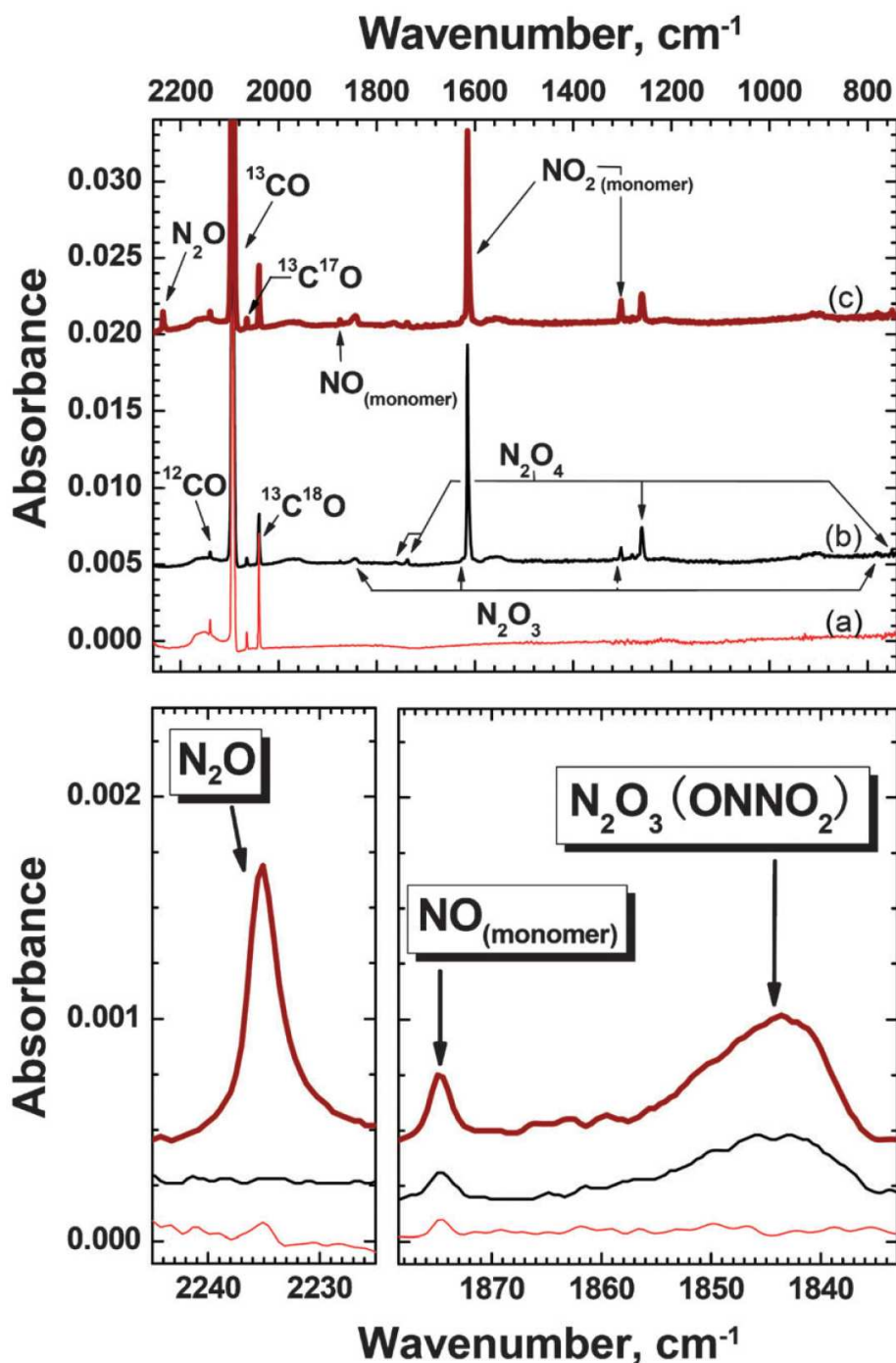
Figure 5.7. Top panel: three RAIR co-deposition spectra at 15 K of: (a) ^{13}CO molecules and nitrogen atoms (MWAS) with a ratio of 50:0.1 and an N-atom fluence of $1 \cdot 10^{14}$ atoms cm^{-2}; (b) NO_2 and ^{13}CO with a ratio of 1:50; (c) NO_2, ^{13}CO, and N atoms with a ratio of 1:50:0.1 and the same N-atom fluence as for spectrum (a). The insets show absorption features of solid N_2O, N_2O_3 (ONNO$_2$), and NO monomer.

5.4. Discussion

In Part I, we discussed the surface destruction of NO by means of surface reactions with hydrogen atoms, oxygen allotropes (O/O_2/O_3), and nitrogen atoms. The formation pathway to solid NO_2 through the oxygenation of NO was thoroughly discussed and several reaction routes were presented (see Fig. 9 in Part I). As previously mentioned, the focus of Part II is the investigation of surface reactions involving solid NO_2 at low temperatures. Here, all the experiments presented in Section 5.3 show the destruction of NO_2 and the formation of new species such as NO, HNO, N_2O, $ONNO_2$, NH_2OH, and H_2O. Since NO is also one of the reaction prod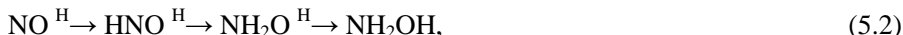ucts, offering a renewed starting point, all the reactions discussed in Part I should also be considered in the full reaction scheme presented here.

The hydrogenation of NO_2 follows:

$$NO_2 + H \rightarrow NO + OH. \tag{5.1}$$

Reaction (5.1) is found to have a small barrier in the gas phase (<50 K, see Su *et al*. 2002). Our results show that reaction (5.1) is efficient and leads to the formation of two reactants that act as parentz species of more complex molecules observed in our experiments:

$$NO \overset{H}{\rightarrow} HNO \overset{H}{\rightarrow} NH_2O \overset{H}{\rightarrow} NH_2OH, \tag{5.2}$$
$$OH + H \rightarrow H_2O, \tag{5.3}$$
$$OH + H_2 \rightarrow H_2O + H. \tag{5.4}$$

Congiu *et al*. (2012a, 2012b) and Fedoseev *et al*. (2012) studied reaction (5.2) under different laboratory conditions and found that the formation of NH_2OH proceeds barrierless. Water formation has been extensively studied in the solid phase over the past decade (Miyauchi *et al*. 2008, Ioppolo *et al*. 2008, Matar *et al*. 2008, Mokrane *et al*. 2009, Ioppolo *et al*. 2010, Cuppen *et al*. 2010, Dilieu *et al*. 2010, Romanzin *et al*. 2011, Oba *et al*. 2012). Figures 5.1 and 5.2 show that NH_2OH and H_2O are the final products of the hydrogenation of NO_2. Furthermore, if NO_2 is mixed in a ^{13}CO matrix, NH_2OH is still the final reaction product at high H-atom fluences. However, the formation of water ice is in competition with other reaction routes leading to the formation of carbon dioxide and formic acid (Ioppolo *et al*. 2011a, Ioppolo *et al*. 2011b):

$$OH + {}^{13}CO \rightarrow HO^{13}CO \rightarrow {}^{13}CO_2 + H, \tag{5.5}$$

$$HO^{13}CO + H \rightarrow \begin{cases} H_2O + {}^{13}CO \\ {}^{13}CO_2 + H_2 \\ H^{13}COOH, \end{cases} \tag{5.6}$$
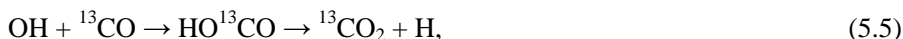
with a purely statistical branching ratio (Ioppolo *et al*. 2011a). Figure 5.3 shows the formation of NH_2OH, $HO^{13}CO$, $^{13}CO_2$, and $H^{13}COOH$, while the formation of water ice is under the detection limit.

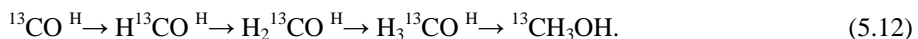OH radicals can also react with NO or NO_2 to form nitrous acid or nitric acid, respectively:

$$NO + OH \rightarrow HNO_2, \tag{5.7}$$
$$NO_2 + OH \rightarrow HNO_3. \tag{5.8}$$

Although our laboratory conditions are not suited to investigate these specific reactions (H atoms $\gg$ OH radicals), HNO_2 and HNO_2 are potentially formed in the ice. However, spectral features from HNO_2 and HNO_3 either overlap with the spectral bands of other molecules or are under the detection limit. Therefore, these species cannot be unambiguously identified in the ice. Joshi *et al*. (2012) investigated in the laboratory the reaction NO + OH. In a future laboratory study we will focus on the formation of nitrogen-bearing acids in space, *i.e.*, through the surface reactions (5.7) and (5.8).

Other reactions that lead to the formation of nitrogen oxides are:

$$NO + NO \rightarrow (NO)_2, \tag{5.9}$$
$$NO + NO_2 \rightarrow N_2O_3, \tag{5.10}$$
$$NO_2 + NO_2 \rightarrow N_2O_4, \textit{i.e. } (NO_2)_2. \tag{5.11}$$

These reactions are all discussed in Part I and are found to be barrierless in the solid phase. The choice to embed NO_2 in a ^{13}CO matrix reduces the probability for reactions (5.9) - (5.11) to occur and, therefore, enables a better investigation of reactions (5.1) - (5.6) under more interstellar relevant conditions.

The hydrogenation of carbon monoxide is also visible in Fig. 5.3 (Hiraoka *et al*. 1994, Watanabe & Kouchi 2002, Fuchs *et al*. 2009):

$$^{13}CO \xrightarrow{H} H^{13}CO \xrightarrow{H} H_2{}^{13}CO \xrightarrow{H} H_3{}^{13}CO \xrightarrow{H} {}^{13}CH_3OH. \tag{5.12}$$

Methanol is under the detection limit in all our co-deposition experiments because the used ^{13}CO:H ratio leads to a low coverage of H atoms on the ice surface. This combined with a low penetration depth of H atoms into carbon monoxide, results in an incomplete

hydrogenation of ^{13}CO ice. $H_2^{13}CO$ is only clearly detected when NO_2 in not present in the mixture. Thus, reactions (5.1) and (5.12) are in competition when NO_2 and ^{13}CO are co-deposited with H atoms, and reaction (5.1) is more efficient than reaction (5.12).

The oxygenation of NO_2 leads to the destruction of NO_2 and the formation of NO and O_2:

$$NO_2 + O \rightarrow NO + O_2. \tag{5.13}$$

This reaction is barrierless in the gas phase (Atkinson *et al.* 2004). Subsequently, N_2O_3 is formed through reaction (5.10), while NO can also react with the oxygen allotropes to form NO_2, as shown in Part I:

$$NO + O \rightarrow NO_2, \tag{5.14}$$
$$2NO + O_2 \rightarrow 2NO_2, \tag{5.15}$$
$$NO + O_3 \rightarrow NO_2 + O_2. \tag{5.16}$$

O_2 is formed in the plasma beam, through reactions (5.13) and (5.16), while O_2 originates from:

$$O_2 + O \rightarrow O_3. \tag{5.17}$$

CO_2 is also formed through the reaction (see Fig. 5.5):

$$^{13}CO + O \rightarrow {}^{13}CO_2. \tag{5.18}$$

Reactions (5.5) and (5.18) have been recently investigated and compared under the same laboratory conditions in Ioppolo *et al.* (2013).

N_2O is the final product of the nitrogenation of NO_2:

$$NO_2 + N \rightarrow N_2O + O. \tag{5.19}$$

Reactions N_2O+H/O/N have barriers and do not lead to the formation of other detectable species (Ioppolo *et al.* 2013). Oxygen atoms can react with NO_2 to form NO and O_2 according to reaction (5.13). O atoms can also react with NO to form NO_2 through reaction (5.14) or with an N atom to form NO, although the latter reaction has not been unambiguously tested in the laboratory yet. N_2O_3 is formed through reaction (5.10). As discussed in Part I, the nitrogenation of NO leads to the formation of:

$$NO + N \rightarrow N_2 + O \qquad\qquad\qquad\qquad (5.20)$$

Reactions 5.19 and 5.20 are found to be both barrierless in the gas-phase (Wennberg *et al.* 1994). However, Figure 5.6 shows that the nitrogenation of NO_2 is not an efficient process. This discrepancy can be explained by the dimerization of NO_2 that occurs when pure NO_2 is deposited in the solid phase. The dimerization process is barrierless, thus Figure 5.6 only shows that reaction $(NO_2)_2 + N$ is not efficient in the solid phase. Figure 5.8 shows the NO_2 use-up during co-deposition of NO_2:[13]CO:H (top panel), NO_2:[13]CO:O (bottom panel), and NO_2:[13]CO:N (bottom panel) *versus* the atom fluence. The NO_2 use-up is calculated by subtracting the NO_2 abundance from the NO_2:[13]CO experiments to the NO_2 abundance of the NO_2:[13]CO:H/O/N experiments, respectively (see Figs. 5.3, 5.5 and 5.7). Although as already mentioned, the efficiency of the hydrogenation reactions cannot be compared directly to that of the oxygenation and nitrogenation reactions because the H-atom flux is orders of magnitude higher than the other atom fluxes, we can still draw conclusions on the (relative) efficiency of each surface reaction. In the results section we showed that reaction (5.1) is efficient and most likely barrierless. The linear trend of the NO_2 consumption in the hydrogenation experiments is consistent with reaction (5.1) being barrierless (top panel in Fig. 5.8). Moreover, since the O- and N-atom fluxes are similar ($1\cdot10^{11}$ atoms cm^{-2} s^{-1} and $8\cdot10^{10}$ atoms cm^{-2} s^{-1}, respectively) and the NO_2 deposition rates are reproducible within ~20%, a comparison between the NO_2 use up in the oxygenation and nitrogenation experiments can be made and indicates that reaction (5.13) is slightly faster and, therefore, more efficient than reaction (5.19) (bottom panel in Fig. 5.8).

In our experiments, O atoms come from the dissociation of N_2O, while N atoms are made by dissociating N_2. N_2O and N_2 stick to the cold surface at 15 K during co-deposition and, therefore, become part of the ice mixture. Moreover, the dissociation rate for the two atom beams is different (O:N_2O = 0.1:1 and N:N_2 = 0.1:25). This means that, even though N_2O and N_2 are not participating in the surface reactions, their presence in different amounts can affect the surface coverage of NO_2 and the penetration depth of O and N atoms in the ice. Thus, although our results clearly indicate that the surface reaction efficiency follows the trend $NO_2 + H > NO_2 + O \geq NO_2 + N$, the presence of N_2O and N_2 in the ice can partially influence the comparison of the NO_2 use up shown in Fig. 5.8.

A schematic cartoon of all the investigated reaction routes is shown in Figure 5.9. Table 5.3 lists the main surface reactions discussed in Parts I and II and divides them in different groups: from barrierless reactions to reactions with a high barrier that do not allow for the reaction to proceed in the solid phase at low temperatures. Given the overall complexity of the full reaction scheme, additional reaction products are expected to form as well, but for the experimental settings studied here, these clearly must be of less importance, as no clear spectroscopic or mass spectrometric data are found.
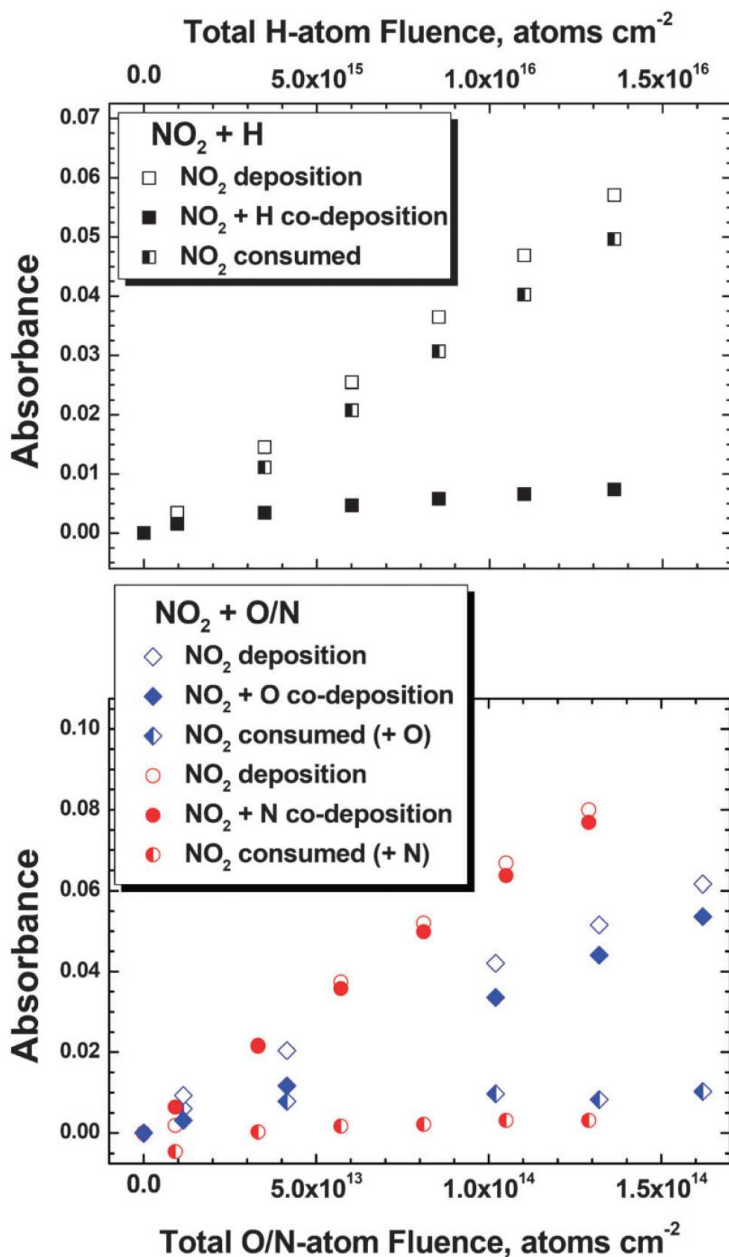
Figure 5.8. Top panel: NO_2 use up during co-deposition of NO_2:^{13}CO:H *versus* the H-atom fluence (half-full squares). The NO_2 abundance during deposition of pure NO_2 (empty squares) and $NO_2 + H$ (full squares) is also plotted in the same panel. Bottom panel: NO_2 use up during co-deposition of NO_2:^{13}CO:O (half-full diamonds) and NO_2:^{13}CO:N (half-full circles) *versus* the atom fluence. As for the top panel, here the full diamonds and circles represent the NO_2 abundance during $NO_2 + O$ and $NO_2 + N$ experiments, respectively. The empty diamonds and circles represent the NO_2 abundance during deposition of pure NO_2 in the $NO_2 + O$ and $NO_2 + N$ experiments, respectively.

5.5 Astrophysical implications

Sub-millimeter and millimeter wavelength observations of "hot cores" - *i.e*., compact (few tens of AUs) regions of dense and warm gas where the chemistry is dominated by the evaporation of grain mantles - reveal a range of interstellar complex organic molecules, such as CH_3OH, $HCOOH$, $HCOOCH_3$, and NH_2CH_2CN (Herbst & van Dishoeck 2009, Belloche *et al*. 2008). The exact origin of these species is still unclear, but recent models indicate that surface reaction mechanisms are most likely the main formation channel (Garrod 2013). Garrod (2013) showed that the gas-phase formation of glycine (NH_2CH_2COOH) in hot cores depends on the timescale of the hot-core evolution and the availability of precursor species in the gas phase. Therefore, glycine is found to form in his model almost exclusively on grain ice mantles.

A potential precursor of amino acids is hydroxylamine (NH_2OH). Congiu *et al*. (2012a), Congiu *et al*. (2012b) and Fedoseev *et al*. (2012) showed that hydroxylamine is efficiently formed in the solid phase under dense core conditions through reaction (5.2). Pulliam *et al*. (2012), using the NRAO 12 m telescope, could not detect NH_2OH toward a range of interstellar sources and found an upper limit of $8 \cdot 10^{-12}$ wrt H_2 toward SgrB2(N). Due to their high desorption temperatures, rotational emission from molecules like hydroxylamine and glycine (still not unambiguously detected in the ISM) is expected for compact regions only. However, emissions from regions smaller than ~5" are not detectable with single-dish telescopes. This may explain the non-detection of these species and indicates that molecules like hydroxylamine can be potentially detected by ALMA at sub-arcsecond resolution toward bright, nearby sources with relatively narrow emission lines.

Understanding the origin of COMs is pivotal to link the formation of simple species in space to life on Earth. In Parts I and II of this work, we focus on the laboratory investigation of the surface formation of nitrogen oxides and more complex species like hydroxylamine. In the discussion section, we showed many reaction routes that proceed under cold cloud conditions and start from $NO + H/O/O_2/O_3/N$ and $NO_2 + H/O/N$.

In this scenario, NO can freeze-out onto the icy grains during the dense cloud phase (Blake *et al*. 1986, Pineau des Forets *et al*. 1990). NO ice can be hydrogenated in a barrierless way to form solid hydroxylamine (Congiu *et al*. 2012a, Congiu *et al*. 2012b, Fedoseev *et al*. 2012). The NO that reacts with the oxygen allotropes in the solid phase will form efficiently NO_2. The nitrogenation of NO will lead to the destruction of NO and the formation of N_2. A feasible reason for the non-detection of NO_2 in the ISM is a very efficient solid-phase destruction pathway (*i.e*., photodissociation and/or non-energetic surface reactions). We showed that NO_2 can be hydrogenated in a barrierless way to form

NO and OH. These two reactants contribute in more realistic interstellar ice to form species like NH_2OH, H_2O, CO_2, and HCOOH, as shown in this work. The oxygenation of NO_2 forms again NO and O atoms, while the nitrogenation of NO_2 forms also N_2O, another interstellar relevant species detected in the ISM (Ziurys *et al*. 1994). Thus, many of the investigated surface reaction routes lead to the formation of NO molecules and therefore NH_2OH. This result is in support of the formation of complex species in the solid phase and is in agreement with the most recent astrochemical models (Garrod 2013). Other nitrogen oxides, like N_2O_3 and N_2O_4, can be formed through the reaction of NO and NO_2, and the reaction of two NO_2 molecules, respectively. However, reactions (5.10) and (5.11) are potentially still limited by the interstellar low abundance of the parent species. Finally, nitrogen-bearing acids, like nitrous acid and nitric acid, can be formed through surface reactions (5.7) and (5.8). Although the formation of these acids was not verified here, their interstellar relevance should not be excluded.

We expect that future astrochemical models will benefit from the implementation of the efficiency of the single surface reactions investigated here and shown in Table 5.3. Moreover, the results found here indicate that it is worth to keep searching for NH_2OH in the ISM, whereas a NO_2 detection is not expected at this stage.
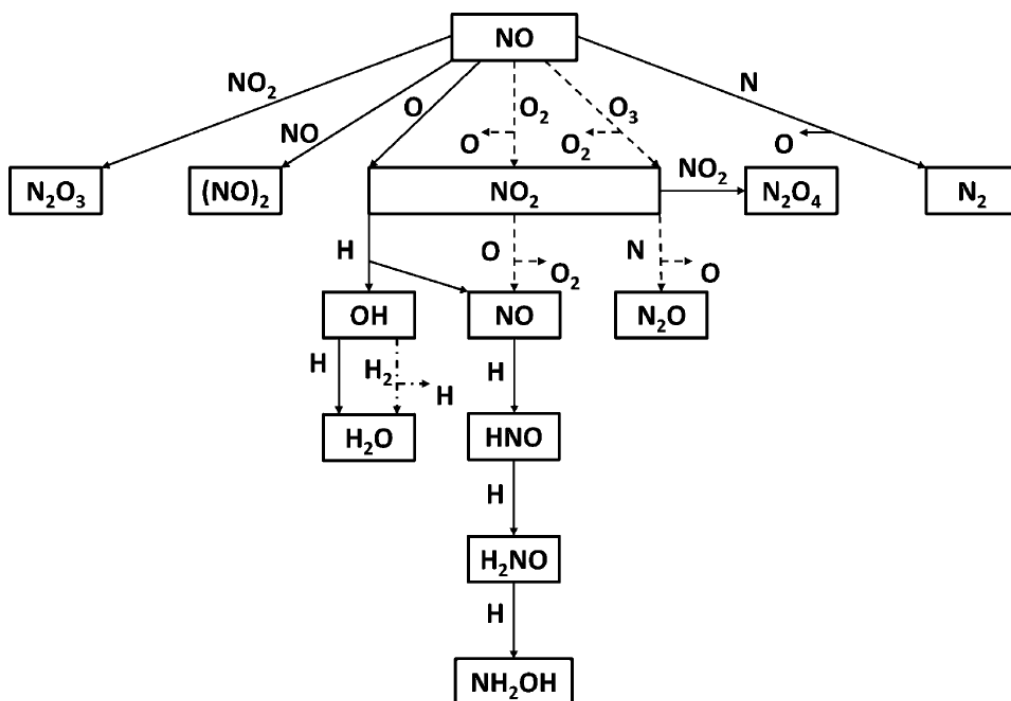

Figure 5.9. Reaction scheme leading to the formation of nitrogen oxides as investigated in Parts I and II of this work. Solid lines are the reaction with no barrier; dashed lines are the reactions with a small barrier; and dashed-dotted lines are the reaction with a noticeable barrier (see also Table 5.3).

Table 5.3. Efficiency of the main surface reactions discussed in Parts I and II.

No barrier	Small barrier	Barrier	No reaction
$NO + H$	$NO + O_2$	$CO + H$	$NO + H_2$
$NO + O$	$NO + O_3$	$H_2CO + H$	$NO + N_2$
$NO + N$		$OH + H_2$	$NO_2 + H_2$
$NO + NO$		$(NO)_2 + O_2$	$NO_2 + O_2$
$NO + NO_2$		$(NO_2)_2 + N$	$NO_2 + N_2$
$NO_2 + H$			$N_2O + H$
$NO_2 + O$			$N_2O + O$
$NO_2 + N$[a]			$N_2O + N$
$NO_2 + NO_2$			
$OH + H$			

[a]This reaction may have a small barrier.

5.6 Conclusions

The surface formation and destruction of nitrogen oxides is tested under ultra high vacuum conditions, at low temperatures, and by means of RAIR spectroscopy, mass spectrometry, and TPD techniques. From this study we draw the following conclusions:

1. NO_2 is efficiently formed in the solid state via $NO+O/O_2/O_3$ reactions (Part I).
2. The non-detection of (gaseous) NO_2 in space can be related to efficient destruction mechanisms, such as surface $NO_2 + H/O/N$ reactions (Part II).
3. The final products of NO_2 hydrogenation are NH_2OH and H_2O. Hydroxylamine is found to be formed through a series of barrierless surface reactions as previously shown by (Congiu *et al*. 2012a), Congiu *et al*. (2012b), Fedoseev *et al*. (2012). Both water and hydroxylamine are important molecules for the formation of COMs in space (Part II).
4. N_2O is formed through the nitrogenation of NO_2 and is not destroyed in reactions with H-, O-, and N-atoms (Part II).
5. Several nitrogen oxides, such as $(NO)_2$, N_2O_3, and N_2O_4, are formed through surface $NO + H/O/O_2/O_3/N$ and $NO_2 + H/O/N$ reactions due to high concentration of parent species (Parts I and II).
6. Surface coverage (submonolayer and multilayer regimes) have a small but noticeable impact on the final products. For instance, dimerization reactions are most likely to occur in a multilayer regime rather than in submonolayer thick ices (Parts I and II).
7. Different substrates (silicate, graphite, compact ASW ice, and gold) and ice composition (pure ices, polar and apolar mixtures) do not affect the results in a detectable way (Parts I and II).

8. Table 5.3 lists the efficiency of all the investigated reaction routes (see Fig. 5.9) and therefore can be used as an input in astrochemical models to better understand the formation and evolution of nitrogen oxides in space (Parts I and II).

9. We expect ALMA to be ideally suited to detect species like hydroxylamine at sub-arcsecond resolution toward bright, nearby sources with relative narrow emission lines.

References

Amiaud L., Fillion J. H., Baouche S., Dulieu F., Momeni A., Lemaire J. L., 2006, JCP, 124, 094702

Anton R., Wiegner T., Naumann W., Liebmann M., Klein C., Bradley C., 2000, Rev. Sci. Instrum., 71, 1177

Atkinson R., Baulch D. L., Cox R. A., Crowley J. N., Hampson R. F., Hynes R. G., Jenkin M. E., Rossi M. J., Troe J., 2004, Atmos. Chem. Phys., 4, 1461

Belloche A., Menten K. M., Comito C., Müller H. S. P., Schilke P., Ott J., Thorwirth S., Hieret C., 2008, A&A, 482, 179

Bennett C. J. & Kaiser R. I., 2005, ApJ, 635, 1362

Berney C. V. & Eggers D. F., Jr., 1964, JCP, 40, 990

Blake G. A., Masson C. R., Phillips T. G., Sutton E. C., 1986, ApJS, 60, 357

Boduch P., Domaracka A., Fulvio D., Langlinay T., Lv X. Y., Palumbo M. E., Rothard H., Strazzulla G., 2012, A&A, 544, A30

Brosset P., Dahoo R., Gauthierroy B., Abouafmarguin L., Lakhlifi A., 1993, Chem. Phys., 172, 315

Chaabouni H., Schriver-Mazzuoli L., Schriver A., 2000, Low Temp. Phys., 26, 712

Charnley S. B., Tielens A. G. G. M., Millar T. J., 1992, ApJL, 399, L71

Congiu E., Chaabouni H., Laffon C., Parent P., Baouche S., Dulieu F., 2012b, JCP, 137, 054713

Congiu E., Fedoseev G., Ioppolo S., Dulieu F., Chaabouni H., Baouche S., Lemaire J. L., Laffon C., Parent P., Lamberts T. *et al*., 2012a, ApJL, 750, L12

Cuppen H. M., Ioppolo S., Romanzin C., Linnartz H., 2010, PCCP, 12, 12077

van Dishoeck E. F. & Blake G. A., 1998, Annu. Rev. Astron. Astrophys., 36, 317

Dows D. A., 1957, JCP, 26, 745

Dulieu F., Amiaud L., Congiu E., Fillion J., Matar E., Momeni A., Pirronello V., Lemaire J. L., 2010, A&A, 512, A30

Ewing G. E. & Pimentel G. C., 1961, JCP, 35, 925

Fateley W. G., Bent H. A., Crawford B., Jr., 1959, JCP, 31, 204

Fedoseev G., Ioppolo S., Lamberts T., Zhen J. F., Cuppen H. M., Linnartz H., 2012, JCP, 137, 054714

Fuchs G. W., Cuppen H. M., Ioppolo S., Bisschop S. E., Andersson S., van Dishoeck E. F., Linnartz H., 2009, A&A, 505, 629

Garrod R. T., 2013, ApJ, 765, 60

Herbst E. & E. F. van Dishoeck, 2009, Annu. Rev. Astron. Astrophys., 47, 427

Hidaka H., Watanabe M., Kouchi A., Watanabe N., 2011, PCCP, 13, 15798

Hiraoka K., Ohashi N., Kihara Y., Yamamoto K., Sato T., Yamashita A., 1994, Chem. Phys. Lett., 229, 408

Hiraoka K., Yamashita A., Yachi Y., Aruga K., Sato T., Muto H., 1995, ApJ, 443, 363

Holland R. F. & Maier II W. B., 1983, JCP, 78, 2928

Ioppolo S., Cuppen H. M., Romanzin C., van Dishoeck E. F., Linnartz H., 2008, ApJ, 686, 1474

Ioppolo S., Cuppen H. M., Romanzin C., van Dishoeck E. F., Linnartz H., 2010, PCCP, 12, 12065

Ioppolo S., Cuppen H. M., van Dishoeck E. F., Linnartz H., 2011a, MNRAS, 410, 1089

Ioppolo S., Fedoseev G., Lamberts T., Romanzin C., Linnartz H., 2013, Rev. Sci. Instrum., 84, 073112

Ioppolo S., van Boheemen Y., Cuppen H.M., van Dishoeck E. F., Linnartz H., 2011b, MNRAS, 413, 2281

Jacox M. E. & Milligan D. E., 1973, J. Mol. Spectrosc., 48, 536

Jamieson C. S., Bennett C. J., Mebel A. M., Kaiser R. I., 2005, ApJ, 624, 436

Joshi P. R., Zins E.-L., Krim L., 2012, MNRAS, 419, 1713

Loeffler M. J., Baratta G. A., Palumbo M. E., Strazzulla G., Baragiola R. A., 2005, A&A, 435, 587

Łpiński A., Spanget-Larsen J., Waluk J., Radziszewski J. G., 2001, JCP, 115, 1757

Matar E., Congiu E., Dulieu F., Momeni A., Lemaire J. L., 2008, A&A, 492, L17

McElroy D., Walsh C., Markwick A. J., Cordiner M. A., Smith K., Millar T. J., 2013, A&A, 550, A36

Milligan D. E. & Jacox M. E., 1971, JCP, 54, 927

Minissale M., Congiu E., Baouche S., Chaabouni H., Moudens A., Dulieu F., Manicó G., Pirronello V., 2013, Chem. Phys. Lett., 565, 52

Minissale M., Fedoseev G., Congiu E., Ioppolo S., Dulieu F., Linnartz H., 2014, PCCP, 16, 8257

Miyauchi N., Hidaka H., Chigai T., Nagaoka A., Watanabe N., Kouchi A., 2008, Chem. Phys. Lett., 456, 27

Mokrane H., Chaabouni H., Accolla M., Congiu E., Dulieu F., Chehrouri M., Lemaire J. L., 2009, ApJL, 705, L195

Nour E. M., Chen L. H., Laane J., 1983, J. Phys. Chem., 87, 1113

Nour E. M., Chen L. H., Strube M. M., Laane J., J. Phys. Chem., 1984, 88, 756

Oba Y., Watanabe N., Hama T., Kuwahata K., Hidaka H., Kouchi A., 2012, ApJ, 749, 67

Pineau des Forets G., Roueff E., Flower D. R., 1990, MNRAS, 244, 668

Pulliam R. L., McGuire B. A., Remijan A. J., 2012, ApJ, 751, 1

Qi C., Öberg K. I., Wilner D. J., D'Alessio P., Bergin E., Andrews S. M., Blake G. A., Hogerheijde M. R., van Dishoeck E. F., 2013, Science, 341, 630

Romanzin C., Ioppolo S., Cuppen H. M., van Dishoeck E. F., Linnartz H., 2011, JCP, 134, 084504

Sandford S. A., Allamandola L. J., Tielens A. G. G. M., Valero G. J., 1988, ApJ, 329, 498

Schmidt A., Offermann J., Anton R., 1996, Thin Solid Films, 281, 105

Sicilia D., Ioppolo S., Vindigni T., Baratta G. A., Palumbo M. E., 2012, A&A, 543, A155

Su M.-C., Kumaran S. S., Lim K. P., Michael J. V., Wagner A. F., Harding L. B., Fang D.-C., 2002, J. Phys. Chem. A, 106, 8261

Theulé P., Duvernay F., Danger G., Borget F., Bossa J. B., Vinogradoff V., Mispelaer F., Chiavassa T., 2013, Adv. Space Res., 52, 1567

Tschersich K. G. & von Bonin V., 1998, J. Appl. Phys., 84, 4065

Tschersich K. G., 2000, J. Appl. Phys., 87, 2565

Tschersich K. G., Fleischhauer J. P., Schuler H., 2008, J. Appl. Phys., 104, 034908

Watanabe N. & Kouchi A., 2002, ApJL, 571, L173

Wennberg P. O., Anderson J. G., Weisenstein D. K., 1994, J. Geophys. Res., 99, 18839

Withnall R., Andrews L., 1988, J. Phys. Chem., 92, 2155

Wohar M. M. & Jagodzinski P. W., 1991, J. Mol. Spectrosc., 148, 13

Yeo G. A. & Ford T. A., 1990, J. Mol. Struct., 217, 307

Ziurys L. M., Apponi A. J., Hollis J. M., Snyder L. E., 1994, ApJL, 436, L181

VI

Low Temperature Surface Formation of NH_3 and HNCO: Hydrogenation of Nitrogen Atoms in CO-rich Interstellar Ice Analogues

Solid state astrochemical reaction pathways have the potential to link the formation of small nitrogen-bearing species, like NH_3 and HNCO, and prebiotic molecules, specifically amino acids. To date, the chemical origin of such small nitrogen containing species is still not well understood, despite the fact that ammonia is an abundant constituent of interstellar ices toward young stellar objects and quiescent molecular clouds. This is mainly because of the lack of dedicated laboratory studies. The aim of the present work is to experimentally investigate the formation routes of NH_3 and HNCO through non-energetic surface reactions in interstellar ice analogues under fully controlled laboratory conditions and at astrochemically relevant temperatures. This study focuses on the formation of NH_3 and HNCO in CO-rich (non-polar) interstellar ices that simulate the CO freeze-out stage in dark interstellar cloud regions, well before thermal and energetic processing start to become relevant. We demonstrate and discuss the surface formation of solid HNCO through the interaction of CO molecules with NH radicals - one of the intermediates in the formation of solid NH_3 upon sequential hydrogenation of N atoms. The importance of HNCO for astrobiology is discussed.


6.1 Introduction

The detection of glycine, the simplest amino acid, in cometary samples recently returned to Earth by the STARDUST mission has boosted detailed investigations of the origin and fate of (pre)biotic molecules in the interstellar medium (ISM) (Elsila *et al*. 2009, Garrod 2013). However, although an increasing number of laboratory and theoretical studies show that complex species form in the solid phase, on the surface of icy grains, we still lack understanding of the complete surface formation pathways at play. The nitrogen chemistry of the ISM is particularly important within this context, because of its potential to reveal the formation routes of the simplest amino acids or their possible precursors. From the ~180 species unambiguously identified in the ISM, about one third contains nitrogen atoms, but only NH_3, XCN, and possibly NH_4^+ are identified as constituents of interstellar ices. Solid NH_3 is generally found with a typical abundance of 5% with respect to water ice toward low- and high-mass young stellar objects (YSOs) (Gibb *et al*. 2004, Bottinelli *et al*. 2010, Öberg *et al*. 2011). Solid isocyanic acid (HNCO) has not been identified in the solid phase yet, but its direct derivative, the cyanate ion (OCN^-), has been found in interstellar ices with abundances between 0.3-0.6% with respect to water ice. The assignment of solid OCN^- is often attributed to either the entire, so called, XCN band or to a single component ($2165 \ cm^{-1}$) of the full band (van Broekhuizen *et al*. 2005). More recently, Öberg *et al*. (2011) found a correlation between CO and the XCN band that supports the identification of the latter as OCN^-. Another possible N-bearing component of interstellar ices is NH_4^+. Although the unambiguous assignment of NH_4^+ is still under debate (Gálvez *et al*. 2010), it can potentially be one of the carriers of the 5-8 µm bands, and its presence in interstellar ices is consistent with previously obtained laboratory results (Boogert *et al*. 2008). The existence of interstellar solid NH_4^+ is indeed constrained by the hypothesis that NH_4^+ helps to maintain charge balance between positive and negative ions within interstellar ices. Öberg *et al*. (2011) assigned NH_4^+ abundances of 2.3 and 4.3% with respect to water ice toward low- and high-mass protostars, respectively. The formation of OCN^- and NH_4^+ is commonly associated with a later stage of molecular cloud evolution, when thermal processing of the ice by a newly formed protostar becomes important. NH_3 and HNCO are commonly considered the precursors of NH_4^+ and OCN^- (Demyk *et al*. 1998), and therefore are expected to be formed in an earlier evolutionary stage of dark clouds, when temperatures are as low as 10-20 K and the formation routes through non-energetic atom and radical addition surface reactions dominate.

To date, laboratory experiments on the non-energetic surface formation routes of nitrogen-containing species have mainly focused on the formation of ammonia (NH_3), hydroxylamine (NH_2OH), and various nitrogen oxides (NO, NO_2, N_2O) (Hiraoka *et al*. 1995, Hidaka *et al*. 2011, Congiu *et al*. 2012a and 2012b, Fedoseev *et al*. 2012, Minissale

et al. 2014, Ioppolo *et al.* 2014). The present work extends previous studies on the solid-state formation of ammonia to non-polar (CO-rich) ices, and, at the same time, discusses the link between the surface formation of HNCO. In the accompanying paper (Fedoseev *et al.* 2014), we investigate the deuterium enrichment of all the ammonia isotopologues as produced through the competition between hydrogenation and deuteration of nitrogen atoms. These results are not further discussed in the present paper.

It is commonly believed that in addition to the depletion from the gas phase, where NH_3 is produced through a series of ion-molecular reactions (*e.g.*, Herbst & Klemperer 1973 and Scott *et al.* 1997), ammonia formation proceeds through the sequential addition of three H atoms to a single nitrogen atom on the surface of ice dust grains:

$$N + H \rightarrow NH, \tag{6.1}$$
$$NH + H \rightarrow NH_2, \tag{6.2}$$
$$NH_2 + H \rightarrow NH_3. \tag{6.3}$$
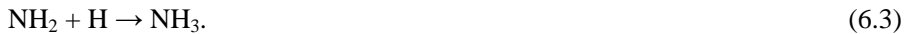
Reactions (6.1)-(6.3) were first tested at cryogenic temperatures by Hiraoka *et al.* (1995), who performed a temperature programmed desorption experiment upon hydrogenation of N atoms trapped in a matrix of solid N_2. Recently, Hidaka *et al.* (2011) confirmed the formation of ammonia in a solid N_2 matrix at low temperatures. Their laboratory detection of NH_3 was made after annealing the ice to 40 K in order to desorb the N_2 matrix. So far, studies of N-atom hydrogenation in more realistic and astronomically relevant H_2O- and CO-rich ice analogues have not been reported. Under such conditions, the intermediate free radicals, NH and NH_2, can potentially react with other molecules or free radicals to form new and more complex species, such as HNCO:

$$NH + CO \rightarrow HNCO, \tag{6.4}$$
$$NH_2 + CO \rightarrow HNCO + H. \tag{6.5}$$

Reaction (6.4) is exothermic. The reactivity of CO with NH has been investigated in a combined experimental and quantum chemical study by Himmel *et al.* (2002) *via* photo-induced dissociation of HN_3 in a 12 K Ar matrix. In their work, matrix experiments indicated that $NH(^3\Sigma)$ reacts with CO under laboratory conditions to form $HNCO(^1A')$. An activation barrier of ~4200 K was derived by means of CCSD(T), CASSCF, and MP2 calculations carried-out to evaluate geometries and energies at the transition state for this spin-forbidden reaction. Although the value of this barrier could be considered quite high (*e.g.*, the activation barrier for CO + H coulf be as low as as 1800 K; Woon 2002), experiments and simulations yield consistent data when taking into account experimental and computational inaccuracies. Reaction (6.4) has often been proposed in spectroscopic

studies to explain the formation of HNCO in mixed interstellar ice analogues processed by proton or UV radiation (*e.g.*, Raunier *et al*. 2003, van Broekhuizen *et al*. 2004 and references therein). However, to the best of our knowledge, there are no studies available from literature on the investigation of reaction (6.4) with non-energetic input. Reaction (6.5) is endothermic (4800 K) and therefore is unlikely to occur under cold dense molecular cloud conditions (Nguyen *et al*. 1996).

Once formed in the ice, NH_3 and HNCO may react through

$$HNCO + NH_3 \rightarrow NH_4^+ NCO^-, \hspace{4cm} (6.6)$$
$$HNCO + H_2O \rightarrow H_3O^+ NCO^-, \hspace{4cm} (6.7)$$

(see Raunier *et al*. 2003 and Theule *et al*. 2011, respectively) to form OCN^- and NH_4^+ during a later stage of the molecular cloud evolution. Theule *et al* 2011 found an activation energy barrier for reaction (6.7) of 3127 K, and concluded that it is too high to make this reaction important for the conditions and timescales typical for young stellar objects. In a follow-up study, Mispelaer *et al*. (2012) determined a barrier of 48 K for reaction (6.6), indicating the latter pathway as the most promising one to form OCN^- and NH_4^+. As stated before, OCN^- has been observed, and NH_4^+ may have been identified in the solid state, but the focus in our work is to simulate dense molecular cloud conditions, well before thermal and energetic processing of ices become important. The goal of the present study is to experimentally verify the formation of NH_3 through reactions (6.1)-(6.3), as well as the formation of HNCO through reaction (6.4) in an astrochemically representative **ice** and for astronomically relevant temperatures.

6.2 Experimental procedure

6.2.1 Experimental setup

All experiments are performed in an ultrahigh vacuum (UHV) setup (SURFRESIDE^2), constructed to investigate solid-state atom addition reactions at cryogenic temperatures. The system has been extensively described in Ioppolo *et al*. (2013), and therefore only a brief description is given here. SURFRESIDE^2 consists of three UHV chambers with a room-temperature base-pressure in the range of 10^{-9}-10^{-10} mbar. A rotatable gold-coated copper substrate is placed in the centre of the main chamber, where gases are introduced and deposited with monolayer precision onto the substrate surface through two metal deposition lines. A monolayer (ML) corresponds to about 10^{15} molecules cm^{-2}. The substrate temperature is varied between 13 and 300 K using a He closed-cycle cryostat with an absolute temperature accuracy better than ~2 K. Both of the two other UHV chambers

contain an atom beam line and are connected to the main chamber with angles of 45° and 135° with respect to the substrate (see Figs. 1, 3, and 4 in Ioppolo *et al*. 2013). In one atom line a commercially available thermal cracking source (Dr. Eberl MBE-Komponenten GmbH, see Tschersich 2000) is used to generate H/D atoms. In the other atom line a microwave plasma atom source (Oxford Scientific Ltd, see Anton *et al*. 2000) can be used to generate H/D/N/O atoms or radicals, such as OH. A custom made nose-shape quartz-pipe is placed in between each atom source and the substrate. These pipes are designed in a way that products formed upon thermal cracking (*e.g.*, H from H_2) or plasma dissociation (*e.g.*, N from N_2) experience at least four collisions with the pipe walls before reaching the substrate. This is done to quench electronically or ro-vibrationally excited states before impacting on the ice. A considerable fraction of non-dissociated molecules (*e.g.*, H_2/D_2 and N_2) are present in the beam. The method to derive atom flux values is described in Ioppolo *et al*. (2013). We want to stress that the N-atom flux is an effective flux, estimated by measuring the amount of products of a series of barrierless reactions involving N atoms in the solid phase. The H-atom flux used here is an absolute flux. In this case, the amount of H atoms present in the beam is directly measured by the QMS in the gas phase. The latter measurement does not take into account that not every H atom will stick to the surface of the substrate and therefore will be unavailable for further reactions, and it also neglects H-atom recombination on the ice surface. The absolute H-atom flux, therefore, is an upper limit for the effective H-atom flux.

Metal shutters separate the atom beam lines from the main chamber. The atom beam sources as well as the molecular dosing lines in the main chamber can be operated independently. This versatile design allows for the sequential (pre-deposition) or simultaneous (co-deposition) exposure of selected interstellar ice analogues to different atoms (*e.g.*, H/D/O/N). In the present study, co-deposition experiments are largely used. The ice composition is monitored *in situ* by means of reflection absorption infrared spectroscopy (RAIRS) in the range between 4000-700 cm^{-1} and with a spectral resolution of 1 cm^{-1} using a Fourier transform infrared (FTIR) spectrometer. The main chamber gas-phase composition is monitored by a quadrupole mass spectrometer (QMS), which is placed behind the rotatable substrate, and is mainly used during temperature programmed desorption (TPD) experiments. Here, RAIRS is used as the main diagnostic tool, complemented with TPD data to constrain the experimental results**.** Although QMS provides us with a better sensitivity, preference is given to the RAIRS due to the *in-situ* nature of the method.

6.2.2 Performed experiments

The formation of solid NH_3 and HNCO is studied for a selected set of well defined experimental conditions. Firstly, all the used gases (CO, H_2/D_2, and N_2) are prepared in distinct pre-pumped ($< 10^{-5}$ mbar) dosing lines. Pure H_2/D_2 gas (Praxair 5.0/Praxair 2.8) is introduced into the tungsten capillary pipe of the thermal cracking source. Pure N_2 gas (Praxair 5.0) is dissociated in the plasma chamber of the microwave plasma source. A simultaneous co-deposition of H/D and N atoms with CO gas (Linde 2.0) is performed on the surface of the bare gold substrate, typically at 13 K. RAIR difference spectra are acquired every 5 minutes with respect to the spectrum of the bare gold substrate. For the crucial experiments, once the co-deposition is completed, a new spectrum is taken and used as background reference. Two additional control experiments are then performed on top of the previously grown ice. The first one is a co-deposition of CO molecules with H/D (*i.e.*, without N) atoms and the second one is a co-deposition of CO molecules with N (*i.e.*, without H/D) atoms. These two experiments are performed under exactly the same experimental conditions used for the very first co-deposition experiment in order to allow a direct comparison. This procedure guarantees that the production of NH_3 and HNCO is the cumulative outcome of a low temperature co-deposition of H/D, N, and CO, ruling-out other possible formation pathways due to contaminations in the atom lines or in the main chamber. Co-deposition experiments of H/D + N + CO are repeated a second time and a TPD experiment is performed right afterward to monitor desorption of the formed species by means of the QMS.

A complementary set of control experiments is used to further verify the HNCO formation under astronomically relevant conditions. In this case, pure NH_3 vapour is introduced into the microwave plasma source, and the plasma dissociation products (*i.e.*, NH and NH_2 radicals together with NH_3, H, N, H_2 and N_2) are co-deposited with CO molecules. During this co-deposition experiment, RAIR difference spectra are acquired every 5 minutes with respect to a spectrum of the bare gold substrate. After completion of the co-deposition, a TPD experiment is performed and desorbing species are monitored by means of the QMS. The presence of NH and NH_2 radicals in the beam is verified by performing a co-deposition of NH_3 plasma dissociation products with D atoms and observing the N-D stretching mode in the mid-IR. For clarity, in Table 6.1 only the relevant experiments performed in this study are listed.

Table 6.1. List of the performed experiments.

Ref. N	Experiment	Ratio	T_{sample} (K)	R_{dep} (ML min^{-1})	Atom-flux^{TL} (10^{15} cm^{-2} min^{-1})	Atom-flux^{PL} (10^{15} cm^{-2} min^{-1})	t (min)	TPD[a]	Detection of NH$_3$[b]	Detection of HNCO[b]
Verification of NH$_3$ formation										
				CO	H (from H$_2$)	N (from N$_2$)				
1.1	N:H:N$_2$:CO	1:20:100:100	13	0.5	0.1	0.005	60	-	Y	N
1.2	N:H:N$_2$:CO	1:20:100:100	13	0.5	0.1	0.005	180	-	Y	N
1.3	N:H:N$_2$:CO	1:20:100:500	13	2.5	0.1	0.005	60	-	Y	N
1.4	N:H:N$_2$:CO	1:100:100:100	13	0.5	0.5	0.005	60	-	Y	N
1.5	N:H:N$_2$:CO	1:100:100:100	25	0.5	0.5	0.005	60	-	N	N
				CO	D (from D$_2$)	N (from N$_2$)				
1.6	N:D:N$_2$:CO	1:20:100:100	13	0.5	0.1	0.005	60	-	Y	N
				H$_2$O	H (from H$_2$)	N (from N$_2$)				
2.1	N:H:N$_2$:H$_2$O	1:20:100:500	15	2.5	0.1	0.005	90	-	-	-
2.2	N:H:N$_2$:H$_2$O	1:20:100:100	13	0.5	0.1	0.005	60	-	-	-
Verification of HNCO formation through hydrogenation of N atoms in CO-rich ice analogues										
				CO	H (from H$_2$)	N (from N$_2$)				
3.1	N:H:N$_2$:CO	1:20:100:100	13	0.5	0.1	0.005	90	QMS$^{2K/5K}$	Y	N
3.2	N:H:N$_2$:CO	1:6:100:100	13	0.5	0.03	0.005	90	QMS$^{2K/5K}$	Y	Y/N
3.3	N:H:N$_2$:CO	1:6:100:100	13	0.5	0.03	0.005	90	RAIRS^c	Y	Y/N
3.4	N:H:N$_2$:CO	1:4:100:100	13	0.5	0.02	0.005	90	QMS$^{2K/5K}$	Y	Y
3.5	N:H:N$_2$:CO	1:2:100:100	13	0.5	0.01	0.005	90	QMS$^{2K/5K}$	Y/N	Y
3.6	N:H:N$_2$:CO	1:2:100:100	13	0.5	0.01	0.005	90	QMS$^{0.4K/5K}$	Y/N	Y
3.7	N:H:N$_2$:CO	1:2:100:100	13	0.5	0.01	0.005	180	QMS$^{2K/5K}$	Y/N	Y
3.8	N:H:N$_2$:CO	1:1.5:100:100	13	0.5	0.0075	0.005	90	QMS$^{2K/5K}$	N	Y
3.9	N:H:N$_2$:CO	1:1:100:100	13	0.5	0.005	0.005	90	QMS$^{2K/5K}$	N	Y
3.10	N:H:N$_2$:CO	1:2:100:100	25	0.5	0.01	0.005	90	QMS$^{1K/5K}$	N	N
3.11	N:H:N$_2$:CO	1:1.5:100:100	25	0.5	0.0075	0.005	90	QMS$^{2K/5K}$	N	N
Isotope shift experiments confirming the formation of HN^{13}CO, H^{15}N^{13}CO and D^{15}NCO										
				^{13}CO	H (from H$_2$)	N (from N$_2$)				
4.1	N:H:N$_2$:^{13}CO	1:2:100:100	13	0.5	0.01	0.005	90	QMS$^{2K/5K}$	Y/N	Y
4.2	N:H:N$_2$:^{13}CO	1:2:100:100	13	0.5	0.01	0.005	360	RAIRS^c	Y	Y
				^{13}CO	H (from H$_2$)	^{15}N (from ^{15}N$_2$)				
4.3	^{15}N:H:^{15}N$_2$:^{13}CO	1:2:100:100	13	0.5	0.01	0.005	90	QMS$^{2K/5K}$	Y/N	Y
				^{13}CO	D (from D$_2$)	^{15}N (from ^{15}N$_2$)				
4.4	^{15}N:D:^{15}N$_2$:CO	1:2:100:100	13	0.5	0.01	0.005	90	QMS$^{2K/5K}$	Y/N	Y/N
Formation of HNCO further constrained *via* interaction of CO with NH$_3$ plasma dissociation products										
				CO		NH$_3$$^{(dissociated)}$				
5.1	CO:NH$_3$$^{(dissociated)}$	nn	13	0.5	-	n	90	QMS$^{2K/5K}$	-	Y
5.2	CO:NH$_3$	nn	13	0.5	-	-	90	QMS$^{2K/5K}$	-	N
5.3	CO:NH$_3$$^{(dissociated)}$	nn	70	0.5	-	n	90	QMS^{5K}	-	N
				^{13}CO		NH$_3$$^{(dissociated)}$				
5.4	^{13}CO:NH$_3$$^{(dissociated)}$	nn	13	0.5	-	n	90	QMS$^{2K/5K}$	-	Y
Confirmation of the presence of NH$_3$ plasma dissociation products in the beam										
					D (from D$_2$)	NH$_3$$^{(dissociated)}$				
6.1	D:NH$_3$$^{(dissociated)}$	nn	13	-	0.05	n	60	-	-	-
6.2	D:NH$_3$	nn	13	-	0.05	-	60	-	-	-
6.3	NH$_3$$^{(dissociated)}$	nn	13	-	-	n	60	-	-	-

Experiments are performed in co-deposition under different laboratory conditions; different co-deposition ratios are given; Ref. N is the reference number; T_{sample} is the substrate temperature during co-deposition; R_{dep} is the deposition rate of a selected molecule expressed in ML min^{-1} under the assumption that 1 L (Langmuir) exposure leads to the surface coverage of 1 ML; Atom-flux^{TL} is the thermal cracking source atom flux; Atom-flux^{PL} is the MW plasma source atom flux; absolute uncertainties of H/D- and N- fluxes are 50 and 40%, respectively; t is the time of co-deposition; *TPD* is the temperature programmed desorption experiment performed afterward with the TPD rate indicated; *Detection of NH$_3$* is the detection of ammonia either by RAIRS or QMS at the end of co-deposition; *Detection of HNCO* is the detection of isocyanic acid at the end of co-deposition; n – the exact NH$_3$ plasma beam composition is not determined, nn – since the exact NH$_3$ plasma beam composition is unknown the co-deposition ratio is not listed.
[a]Two numbers are given for the TPD rate: the first number is the TPD rate that is used below 50 K to gently remove the bulk of CO/N$_2$ ice, the second number is the TPD rate above 50 K. A higher TPD rate above 50 K is used in order to have a higher peak-to-noise ratio in the QMS. Routinely, 1.5 K/min or 2 K/min are used as TPD rates below 50 K. Since no difference is found in the results between the two rates, 2 K/min is indicated everywhere.
[b]Y/N means that the detection is uncertain.
[c]gradual warm-up followed by the acquisition of RAIR spectra is used instead of QMS

6.3 Results and dicussion

6.3.1 Formation of NH$_3$

A series of co-deposition experiments (see experiments 1.1-1.6 in Table 6.1) is performed to simulate the formation of NH$_3$ under dense cold interstellar cloud conditions, *i.e.*, when gas-phase CO has accreted onto the grains and the UV field is still negligible. A RAIR difference spectrum from a co-deposition of N:H:N$_2$:CO = 1:20:100:100 at 13 K with a total N-atom fluence of $3 \cdot 10^{14}$ atoms cm^{-2} ($\pm 40\%$) is shown in the large panel of Figure 6.1. ^{12}CO (2140 cm^{-1}) and ^{13}CO (2092 cm^{-1}) are both visible. The inset in Figure 6.1 shows this experiment in a smaller spectral range (Fig. 6.1a), as well as two more N:H:CO co-deposition experiments at 13 K for different mixing ratios (Figs. 6.1b-c), and a control experiment with only NH$_3$ and CO molecules co-deposited at 13 K (Fig. 6.1d). The same N-atom effective flux ($8 \cdot 10^{10}$ atoms s^{-1} cm^{-2}) within a 40% accuracy and total N-atom total fluence are used in the first three experiments. It should be noted that the amount of N$_2$ in the final mixed ice cannot be disregarded, since the N-atom beam comprises a considerable amount of non-dissociated N$_2$ molecules that, unlike H$_2$, can freeze out at 13 K and form a solid layer of ice (Cuppen & Herbst 2007).

The formation of NH$_3$ is confirmed in Fig. 6.1 and 6.1(a) by the appearance of two absorption features at $\nu_2 = 975$ cm^{-1} and $\nu_4 = 1625$ cm^{-1} (Abouaf-Marguin *et al*. 1977, Nelander 1984, Koops *et al*. 1983). In addition, a third feature at $\nu_3 = 3430$ cm^{-1} is observed in the region of the N-H and O-H stretching modes (not shown in the figure). Furthermore, solid H$_2$CO ($\nu_2 = 1728$ cm^{-1} and $\nu_3 = 1499$ cm^{-1}) shows up as a result of CO hydrogenation. Formation of H$_2$CO by H-atom addition to CO has been previously studied (*e.g.*, Hiraoka *et al*. 1994, Zhitnikov & Dmitirev 2002, Watanabe *et al*. 2002, Fuchs *et al*. 2009). Ongoing hydrogenation can form solid CH$_3$OH that is below its detection limit here. A small feature around 1600 cm^{-1} can be assigned to either H$_2$O impurity or to the aggregate of NH$_3$. The former assignment is supported by a possible admixtures of O$_2$ or H$_2$O in the N$_2$ bottle used in the experiments. Small negative peaks in the range between 1350 and 1750 cm^{-1} are water vapour absorptions along the path of the FTIR beam outside the UHV chamber. Unfortunately, these absorptions are still visible in some of the spectra despite the use of a dry air purged system.

Figure 1(b) shows the co-deposition of N:H:N$_2$:CO = 1:20:100:500 at 13 K. In this case, the deposition rate of CO is five times higher than in the experiment plotted in Fig. 6.1(a). Figures 6.1(a) and 6.1(b) show the same NH$_3$ final amount, but the H$_2$CO peaks are more prominent in the spectrum with higher CO abundance. This is expected, since the effective CO surface coverage for the experiment with N$_2$:CO = 100:500 is about 1.7 times higher than for N$_2$:CO = 100:100 (*i.e.*, 50% CO surface coverage for N$_2$:CO = 100:100 vs.

87% CO surface coverage for N_2:CO = 100:500). Clearly, CH_3OH abundances are still below the detection limit.

Figure 6.1(c) shows a co-deposition spectrum with an absolute H-atom flux five times higher (N:H:N_2:CO = 1:100:100:100) than the one in Fig. 6.1(a). This results in a further increase of the formed H_2CO, consistent with previous work (*e.g.*, Fuchs *et al.* 2009). In contrast with the H_2CO final yield, ammonia absorption features and, therefore, the corresponding formation yield does not increase: the ν_4 total absorbance shows the same value, while the ν_2 total absorption is even 35-40% less intense than the one in Fig. 6.1(a). This apparent inconsistency can be explained by the ν_2 mode (symmetrical deformation) being more sensitive to the ice mixture composition than the ν_4 mode (degenerate deformation), particularly with H_2CO around which can form hydrogen bonds with NH_3. The fact that the ν_2 mode is significantly more sensitive to environmental changes than the ν_4 mode was also found by Abouaf-Marguin *et al.* (1977). The latter work shows that when the hydrogen bonds are formed, the position of the ν_2 band is shifted as much as 70-80 cm^{-1} with respect to the position of the monomeric NH_3, while this difference is only 10-30 cm^{-1} for the ν_4 mode. Figure 6.1 in Hagen & Tielens (1982) further illustrates this for a 10 K CO matrix. In addition, more H_2 is expected to be trapped in the growing matrix in the higher H-atom flux experiment, and this will further affect the environment in which NH_3 is isolated.

Finally in Fig. 6.1(d), a RAIR spectrum of NH_3 co-deposited with CO molecules is shown. The total amount of deposited NH_3 is 0.3 ML. This number is about the same as for the N-atom total fluence in each of the three aforementioned experiments. A ratio NH_3:CO = 1:500 is chosen to reproduce the ratio used in Fig. 1b. The total absorbance of deposited NH_3 molecules in Fig. 6.1(d) is about 10% and 40% higher for the ν_4 and ν_2 modes, respectively, compared to the abundances of NH_3 formed by N-atom hydrogenation in the experiments depicted in Figs. 6.1(a) and 6.1(b). Although these differences are within the flux uncertainties, the larger difference in the ν_2 mode is likely due to the higher sensitivity of the ν_2 mode toward its environment.

In general, Figure 6.1 shows that under our experimental conditions the final NH_3 yield is determined by the total amount of available nitrogen atoms at the ice surface, as the integrated area of the ν_4 mode stays near constant in all four plots, while for the ν_2 mode this varies significantly in plot c. The experiments indicate that the hydrogenation of the deposited N atoms is a faster and more efficient process than the hydrogenation of CO ice. Very low activation barriers are therefore expected for reactions (6.1)-(6.3). This is consistent with N-atom hydrogenation experiments in a solid N_2 matrix by Hiraoka *et al.* (1994) and Hidaka *et al.* (2011). Furthermore, these later results of Hidaka *et al.* (2011) are tested under our experimental conditions, *i.e.* co-deposition of N:H:N_2 = 1:20:100 is performed at 15 K, and formation of NH_3 is observed in this experiment.

Finally, we performed a few co-deposition (control) experiments of H- and N-atom beams with H_2O instead of CO (see experiments 2.1 and 2.2 in Table 6.1). A strong broadening of the NH_3 absorbance features due to hydrogen bonds and a considerable overlap of H_2O and NH_3 absorption features do not allow for an unambiguous assignment of NH_3 peaks in these experiments, TPD using QMS does not help to overcome the problem since co-desorbing H_2O gives similar m/z numbers to NH_3 complicating the assignments. Therefore these will not be further discussed in the results section.
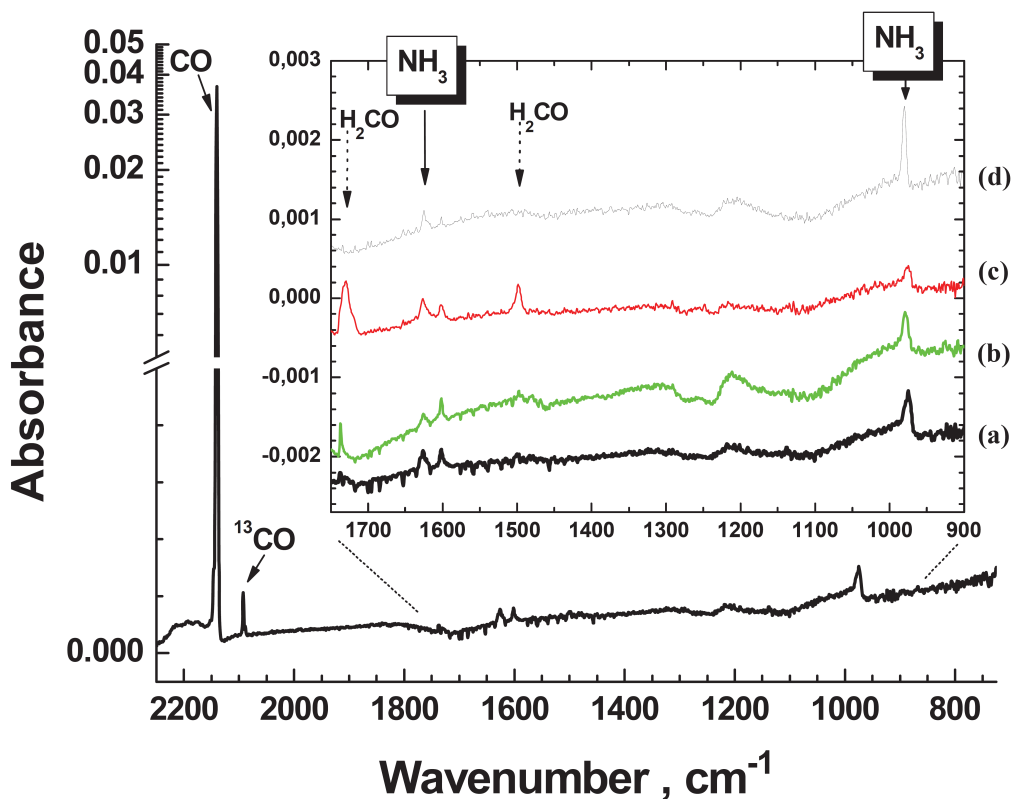
Figure 6.1. A RAIR difference spectrum from a co-deposition of $N:H:N_2:CO = 1:20:100:100$ at 13 K with a total N-atom fluence of $3 \cdot 10^{14}$ (± 40 %) atoms cm^{-2} (experiment 1.1) is shown in the large panel. In the inset four spectra from different co-deposition experiments are shown in a narrower spectral range: (a) is a zoom-in of the aforementioned spectrum; (b) is for a co-deposition of $N:H:N_2:CO = 1:20:100:500$ (experiment 1.3); (c) is for a co-deposition of $N:H:N_2:CO = 1:100:100:100$ (experiment 1.4); and (d) is for the deposition of $NH_3:CO = 1:500$ with a total deposited NH_3 amount of 0.3 ML, corresponding to the N-atom total fluence of the experiments (a)-(c). All spectra are for 13 K and plotted with offsets for clarity.

6.3.2 Temperature dependence

A co-deposition experiment using the same deposition rates discussed before (N:H:N$_2$:CO = 1:100:100:100) is repeated for different substrate temperatures (13 and 25 K) to study the temperature effect on the N-atom hydrogenation in CO-rich ices. The temperatures chosen are below desorption values of N$_2$, N, and CO molecules (Acharyya *et al*. 2007). The goal of these experiments is to determine which mechanism is responsible for the formation of NH$_3$ in a CO rich environment, *i.e.*, Langmuir-Hinshelwood (L-H) or Eley-Rideal (E-R) or "hot-atom" mechanisms. Since both E-R and "hot-atom" mechanisms exhibit very limited sample temperature dependency over the short range of temperatures, one can expect to find similar NH$_3$ final yields in both experiments**.** Since the E-R mechanism is temperature independent, one can expect to find similar NH$_3$ final yields in both experiments. This kind of dependency is found for example for NO + N co-deposition experiments (Ioppolo *et al*. 2013). In the case that L-H is responsible for the formation of ammonia, then the resulting NH$_3$ formation rate is a rather complex combination of many individual processes that are temperature dependent (*i.e.*, lifetime of H atoms on the surface, hopping rate of H and N atoms, and H-atom recombination rate). In this case, the NH$_3$ yield should drop significantly at 25 K due to the shorter residence time of H atoms on the ice surface. For instance, the lifetime of H atoms on a water ice surface at 25 K is more than 1000 times shorter than at 13 K (Cuppen & Herbst 2007). A decrease of H$_2$CO and CH$_3$OH formation yields with increasing temperature was observed by Watanabe *et al*. (2006) and Fuchs *et al*. (2009) in CO hydrogenation experiments, and this observation was explained assuming a L-H formation mechanism. Figure 4 of Fedoseev et al. 2014 where substantial drops in the amount of ammonia formed is observed between 15 and 17 K under similar experimental conditions further constrain the proposed L-H mechanism.

The two spectra in Fig. 6.2 show that neither H$_2$CO nor NH$_3$ are detected at 25 K by means of RAIRS. This is fully consistent with surface processes following a L-H mechanism, as suggested in previous work that focused on the hydrogenation of N atoms trapped in a N$_2$ matrix (Hidaka *et al*. 2011).
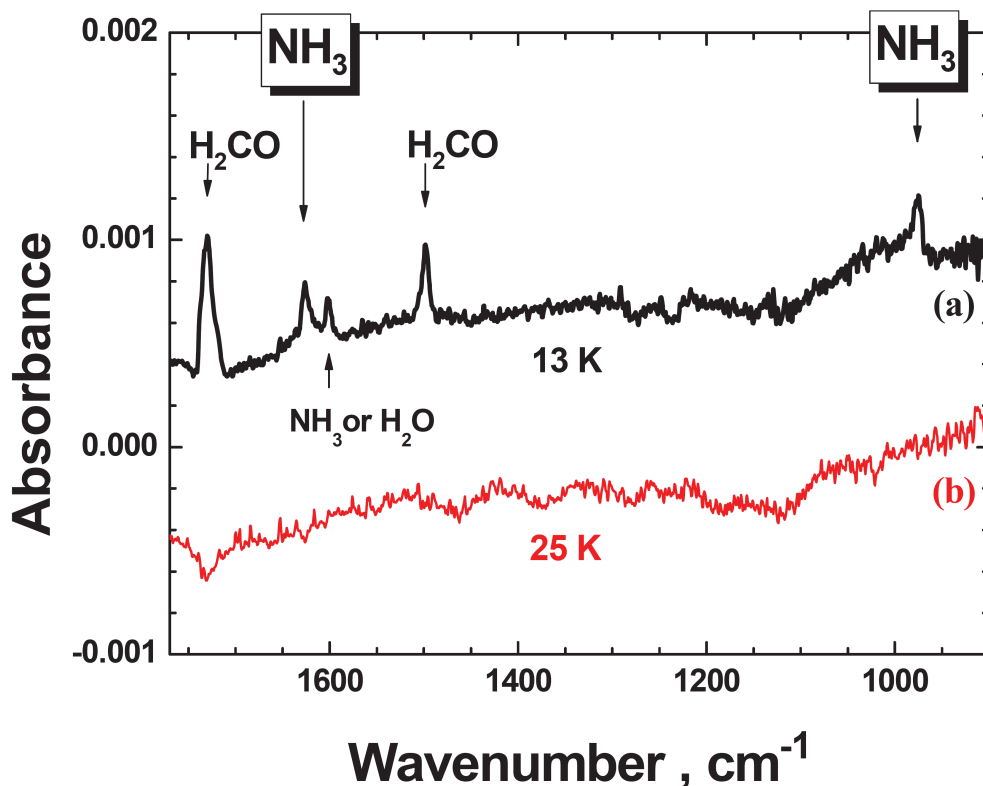
Figure 6.2. Two RAIRs difference spectra of the same co-deposition experiment N:H:N_2:CO = 1:100:100:100 with the same total N-atom fluence of $3 \cdot 10^{14}$ (± 40 %) atoms cm^{-2} at 13 K (a) and 25 K (b) (see experiments 1.4 and 1.5). Spectra are plotted with offsets.

6.3.3 Formation of HNCO

The surface formation pathway of ammonia through the sequential hydrogenation of N atoms leads to the formation of NH and NH_2 intermediates that also can react with other species in the ice to form different molecules. One obvious candidate in a CO surrounding is HNCO formed through surface reactions (6.4) and (6.5). In the experiments shown in Figures 6.1 and 6.2, each NH and NH_2 intermediate will face at least one neighbouring CO molecule as with the chosen co-deposition ratios for deposited N atoms there are one hundred CO and one hundred N_2 molecules. However, in our RAIR spectra, solid HNCO and its hydrogenation products (*e.g.*, NH_2CO and NH_2CHO) cannot be detected. Even sensitive mass spectrometry does not show any clear evidence for the formation of these species (masses 42 – 45 m/z). Thus, reactions (6.4) and (6.5) most likely experience an activation barrier and consequently are overtaken by reactions leading to NH_3 formation. This is consistent with Himmel *et al*. (2002), who indeed suggested the presence of an activation barrier even though some reactivity of NH toward CO at 10 K was found.

Here, a new set of experiments is presented to study the surface formation of HNCO through the reaction of CO molecules with NH and NH_2. The specific goal of these experiments is to prohibit the (fast) formation of ammonia, and to simultaneously increase the probability for NH and NH_2 intermediates to react with CO molecules, overcoming any activation barriers. Such a set of experiments, in fact, is more representative for the actual processes taking place on interstellar grains, where H- and N-atom accretion rates are so low that once NH and NH_2 radicals are formed, these experience a relatively long time to react with other ice molecules (~ several days) before another impacting H atom contributes to the formation of ammonia. Thus, to reproduce this scenario, N atoms are co-deposited with CO molecules with the same rates as described in section 6.3.1, while the H-atom co-deposition rate is substantially decreased (20 times less) to prevent full hydrogenation of N atoms, offering a pathway to the formed NH and NH_2 to react with CO (see experiments 3.1-3.11 in Table 6.1). TPD experiments combined with QMS data are used to study the expected low HNCO final yield.

Three selected N + H + CO co-deposition experiments are presented in Fig. 6.3. After co-deposition of CO molecules with H and N atoms with a given ratio at 13 K, the ice is gently and linearly warmed up to 50 K with a rate of 2 K/min to remove the bulk of the CO ice. A rate of 5 K/min is used during the second part of the TPD (up to 225 K) in order to have a higher peak-to-noise ratio of the selected masses in the mass spectrometer. The correlation between the NH_3 and HNCO final yields for different H-atom co-deposition ratios is investigated by integrating the corresponding area of the selected species from their QMS mass signal over time (*i.e.*, m/z = 17 for NH_3, and m/z = 42, 43 for HNCO). Figure 6.3 shows the decrease of the NH_3 formation yield (peak centred at 120 K), and the corresponding gradual increase of the HNCO formation yield (peak centred at 185 K) that follows the decrease of H-atom co-deposition ratio from $N:H:N_2:CO$ = 1:20:100:100 to $N:H:N_2:CO$ = 1:2:100:100. In the first experiment, only traces of HNCO are detected by the QMS, while the NH_3 signal is maximum. In the third experiment, with a 10 times smaller H flux, the HNCO final yield is maximum while only traces of NH_3 are present. The intermediate case, corresponding to a co-deposition ratio of $N:H:N_2:CO$ = 1:6:100:100 results in the presence of both NH_3 and HNCO molecules.

HNCO can be assigned in the TPD experiments to the desorbing species peaked at 185 K by looking at the electron ionization fragmentation pattern (see Bogan & Hand 1971, Fischer *et al*. 2002). The inset in Figure 6.3 compares the ratio between m/z = 43, 42, and 15 (*i.e.*, $HNCO^+$, NCO^+, HN^+) in our experiment and literature values.

To further constrain this assignment, similar experiments are performed with H atoms co-deposited with $^{14/15}N$ atoms and ^{13}CO molecules (see experiments 4.1-4.3 in Table 6.1). In both cases (^{14}N and ^{15}N), a consistent isotopic shift of both peaks at m/z = 42 and 43 is observed, while the ratio between these two peaks stays constant.

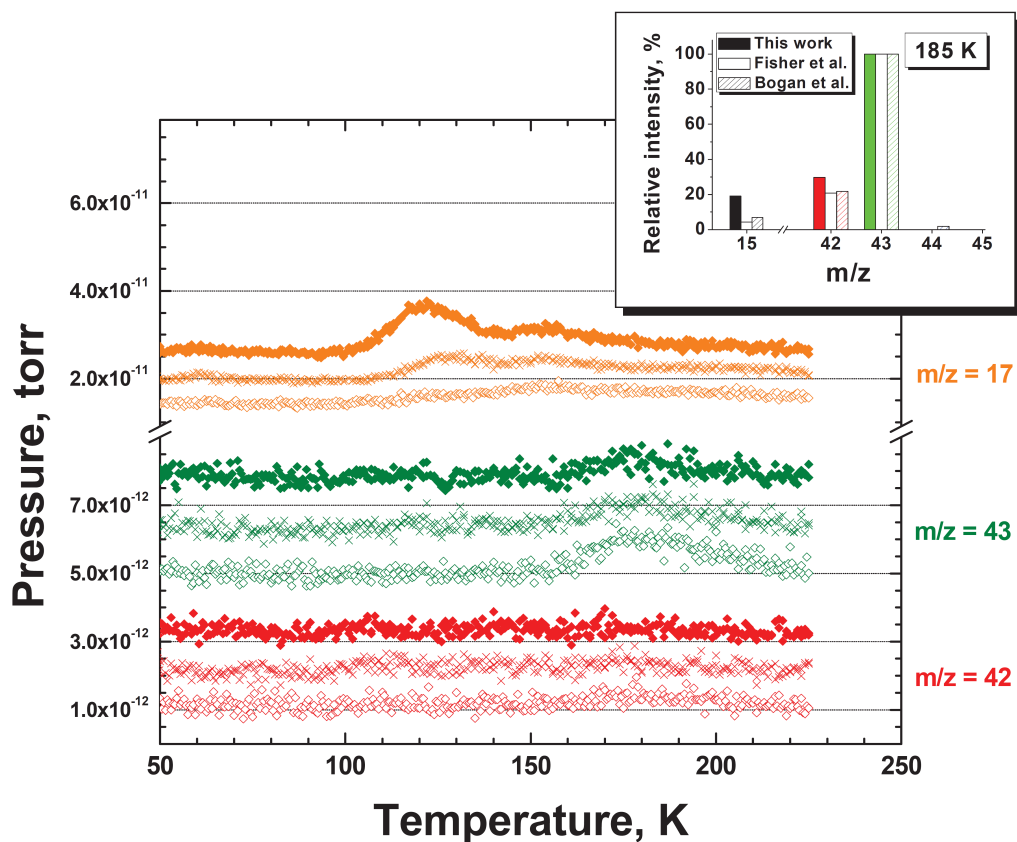**Figure 6.3.** The TPD spectra for three different experiments: co-deposition of $N:H:N_2:CO = 1:20:100:100$ at 13 K (filled diamonds); co-deposition of $N:H:N_2:CO = 1:6:100:100$ at 13 K (x-crosses); and co-deposition of $N:H:N_2:CO = 1:2:100:100$ at 13 K (empty diamonds), see experiments 3.1, 3.2, and 3.5 in Table 6.1, respectively. The total N-atom fluence in each of the three experiments is $4.5 \cdot 10^{14} \pm 40\%$ atom cm^{-2}. Peaks at $m/z = 17$ are due to NH_3 (centered at 120 K) and background H_2O (centered at 155 K), $m/z = 42$ and 43 (middle and lower panel) are the two most intense signals from HNCO. Plots are shown with offsets. In the top right corner, an inset is shown with the relative intensities for $m/z = 15$, 42, and 43 (HNCO), as derived in this study and compared to the available literature.

Pure HNCO is known to desorb slightly above 120 K (Theule *et al.* 2011). However, as shown in Figure 6.3, a much higher desorption temperature is found in our experiments. Upon desorption of the bulk of CO ice, HNCO may form ammonium isocyanate ($NH_4^+OCN^-$) or hydronium isocyanate ($H_3O^+OCN^-$) in presence of NH_3 or H_2O, respectively (reactions (6.6) and (6.7)). This indeed shifts the desorption temperature of HNCO to higher values. Reactions (6.6) and (6.7) can take place during the thermal processing of mixed $NH_3:HNCO$ and $H_2O:HNCO$ ices and have been extensively studied by Raunier *et al.* (2003) and Theule *et al.* (2011), respectively. Under our experimental

conditions, both NH_3 and H_2O are present in the ice sample during the TPD: *i.e.*, NH_3 is a product of N-atom hydrogenation, and H_2O originates from background deposition (see the second peak around 155 K for m/z = 17 (OH^+) in Fig. 6.3). In addition, the low final yield of HNCO (< 1 ML) indicates that this molecule likely occupies the surface spots with the highest binding energy. This further shifts the desorption temperature to higher values. Unfortunately the presence of the background water in the main chamber of our UHV setup gives both m/z = 18 (H_2O^+) and m/z = 17 (OH^+), furthermore CO that is present in the main chamber after co-deposition gives m/z = 16 signal (O^+). As a consequence unambiguous assignment of the base counter parting HNCO acid is not possible. Finally, it should be noted that both NH_2CHO (formamide) and $(NH_2)_2CO$ (urea), two possible chemical derivatives of HNCO and $NH_4^+NCO^-$, respectively, cannot be observed under our experimental conditions and must be under the detection limit of both QMS and RAIRS.

6.3.3.1 Control Experiments

We performed several control experiments to constrain the formation of HNCO and OCN^- at low temperatures by using RAIRS and QMS techniques during TPD experiments (see experiments 3.3 and 4.2 in Table 6.1). RAIR spectra can only be used to identify new species formed in the ice when their final yield is > 0.1 ML. To enhance the RAIR signal for species like HNCO and OCN^-, we performed co-deposition experiments two times longer (experiment 3.3) and four times longer (experiment 4.2) than the corresponding experiments shown in Fig. 6.3. Unfortunately, the main infrared absorption band of HNCO at 2260 cm^{-1} (Teles *et al.* 1989) lies too close to the absorption features of atmospheric CO_2 that is present along the path of our IR beam, outside the UHV chamber. In addition, CO infrared features overlap with the strongest OCN^- band (van Broekhuizen *et al.* 2005), making OCN^- detectable only after desorption of the bulk of CO ice. Therefore, a co-deposition experiment with ^{13}CO (experiment 4.2) is shown in Fig. 6.4. In this figure, some infrared spectra acquired at different temperatures during TPD are presented in two selected spectral regions. The left panel covers the spectral range where $HN^{13}CO$ should be observed (Teles *et al.* 1989), while the right panel shows the range where $O^{13}CN^-$ is expected. Solid $HN^{13}CO$ can only be observed at 13 K, while $O^{13}CN^-$ is clearly present in the spectra taken at 35 and 50 K, well before desorption at 185 K. Thus, the present results support the hypothesis that $HN^{13}CO$ is formed already at 13 K, during co-deposition, and as soon as ^{13}CO desorbs, $HN^{13}CO$ reacts with NH_3 or H_2O to yield $NH_4^+O^{13}CN^-$ and $H_3O^+O^{13}CN^-$, respectively. Formation of OCN^- is also observed upon desorption of the bulk of the ice in experiment 3.3 using regular ^{12}CO isomers.
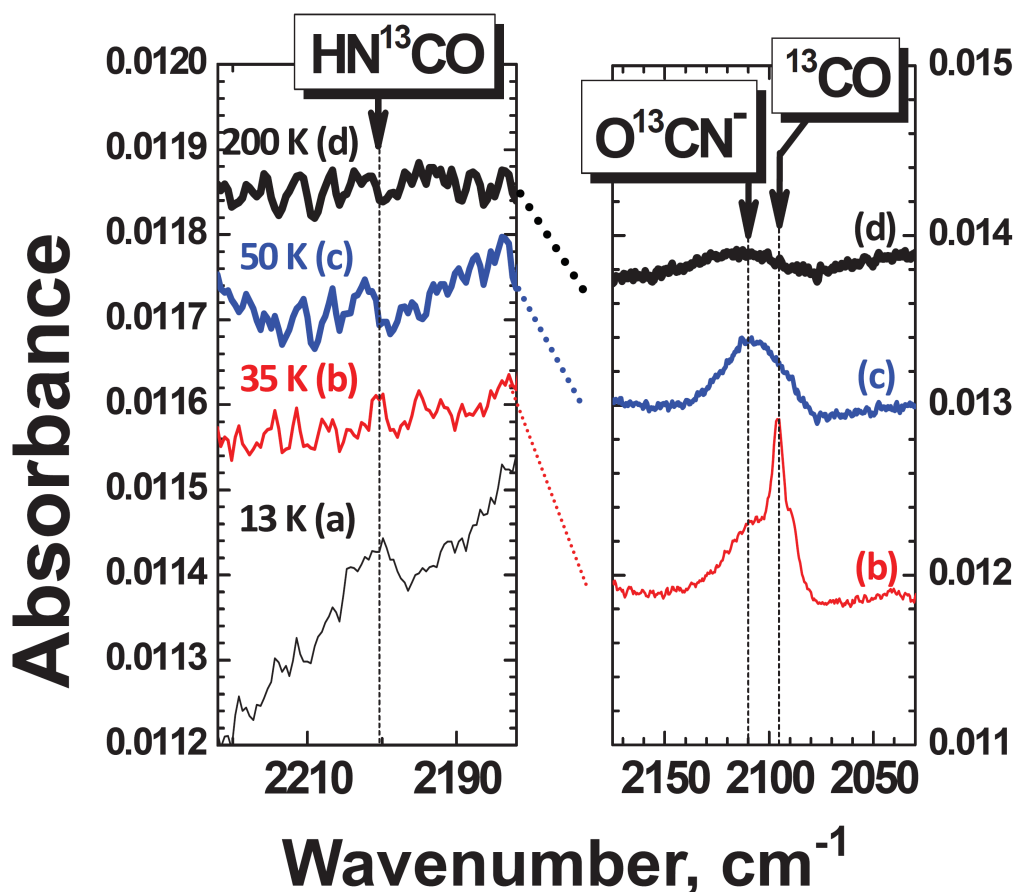
Figure 6.4. Four RAIR difference spectra obtained after co-deposition of $N:H:N_2:^{13}CO = 1:2:100:100$ at 13 K followed by a TPD of the ice (experiment 4.2): a) 13 K b) 35 K c) 50 K and d) 200 K. The left panel shows the strongest absorption feature of $HN^{13}CO$ in the mid-IR; the right panel shows the strongest absorption feature of $O^{13}CN^-$. The total N-atom fluence is $1.8 \cdot 10^{15}$ atoms cm^{-2} ($\pm$ 40%). In the right panel, the 13 K plot is not shown because of the very high absorption of bulk ^{13}CO. Some non-desorbed ^{13}CO is still present in the plot at 35 K.

Below, additional arguments are discussed that are in favour of the HNCO formation through the interaction of NH/NH_2 with CO molecules: (*i*) the co-deposition experiment that yields HNCO at 13 K is repeated for 25 K where it does not result in a QMS detection of HNCO or NH_3 (experiments 3.10 and 3.11). This indicates that the involved formation mechanism for both species depends on the H-atom life-time on the ice surface that is known to decrease substantially for increasing co-deposition temperature; (*ii*) a two times longer co-deposition time is applied for identical settings and leads to a two times larger HNCO area on the QMS TPD spectra (experiment 3.7); (*iii*) neither HNNH nor H_2NNH_2 are observed (within our detection limits) but but are expected to show up during TPD in

the case that non-reacted NH and NH_2 become mobile after the bulk of the ice has desorbed.

To further verify the reactivity of NH/NH_2 radicals with CO molecules, we performed another set of RAIRS experiments (see experiments 5.1-5.4): a co-deposition of CO molecules with fragmentation products formed by discharging NH_3 in the microwave plasma for different experimental conditions. The microwave discharge of ammonia results in the beam containing various products of plasma dissociation (*i.e.*, along with the non-dissociated NH_3 molecules, the beam can contain NH and NH_2 radicals, H and N atoms as well as H_2 and N_2 molecules). The presence of NH and NH_2 radicals is confirmed by co-depositing the products of NH_3 plasma dissociation with an overabundance of D atoms under the same experimental conditions as in experiments 5.1-5.4. In this case, two broad features are observed in the N-D stretching vibrational mode region (2438 and 2508 cm^{-1}, respectively) together with the absorption features due to non-dissociated NH_3. This indicates that at least part of the NH_3 is decomposed into NH and NH_2 radicals and N atoms that then react with D atoms to form the observed N-D bonds.

The QMS TPD spectra obtained after co-deposition of CO molecules with NH_3 plasma dissociation products at 13 K results again in a mass peak at m/z=43 for 185 K that can be assigned to HNCO according to the electron ionisation fragmentation pattern (see filled diamonds in the main panel and the inset in Fig. 6.5). Additionally, the empty diamonds in Fig. 6.5 represent a TPD spectrum after co-deposition of unprocessed NH_3 and CO that proves that the formed HNCO is not the result of thermal processing of mixed NH_3:CO ice. Cross symbols in Fig. 6.5 represent data from the experiment where CO molecules are co-deposited with NH_3 plasma dissociation products at a substrate temperature of 70 K, well above the CO desorption temperature (peaked at 29 K, Acharyya *et al.* 2007). This experiment confirms that the formed HNCO does not originate from gas-phase reactions or contaminations in the microwave plasma source and that the presence of CO on the surface is a prerequisite to form HNCO. All the aforementioned experiments are performed by using the same procedure: first the ice is warmed up with a 2 K/min rate from 13 to 50 K to remove the bulk of CO ice; then a rate of 5 K/min is used from 50 K to 225 K. A control experiment is performed with a different isotope (experiment 5.4); when NH_3 plasma dissociation products are co-deposited with ^{13}CO, m/z values of 43 and amu present a clear feature at 185 K, the ratio 44/43 is 0.27, while m/z=42 is not found.
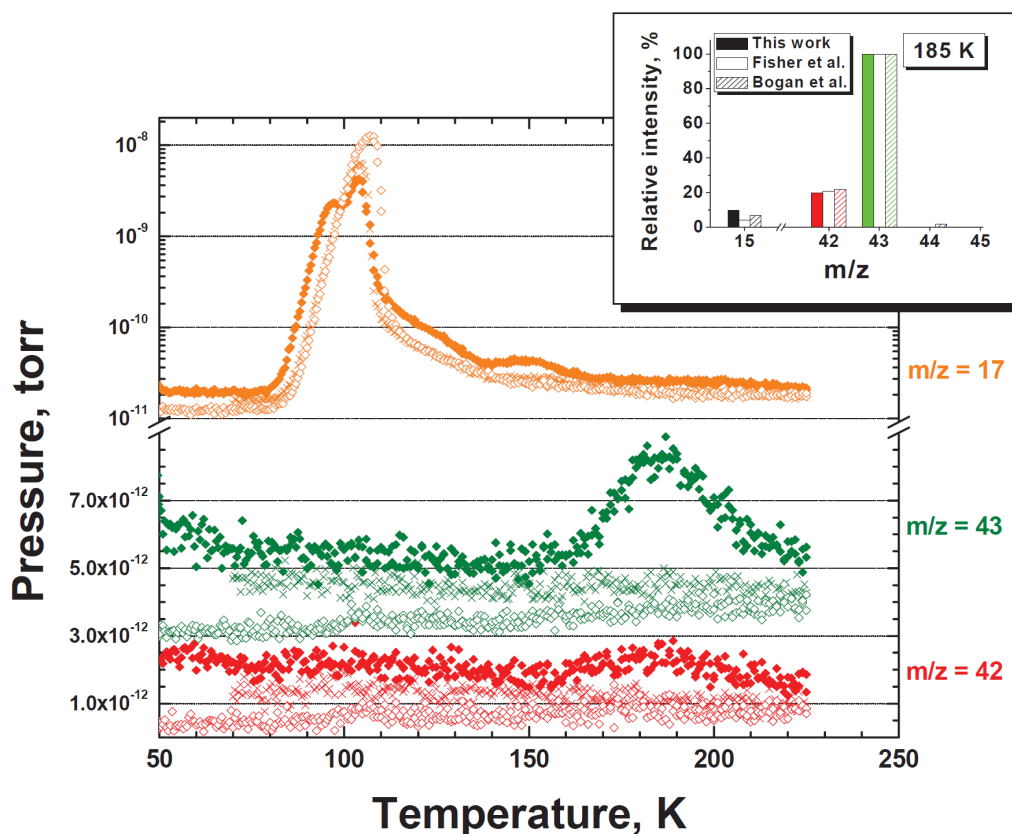
Figure 6.5. The TPD spectra of three distinct experiments: co-deposition of NH_3 plasma fragments with CO at 13K (filled diamonds); co-deposition of NH_3 plasma fragments with CO at 70 K (x-crosses); and co-deposition of NH_3 and CO at 13 K when the microwave discharge is turned off (empty diamonds), see experiments 5.1, 5.3, and 5.2, respectively. Three m/z values are selected: masses 42 and 43 are the two most intense signals from HNCO, while 17 comes from NH_3. Plots are shown with offsets for clarity. In the top right corner, the inset compares the relative intensities of the masses assigned in this study to HNCO and the available literature values.

6.3.3.2 HNCO Formation Pathway

Although our experimental data do not allow us to derive values for activation barriers for the reactions (6.4) or (6.5), some important conclusions can be drawn**.** As we mentioned before, reaction (6.5) is endothermic (~4800 K) and therefore unlikely to proceed for non-energetic processing at 13 K. The excess energy of the reactions (6.1) and (6.2) does not help to overcome the barrier, because in this case we would observe the formation of HNCO independently from the co-deposition ratio used. Moreover, we would expect a higher HNCO yield for the experiment with a higher H-atom flux over experiments where

this flux is insufficient to hydrogenate all N atoms. And this is in contradiction with our experimental observations. Apart from reactions (6.4) and (6.5), the following reactions

$$N + CO \rightarrow NCO, \hspace{4cm} (6.8)$$
$$H + NCO \rightarrow HNCO, \hspace{3.5cm} (6.9)$$
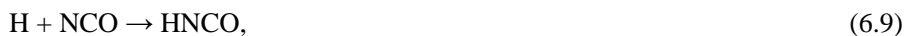
could also lead to the sequential formation of HNCO. However, within our detection limits NCO radicals are not observed after co-deposition of CO molecules with just N atoms. Taking these considerations into account, we conclude that reaction (6.4) is the main pathway for HNCO formation. Since H_2CO is not detected in the experiments where HNCO is formed, we expect that the activation barrier for the formation of HNCO is not much higher than the one proposed for the H + CO. Fuchs *et al*. (2009) and Cuppen *et al*. (2009) used an effective barrier of 435 K to model their observed experimental results on hydrogenation of CO. Such a direct comparison, however, has to be treated with care, as different settings and laboratory conditions have been used and both mobility and life-time of NH and H differ significantly from each other.

As mentioned in section 6.3.3 NH_2CHO (the product of sequential HNCO hydrogenation) is not observed in any of our experiments. This is not surprising since H-atom addition to HNCO involves an activation barrier. Nguyen *et al*. (1996) used *ab initio* calculations to study the reaction of H atoms with isocyanic acid and an activation barrier of 1390 K was found for H-atom addition to the nitrogen atom of HNCO. This makes the formation of NH_2CHO unlikely under our experimental conditions, since it would imply a second consequent reaction involving an activation barrier, while the lack of H atoms is used in the experiments resulting in HNCO formation.

6.4 Astrochemical implications

This laboratory work is motivated by several of the main conclusions of the ISO and *Spitzer* c2d Legacy ice survey (Gibb *et al*. 2004, Öberg *et al*. 2011). The evolutionary steps of interstellar ice formation can be divided into three main stages: an early phase, driven by fast H-atom addition reactions in cold molecular clouds, before cloud core formation; a later CO freeze-out stage, when chemistry in the ices is driven by accreting CO molecules to a large extent; and the protostellar phase, where thermal and UV processing shape the ice content.

During the first stage, a H_2O-rich (polar) ice is formed. In this phase, the relative abundances of CO_2 (in H_2O), CH_4, and NH_3 correlate with H_2O ice suggesting their co-formation. This indicates that most of the solid NH_3 is formed during an early evolutionary stage. Our laboratory experiments are designed to study the non-energetic

surface formation of NH_3 through the hydrogenation of N atoms under cold dense cloud conditions. These conditions aproximatelly resemble the first stage of interstellar ice formation. We therefore performed some experiments co-depositing H and N atoms with water, but the spectral confusion due to the overlap of features from H_2O and NH_3, as well as the strong broadening of the NH_3 absorption bands in a polar ice made an unambiguous assignment of NH_3 ice formation far from trivial. Therefore, this work mostly focuses on the investigation of the NH_3 formation in non-polar mixtures containing CO ice. This way, newly formed NH_3 can be easily identified, because ammonia features are sharper and do not overlap with features of other species in the ice. Although CO-rich ices better represent the second phase of interstellar ices, when CO molecules freeze-out onto the grains, some of our conclusions on the surface formation of ammonia in CO-rich ice can also be partially extended to the formation of NH_3 in H_2O-rich ice. For instance, we find that the formation of NH_3 by hydrogenation of N atoms proceeds barrierless or through a very small activation barrier at 13 K. Moreover, in agreement with previous works, we confirm a Langmuir-Hinshelwood mechanism as the main channel for the formation of solid NH_3 (Hiraoka *et al.* 1995 and Hidaka *et al.* 2011). Our experimental results further constrain the findings described in Charnley *et al.* (2001), where the accretion of gas-phase ammonia in their model results in a solid NH_3/H_2O ratio of only ~2%, which is less than the observed values of 5% (Gibb *et al.* 2004, Bottinelli *et al.* 2010, Öberg *et al.* 2011). However, the amount of NH_3 ice on the grains could be higher assuming that N atoms also accrete onto grains and undergo hydrogenation. If this surface formation route of ammonia is included in the Charnley *et al.* (2001) model, the solid NH_3/H_2O ratio becomes ~10%, which is even above the observed value. Moreover, recent models that account for the formation of NH_3 in the solid phase through hydrogenation of N atoms indicate a NH_3/H_2O ratio as high as 25% (Garrod & Pauly 2011 and Vasyunin & Herbst 2013).

Our experimental results can explain why recent astrochemical models overestimate the surface production of NH_3. We observe an efficient formation of HNCO ice in H+N+CO experiments. Solid HNCO is a product of the interaction between CO molecules and intermediates involved in the surface formation of NH_3. In this scenario, NH_3 ice is formed efficiently in a polar ice together with water during the first phase of interstellar ices. However, as soon as densities are high enough for CO to freeze-out onto the grains, the formation of NH_3 competes with the formation of HNCO in a non-polar ice. Our experiments reveal that the formation of NH_3 in CO-rich ices is only efficient when the H-atom deposition rate is high enough to quickly hydrogenate all the N atoms to NH_3 which can only occur on rather fast laboratory time-scales. If a slower H-atom deposition rate is used to simulate the slow accretion rate observed in the ISM as much as possible, the formation of NH_3 is suppressed in favour of the formation of HNCO. In this case, formed NH or NH_2 radicals have significantly more time to overcome the activation barrier of the

reaction with the surrounding CO molecules before the next H atom arrives and eventually converts it to NH_3. In space, the extremely low accretion rate of H atoms on the surface of the icy grains (unfortunately, not reproducible in the laboratory) gives days to each of the intermediates to overcome activation barriers and to react with the surrounding molecules (*i.e.*, CO ice), before the next hydrogenation event occurs. This potentially explains the observed low ammonia abundances in non-polar ices and, at the same time, shows that solid HNCO is formed in molecular clouds.

Interstellar HNCO was first detected in the Sgr B2 molecular cloud complex by Snyder & Buhl 1972. Since its discovery, HNCO has been detected in different environments, as diverse as dark molecular clouds and hot cores in massive star-forming regions. Li *et al.* 2013 studied the spatial distribution of HNCO in massive YSOs that is consistent with a "hot" gas-phase formation route. In cold dark molecular clouds, however, HNCO is expected to be efficiently formed in the solid phase. Quan *et al.* (2010) were able to reproduce the observed gas-phase abundances of HNCO and its isomers in cold and warm environments using gas-grain simulations, which include both gas-phase and grain-surface routes. Our work shows that HNCO is efficiently formed under dense cold cloud conditions, *i.e.*, in non-polar ices with a reaction pathway that is linked to the formation of ammonia ice and does not require any energetic input, such as UV light or cosmic ray irradiation. Although our work indicates that HNCO should be detectable in CO-rich ices through its anti-symmetric stretch mode at ~2250 cm^{-1}, this is not the case; the non-detection of solid HNCO in the ISM can be explained by efficient destruction pathways that include the hydrogenation of HNCO as well as thermal reactions with solid ammonia at temperatures slightly higher than its formation temperature. The latter mechanism is supported by a combined laboratory and modelling study that derives a low (48 K) activation energy barrier for reaction (6.6) to occur (Mispelaer *et al.* 2012).

Öberg *et al.* (2011) reported a close correlation between CO, CO_2 (in CO), CO (in H_2O), and the XCN band in support of their co-formation during the CO freeze-out stage as well as the identification of OCN^- as a main carrier of the interstellar XCN band. Our TPD experiments shown in Fig. 6.4 simulate the heating of ice mantles by a newly formed protostar (*i.e.*, the third phase of interstellar ices). This process leads to the formation of $O^{13}CN^-$ detectable from its infrared absorption feature centred at 2202 cm^{-1} (in our experiments we used ^{13}CO instead of the regular ^{12}CO). While NH_3 and $HN^{13}CO$ are formed through non-energetic surface reactions at low temperature, the formation of $O^{13}CN^-$ occurs through the interaction of $HN^{13}CO$ with NH_3 or H_2O molecules at higher temperatures, when highly volatile species leave the ice. Thus, our results further constrain the assignment of either the entire or a single component (2165 cm^{-1}) of the XCN band observed toward numerous YSOs to solid OCN^- and show that OCN^- is successfully

formed in the interstellar ices without any UV or cosmic ray processing involved (see Gibb *et al*. 2004, Bottinelli *et al*. 2010, Öberg *et al*. 2011).

The presence of HNCO and OCN⁻ in interstellar ices during the protostellar phase may be very important for astrobiology. The recent detection of amino acids in comets has boosted efforts to investigate the astrochemical origin of species such as glycine and alanine (Elsila *et al*. 2009). Since gas-phase routes to form these complex species seem to be inefficient, solid-phase formation pathways offer a strong alternative (Barrientos *et al*. 2012). During protostar formation, interstellar grains are exposed to thermal, UV, electron, and ion processing that can drastically modify the composition of the icy mantles. Especially in the case of cosmic ray irradiation, the energy released by the ions passing through a material causes the dissociation of hundreds of molecules along their path. These fragments can then recombine forming new and more complex species. Eventually, a complex polymeric refractory residue can be formed. As shown in Figure 6.6, HNCO molecules are included as a peptide bond [-(H)N-C(O)-] between any two single amino acid. Moreover, even the simplest peptide, polyglycine, contains nothing but HNCO and CH_2 components. Therefore, energetic processing (*e.g.*, UV photolysis and cosmic ray irradiation) of $HNCO:CH_4$ and $HNCO:CH_4:CH_3OH$-rich ices can be a possible pathway to form amino acids or peptide fragments. If OCN⁻ is used in the aforementioned mixtures instead of HNCO, amino acid anions and their fragments can be formed as well. Such experiments will be the focus of a future laboratory study aimed to investigate the formation of the simplest amino acids and peptide fragments, but for now, it is important to conclude that convincing solid state pathways are found that explain the effective formation of the elementary precursor species.
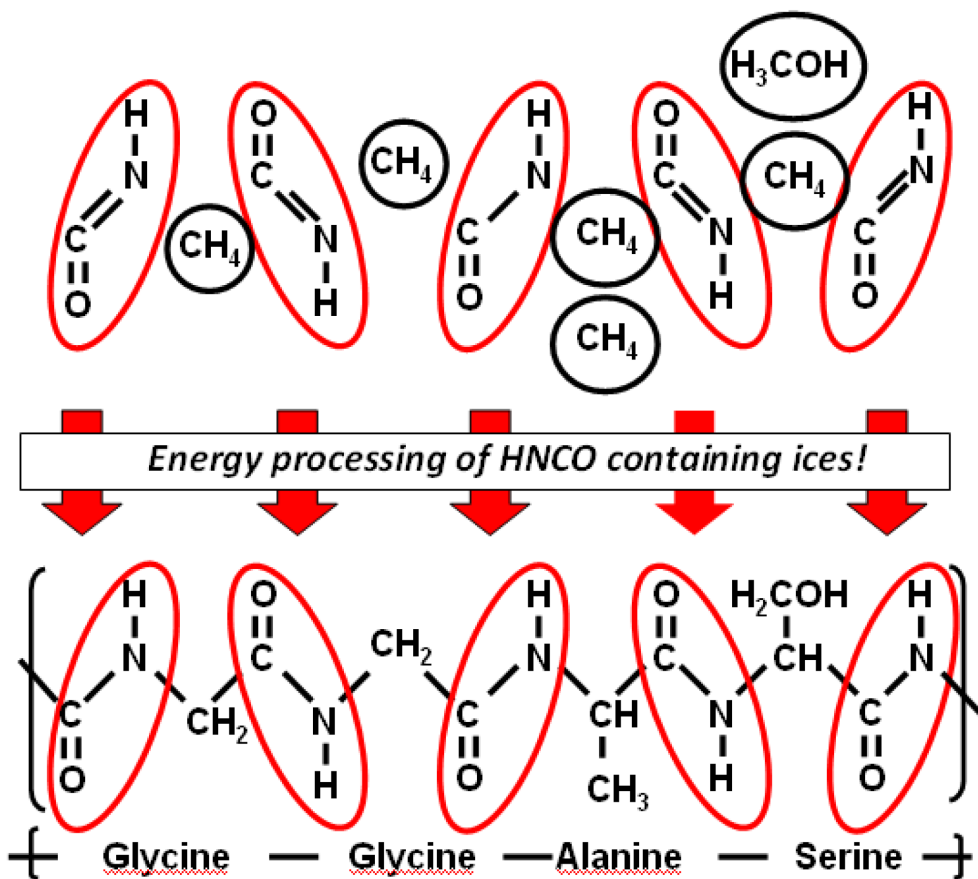
Figure 6.6. A schematic that illustrates the potential importance of HNCO as a simple bearer of peptide bonds for the production of amino acids in interstellar ices.

References

Abouaf-Marguin L., Jacox M. E., Milligan D. E., 1977, J. Mol. Spectrosc., 67, 34

Acharyya K., Fuchs G. W., Fraser H. J., van Dishoeck E. F., Linnartz H., 2007, A&A, 466, 1005

Anton R., Wiegner T., Naumann W., Liebmann M., Klein Chr., Bradley C., 2000, RSI, 71, 1177

Barrientos C., Redondo P., Largo L., Rayón V. M., Largo A., 2012, ApJ, 748, 99

Bogan D.J., Hand C.W., 1971, JPC, 75, 1532

Boogert A. C. A. *et al*., 2008, ApJ, 678, 985

Bottinelli S. *et al*., 2010, ApJ, 718, 1100

van Broekhuizen F. A., Pontoppidan K. M., Fraser H. J., van Dishoeck E. F., 2005, A&A, 441, 249

Charnley S. B., Rodgers S. D., Ehrenfreund P., 2001, A&A, 378, 1024

Congiu E. *et al*., 2012a, ApJL, 750, L12

Congiu E., Chaabouni H., Laffon C., Parent P., Baouche S., Dulieu F., 2012b, JCP, 137, 054713

Cuppen H. M., Herbst E., 2007, ApJ, 668, 294

Cuppen H. M., van Dishoeck E. F., Herbst E., Tielens A. G. G. M., 2009, A&A, 508, 275

Demyk K., Dartois E., D'Hendecourt L., Jourdain de Muizon M., Heras A. M., Breitfellner M., 1998, A&A, 339, 553

Elsila J. E., Glavin D. P., Dworkin J. P., 2009, MAPS, 44, 1323

Fedoseev G., Ioppolo S., Lamberts T., Zhen J. F., Cuppen H. M., Linnartz H., 2012, JCP, 137, 054714

Fedoseev G., Ioppolo S., Linnartz H., 2014, MNRAS, in press, article doi: 10.1093/mnras/stu1852

Fischer G., Geith J., Klapötke T. M., Krumm B., 2002, Z. Naturforschung, 57b, 19

Fuchs G. W., Cuppen H. M., Ioppolo S., Bisschop S. E., Andersson S., van Dishoeck E. F., Linnartz H., 2009, A&A, 505, 629

Gálvez O., Maté B., Herrero V. J., Escribano R., 2010, ApJ, 724, 539

Garrod R.T., Pauly T., 2011, ApJ, 735, 15

Garrod R.T., 2013, ApJ, 765, 60

Gibb E. L., Whittet D. C. B., Boogert A. C. A., Tielens A. G. G. M., 2004, ApJS, 151, 35

Hagen W., Tielens A. G. G. M., 1982, Spectrochim. Acta, Part A, 38, 1203

Herbst E., Klemperer W., 1973, ApJ, 185, 505

Hidaka H., Watanabe M., Kouchi A., Watanabe N., 2011, PCCP, 13, 15798

Himmel H.-J., Junker M., Schnöckel H., 2002, JCP, 117, 3321

Hiraoka K., Ohashi N., Kihara Y., Yamamoto K., Sato T., Yamashita A., 1994, Chem. Phys. Lett., 229, 408

Hiraoka K., Yamashita A., Yachi Y., Aruga K., Sato T., Muto H., 1995, ApJ, 443, 363

Ioppolo S., Fedoseev G., Lamberts T., Romanzin C., Linnartz H., 2013, RSI., 84, 073112

Ioppolo S., Fedoseev G., Minissale M., Congiu E., Dulieu F., Linnartz H., 2014, PCCP, 16, 8270

Koops T., Visser T., Smit W. M. A., 1983, J. Mol. Struct., 96, 203

Li J., Wang J. Z., Gu Q. S., Zheng X. W., 2013, A&A, 555, A18

Minissale M., Fedoseev G., Congiu E., Ioppolo S., Dulieu F., Linnartz H., 2014, PCCP, 16, 8257

Mispelaer F., Theule P., Duvernay F., Roubin P., Chiavassa T., 2012, A&A, 540, A40

Nelander B., 1984, Chem. Phys., 87, 283

Nguyen M. T., Sengupta D., Vereecken L., Peeters J., Vanquickenborne L. G., 1996, J. Phys. Chem., 100, 1615

Öberg K. I. *et al*., 2011, ApJ, 740, 109

Quan D., Herbst E., Osamura Y., Roueff E., 2010, ApJ, 725, 2101

Raunier S., Chiavassa T., Marinelli F., Allouche A., Aycard J. P., 2003, Chem. Phys. Lett., 368, 594

Scott G. B. I., Fairly D. A., Freeman C. G., Mcewan M. J., 1997 Chem. Phys. Lett., 269, 88

Snyder L. E., Buhl D., 1972, ApJ, 177, 619

Teles J. H., Maier G., Hess B. A., Jr., Schaad L. J., Winnewisser M., Winnewisser B. P., 1989, Chem. Ber. 122, 753

Theule P., Duvernay F., Ilmane A., Hasegawa T., Morata O., Coussan S., Danger G., Chiavassa T., 2011, A&A, 530, A96

Tschersich K. G., 2000, J. Applied Phys., 87, 2565

Vasyunin A. I., Herbst E., 2013, ApJ, 762, 86

Watanabe N., Kouchi A., 2002, ApJ, 571, L173

Watanabe N., Nagaoka A., Hidaka H., Shiraki T., Chigai T., Kouchi A., 2006, Planet. Space Sci., 54, 1107

Woon D. E., 2002, ApJ, 569, 541

Zhitnikov R. A., Dmitriev Yu. A., 2002, A&A, 386, 1129

VII

Deuterium Enrichment of Ammonia Produced by
Surface N+H/D Addition Reactions
at Low Temperature

The surface formation of NH_3 and its deuterated isotopologues - NH_2D, NHD_2, and ND_3 - is investigated at low temperatures through the simultaneous addition of hydrogen and deuterium atoms to nitrogen atoms in CO-rich interstellar ice analogues. The formation of all four ammonia isotopologues is only observed up to 15 K, and drops below the detection limit for higher temperatures. Differences between hydrogenation and deuteration yields result in a clear deviation from a statistical distribution in favour of deuterium enriched species. The data analysis suggests that this is due to a higher sticking probability of D atoms to the cold surface, a property that may generally apply to molecules that are formed in low temperature surface reactions. The results found here are used to interpret ammonia deuterium fractionation as observed in pre-protostellar cores.

7.1 Introduction

The characterization of different evolutionary stages of star formation is essential to understand the origin of molecular complexity in space. The ratio of a deuterated species over its counterpart containing H, *i.e.*, the deuterium fractionation, is known to be a good tool to discriminate between different processes taking place along this evolutionary trail. The D/H ratio in the interstellar medium (ISM) is $\sim 1.5 \cdot 10^{-5}$. In cold dense cores ($T \sim$ 10-20 K and $n \sim 10^6$ cm^{-3}), the depletion of C-bearing molecules leads to an enhancement of the deuterium fractionation, because the H_2D^+ ion, the gas-phase progenitor of most of the deuterated species, is not destroyed by CO (*e.g.*, Roberts & Millar 2006, Bacmann *et al.* 2003, Pillai *et al.* 2007). Apart from gas-phase reactions, also grain surface chemistry enhances molecular D/H ratios under cold dense cloud conditions: *e.g.*, *via* low-temperature surface reactions, ion- and photo-dissociation of solid species, and thermally induced exchange reactions on icy grains (*e.g.*, Tielens 1983, Brown & Millar 1989a, 1989b). The idea that such processes lead to deuterium enrichment is usually based on the "zero-point energy argument", *i.e.*, the assumption that species with D atoms have a lower zero-energy and, therefore, are more stable and more likely to be formed over their H-atom counterparts at low temperatures (10-20 K). Moreover, if processes are recurrent in space, then deuterium enrichment can be further enhanced over a number of cycles (Tielens 1983). During the formation stage of a protostar, the D/H value is found to decrease again because of the strong UV field and shocks in the outflows caused by the newborn star (Crapsi *et al.* 2005, Emprechtinger *et al.* 2009). Also much later, during the planetary stage, D/H ratios are important. Recent observations with the *Herschel* Space Observatory have revealed that although the D/H mean value in Oort-cloud comets is $\leq 3 \cdot 10^{-4}$, the D/H ratio in Jupiter-family comets is very close to the Vienna standard mean ocean water (VSMOW) value of $\sim 1.5 \cdot 10^{-4}$. This result seems to suggest that a significant delivery of cometary water to the Earth-Moon system occurred shortly after the Moon-forming impact (Hartogh *et al.* 2011, Bockelée-Morvan *et al.* 2012, Lis *et al.* 2013). In this scenario, also other complex prebiotic species may have been delivered to Earth following the same route of water molecules.

To date, a conspicuous number of molecules detected in the ISM, including methanol, water and ammonia exhibit deuterium enrichment. Laboratory experiments show that all these species are formed on the surface of icy dust grains mostly through hydrogenation reactions at low temperatures. In particular, the presence of species like H_2CO and CH_3OH (CO+H), NH_3 (N+H), CH_4 (C+H), H_2O (O/O_2/O_3+H), and possibly also NH_2OH (NO+H, NO_2+H) is (largely) explained through sequential H-atom addition to various precursors (*e.g.*, Hiraoka *et al.* 1994, Hiraoka *et al.* 1995, Hiraoka *et al.* 1998, Zhitnikov & Dmitriev 2002, Watanabe & Kouchi 2002, Miyauchi *et al.* 2008, Ioppolo *et al.* 2008, Mokrane *et al.*

2009, Congiu *et al* 2012, Ioppolo *et al* 2014). As a consequence, surface deuteration reactions will be at play as well, contributing with different efficiencies. Indeed, laboratory work shows that different molecules undergo different surface deuterations (Nagaoka at al 2005, Ratajczak *et al* 2009, Hidaka at al 2009, Weber *et al* 2009, Kristensen *et al* 2011). For example, the formation of H_2O/HDO through $OH+H_2/D_2$ and H_2O_2+H/D (Oba *et al* 2012, Oba *et al* 2014) shows a preference for hydrogenation that has been explained by a higher quantum tunneling efficiency. In fact, the different transmission mass involving abstraction/addition of hydrogen atoms over similar reactions with deuterium is assumed to cause higher hydrogenation rates. On the other hand, Nagaoka at al. (2005), Nagaoka (2007), and Hidaka at al. (2009) demonstrated that hydrogen atoms can be abstracted from methanol and its isotopologues and substituted by D atoms upon D-atom exposure of solid CH_3OH, CH_2DOH, and CHD_2OH. However, H-atom exposure of CD_3OH, CD_2HOH, and CDH_2OH does not result in abstraction or substitution of D atoms with H atoms. Therefore, (partially) deuterated methanol is expected to be enriched in space. These examples make clear that a straight forward interpretation of H/D ratios in the ISM is far from trivial. Nevertheless, understanding the mass dependence of all possible processes helps in pinning down the relevant reactions taking place.

The present laboratory work focuses on the competition between hydrogenation and deuteration during the solid state formation of ammonia. It is commonly believed that NH_3 can be formed both in the gas phase - through a series of ion-molecule reactions (see Herbst & Klemperer 1973, Scott *et al*. 1997) - and in the solid state - through three sequential H-atom additions to a single nitrogen atom on the surface of an interstellar ice grain. Gas-phase observations toward 'pre-protostellar cores' show an increased D/H fractionation of NH_3 (Hatchell 2003, Busquet *et al*. 2010). NH_2D and NHD_2 are also detected in the dark cloud L134N and in IRAS 16293E (Rouef *et al*. 2000, Loinard *et al*. 2001). In these sources, the $NH_3:NH_2D:NHD_2$ gas-phase abundances (1:0.1:0.005 and 1:0.07:0.03, respectively) are orders of magnitudes higher than the ratios expected from cosmic D/H abundances. To date, there is no direct astronomical observation of the D/H ratio for ammonia ice, but the astronomical gas-phase data may actually reflect the solid state deuterium enrichment as well. For instance, observations toward the shocked region L1157-B1 provide evidence for a chemical enrichment of the interstellar gas by the release of dust ice mantles and show an indirect upper limit for NH_2D/NH_3 of $3 \cdot 10^{-2}$ (Codella *et al*. 2012).

Recently, several groups studied the surface hydrogenation of N atoms (see Hiraoka *et al*. 1995, Hidaka *et al*. 2011, Fedoseev *et al*. 2014). It is clear that a better understanding of the D/H fractionation mechanism of this process is required to interpret the gas-phase observations of deuterium enriched NH_3. Moreover, both Hidaka *et al*. (2011) and Fedoseev *et al*. (2014) – see the accompanying paper - conclude experimentally that the

formation of NH_3 by hydrogenation of N atoms involves a Langmuir-Hinshelwood (L-H) mechanism. Therefore, key parameters for the formation rates of $NH_3:NH_2D:NHD_2:ND_3$ during hydrogenation/deuteration of N atoms, are the sticking coefficients for H and D atoms, the activation energies needed for surface diffusion and desorption and the reaction barriers for interactions with other species. Thus, the deuterium enrichment of ammonia offers a diagnostic tool to investigate the L-H mechanism. In this paper the astronomical implications and details on the physical-chemical properties of the deuterium enrichment of ammonia are discussed.

7.2 Experimental procedure

7.2.1 Experimental setup

The experiments are performed under ultra-high vacuum (UHV) conditions, using our SURFRESIDE[(2)] setup, first in a one-atom beam, and since 2012 in a double-atom beam configuration. The latter setup allows for the simultaneous use of two atom-beams together with regular molecular dosing lines as described in the accompanying paper. Further details of the original and extended setups are available from Fuchs *et al.* (2009) and Ioppolo *et al.* (2013), respectively.

SURFRESIDE[2] consists of three distinct UHV sections, including a main chamber and two atom-beam line chambers. Shutters separate the beam lines from the main chamber and allow for an independent operation of the individual parts. Two different atom sources are implemented: a Hydrogen Atom Beam Source (HABS, Dr. Eberl MBE-Komponenten GmbH, see Tschersich 2000) that produces H or D atoms through thermal cracking of H_2 or D_2; and a Microwave Atom Source (MWAS, Oxford Scientific Ltd, see Anton *et al.* 2000) that generates H, D, O, and, specifically for this work, N atoms using a microwave discharge (300 W at 2.45 GHz). H_2 (Praxair 5.0), D_2 (Praxair 2.8), and N_2 (Praxair 5.0) are used as precursor gasses. A nose-shaped quartz pipe is placed after each shutter along the path of the atom beam to efficiently quench the excited electronic and ro-vibrational states of the formed atoms and non-dissociated molecules through collisions with the walls of the pipe before they reach the ice sample. The geometry is designed in such a way that this is realized through at least four wall collisions before atoms can leave the pipe. In this way, "hot" species cannot reach the ice. All atom fluxes are in the range between 10^{11} and 10^{13} atoms cm^{-2} s^{-1} at the substrate position. The calibration procedures are described in Ioppolo *et al.* (2013).

In the main chamber, ices are deposited with monolayer precision (where 1 ML = 10^{15} molecules cm^{-2}) at astronomically relevant temperatures (starting from 13 K and upwards) onto a 2.5 x 2.5 cm^2 gold substrate. The substrate is mounted on the tip of a cold head and

full temperature control is realized using a Lakeshore temperature controller. The absolute temperature precision is ~2 K, and the relative precision between two experiments is below 0.5 K. Two additional dosing lines are implemented to allow for a separate deposition of stable molecules. In this way, it becomes possible to co-deposit atoms and molecules and to simulate various molecular environments as typical for different evolutionary stages in interstellar ices: *e.g.*, elementary processes in polar (H_2O-rich) or non-polar (CO-rich) interstellar ice analogues (see Ioppolo *et al*. 2014). Pre-deposited ices can also be studied with this system. Reflection Absorption Infrared Spectroscopy (RAIRS) and Temperature Programmed Desorption (TPD) in combination with a quadrupole mass spectrometer (QMS) are used as analytical tools to characterize the ice composition both spectroscopically and mass spectrometrically. Since NH_3 and ND_3 molecules can participate in thermally induced deuterium exchange reactions, RAIRS is used as main diagnostic tool, complemented with TPD data.

7.2.2 Performed experiments

Two sets of conceptually different (control) experiments are performed. The first set focuses on H/D exchange reactions with pre- and co-deposited NH_3 with D atoms. The second set, which is the core of this work, deals with the isotopic fractionation in sequential H- and D-atom reactions with atomic nitrogen in co-deposition experiments:

- $NH_3 + D$ studies are performed using both pre- and co-deposition experiments. NH_3 (Praxair 3.6) and D_2 are prepared in distinct pre-pumped ($< 10^{-5}$ mbar) all-metal dosing lines. The pre-deposition of NH_3 ice is performed under an angle of 45° and with a controllable rate of 4.5 ML/min on a 15 K gold substrate. During deposition, RAIR difference spectra are acquired every minute with respect to a pre-recorded spectrum of the bare gold substrate. After NH_3 deposition, a new background reference spectrum is acquired, and the pre-deposited NH_3 ice is exposed to a constant flux of D atoms normal to the surface of the sample. RAIR difference spectra are acquired every 10 minutes to monitor the ice composition *in situ*. During the co-deposition experiment, NH_3 and D atoms are deposited simultaneously on the gold substrate with a constant rate. Also here, RAIR difference spectra are acquired every 10 minutes with respect to a spectrum of the bare substrate.

- Significantly more complex from an experimental point of view is the study of H/D fractionation in ammonia isotopologues formed upon co-deposition of hydrogen, deuterium, and nitrogen atoms. This experiment can be performed by co-depositing H and D atoms generated in the HABS with N atoms from the MWAS. A mixed H- and D-atom beam is obtained by thermal cracking a $H_2:D_2=1:1$ gas mixture. The mixture is prepared by filling up two independent pre-pumped ($<10^{-5}$ mbar) parts of the dosing line with a known

volume-to-volume ratio of H_2 and D_2 gasses. The gasses are subsequently allowed to mix in the total volume of the dosing line. The pre-mixed gas is then introduced in the thermal cracking source using a precise leak valve to control the gas flow. In a similar way, a N_2 gas line is used as input for the microwave plasma source. Another pre-pumped ($< 10^{-5}$ mbar) dosing line is used to deposit CO under the same experimental conditions as previously described in the accompanying paper by Fedoseev *et al.* (2014). As explained there the addition of CO simulates a more realistic interstellar ice environment. To guarantee stable operational conditions, both thermal cracking and microwave plasma sources are operated ('backed') for at least 30 minutes prior to co-deposition. A simultaneous co-deposition experiment is then performed at the desired sample temperatures (13-17 K) by using all three H-, D-, and N-atom beams as well as a molecular CO beam for a period of typically four hours. During this co-deposition experiment, RAIR difference spectra are acquired every 5 minutes with respect to a spectrum of the bare gold substrate. All relevant experiments are summarized in Table 7.1.

Here, the main challenge is to evaluate with the highest possible precision the H:D ratio in the mixed atom beam to allow for a quantitative study of the competition between hydrogenation and deuteration of ammonia ice. Ioppolo *et al.* (2013) characterized the atom fluxes produced by SURFRESIDE[2] and found that, for identical settings and with H_2 and D_2 used separately, the resulting H-atom fluxes at the surface are a factor of ~2 higher than the measured D-atom fluxes. However, this does not necessarily mean that using a H_2:D_2 = 1:1 mixed gas will result in a production of H and D atoms in a 2:1 ratio. This is because differences in the H_2 and D_2 flow rates through the leaking valve as well as different recombination efficiencies of H+H, D+D, and H+D on the walls of the quenching quartz pipe can change the final H:D ratio. Moreover, the absolute flux calibrations come with large uncertainties (~30-50%).

Therefore, after each H:D:N experiment, we performed a control co-deposition experiment of H:D:O_2 ~ 1:1:100 at the same temperature of the H:D:N experiment to derive the effective H and D fluxes at the substrate surface for all the different temperatures investigated. These control experiments lead to the formation of two products: HO_2 and DO_2 through the reactions H/D + O_2 = HO_2/DO_2. The surface formation of HO_2 and DO_2 has been the topic of several studies and is known to be a nearly barrierless process (*e.g.*, Cuppen *et al.* 2010). Therefore, the total amount of final products and the HO_2:DO_2 ratio are expected to be independent of temperature - as we verified here in the range between 13 and 17 K - and reflect the effective H- and D-atom fluxes at the surface. Band strengths of selected mid-IR vibrational modes are needed to quantify the final abundances of HO_2 and DO_2 formed in our control experiments. Unfortunately, there is no experimental data on HO_2 and DO_2 band strengths in an O_2 matrix. Therefore, we used integrated band areas to calculate the ratio between OD:OH stretching modes and the ratio between DOO:HOO

bending modes for all the investigated temperatures. The two ratios give the following values of 1.48 and 1.47, respectively, which are temperature independent.

To quantitatively link the OD:OH and DOO:HOO ratios as obtained from the integrated band areas with the ratio of the final amount of HO_2 and DO_2, we still need to know at least the band strength ratios for the selected vibrational modes. Therefore, we assume that the band strength ratio between the DOO and the HOO bending modes of DO_2 and HO_2, respectively, is the same as for the band strength ratio between the DOO and the HOO bending modes of H_2O_2 and D_2O_2 obtained in O_2 + H/D experiments by Miyauchi *et al*. (2008) and Oba *et al*. (2014). As shown in Oba *et al*. (2014), the peak positions of H_2O_2 (1385 cm^{-1}) and D_2O_2 (1039 cm^{-1}) are similar to the peak positions of HO_2 (1391 cm^{-1}) and DO_2 (1024 cm^{-1}) in our O_2 matrix experiments (Bandow & Akimoto 1985). The DOO:HOO band strength ratio in Miyauchi *et al*. (2008) and Oba et al. (2014) is determined as 1.4. We also assume that the OD:OH band strength ratio from the stretching modes of HO_2 and DO_2 is the same as for the OD:OH band strength ratio from the stretching modes of H_2O and D_2O determined by Bergren *et al*. (1978) and Miyauchi *et al*. (2008). In this case, an OD/OH band strength ratio of 1.5 was found. By scaling the integrated band area ratios of the two selected vibrational modes (OD:OH = 1.48 and DOO:HOO = 1.47) for their respective band strength ratios (OD:OH = 1.5 and DOO:HOO = 1.4) we conclude that the ratio of our effective H- and D-atom fluxes is equal to one within the experimental uncertainties.

Once the first H:D:O_2 ~ 1:1:100 control experiment is completed, the ice is usually sublimated and a second control co-deposition experiment of H and D atoms with O_2 molecules is repeated always at 13 K. This second control experiment is meant to monitor the day-to-day reproducibility of the H- and D-atom fluxes. We did not find any major fluctuations in the H:D-atom beam over the course of our experiments.

Table 7.1. List of the performed experiments.

Ref. N	Experiment	Method[a]	Ratio	T_{sample} (K)	R_{dep} (ML min^{-1})	Atom-flux^{TL} (10^{15} cm^{-2} min^{-1})[b]	Atom-flux^{PL} (10^{15} cm^{-2} min^{-1})[b]	t_{total} (min)	TPD
SURFRESIDE									
Isotopic exchange in NH$_3$+D system									
					NH$_3$	D (from D$_2$)			
1.1	NH$_3$:D	pre-dep	-	15	4.5 (50 ML)	0.7	-	120	-
						2.5	-	60	QMS
1.2	NH$_3$:D	co-dep	1:5	15	0.5	2.5	-	120	-
SURFRESIDE^2									
Deuterium fractionation of ammonia isotopologues produced by simultaneous surface (H+D)-atom addition to N-atoms									
					CO	H+D (H$_2$:D$_2$ = 1:1)	N (from N$_2$)		
2.1	N:(H+D):N$_2$:CO	co-dep	1:15^b:100:100	13	0.5	0.075^b	0.005	180	QMS$^{1K/5K}$
2.2	N:(H+D):N$_2$:CO	co-dep	1:15^b:100:100	13	0.5	0.075^b	0.005	240	-
2.3	N:(H+D):N$_2$:CO	co-dep	1:15^b:100:100	14	0.5	0.075^b	0.005	240	-
2.4	N:(H+D):N$_2$:CO	co-dep	1:15^b:100:100	15	0.5	0.075^b	0.005	240	-
2.5	N:(H+D):N$_2$:CO	co-dep	1:15^b:100:100	16	0.5	0.075^b	0.005	240	-
2.6	N:(H+D):N$_2$:CO	co-dep	1:15^b:100:100	17	0.5	0.075^b	0.005	240	-
					CO	H (from H$_2$)	N (from N$_2$)		
3.1	N:H:N$_2$:CO	co-dep	1:20:100:100	13	0.5	0.1	0.005	90	-
					CO	D (from D$_2$)	N (from N$_2$)		
3.2	N:D:N$_2$:CO	co-dep	1:20:100:100	13	0.5	0.1	0.005	90	-
Determination of H:D atom ratio in produced mixed (H+D)-atom beam									
					O$_2$	H+D (H$_2$:D$_2$ = 1:1)			
4.1	(H+D):O$_2$	co-dep	1:600	13	45	0.075^c	-	10	-
4.2	(H+D):O$_2$	co-dep	1:600	14	45	0.075^c	-	10	-
4.3	(H+D):O$_2$	co-dep	1:600	15	45	0.075^c	-	10	-
4.4	(H+D):O$_2$	co-dep	1:600	16	45	0.075^c	-	10	-
4.5	(H+D):O$_2$	co-dep	1:600	17	45	0.075^c	-	10	-

[a]Experiments are performed by pre-depositon (pre-dep) and co-deposition (co-dep) techniques; R_{dep} is the deposition rate of a selected molecule expressed in ML min^{-1} under the assumption that 1 L (Langmuir) exposure leads to the surface coverage of 1 ML; T_{sample} is the substrate temperature during co-deposition; Atom-flux^{TL} is the HABS atom flux; Atom-flux^{PL} is the plasma cracking line atom flux; t_{total} is the total time of co-deposition; TPD is the temperature programmed desorption experiment performed afterward with the TPD rate indicated.

[b]Absolute uncertainties of H/D- and N- fluxes are 50 and 40%, respectively; the relative uncertainty between two of the same N+H/D experiments is <20%, and is as low as a few percent for H/D+O$_2$ experiments.

[c]Since the exact atom-beam composition for H$_2$:D$_2$ = 1:1 feeding mixture is unknown, the absolute atom flux corresponding to the sum of the two distinct fluxes (one for pure H$_2$ and one for pure D$_2$) divided by 2 is used to present co-deposition ratios and total fluences.

7.3 Results and conclusions

7.3.1 Deuterium exchange in NH$_3$ + D system

Nagaoka *et al.* (2005) and Hidaka *et al.* (2009) found that both solid H$_2$CO and CH$_3$OH participate in abstraction reactions with D atoms in the 10-20 K temperature range yielding D-substituted methanol isotopologues in H$_2$CO+D and CH$_3$OH+D experiments. In the same work, Nagaoka *et al.* (2005) investigated similar reactions for the NH$_3$+D system and reported that no abstraction is observed in the exposure of pre-deposited NH$_3$ to cold D atoms at temperatures below 15 K. In the present work, we verify this conclusion for our experimental pre-deposition conditions and we further expand on this by performing co-deposition experiments.

In the top panel of Figure 7.1, two RAIR spectra are presented: (a) a spectrum obtained after 50 ML deposition of pure NH$_3$ ice, and (b) the RAIR difference spectrum obtained after exposure of this ice to $8 \cdot 10^{16}$ D atoms cm^{-2}. One can see that all four main spectroscopic absorption features of NH$_3$ (v_1 = 3217 cm^{-1}, v_2 = 1101 cm^{-1}, v_3 = 3385 cm^{-1}, v_4

= 1628 cm^{-1}, see Reding & Hornig 1954) are visible in the spectra of pure NH$_3$ ice. It should be noted that the peak positions are significantly shifted in this pure ammonia environment from the ones in rare gas matrix-isolated NH$_3$ due to the presence of hydrogen bonds between NH$_3$ molecules (H$_2$N-H···NH$_3$) (compare for example data in Reding & Hornig 1954 with those in Abouaf-Marguin *et al.* 1977 and Hagen & Tielens 1982). Spectrum (b), in turn, shows that none of the NH$_2$D absorption bands demonstrates a noticeable growth upon D-atom exposure, at least not within our experimental detection limits. A small feature in the N-H/O-H stretching region (3000-3500 cm^{-1}), and a shift of the peak centred at 1100 cm^{-1} (see the negative bump in spectrum b) is likely due to background water deposition on top of NH$_3$ during the 2 hours of D-atom exposure. It is known that position and strength of NH$_3$ absorption bands can vary in presence of H$_2$O ice, since new hydrogen bonds are formed with H$_2$O molecules, *i.e.*, HOH···NH$_3$, H$_2$O···HNH$_2$ (Bertie & Shehata 1985).

In order to further increase the sensitivity of our experimental technique, co-deposition experiments of NH$_3$ molecules with D atoms are performed. With a sufficiently high number of D atoms over NH$_3$ molecules (*e.g.*, 5:1 ratio), virtually, every deposited NH$_3$ molecule is available for reaction with D atoms, and a greater amount of products may be formed and be available for detection by RAIRS. In the lower panel of Figure 7.1, the results of this experiment are shown; there is no observable difference between the NH$_3$ + D and pure NH$_3$ deposition experiments at 15 K, and none of the possible D-substituted NH$_3$ isotopologues, *i.e.,* NH$_2$D, NHD$_2$, ND$_3$, can be spectroscopically identified. This further constrains the conclusion made by Nagaoka *et al.* (2005) that the reaction NH$_3$ + D does not take place at temperatures lower than 15 K. Moreover, because of the aforementioned "zero-point energy argument", we expect that also reaction ND$_3$+H is not efficient at low temperatures as well.

It should be noted that hydrogen bonds between NH$_3$ molecules stabilise NH$_3$ and make abstraction reactions by D atoms thermodynamically less favourable (in a way similar to the H$_2$O + D case). Therefore, performing the NH$_3$ + D experiments in a non-polar matrix could potentially prevent the hydrogen bond formation and in return help to overcome the activation barrier for the exchange reaction at low temperatures. Although this is an interesting project, we decided to perform another challenging set of experiments with the intent to study the deuterium fractionation during ammonia formation. The outcome of these experiments is presented in the next section.
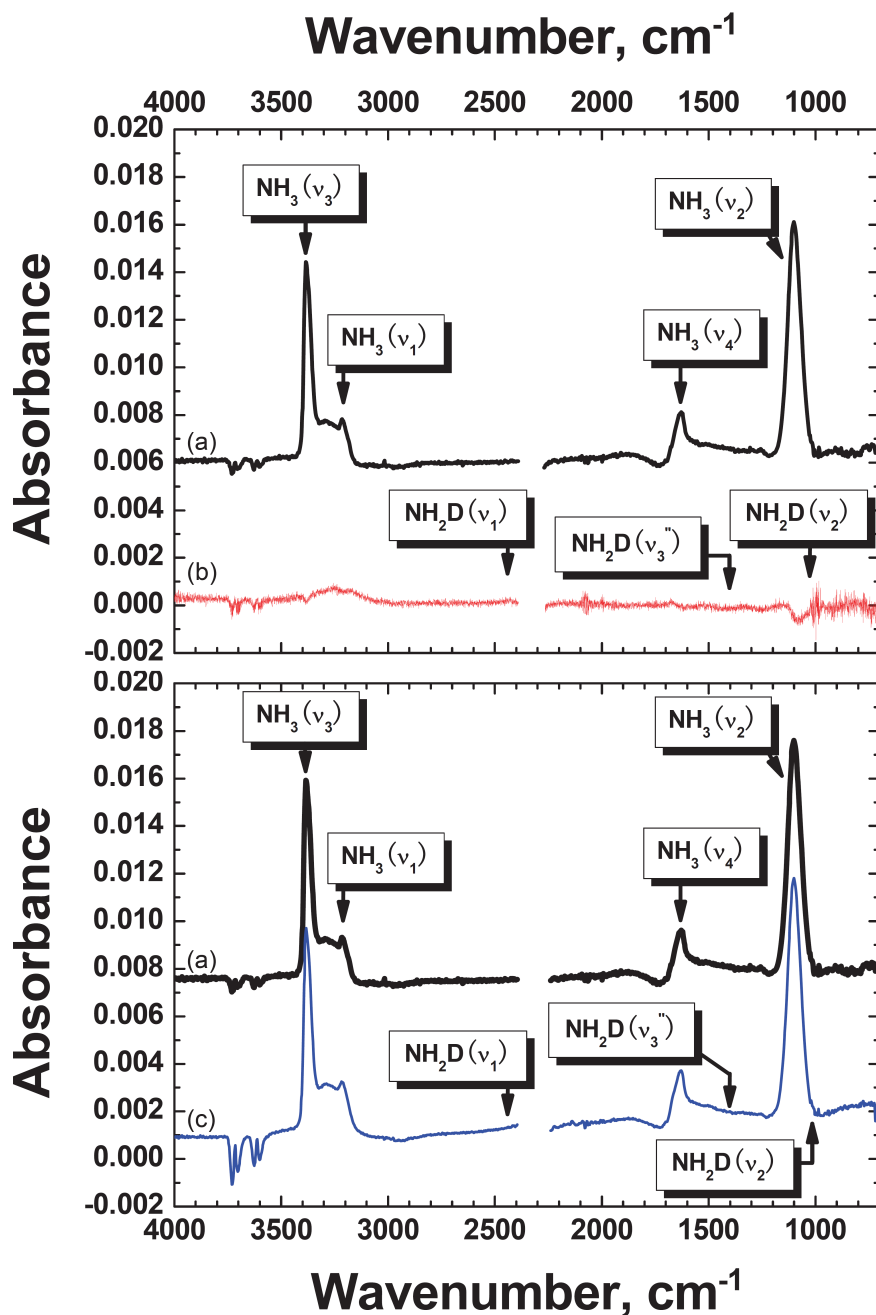
Figure 7.1. Upper panel: (a) RAIR spectrum of 50 ML of pure NH_3 at 15 K (experiment 1.1); (b) RAIR difference spectrum obtained after exposure of 50 ML of pre-deposited NH_3 ice with $8 \cdot 10^{16}$ D atoms cm^{-2} at 15 K (experiment 1.1). Lower panel: (c) simultaneous co-deposition of 50 ML of NH_3 with $3 \cdot 10^{17}$ D atoms cm^{-2} at 15 K, where $D:NH_3 = 5:1$ (experiment 1.2). The removed window between 2250 and 2380 cm^{-1} and the region from 3550 to 3650 cm^{-1} present absorption bands due to atmospheric CO_2 along the path of the IR beam outside the UHV setup.

7.3.2 H/D fractionation of ammonia (isotopologues) produced by hydrogenation of N atoms at low temperatures

Here, we show the first experimental results for deuterium fractionation in NH_3 molecules during the formation of ammonia through N-atom hydrogenation/deuteration in interstellar ice analogues. A number of experiments has been performed in which N atoms are co-deposited at 13 K with CO molecules and a mixture of H and D atoms in a single beam (see Table 7.1 experiments 2.1-3.2). Now, all four possible ammonia D-isotopes can be identified following the identification of several spectral features: NH_3 ($v_2 = 975$ cm^{-1} and $v_4 = 1625$ cm^{-1}); NH_2D ($v_2 = 909$ cm^{-1} and $v_4 = 1389$ cm^{-1}); NHD_2 ($v_2 = 833$ cm^{-1}, $v_4 = 1457$ cm^{-1}, and $v_3 = 2551$ cm^{-1}); and ND_3 ($v_2 = 762$ cm^{-1} and $v_3 = 1187$ cm^{-1}). Assignments are taken from Reding & Hornig (1954), Abouaf-Marguin *et al*. (1977), Nelander (1984), and Koops *et al*. (1983). Figure 7.2(a) shows the RAIR spectrum of a co-deposition of N:(H+D):N_2:CO = 1:15:100:100 at 13 K with a $H_2/D_2 = 1$ ratio and the N_2 is due to the undissociated precursor gas. In this experiment, also HDCO can be observed at $v_2 = 1708$ cm^{-1} and $v_3 = 1395$ cm^{-1} (Hidaka *et al*. 2009), while both H_2CO and D_2CO are present only as trace signals at 1733 cm^{-1} and 1682 cm^{-1}, respectively.

In order to make the interpretation of our data quantitative, absolute band strengths are needed. For NH_3 and ND_3 absolute intensity measurements exist. There are no available data for the band strengths of the partially deuterated ammonia isotopes - NH_2D and NHD_2 - for which only predictions have been reported so far (Koops *et al*. 1983). Since in our study v_2 is the only mode that is present for all ammonia isotopologues and this vibrational mode can be affected by the ice lattice, we have decided to apply a different method for the quantitative characterization of ammonia deuterium fractionation at low temperatures. In the accompanying paper (Fedoseev *et al*. 2014), we have already shown that under our experimental conditions the amount of produced ammonia is determined by the amount of nitrogen atoms available for hydrogenation. In the case of a pure statistical (*i.e*., mass independent) distribution of the products of simultaneous H- and D-atom additions to nitrogen atoms, the final yield distribution of NH_3:NH_2D:NHD_2:ND_3 should be about 1:3:3:1, assuming a H:D = 1:1 ratio, as determined in the experimental section.

Therefore, in Figure 7.2 we compare the spectrum from a co-deposition of N:(H+D):N_2:CO = 1:15:100:100 at 13 K (Fig. 7.2a) with spectra from a nitrogen-atom co-deposition experiment with only H atoms (Fig 7.2b) or only D atoms (Fig 7.2c), in such a way that the total amount of deposited N atoms in the experiment shown in Fig. 7.2(a) is 8 times higher than that shown in each of the two other spectra. It is illustrated in Fedoseev *et al*. (2014) that under our experimental conditions a full conversion of N atoms into the final product (NH_3) is achieved. Therefore, if our assumption of a 1:3:3:1 distribution of the formed isotopologues is correct, Fig. 7.2(b) should represent a statistical weight of the

formed NH_3, and Fig. 7.2(c) of ND_3. In this distribution, the amount of produced NH_3 is 8 times lower than the total amount of all the formed ammonia isotopologues, *i.e.*, only 1/8 part of the deposited N atoms should be converted to NH_3. The same applies to ND_3. The comparison of the NH_3 and ND_3 band areas in Fig. 7.2(a) with the NH_3 band area in Fig. 7.2(b) and the ND_3 band area in Fig. 7.2(c) shows that, for the chosen settings, there is a deviation from the statistical 1:3:3:1 distribution in favor of an increase in the production of deuterated species. In particular, by comparing the total amount of ND_3 in Figs. 7.2(a) and 7.2(c), we estimate that every deuteration reaction has a probability of almost a factor 1.7 higher to occur over the corresponding hydrogenation reactions. The area of ND_3 in Fig. 7.2(a) is two times larger than the ND_3 area in Fig. 7.2(c). To achieve such enhancement of ND_3 production over three subsequent additions of H or D atoms to an N atom, every deuteration reaction should have a probability of a factor 1.7 higher to occur, resulting in a final NH_3:NH_2D:NHD_2:ND_3 distribution of 0.4:2.1:3.5:2. This is further discussed in the following sections.
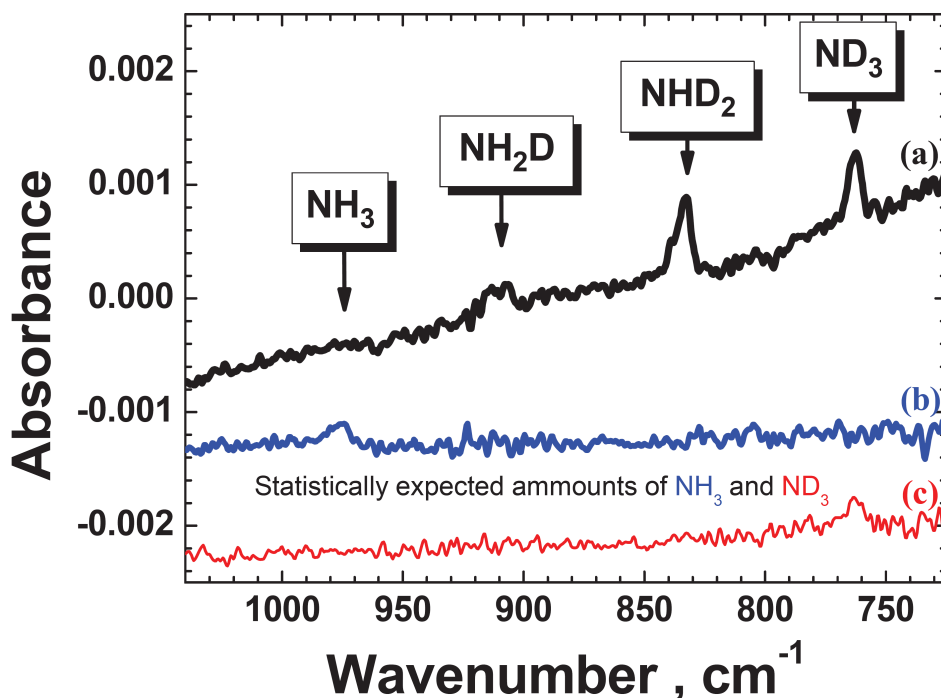
Figure 7.2. Three RAIR difference spectra: (a) co-deposition of N:(H+D):N_2:CO = 1:15:100:100 at 13 K (experiment 2.1); here, the H- and D-atom beams are prepared in the thermal cracking line by feeding the line with a mixture of H_2:D_2 = 1:1; (b) co-deposition of N:H:N_2:CO = 1:20:100:100 at 13 K (experiment 3.1); (c) co-deposition of N:D:N_2:CO = 1:20:100:100 at 13 K (experiment 3.2). The total N-atom fluence in (a) is 8 times higher than in (b) and (c). This factor 8 represents the weight of NH_3 or ND_3 molecules in a pure statistical distribution of final hydrogenation products assuming that H:D = 1:1 (*i.e.*, NH_3:NH_2D:ND_2H:ND_3 = 1:3:3:1).

Figure 7.3 shows the amount of ammonia isotopes formed as a function of the N-atom fluence. The uncertainties are large, but the derived data points hint for a linear growth for all the produced species. This is consistent with the assumption that the formation of all NH_3 isotopologues proceeds through subsequent H/D-atom addition to a single nitrogen atom, and no secondary processes like abstractions are involved (Hidaka *et al.* 2011, Fedoseev *et al.* 2014).
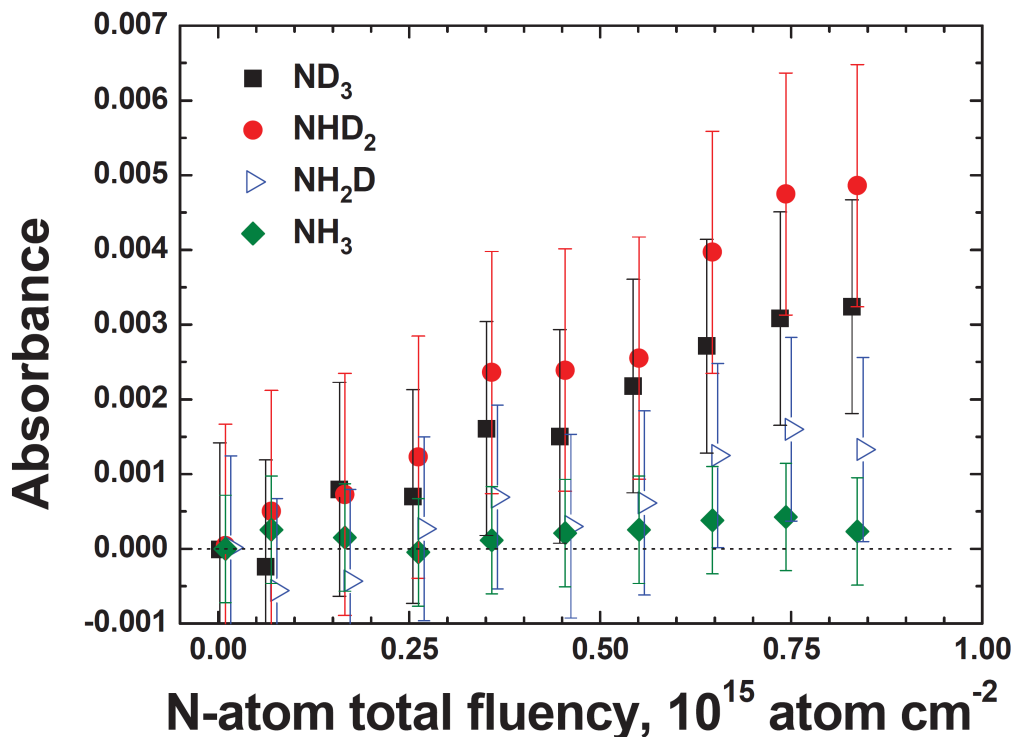

Figure 7.3. Co-deposition of N:(H+D):N_2:CO = 1:15:100:100 at 13 K (experiment 3.1). The absorbance of NH_3, NH_2D, ND_2H and ND_3 (taken from the integration of the ν_2 mode) is shown as a function of the N-atom fluence.

7.3.3 Temperature dependency of deuterium enrichment of the produced $NH_{3-n}D_n$ isotopologues in N+H+D atom addition reactions

The N+H+D co-deposition experiments described in the previous section are here repeated for a number of different temperatures with the goal to study the thermal dependence of $NH_{3-n}D_n$ (with $n = 0, 1, 2, 3$) formation. The RAIR spectra obtained after co-deposition of $1.1 \cdot 10^{15}$ N atoms cm^{-2} with a mixed H:D-atom beam at 13, 14, 15, 16, and 17 K are shown in Figure 7.4. Two conclusions can be derived from these plots. First, the formation of all

four isotopologues is observed in the 13-15 K range, but drops below the detection limit between 16 and 17 K. This decrease of the total $NH_{3-n}D_n$ production confirms, once again, the conclusions in Fedoseev *et al.* (2014) that hydrogenation of N atoms in CO-rich ices takes place through the L-H mechanism. In the case of Eley-Rideal (E-R) or hot-atom mechanisms, no significant temperature dependence, specifically within such a small range, is expected. Secondly, the deviation of the observed signals from a statistical distribution in the amount of formed NH_3, NH_2D, NHD_2, and ND_3 in favour of D-substituted isotopologues remains constant, despite a gradual decrease of the total amount of products. In other words the observed preference in deuteration events over hydrogenation events is within our detection levels the same for all the tested temperatures.
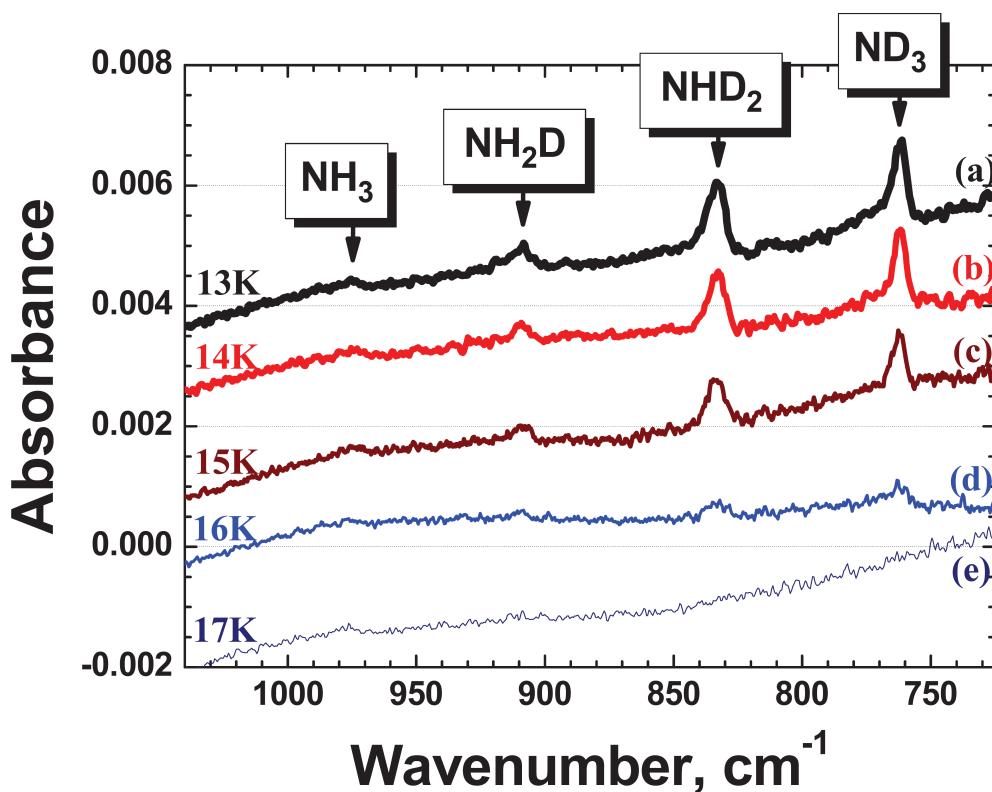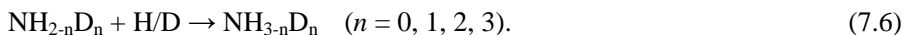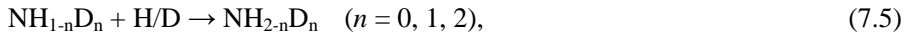

Figure 7.4. RAIR spectra obtained after co-deposition of N:(H+D):N_2:CO = 1:15:100:100 at five different temperatures: (a) 13 K, (b) 14 K, (c) 15 K, (d) 16 K, and (e) 17 K (see experiments 2.2-2.6). The mixed H- and D-atom beam is prepared in the thermal cracking line by feeding the line with a mixture of H_2:D_2 = 1:1.

7.3.4 Discussion

All four $NH_{3-n}D_n$ isotopologues are observed among the products of simultaneous co-deposition of N atoms with H and D atoms. This allows us to study for the first time the competition between hydrogenation and deuteration of N atoms in the solid phase at low temperatures. Previous work aimed at studying the hydrogenation of N atoms in a N_2 matrix (Hiraoka *et al*. 1995, Hidaka *et al*. 2011) as well as in CO-rich ices (Fedoseev *et al*. 2014). All three studies suggest that hydrogenation of nitrogen atoms takes place through subsequent H-atom addition to a single N-atom:

$$N + H \rightarrow NH, \tag{7.1}$$
$$NH + H \rightarrow NH_2, \tag{7.2}$$
$$NH_2 + H \rightarrow NH_3. \tag{7.3}$$
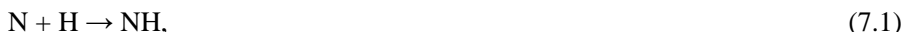
When D atoms are introduced simultaneously with H atoms, it is logical to assume that these also will participate in competing deuteration reactions, following the same chemical pathway:

$$N + H/D \rightarrow NH_{1-n}D_n \quad (n = 0, 1), \tag{7.4}$$
$$NH_{1-n}D_n + H/D \rightarrow NH_{2-n}D_n \quad (n = 0, 1, 2), \tag{7.5}$$
$$NH_{2-n}D_n + H/D \rightarrow NH_{3-n}D_n \quad (n = 0, 1, 2, 3). \tag{7.6}$$
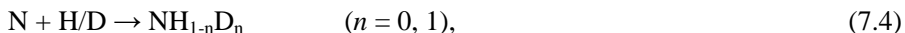
As stated before, in the case that there is no chemical preference for H- or D-addition reactions, then for a H:D = 1:1 mixture, the final isotopologue distribution follows a statistical weighting of $NH_3:NH_2D:ND_2H:ND_3$ = 1:3:3:1. However, the actually observed distribution deviates, and is determined as 0.4:2.1:3.5:2, in favour of a higher (1.7 times) deuteration efficiency compared to hydrogenation. To determine the exact process responsible for this enrichment, we have considered different possibilities: experimental artefacts, specifically, (*i*) deviations from the H:D = 1:1 ratio in the mixed atom beam fluxes in favour of D atoms; or a physically and chemically different behaviour, *i.e.*, (*ii*) differences in accretion rates (sticking probabilities) of H and D atoms, (*iii*) differences in desorption and diffusion rates of the adsorbed H and D atoms, and (*iv*) other competing reactions involved, like for example atom abstraction reactions. These possibilities are discussed separately.

(*i*) *Lower H-atom flux over D-atom flux in the mixed beam*.
As we described before, a $H_2:D_2$ = 1:1 gas mixture is used as a feeding gas for the thermal cracking line to obtain a mixed H/D-atom beam. The difference in mass and bond energy

of both precursor species may yield an H:D:H$_2$:D$_2$:HD beam reflecting a deviating distribution, causing experiments to start from (unknown) initial conditions. Therefore, to evaluate the exact H:D ratio in the atom beam, co-deposition experiments are performed, where mixed H/D atoms are co-deposited with large overabundances of O$_2$ molecules and - as discussed in the experimental section - the amount of HO$_2$ and DO$_2$ formed through barrierless reactions can be directly linked to the H/D ratio. The test shows that the same amount of HO$_2$ and DO$_2$ is formed in all experiments at all tested temperatures. The temperature independence of the obtained results is in strong support of an E-R mechanism for HO$_2$ and DO$_2$ formation. Therefore, assuming the same probability for H and D atoms to react with O$_2$ molecules upon encounter, the H:D-atom ratio at the ice surface is equal to 1 and cannot explain the observed deuterium enrichment in N+H+D co-deposition experiments.

(*ii*) *Different sticking probabilities for H and D atoms at the surface of the ice.*
Several studies have been devoted to the investigation of the sticking coefficients of H atoms to cryogenically cooled surfaces as a function of the translational energy of the H atoms (for an overview see Watanabe *et al*. 2008). Buch & Zhang (1991) performed molecular dynamic simulations showing that D atoms have a higher sticking probability (to H$_2$O ice) than H atoms for all studied temperatures (50-600 K). For instance, a 300 K D-atom beam has a calculated sticking probability to water ice 2.5 higher than H atoms. Unfortunately, to date, no experimental data is available on a mixed CO:N$_2$ ice surface and a 300 K estimated D/H-atom beam temperature. However, following the simulations, we expect a higher surface density of D atoms (w.r.t. H atoms) on the surface of the ice, consistent with the observed results. It should be noted, though, that this may not be the full story. The nose-shaped quartz pipe is used to collisionally quench 'hot' atoms. Therefore, it is not necessarily true that H and D atoms have identical translational energies at the ice surface; both species are light and this makes efficient collisional quenching even more challenging. Finally, the factor 2 difference in mass may affect the resulting distribution of translational energies, further changing the sticking coefficients for H and D atoms. Bottom line, the sticking probability for H and D atoms at cold surfaces seems to be a key parameter to explain the experimentally observed deuterium fractionation.

(*iii*) *Difference in desorption and diffusion rates for H and D atoms.*
If D atoms have a higher binding energy to CO-ice than H atoms, this can affect the system in two opposite ways. On one hand, a lower binding energy of H atoms means that they have a higher probability to desorb from the surface of the ice before a reaction with other species takes place. On the other hand, a lower binding energy means that, for the studied temperature range, thermal hopping of H atoms is to occur more frequently than thermal

hopping of D atoms. If quantum tunnelling is responsible for the diffusion of H/D atoms, this further enhances the mobility of H atoms and the probability to find an N-atom to yield $NH_{1-n}D_n$ ($n = 0, 1$) and $NH_{2-n}D_n$. ($n = 0, 1, 2$). To verify this hypothesis, a set of experiments as described in section 3.3 was performed. No significant difference upon sample temperature variation is found up to 17 K, where none of the reaction products could be detected. In the case that either a difference in desorption or diffusion rate would be responsible for the observed deuterium enrichment, one would expect to find a significant change in the $NH_3:NH_2D:ND_2H:ND_3$ distribution with temperature from maximum production to non-production of ammonia isotopologues. This is not observed and hints for the conclusion that different diffusion rates are not case determining. This is also consistent with the small isotopic difference between the diffusion of H and D atoms on amorphous water ice as observed by Hama *et al*. (2012).

(*iv*) *Competing reaction channels*.

Taking into account an overabundance of H/D atoms compared to N atoms on the surface of the ice, the main competing reaction channels are expected to be:

$$H + H \rightarrow H_2, \tag{7.7}$$
$$D + D \rightarrow D_2, \tag{7.8}$$
$$H + D \rightarrow HD. \tag{7.9}$$

If two separate systems would be studied (*i.e.*, N+H and N+D), the rates of the competing barrierless reactions (7.7) and (7.8) would affect the rates of NH_3 and ND_3 formation through the consumption of the available H and D atoms, and would decrease the corresponding H and D surface densities. This is especially important if the NH_3 and ND_3 formation mechanism would involve activation barriers, slowing down reactions in comparison to reactions (7.7) and (7.8). However, this is not the case. In addition, in our system, where H and D atoms are co-deposited, reaction (7.9), which decreases surface densities of H and D atoms in an equal way, should dominate. Our data cannot conclude precisely on the difference in surface H- and D-atom densities during the experiments, and knowledge of the activation barrier for H and D diffusion and desorption is required to build a precise model to investigate it. Other possible competing reactions that should be mentioned here are abstraction reactions. Although reaction

$$NH_3 + D \rightarrow NH_2 + HD, \tag{7.10}$$

can be excluded experimentally from the list (see section 7.3.1), reactions

$$NH_2 + D \rightarrow NH + HD, \tag{7.11}$$
$$NH + D \rightarrow N + HD, \tag{7.12}$$

and similar reactions, including deuterated isotopologues +H atoms instead of D atoms, should not be disregarded. Also abstraction reactions:

$$NH_2 + H_2/D_2 \rightarrow NH_3/NH_2D + H/D, \tag{7.13}$$
$$NH + H_2/D_2 \rightarrow NH_2/NHD + H/D, \tag{7.14}$$
$$N + H_2/D_2 \rightarrow NH/ND + H/D, \tag{7.15}$$

should be considered. Both reactions (7.11) and (7.12) are expected to have activation barriers. Similar reactions involving only H atoms show barriers of 6200 K for reaction (7.11) and 400 K for reaction (7.12) (Ischtwan & Collins 1994, Poveda & Varandas 2005). Reactions (7.13) - (7.15) are expected to have activation barriers as well and are endothermic (see Hidaka *et al*. 2011 and references therein). Since reactions (7.4)-(7.6) are all barrierless, they should proceed much faster than reactions (7.11)-(7.15). Therefore, we assume that reactions (7.11)-(7.15) do not contribute significantly to the formation of ammonia and its isotopologues under our experimental conditions.

After discussing these arguments, we consider the difference in sticking probabilities of H and D atoms to the surface of CO-rich ices (resulting in a higher surface density of D atoms over H atoms) as the main reason for the observed deuterium enrichment of ammonia isotopologues produced by surface hydrogenation/deuteration of N atoms at low temperatures.

7.4 Astochemical implications and conclusions

The observed high deuterium fractionation in prestellar cores (high densities $n \geq 10^6$ cm^{-3} and low temperatures $T \leq 10$ K) is the result of a combination of gas-phase and surface reactions. Under molecular cloud conditions, the D/H ratio of molecules is found orders of magnitude higher (between 0.02-0.09 for DNC/HNC) than the elemental abundance of D/H $= 1.5 \times 10^{-5}$ (Linsky 2003, Hirota *et al*. 2003). It is well established that this enhancement is largely due to exothermic exchange gas-phase reactions involving H_3^+ (Oka 2013, Millar *et al*. 1989, Roberts *et al*. 2004). A process that can counterbalance the deuterium enrichment of gas-phase species is the reaction between H_2D^+ and CO. However, for cloud densities higher than a few 10^5 cm^{-3}, timescales for collisions of CO with grains become so short that most of the gaseous CO is depleted from the gas to form a layer of pure CO ice on the grains. This so-called "catastrophic" freeze-out of CO, observed directly through infrared ice-mapping observations (Pontoppidan 2006) and indirectly through the lack of gas-phase

CO and other molecules in dense regions (Bergin *et al.* 2002, Caselli *et al.* 1999), causes a rise in gaseous H_2D^+ and deuterated molecules. Moreover, electron recombination of H_2D^+ enhances the abundance of D atoms, which then can participate in surface reactions on dust grains to form deuterated ice (Aikawa 2013).

Recent laboratory experiments proved that surface reactions involving deuterium - including hydrogen abstraction reactions - lead to the deuterium enrichment of interstellar ices. For instance, the deuteration of solid $O/O_2/O_3$ induces the formation of deuterated water ice (*e.g.*, Dulieu *et al.* 2010, Ioppolo *et al.* 2008, Romanzin *et al.* 2011). However, the formation of H_2O/HDO through $OH+H_2/D_2$ and H_2O_2+H/D (Oba *et al* 2012, Oba *et al* 2014) shows a preference for hydrogenation that has been explained by a higher quantum tunneling efficiency. On the other hand, Nagaoka at al. (2005), Nagaoka (2007), and Hidaka at al. (2009) demonstrated that hydrogen atoms can be abstracted from methanol and its isotopologues and substituted by D atoms upon D-atom exposure of solid CH_3OH, CH_2DOH, and CHD_2OH.

Triply deuterated ammonia (ND_3) has been observed in dark clouds with an ND_3/NH_3 abundance ratio of $\sim 8 \cdot 10^{-4}$, which implies an enhancement of more than 10 orders of magnitude over the purely statistical value expected from the abundance of deuterium in the interstellar medium (Lis *et al.* 2002). The deuterium enrichment of ammonia can occur both in the gas phase and in the solid phase (Rodgers & Charnley 2001). The gas-phase synthesis of ammonia in cold dense clouds occurs through a sequence of ion-molecule reactions that start with the fragmentation of N_2 and formation of N^+ ions through the reaction with He^+, which is formed by cosmic-ray ionization of He. Successive reactions with H_2 end with the formation of the NH_4^+ ion, and dissociative recombination with electrons finally yields NH_3 as the dominant product (Vikor *et al.* 1999, Öjekull *et al.* 2004, Agúndez & Wakelam 2013). When deuterated species are involved in the process, triply deuterated ammonia is then formed through the dissociative recombination of NHD_3^+. In their gas-phase chemical model, Lis *et al.* (2002) were able to reproduce the observed abundances of deuterated ammonia only when a non-statistical ratio for the dissociative recombination reaction forming ND_3 was used. An alternative route is the deuterium fractionation on the grains, as studied here.

In the solid phase, the formation of ammonia is a radical-radical process (reactions (1)-(3)) that occurs at low temperatures (<15 K). Previous laboratory work confirms that these surface reactions are nearly barrierless (Hiraoka *et al.* 1995, Hidaka *et al.* 2011, Fedoseev *et al.* 2014). Therefore, one would expect the deuterium fractionation of ammonia to reflect the atomic D/H ratio in the accreted gas. Disregarding any other surface reaction and assuming that the probability for accretion of N atoms and reaction with D atoms is p_D, then the probability for reaction with H atoms is (1- p_D). The expected fractionation for NH_2D/NH_3 is $3p_D/(1- p_D)$, where the factor 3 accounts for the three

chances to deuterate ammonia, and is $3p^2_D/(1-p_D)^2$ for ND_2H/NH_3 (Tielens 2005). Although this simple calculation strongly depends on the local cloud conditions, it is based on a statistical distribution of the $NH_{3-n}D_n$ isotopologues and does not fully reflect the observed gas-phase abundances for the $NH_{3-n}D_n$ isotopologues in dense cold clouds (Rouef *et al*. 2000, Loinard *et al*. 2001).

Our laboratory results indicate that the simultaneous addition of H and D atoms to N atoms on a cold surface leads to the formation of all the deuterated isotopologues of ammonia with a distribution that is non-statistical at low temperatures and that leads to a higher deuterium fractionation of ammonia ice. Our experiments are performed in CO-rich ices to resemble the conditions found in dense cold cores, where CO freezes-out onto dust grains and the D/H ratio increases. The use of a CO matrix in our experiments also helps to overcome the IR spectral broadening that occurs in polar ices and that induces spectral confusion. Moreover, the D/H ratio (~1:1) chosen for our experiments is somehow representative to the densest prestellar cores and, at the same time, simplifies the data analysis. Under our experimental conditions, every deuteration event has a probability of at least a factor 1.7 higher to occur over a regular hydrogenation event, independently from the surface temperature. A higher sticking probability of D atoms over H atoms to the surface of the ice can explain our experimental findings. In this scenario, the surface D/H ratio is higher than the already enhanced gas-phase D/H ratio as in dense cores, because D atoms have a higher binding energy to the surface than H atoms. This will further increase the deuterium fractionation of species that are formed in the solid phase and then later released into the gas-phase. Therefore, our results show that the deuterium fractionation of species in the solid phase is potentially a more important process than previously considered.

This conclusion can be extrapolated to other chemical systems than simply ammonia ice, where isotopologues are formed by a series of competing and barrierless H/D-atom addition reactions to a single atom. For instance, we expect that the competition between hydrogenation and deuteration of CH_4 leads to an enhancement of deuterated species. Our H- and D-atom beam has a temperature of 300 K, as opposed to the temperature of H and D atoms in dark cloud regions that is roughly an order of magnitude lower. Buch & Zhang (1991) reported that the sticking probability of 300 K deuterium atoms to the surface of an amorphous H_2O cluster is 2.5 higher than the sticking probability of hydrogen atoms. The same ratio goes down to 1.42, when the D and H atoms are at 50 K. Moreover, different surface properties, *i.e.*, polar (H_2O-rich) *versus* non-polar (CO-rich) ice, can potentially affect the sticking probabilities of H and D atoms as well. Therefore, we expect that complementary systematic experiments performed with H- and D-atom beams at different kinetic temperatures and in both polar and non-polar ice analogues will be pivotal to determine the role of ice grain chemistry in the interstellar deuterium fractionation of

molecules like ammonia. The present study already shows that surface reactions clearly can contribute to the observed gas phase abundances.

References

Abouaf-Marguin L., Jacox M. E., Milligan D. E., 1977, J. Mol. Spectrosc., 67, 34

Agúndez M., Wakelam V., 2013, Chem. Rev., 113, 8710

Aikawa Y., 2013, Chem. Rev., 113, 8961

Anton R., Wiegner T., Naumann W., Liebmann M., Klein Chr., Bradley C., 2000, RSI, 71, 1177

Bacmann A., Lefloch B., Ceccarelli C., Steinacker J., Castets A., Loinard L., 2003, ApJ, 585, L55

Bandow H., Akimoto H., 1985, J. Phys. Chem., 89, 845

Bergin E. A., Alves J., Huard T., Lada C. J., 2002, ApJ, 570, L101

Bergren M. S., Schuh D., Sceats M. G., Rice S. A., 1978, JCP, 69, 3477

Bertie J. E. & Shehata M. R., 1985, Chem. Phys., 83, 1449

Bockelée-Morvan D. *et al*., 2012, A&A, 544, L15

Brown P. D., Millar T. J., 1989a, MNRAS, 237, 661

Brown P. D., Millar T. J., 1989b, MNRAS, 240, 25P

Buch V., Zhang Q., 1991, ApJ, 379, 647

Busquet G., Palau A., Estalella R., Girart J. M., Sánchez-Monge Á., Viti S., Ho P. T. P., Zhang Q., 2010, A&A, 517, L6

Caselli P., Walmsley C. M., Tafalla M., Dore L., Myers P. C., 1999, ApJ, 523, L165

Codella C. *et al*., 2012，ApJL, 757, L9

Congiu E. *et al*., 2012, ApJL, 750, L12

Crapsi A., Caselli P., Walmsley C. M., Myers P. C., Tafalla M., Lee C. W., Bourke T. L., 2005, ApJ, 619, 379

Cuppen H. M., Ioppolo S., Romanzin C., Linnartz H., 2010, PCCP, 12, 12077

Dulieu F., Amiaud L., Congiu E., Fillion J.-H., Matar E., Momeni A., Pirronello V., Lemaire J. L., 2010, A&A, 512, A30

Emprechtinger M., Caselli P., Volgenau N. H., Stutzki J., Wiedner M. C., 2009, A&A, 493, 89

Fedoseev G., Ioppolo S., Zhao D., Lamberts T., Linnartz H., 2014, submitted to MNRAS

Fuchs G. W., Cuppen H. M., Ioppolo S., Bisschop S. E., Andersson S., van Dishoeck E. F., Linnartz H., 2009, A&A, 505, 629

Hagen W., Tielens A. G. G. M., 1982, Spectrochim. Acta, Part A, 38, 1203

Hama T., Kuwahata K., Watanabe N., Kouchi A., Kimura Y., Chigai T., Pirronello V., 2012, ApJ, 757, 185

Hartogh P. *et al*., 2011, Nature, 478, 218

Hatchell J., 2003, A&A, 403, L25

Herbst E., Klemperer W., 1973, ApJ, 185, 505

Hidaka H., Watanabe M., Kouchi A., Watanabe N., 2009, ApJ, 702, 291

Hidaka H., Watanabe M., Kouchi A., Watanabe N., 2011, PCCP, 13, 15798

Hiraoka K., Miyagoshi T., Takayama T., Yamamoto K., Kihara Y., 1998, ApJ, 498, 710

Hiraoka K., Ohashi N., Kihara Y., Yamamoto K., Sato T., Yamashita A., 1994, Chem. Phys. Lett., 229, 408

Hiraoka K., Yamashita A., Yachi Y., Aruga K., Sato T., Muto H., 1995 ApJ, 443, 363

Hirota T., Ikeda M., Yamamoto S. 2003, ApJ, 594, 859

Ioppolo S., Cuppen H. M., Romanzin C., van Dishoeck E. F., Linnartz H., 2008, ApJ, 686, 1474

Ioppolo S., Fedoseev G., Lamberts T., Romanzin C., Linnartz H., 2013, RSI., 84, 073112

Ioppolo S., Fedoseev G., Minissale M., Congiu E., Dulieu F., Linnartz H., 2014, PCCP, 16, 8270

Ischtwan J., Collins M. A., 1994, JCP, 100, 8080

Koops T., Visser T., Smit W. M. A., 1983, J. Mol. Struct., 96, 203

Kristensen L. E., Amiaud L., Fillion J.-H., Dulieu F., Lemaire J.-L., 2011, A&A, 527, A44

Linsky J. L., 2003, Space Sci. Rev., 106, 49

Lis D. C., Roueff E., Gerin M., Phillips T. G., Coudert L. H., van der Tak F. F. S., Schilke P., 2002, ApJ, 571, L55

Lis D. C. *et al.*, 2013, ApJL, 774, L3

Loinard L., Castets A., Ceccarelli C., Caux E., Tielens A. G. G. M., 2000, ApJ, 552, 163

Millar T. J., Bennett A., Herbst E., 1989, ApJ, 340, 906

Miyauchi N., Hidaka H., Chigai T., Nagaoka A., Watanabe N., Kouchi A., 2008, Chem. Phys. Lett., 456, 27

Mokrane H., Chaabouni H., Accolla M., Congiu E., Dulieu F., Chehrouri M., Lemaire J. L., 2009, ApJL, 705, L195

Nagaoka A., Watanabe N., Kouchi A., 2005,   ApJ, 624, L29

Nagaoka A., Watanabe N., Kouchi A., 2007, J. Phys. Chem. A, 111, 3016

Nelander B., 1984,   Chem. Phys., 87, 283

Oba Y., Osaka K., Watanabe N., Chigai T., Kouchi A., 2014, Faraday Discuss., 168, accepted

Oba Y., Watanabe N., Hama T., Kuwahata K., Hidaka H., Kouchi A., 2012, ApJ, 749, 67

Öjekull J. *et al*., 2004, JCP, 120, 7391

Oka T., 2013, Chem. Rev., 113, 8738

Pillai T., Wyrowski F., Hatchell J., Gibb A. G., Thompson M. A., 2007, A&A, 467, 207

Pontoppidan K. M., 2006, A&A, 453, 2006, L47

Poveda L. A., Varandas A. J. C., 2005, PCCP, 7, 2867

Ratajczak A., Quirico E., Faure A., Schmitt B., Ceccarelli C., 2009, A&A, 496, L21

Reding F. P., Hornig D. F., 1954, JCP, 22, 1926

Roberts H., Herbst E., Millar T. J., 2004, A&A, 424, 905

Roberts H., Herbst E., Millar T. J., 2004, A&A, 424, 905

Roberts H., Millar T. J., 2006, Philos. Trans. R. Soc. Lond., A, 364, 3063

Rodgers S. D., Charnley S. B., 2001, ApJ, 553, 613

Romanzin C., Ioppolo S., Cuppen H. M., van Dishoeck E. F., Linnartz H., 2011, JCP, 134, 084504

Roueff E., Tiné S., Coudert L. H., Pineau des Forêts G., Falgarone E., Gerin M., 2000, A&A, 354, L63

Scott G. B. I., Fairly D. A., Freeman C. G., Mcewan M. J., 1997 Chem. Phys. Lett., 269, 88

Smith D., Adams N. G., Alge E., 1982, ApJ, 263, 123

Tielens A. G. G. M.   , 2005, The Physics and Chemistry of the Interstellar Medium. Cambridge University Press, Cambridge, UK.

Tielens A. G. G. M., 1983, A&A, 119, 177

Tschersich K. G., 2000, J. Applied Phys., 87, 2565

Vikor L., Al-Khalili A., Danared H., Djuric N., Dunn G. H., Larsson M., Le Padellec A., Rosaen S., Af Ugglas M., 1999, A&A, 344, 1027

Watanabe N., Kouchi A., 2002, ApJ, 571, L173

Watanabe N., Kouchi A., 2008, Prog. Surf. Sci., 83, 439

Weber A. S., Hodyss R., Johnson P. V., Willacy K., Kanik I., 2009, ApJ, 703, 1030

Zhitnikov R. A., Dmitriev Yu. A., 2002, A&A, 386, 1129

VIII

Experimental Evidence for Glycolaldehyde and Ethylene Glycol Formation by Surface Hydrogenation of CO Molecules under Dense Molecular Cloud Conditions
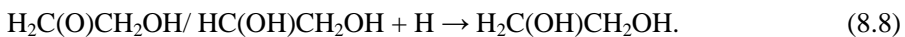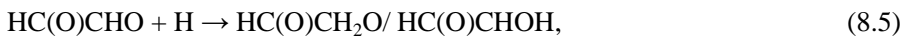
This study focuses on the formation of two molecules of astrobiological importance - glycolaldehyde (HC(O)CH$_2$OH) and ethylene glycol (H$_2$C(OH)CH$_2$OH) - by surface hydrogenation of CO molecules. Our experiments aim at simulating the CO freeze-out stage in interstellar dark cloud regions, well before thermal and energetic processing become dominant. It is shown that along with the formation of H$_2$CO and CH$_3$OH – two well established products of CO hydrogenation – also molecules with more than one carbon atom form. The key step in this process is thought to be the recombination of two HCO radicals followed by the formation of a C-C bond. The experimentally established reaction pathways are implemented into a continuous-time random-walk Monte Carlo model, previously used to model the formation of CH$_3$OH on astrochemical time-scales, to study their impact on the solid-state abundances in dense interstellar clouds of glycolaldehyde and ethylene glycol.

8.1 Introduction

Among approximately 180 molecules identified in the inter- and circumstellar medium over 50 molecules comprise of six or more atoms. For astrochemical standards, these are seen as 'complex' species. Most of these molecules contain H-, C- and O- atoms and can be considered as organic molecules. The sources where these complex organic molecules (COMs) are detected include cold interstellar cores, circumstellar envelopes around evolved stars, hot cores and corinos, outflows as well as other regions. The detection of COMs around young stellar objects (YSOs) in the early stages of their evolution may indicate that COMs are part of the material from which comets, planetesimals and ultimately planets are made. Therefore, it is not surprising that prebiotic molecules and chemical pathways leading to their formation at prestellar stages have become topic of an increasing number of observational, theoretical and laboratory studies. A clear focus has been on amino acids, specifically the simplest amino acid, glycine. Despite theoretical studies and laboratory based work that show that glycine as well as several other amino-acids should form in space (Muñoz Caro *et al.* 2002, Blagojevic *et al.* 2003, Congiu *et al* 2012, Garrod *et al.* 2013) unambiguous detections are still lacking (Snyder *et al.* 2005). The search for two other classes of prebiotic compounds – aldoses (polyhydroxy aldehydes) and polyols – has been more successful. Aldoses are compounds with chemical formula $(CH_2O)_n$ containing one aldehyde (-CHO) group. Well-known members of this series are the simple sugars (monosaccharides) glycose, ribose and erythrose. The simplest representative of this class – glycoladehyde ($HC(O)CH_2OH$) – has been successfully detected towards the solar mass protostar IRAS 16293-2422 by ALMA, see Jørgensen *et al.* (2012) and toward two other objects, the Galactic center source SgrB2(N) (Hollis *et al.* 2000) and high-mass hot molecular core G31.41+0.31 (Beltran *et al.* 2009). The best-known representative of the polyols series is glycerine – a basic compound of fats. Glycerine is a triol and has not been detected in space so far, but ethylen glycol ($H_2C(OH)CH_2OH$), a diol, has been observed toward the Galactic center source SgrB2(N) (Hollis *et al.* 2002) as well as around the low-mass Class 0 protostar NGC 1333-IRAS2A (Maury *et al.* 2014).

From the chemical structure of both aldoses and polyols it is expected that the key stage in the formation of both molecule classes must be the formation of a chain of carbon-carbon bonds. Furthermore each carbon atom in this chain is attached to an oxygen atom resulting in a $-C(O)-C(O)-(C(O))_n-$ backbone. So the crucial stage in the mechanism describing the formation of both $HC(O)CH_2OH$ and $H_2C(OH)CH_2OH$ and other aldoses or polyols not detected in space so far, is the formation of a $-C(O)-C(O)-$ bond. It is here that surface chemistry can play a role. It is generally accepted that carbon-bearing species like CH_3OH, H_2CO, CO_2, and possibly CH_4 form on icy dust grains, as these provide surfaces

on which gas-phase species accrete, meet, and react. Moreover, these icy grains can absorb excess energy released in a chemical reaction, effectively stabilizing products and changing the branching ratio of the reactions. Therefore, in dense cold clouds, icy dust grains act both as a molecular reservoir and as a solid-state catalyst (though they are not considered as a catalyst in the chemical sense). Charnley *et al*. (2001) suggested that the formation of both glycolaldehyde and ethylen glycol proceeds through the following reaction chain:

$$CO + H \rightarrow HCO, \tag{8.1}$$
$$HCO + C \rightarrow HCCO, \tag{8.2}$$
$$HCCO + O \rightarrow HC(O)CO, \tag{8.3}$$
$$HC(O)CO + H \rightarrow HC(O)CHO, \tag{8.4}$$
$$HC(O)CHO + H \rightarrow HC(O)CH_2O/ HC(O)CHOH, \tag{8.5}$$
$$HC(O)CH_2O/ HC(O)CHOH + H \rightarrow HC(O)CH_2OH, \tag{8.6}$$
$$HC(O)CH_2OH + H \rightarrow H_2C(O)CH_2OH/HC(OH)CH_2OH, \tag{8.7}$$
$$H_2C(O)CH_2OH/ HC(OH)CH_2OH + H \rightarrow H_2C(OH)CH_2OH. \tag{8.8}$$

Another formation route suggested later by Charnley & Rodgers (2005) is very similar but with altered sequences of H- and O-atom additions. The reduction reactions (8.1), (8.5)-(8.8) (or similar reactions) are reported to proceed under cold molecular cloud conditions (Hiraoka *et al* 1994, Zhitnikov *et al*. 2002, Watanabe *et al*. 2002, Bisschop *et al*. 2007, Fuchs *et al*. 2009). The reactions (8.2) and (8.3), however, have not been verified experimentally. Furthermore, the formation of a triple -C(O)- backbone will require another place selective addition of a carbon atom to the product of reaction (8.4) followed by an O-atom addition or alternatively will require the addition of a C-atom to the product of reaction (8.2) followed by two place specific oxygen atoms additions. These channels are not considered as effective pathways to form a triple -C(O)- chain.

A considerably more realistic scenario involves reactions between two HCO radicals as produced in the reaction (8.1) yielding Glyoxal:

$$HCO + HCO \rightarrow HC(O)CHO. \tag{8.9}$$

Sequential hydrogenation by 2 or 4 H-atoms turns HC(O)CHO into glycoladehyde and ethylen glycol, respectively, *i.e*., reactions (8.2)-(8.4) in this scheme are replaced by reaction (8.9), see Figure 8.1 for comparison of both schemes. This reaction route may be more relevant than the mechanism suggested by Charnley *et al*. (2001), as: (i) CO-molecules and H-atoms are among the most abundant species in dense molecular clouds and CO is the second most abundant molecule in interstellar ices in the coldest clouds; (ii) the formation of CH_3OH proceeds through sequential hydrogenation of CO

molecules with HCO as a necessary intermediate which guarantees that this radical is formed on the surface of interstellar grains; (iii) reaction (8.9) is a radical-radical recombination and expected to be barrierless which is particularly important for the very low temperatures (~10-15 K) of icy grains in space; (iv) the option for further growth of a $(-C(O)-)_n$ backbone through the addition of another HCO radical remains in the case that an H-atom addition in reaction (8.5) or (8.7) takes place on the O-atom instead of the C-atom. The dimerisation of HCO, reaction (8.9) is considered in a recent work by Woods *et al.* (2013) as one of the formation routes of glycolaldehyde. Their astrophysical model consistent with the observed estimates in the hot molecular core G31.41+0.31 and low-mass binary protostar IRAS 1629-32422.

In this work, we experimentally investigate surface hydrogenation of CO molecules at dense molecular cloud conditions with the goal to verify the formation of side products of methanol with more than one carbon atom. We will show that for our experimental settings, the formation of glycolaldehyde and ethylen glycol indeed can be realized. This is the first time that a regular hydrogenation scheme of CO is found to result in such complex species. In the discussion section we prove that the key reaction in the formation of these species involves a HCO + HCO recombination. We also discuss the possible formation of methyl formate ($HC(O)OCH_3$) that is not found in this study but may be formed under other experimental conditions. Subsequently, the experimental results of this work are implemented into a model used by Cuppen *et al.* (2009) based on the continuous-time, random walk Monte-Carlo method. This model allows for the simulation of microscopic grain-surface chemistry for the long timescales typical in interstellar space, including the layering of ice during the CO freeze out. The choice of microscopic simulations is because HCO radicals have to stay in close vicinity to each other in order for a reaction to occur. Therefore, a method that accounts for the position of the species in the ice lattice is required for the best representation of the system. The astronomical implications are also discussed. First, an overview on the experimental procedure and the performed experiments is given.
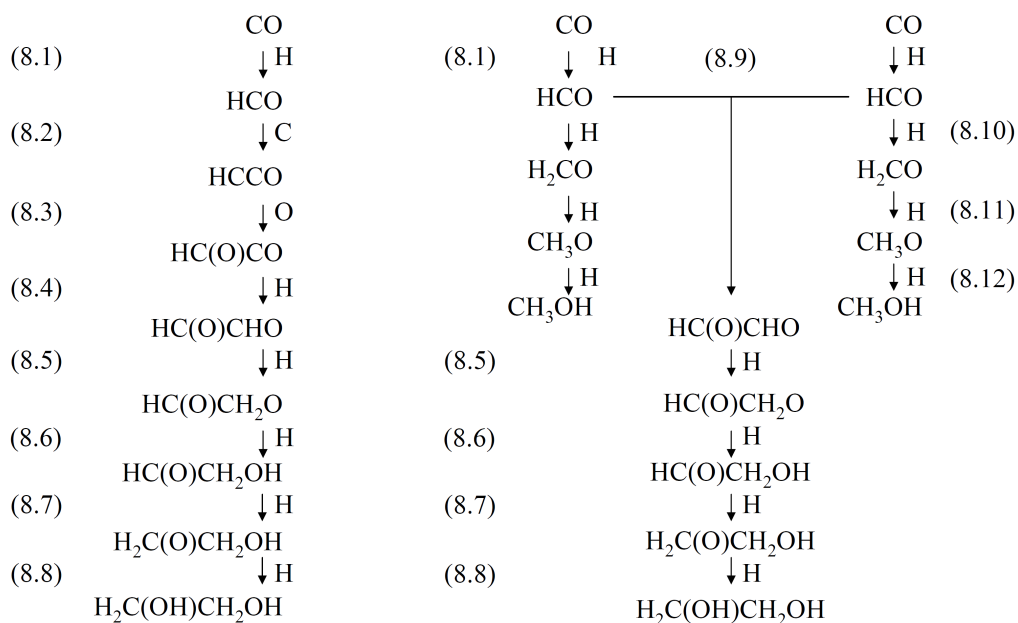
$$
\begin{array}{llll}
(8.1) & \text{CO} \xrightarrow{\text{H}} \text{HCO} & (8.1) & \text{CO} \xrightarrow{\text{H}} \text{HCO} \\
(8.2) & \text{HCO} \xrightarrow{\text{C}} \text{HCCO} & & \text{HCO} \xrightarrow{\text{H}} \text{H}_2\text{CO} \\
(8.3) & \text{HCCO} \xrightarrow{\text{O}} \text{HC(O)CO} & & \text{H}_2\text{CO} \xrightarrow{\text{H}} \text{CH}_3\text{O} \\
(8.4) & \text{HC(O)CO} \xrightarrow{\text{H}} \text{HC(O)CHO} & & \text{CH}_3\text{O} \xrightarrow{\text{H}} \text{CH}_3\text{OH} \\
(8.5) & \text{HC(O)CHO} \xrightarrow{\text{H}} \text{HC(O)CH}_2\text{O} & (8.5) & \text{HC(O)CHO} \xrightarrow{\text{H}} \text{HC(O)CH}_2\text{O} \\
(8.6) & \text{HC(O)CH}_2\text{O} \xrightarrow{\text{H}} \text{HC(O)CH}_2\text{OH} & (8.6) & \text{HC(O)CH}_2\text{O} \xrightarrow{\text{H}} \text{HC(O)CH}_2\text{OH} \\
(8.7) & \text{HC(O)CH}_2\text{OH} \xrightarrow{\text{H}} \text{H}_2\text{C(O)CH}_2\text{OH} & (8.7) & \text{HC(O)CH}_2\text{OH} \xrightarrow{\text{H}} \text{H}_2\text{C(O)CH}_2\text{OH} \\
(8.8) & \text{H}_2\text{C(O)CH}_2\text{OH} \xrightarrow{\text{H}} \text{H}_2\text{C(OH)CH}_2\text{OH} & (8.8) & \text{H}_2\text{C(O)CH}_2\text{OH} \xrightarrow{\text{H}} \text{H}_2\text{C(OH)CH}_2\text{OH}
\end{array}
$$

Right scheme:

$$
\begin{array}{l}
\text{CO} \xrightarrow{\text{H}} \text{HCO} \quad (8.1) \\
\text{HCO} \xrightarrow{\text{H}} \text{H}_2\text{CO} \quad (8.10) \\
\text{H}_2\text{CO} \xrightarrow{\text{H}} \text{CH}_3\text{O} \quad (8.11) \\
\text{CH}_3\text{O} \xrightarrow{\text{H}} \text{CH}_3\text{OH} \quad (8.12)
\end{array}
$$

(8.9) HCO — HC(O)CHO

Figure 8.1. A schematic representation of glycolaldehyde and ethylene glycol formation pathways suggested by Charnley *et al.* (2001) (left scheme) and in this study (right scheme).

8.2 Experimental

Experiments are performed using SURFRESIDE[2], an ultrahigh vacuum (UHV) setup that is described in detail by Ioppolo *et al.* (2011). This setup comprises three UHV chambers; a main chamber with a base pressure ~ 10^{-10} mbar and two chambers housing atom beam lines with base pressures in the range 10^{-10}-10^{-9} mbar. In the main chamber, a sample holder is mounted on the tip of the cold head of a close-cycle He cryostat. The deposition temperature can be controlled between 13 and 300 K with an absolute precision of <2 K and relative precision of about 0.5 K. Two different atom beam lines are used. A Hydrogen Atom Beam Source (HABS, Dr. Eberl MBE-Komponenten GmbH, see Tschersich 2000) produces atoms by thermal cracking of parent molecules passing through the hot tungsten capillary, while a Microwave Atom Source (MWAS, Oxford Scientific Ltd, see Anton *et al.* 2000) generates atoms by cracking their parent molecules in a capacity coupled microwave discharge (175 W at 2.45 GHz). In both cases, a nose-shaped quartz pipe is placed along the path of the atom beam to efficiently quench excited electronic or ro-vibrational states of newly formed atoms and non-dissociated molecules through collisions with the walls of the pipe before these reach the ice sample.

The reactivity of CO with H atoms is investigated systematically at 13 K with the goal to verify the formation of C-C bonds. Experiments are performed using co-deposition, *i.e.*,

CO-molecules are co-deposited simultaneously with H atoms with pre-defined deposition rates. This allows overcoming the main problem of a sequential deposition technique as used before to study formaldehyde and methanol formation upon CO hydrogenation, *i.e.*, low final yields of the products of CO-hydrogenation due to the limited penetration depth of H-atoms into the pre-deposited CO ice (Watanabe *et al.* 2003, Fuchs *et al.* 2009). Using a co-deposition technique with an overabundance of H-atoms over CO-molecules makes that virtually all deposited CO molecules are available for hydrogenation reactions and thick (6-30 monolayers) ice of CO-hydrogenation products can be grown. Furthermore, a co-deposition experiment is a more realistic representation of the conditions at which CO is hydrogenated in dense molecular clouds where simultaneous accretion of CO molecules and H-atoms take place but on much longer timescales (see Cuppen *et al.* 2009).

The newly formed species are monitored *in situ* during co-deposition by means of Fourier Transform Reflection Absorption Infrared Spectroscopy (FT-RAIRS). After finishing the co-deposition, a temperature programmed desorption (TPD) of the ice is routinely performed using quadrupole mass-spectrometry (QMS) to monitor in the gas-phase thermally desorbing species. The use of TPD as a main analytical tool is necessary since the strong IR absorption features of glycoladehyde ($HC(O)CH_2OH$), ethylen glycol ($H_2C(OH)CH_2OH$) and also glyoxal ($HC(O)CHO$) overlap with the absorption bands of H_2CO and CH_3OH, making unambiguous spectroscopic assignments challenging (see also Őberg *et al.* 2009).

Several control experiments are performed to confirm that the formation of glycoladehyde and ethylene glycol takes place indeed at 13 K and that this is not the result of thermal processing, recombination of trapped radicals during the TPD, gas-phase reactions or contaminations in the atom beam lines. Isotope shift experiments using ^{13}CO instead of ^{12}CO or D instead of H are performed to further constrain the results. All experiments are summarized in Table 8.1. The numbering in the first column is used for cross-referencing.

Table 8.1. Overview of performed experiments.

	Experiment	T_{sample}, K	Ratio	CO_{flux}, cm^{-2}s^{-1}	H_{flux}, cm^{-2}s^{-1}	t, min	TPD	Detection[c]
1	CO + H	13	1:5	1.5E12	8E12	360	QMS$^{2K/10K}$	Y
2	CO + H	13	1:5	1.5E12	8E12	360	[b]RAIRS^{2K}	Y
3	CO + H	25	1:5	1.5E12	8E12	360	QMS$^{2K/10K}$	N
4	CO + H	13	1:25	3E11	8E12	360	QMS$^{2K/10K}$	Y
5	CO + H[a]	13	1:25[a]	3E11	8E12[a]	360	QMS$^{2K/10K}$	Y
6	CO + D	13	1:25	3E11	8E12	360	QMS$^{2K/10K}$	N
7	^{13}CO + H	13	1:25	3E11	8E12	360	QMS$^{2K/10K}$	Y
8	CO + H	13	1:25	3E11	8E12	72	QMS$^{2K/10K}$	Y
9	CO + H	13	1:25	3E11	8E12	360	QMS^{5K}	Y
10	CO + H	13	1:25	3E11	8E12	600	RAIRS^{5K}	Y
				CH_3OH_{flux}, cm^{-2}s^{-1}	$H/H_{2\ flux}$, cm^{-2}s^{-1}			
11	CH$_3$OH+H	13	1:25	3E11	8E12	360	QMS^{5K}	N
12	CH$_3$OH+H$_2$	13	1:25	3E11	-	360	QMS^{5K}	N

Experiments are performed using co-deposition technique; X_{flux} is the deposition rate of a selected species expressed in particles per cm^2 per s, T_{sample} is the substrate temperature during co-deposition; t is the time of co-deposition; *TPD* is the temperature programmed desorption experiment performed afterward with the TPD rate indicated, normally the ice is gently warmed up to remove the bulk of CO, then high TPD rate is used to increase the sensitivity of a technique, *Detection* indicates whether glycoladehyde and ethylene glycol are identified.
[a]The microwave discharge is used to generate the H-atom beam instead of a thermal cracking source.
[b]Instead of a TPD with a constant rate, annealing at a number of chosen temperatures is made with a simultaneous RAIR spectra recording.
[c]detection of both glycoladehyde and ethylene glycol in the experiment.

8.3 Results

In Figure 8.2, a typical example of a QMS TPD spectrum is presented for a CO + H experiment at 13 K (exp. 4 in Table 8.1). One can see that in the temperature range from 50 to 250 K, four CO hydrogenation products show up. In addition to peaks originating from the previously detected H$_2$CO (~ 100 K) and CH$_3$OH (~ 140 K) (Hiraoka *et al* 1994, Zhitnikov *et al*. 2002, Watanabe *et al*. 2002, Fuchs *et al*. 2009), there are two more desorption peaks, one centered at 160 K and one at 200 K. The higher desorption temperatures w.r.t. the values for H$_2$CO (100 K) and CH$_3$OH (140 K) are consistent with less volatile and heavier carriers. The TPD QMS spectra provide information to identify the origin of these carriers; molecules desorb at specific temperatures and fragmentation patterns upon electron impact induced dissociative ionization are available for different electron energies for many different species. The potential of this method – linking two different physical properties - is illustrated for the H$_2$CO and CH$_3$OH bands. The desorption bands are linked to mass spectra that can be compared to literature values upon 60 eV electron impact ionization for formaldehyde and methanol, as shown in the two top-left insets in Figure 8.2. The experimental and database fragmentation patterns are very similar. Small inconsistencies are likely due to partial co-desorption of CH$_3$OH with H$_2$CO

at 100 K and *vice versa* co-desorption of H_2CO trapped in the bulk of CH_3OH at 140 K.
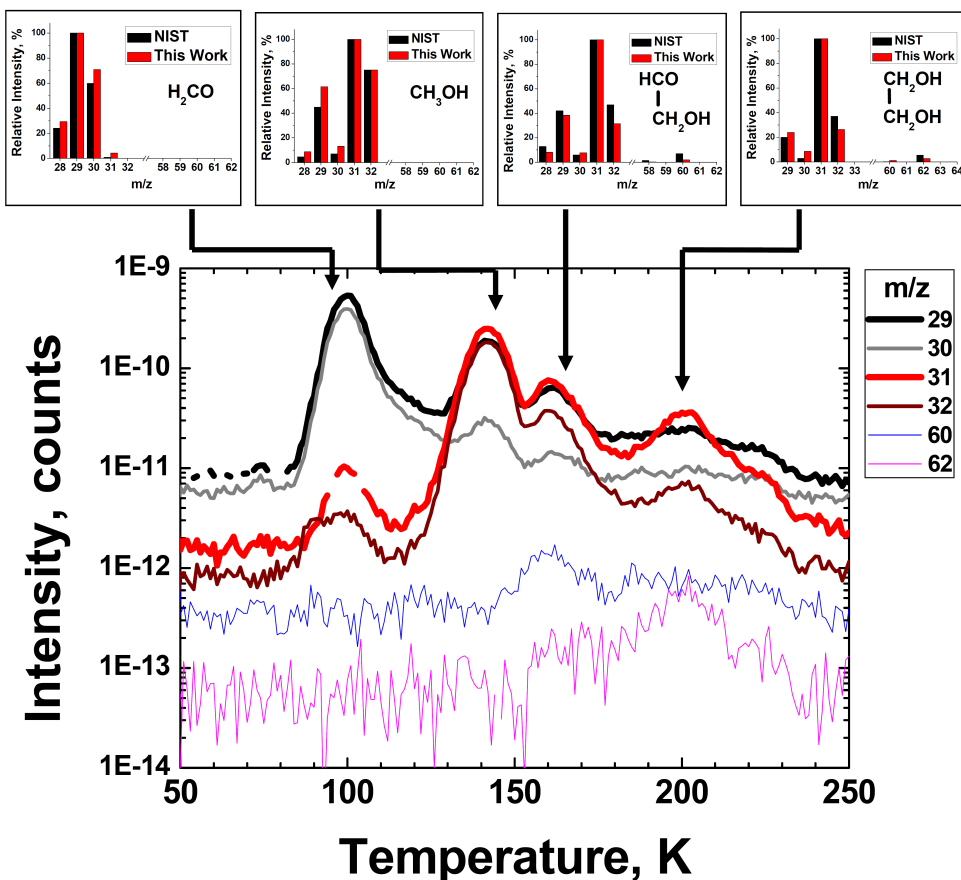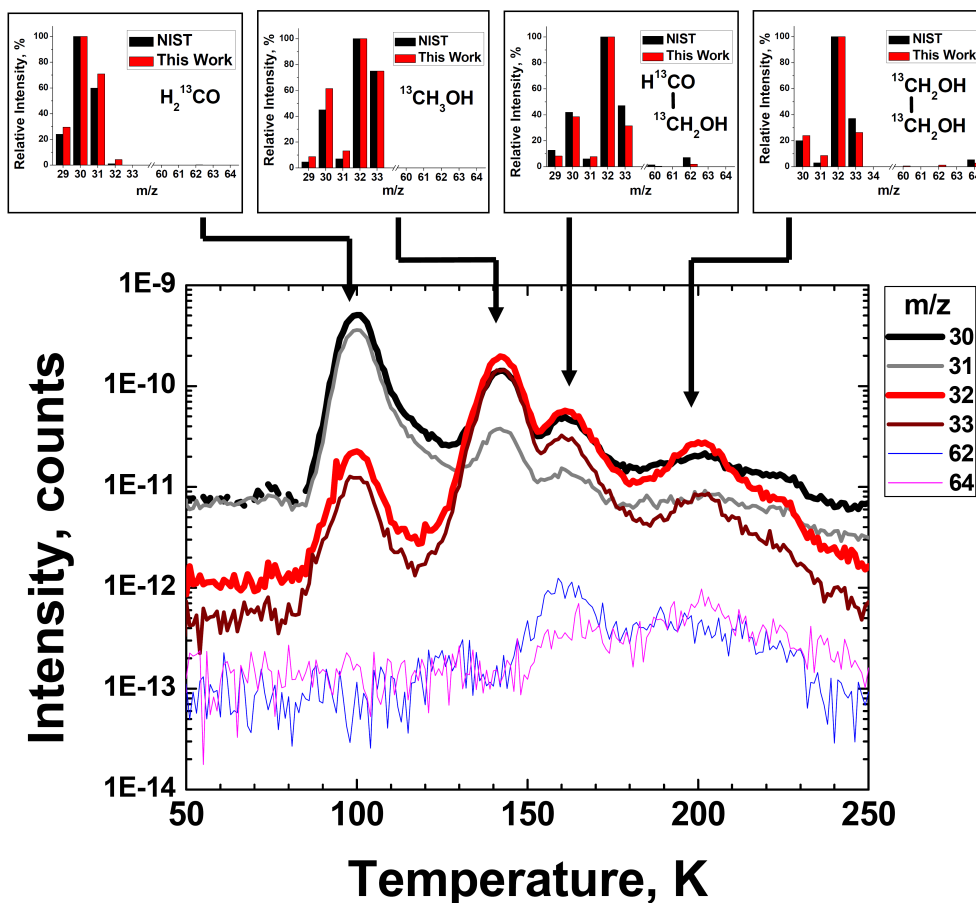

Figure 8.2. TPD spectra obtained after experiment 4 (Table 8.1) for the indicated m/z numbers. Insets on top of the figure compare the fragmentation patterns of desorbing species detected in this experiment upon 60 eV electron impact with those available from literature.

In a similar way, the two additional desorption peaks at 160 K and 200 K can be assigned to glycoladehyde and ethylene glycol, respectively. The desorption temperatures of these species are consistent with the values available from Őberg *et al*. (2009) (see their Figure 12, where CH_3OH, $HC(O)CH_2OH$, and $H_2C(OH)CH_2OH$ desorption peaks are reported to be at 130, 145, and 185 K, respectively). Moreover, the observed fragmentation pattern upon 60 eV electron-impact ionization is very similar to the literature values, as illustrated in the two top-right insets of Figure 8.2.

Figure 8.3. TPD spectra obtained after experiment 7 (Table 8.1) for the indicated m/z numbers. Insets on top of the figure show the comparison between fragmentation patterns of the desorbing species detected in this experiment upon 60 eV electron impact with those available from literature.

This assignment can be further constrained by performing the same experiments using isotopes. Deuteration experiments are not ideal for this. Hidaka *et al.* (2007) found that the CO deuteration rate at 15 K is 12.5 times lower than the corresponding value for hydrogenation. Our experimental results confirm this finding and show a substantial decrease for D-containing products. The D_2CO and CD_3OD formation yields are roughly 10 times lower and the $DC(O)CD_2OD$ and $D_2C(OD)CD_2OD$ signals are below the detection limits. Therefore, ^{13}CO experiments are used to provide additional proof for glycolaldehyde and ethylene glycol formation at our experimental settings. Moreover, with ^{13}CO as precursor, dissociative ionization products containing only one carbon atom will be shifted by one m/z number, while fragments containing two carbon atoms will shift by two. This provides a tool to identify unambiguously C-C bond formations. In Figure 8.3, the

result of co-deposition of H atoms and ^{13}CO molecules is shown, for conditions that are nearly identical to those applied in Figure 8.2. Again, four peaks are found in the TPD QMS spectra. The insets in the top-side of Figure 8.3 compare the fragmentation patterns of desorbing species recorded in our experiment with values obtained by extrapolating literature results. This extrapolation is realized by adding m/z=1 to the masses from 28 to 33 and m/z=2 to the masses from 58 to 64 for the fragmentation pattern of regular ^{12}C glycoladehyde and ethylene glycol, *i.e.*, according to the number of carbon atoms in the corresponding ions. Again the experimental and literature values are very close and fully consistent with the previous finding that glycolaldehyde ($H^{13}C(O)^{13}CH_2OH$) and ethylen glycol ($H_2^{13}C(OH)^{13}CH_2OH$) form along with the formation of $H_2^{13}CO$ and $^{13}CH_3OH$ upon surface hydrogenation of CO molecules.

Repeating experiment 4 depicted in Figure 8.2 for a co-deposition time about twice as long, using RAIRS instead of the QMS allows us to obtain RAIR difference spectra of the two ice constituents desorbing at about 160 and 200 K. The differences are determined by subtracting spectra at 152 and 168 K (Fig. 8.4a), and 183 and 210 K (Fig. 8.4b), *i.e.*, before and after desorption of the two individual TPD features. Low peak-to-noise ratios complicate the identification of absorption features, but tentative assignments can be made. The three strongest absorption features of $HC(O)CH_2OH$ are visible in Fig. 8.4a, *i.e.*, the OH-stretch mode in the range from 3600 to 3000 cm^{-1}, coinciding CH and CH_2 stretching modes in the range from 3000 to 2800 cm^{-1} and the sharp CO stretching mode at 1750 cm^{-1}. Similarly, both OH stretching and CH_2 stretching modes of $H_2C(OH)CH_2OH$ (its strongest absorption features) are visible in Fig. 8.4b, while the absorption feature in the range 1400-1500 cm^{-1} is likely due to CH_2 scissor and OH bending modes. Unfortunately, the C-C stretching mode of $H_2C(OH)CH_2OH$ lies within the range 1000-1100 cm^{-1} that can not be observed due to an artifact caused by difference in the shape of background spectra depending on the temperature of the sample. Furthermore, it overlaps with one of the strongest absorption features of CH_3OH. The C-C stretching mode of $HC(O)CH_2OH$ is expected to be found around 870 cm^{-1} and cannot be assigned due to the low peak-to-noise ratio in this region of the spectra (Buckley & Giguère 1966, Kobayashi *et al*. 1975, Hudson *et al*. 2005, Ceponkus *et al*. 2010).
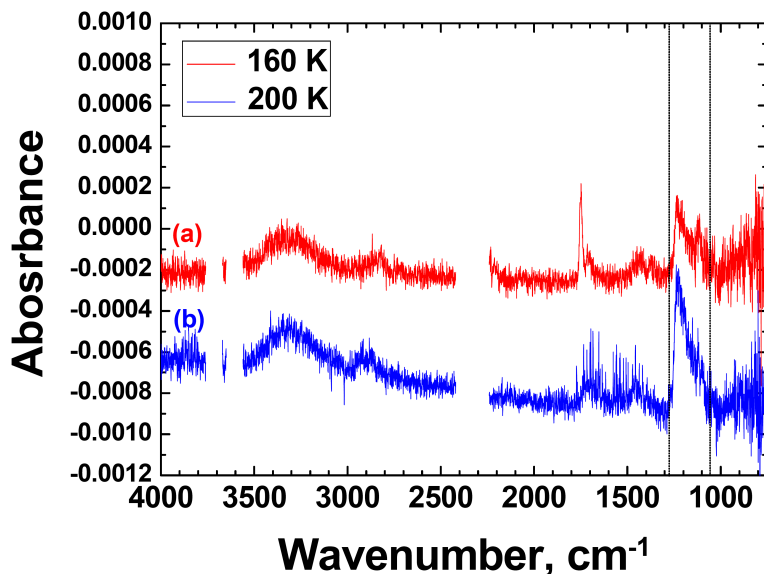
Figure 8.4. RAIR difference spectra obtained between a) 153 and 168 K, and b) 183 and 210 K in experiment 10. The sharp absorption feature in the range between 1270 and 1050 cm^{-1} is an artifact caused by the difference in the shape of background spectra depending on the temperature of the sample. Cuts between 2250-2400 and 3560-3760 cm^{-1} are because of atmospheric CO_2 absorbance along the path of the IR beam outside of the main chamber.

In addition, a number of complementary/control experiments have been performed. An increase of the CO-deposition rate by a factor five (experiment 1), a change of TPD rate or total co-deposition time (experiments 8 and 9), and the use of a microwave discharge source instead of the thermal cracking source to generate the H atoms (experiment 5) all do not qualitatively change the results depicted in Figures 8.2 and 8.3. No HC(O)CH$_2$OH and H$_2$C(OH)CH$_2$OH formation is found for a co-deposition experiment of H atoms with CO molecules at 25 K (instead of 13 K) while only traces of H$_2$CO and CH$_3$OH can be detected (experiment 3). Signatures of glycolaldehyde and ethylene glycol also are not found in CH$_3$OH+H and CH$_3$OH+H$_2$ co-deposition experiments performed under similar conditions and applying similar co-deposition rates (experiments 11 and 12).

8.4 Discussion

The experimental results presented in the previous section show that glycol aldehyde and ethylene glycol can be formed in co-deposition experiments of CO molecules and H atoms. This is an important experimental finding, as so far hydrogenation reactions were mainly shown to be effective in the formation of smaller species (*e.g.*, ammonia from N + H) with

CH₃OH (CO + H) as the largest species systematically studied so far by more than one independent group. Instead, experimental studies showed that solid-state reactions induced by vacuum UV irradiation, cosmic ray or electron bombardment offer pathways to form molecules with up to 10-12 atoms. In Őberg *et al*. (2009), for example, VUV irradiation of a pure methanol ice was shown to result in the formation of both glycolaldehyde and ethylene glycol. The formation scheme presented here does not require energetic processing and can proceed at 13 K. The work discussed here is an extension of the well-studied formaldehyde and methanol (CO+H) formation scheme that is generally accepted as the dominant pathway explaining the observed large CH_3OH abundances in space. Therefore, this process should also be efficient at cold dense clouds conditions, particularly during the CO freeze-out stage that takes place well before radiation from a newly formed protostar becomes important. To which extent, however, the different phases (read processes) in star formation determine glycolaldehyde and ethylene glycol abundances is hard to estimate. Detection of both $HC(O)CH_2OH$ and $H_2C(OH)CH_2OH$ in our experiments as well as a gradual decrease in abundances along the order $H_2CO>CH_3OH>HC(O)CH_2OH>H_2C(OH)CH_2OH$ is consistent with the mechanism proposed in the present work, *i.e*., a sequence of surface reactions (8.1), (8.9), and (8.5)-(8.8).

The only experimental observation that seems to be contradicting our interpretation is the experimental non-detection of glyoxal (HC(O)CHO). A possible explanation is that reaction (8.5) has no or a very low activation barrier, compared to that of reactions (8.1), (8.7) and 8.11):

$$H_2CO + H \rightarrow CH_3O/CH_2OH, \qquad\qquad (8.11)$$

that are the limiting steps in the formation of H_2CO, $H_2C(OH)CH_2OH$, and CH_3OH, respectively. Unfortunately, there exists no experimental data for the activation barrier of reaction (8.5). Galano *et al*. (2004) performed quantum
chemical calculations of the interaction of glyoxal with OH radicals and concluded that the OH addition and formation of an intermediate complex followed by H-atom abstraction proceeds barrierless. This is consistent with experimental gas-phase results of Feierabend *et al*. (2007), who found that H-atom abstraction from glyoxal by OH radicals has a negative temperature dependence with a slight deviation from Arrhenius behavior that is reproduced over the temperature range 210 – 396 K. However, it contradicts the results by Woods *et al*. (2013) who find a barrier of 1100 K in their calculations. Although this activation barrier appears rather high, it can easily be overcome if tunneling is involved, *e.g*., the CO + H barrier is roughly three times higher. In this case we would not necessarily expect to detect glyoxal along with $HC(O)CH_2OH$ and $H_2C(OH)CH_2OH$ for our settings. Therefore, it

seems correct to conclude that the interaction of an H atom with glyoxal proceeds very efficiently, barrierless or through tunneling, followed by an H-atom addition instead of abstraction, consistent with the non-detection of glyoxal in our experiments.

Other possible scenarios leading to the formation of C-C bonds that are mentioned in literature are:

$$HCO + CO \rightarrow HC(O)CO, \tag{8.13}$$

followed by reaction (8.4) to yield HC(O)CHO, and

$$HCO + H_2CO \rightarrow HC(O)CH_2O. \tag{8.14}$$

Reaction (8.13) should possess an activation barrier and leads again to the glyoxal formation, *i.e*., this means that the assumption of a barrierless hydrogenation of glyoxal, as made above, still should hold to explain the observed results. Reaction (8.14) indeed helps to bypass the glyoxal formation as an intermediate and leads directly to the formation of the observed glycolaldehyde through reaction (8.6). However, this reaction also expected to possess an activation barrier and is not reported in literature. Reaction (8.9), therefore, is proposed as the key step responsible for the formation of C-C bonds and we assume that the hydrogenation of glyoxal proceeds barrierless.

We would like to stress that both glycolaldehyde and ethylene glycol are formed *in situ* at 13 K and are not the result of the recombination of the formed HCO and CH_3O/CH_2OH radicals during the TPD. This is because: (i) in the case that trapped radicals do recombine, glyoxal (as the product of HCO dimerisation) should be visible in our experiments (as discussed before, this is not the case); (ii) these radicals are not observed by RAIRS; and iii) a lack of a qualitative difference between experiment 4 and experiments 8 and 9 (where different TPD rates and exposure times are used) is consistent with the conclusion that both glycolaldehyde and ethylene glycol are not the result of thermally induced chemistry.

Moreover, up to our knowledge, there exist no systematic studies for $CO:H_2CO:CH_3OH$ mixtures, while thermally induced chemistry of pure CH_3OH (experiment 12) and H_2CO (Schutte *et al*. 1993, Noble *et al*. 2012) do not result in the formation of $HC(O)CH_2OH$ or substantial amounts of $H_2C(OH)CH_2OH$. Furthermore, in experiments where pure H_2CO and CH_3OH are first irradiated by UV-photons and then analyzed by means of TPD the formation of glycolaldehyde or ethylene glycol are not reported either, while the methyl formate ($HC(O)OCH_3$) is clearly observed (Gerakines *et al*. 1996). The non-detection of abundant $HCOOCH_3$ in our experiments confirms that our results are due to non-energetic processing.

Another important point is that under our experimental conditions, the H$_2$CO yields dominate over the CH$_3$OH yields, and this then applies to intermediate products of H$_2$CO hydrogenation through reaction (8.11) that are expected to be less abundant than HCO – a product of CO hydrogenation. Therefore, we expect that CH$_3$O and CH$_2$OH are not abundant in our experiments and will not contribute significantly to the reactions that lead to the formation of complex species.

However, subsequent interactions of CH$_3$O or CH$_2$OH with HCO radicals may lead to the formation of methyl formate (HC(O)OCH$_3$) and again glycolaldehyde:

$$HCO + CH_3O \rightarrow HC(O)OCH_3, \tag{8.15}$$
$$HCO + CH_2OH \rightarrow HC(O)CH_2OH. \tag{8.16}$$

Only traces of the methyl formate are found in experiment 1 (Table 1), and these are actually within the experimental uncertainty. In the future, another set of experiments with a significantly higher hydrogenation degree of CO may verify the possibility of reactions (8.15) and (8.16) to occur, but for the moment we consider this outside the scope of the present work.

8.5 Astrochemical implications

The astrochemical importance of the experimental findings discussed here is that the formation of complex molecules can be realized in the dark ages of star formation, *i.e.*, in a period than energetic processing is expected not to be very relevant. The focus here has been on two important species: glycolaldehyde is often considered to be the simplest monosaccharide, and ethylene glycol is the first representative of the polyol family, of which the triol glycerine is the best known one.

The solid state reaction schemes at play have to be understood to fully benefit from identifications in the interstellar medium and to understand where molecules of (pre)biotic interest are likely to be formed. To investigate the possible astrochemical relevance of the laboratory findings presented here we have implemented the new suggested reaction route (8.1), (8.9), (8.5)-(8.8) into a model previously used to simulate the formation of H$_2$CO and CH$_3$OH on interstellar ice surfaces. This model utilizes the continuous-time random-walk Monte Carlo method, which simulates microscopic grain-surface chemistry for timescales as typical for the interstellar medium. This model has been described in detail in Fuchs *et al.* (2009) and Cuppen *et al.* (2009), and for details the reader is referred to these papers. The model simulates a sequence of processes that can occur on a grain surface. This grain surface is modeled as a lattice with the number of sites determined by the size of the grain and the site density for the adsorbing CO. The order of this sequence is determined by means of a

random number generator in combination with the rates for the different processes. These processes include deposition onto the surface, hopping from one lattice site to a nearest neighbor, desorption of the surface species, and reactions between two species. Each of these processes is characterized by a specific rate through an activation energy barrier. Here we use reaction activation barriers and energy parameters determining hopping and desorption activation barriers as derived in Fuchs *et al.* (2009). In order to incorporate formation routes to the newly observed species, the model is extended and five new reactions are incorporated in the chemical network. Reactions (8.9), (8.6), and (8.8) are set to be barrierless as radical-radical recombination reactions, reaction (8.5) is also set to be barrierless (see aforementioned discussion), while reaction (8.7) is set to have an activation energy barrier of the same value as the comparable reaction (8.11) obtained by Fuchs *et al.* (2009). The reaction rate coefficients used in the simulations are summarized in Table 8.2. Consequently, five new species, including glycolaldehyde and ethylene glycol, need to be introduced in the simulations and these are $HC(O)CHO$, $HC(O)CH_2O/HC(O)CHOH$, $HC(O)CH_2OH$, $H_2C(O)CH_2OH/HC(OH)CH_2OH$ and $H_2C(OH)CH_2OH$. Since all of them are heavy, low-volatile species, the energy parameter E responsible for the hopping and desorption of species is set to the same value as for CH_3OH, effectively immobilizing these species.

Table 8.2. A list with the reaction rate coefficients, R_{react}, for the key reactions used in the simulations at 12 and 16.5 K grain temperatures (see Fuchs *et al.* 2009 for more details).

N	Reaction	R_{react} (s^{-1}) for 12 K	R_{react} (s^{-1}) for 16.5 K	N	Reaction	R_{react} (s^{-1}) for 12 K	R_{react} (s^{-1}) for 16.5 K
(1)	$CO + H$	$2 \cdot 10^{-3}$	$4 \cdot 10^{-3}$	(9)	$HCO + HCO$	$2 \cdot 10^{11}$	$2 \cdot 10^{11}$
(10)	$HCO + H$	$2 \cdot 10^{11}$	$2 \cdot 10^{11}$	(5)	$HC(O)CHO + H$	$2 \cdot 10^{11}$	$2 \cdot 10^{11}$
(11)	$H_2CO + H$	$2 \cdot 10^{-4}$	$2 \cdot 10^{-2}$	(6)	$HC(O)CH_2O/ HC(O)CHOH$	$2 \cdot 10^{11}$	$2 \cdot 10^{11}$
(12)	$CH_3O/CH_2OH + H$	$2 \cdot 10^{11}$	$2 \cdot 10^{11}$		$+ H$		
				(7)	$HC(O)CH_2OH + H$	$2 \cdot 10^{-4}$	$2 \cdot 10^{-2}$
				(8)	$H_2C(O)CH_2OH/$	$2 \cdot 10^{11}$	$2 \cdot 10^{11}$
					$HC(OH)CH_2OH + H$		

In Figure 8.5, the outcome of four different test simulations is presented. The lower panels show simulations using identical input parameters as for the simulations presented in the lower panels of Figure 3 in Cuppen *et al.* (2009), but with the four new reaction routes added to the code. These parameters are $n_H = 1 \cdot 10^5$ cm^{-3}, $n_{grain} = 1 \cdot 10^{-12} n_H$ and the gas-phase CO initial abundance equals to $n(CO)_{initial} = 1 \cdot 10^{-4} n_H$, *i.e.* 10 cm^{-3}. In these two runs, a high value for the hydrogen atom density $n(H) = 10$ cm^{-3} (Goldsmith & Li 2005) is used as described in Cuppen *et al.* (2009). The corresponding grain temperatures are 12 and 16.5 K

for panels c and d, respectively. In the upper panel the results of the same simulations are presented, but here the H-atom density is set 10 times less than in the simulations presented in the lower panel of Figure 8.5 and equals n(H) = 1 cm^{-3} (Duley & Williams 1984). This represents the low H-atom density case. All results are converted to grains with a standard size of 0.1 μm. The choice of n(H) to be 10 cm^{-3} and 1 cm^{-3} for high- and low-density cases, respectively, reflects two extreme conditions; i) when most of the CO will be hydrogenated to the final product, *i.e.*, CH$_3$OH, and ii) most of the CO will be locked in a non-hydrogenated state. A more realistic n(H) value is likely closer to 2-3 cm^{-3}, and is covered within the two boundary conditions discussed here.

The CO, H$_2$CO and CH$_3$OH abundances shown in the two lower panels of Figure 8.5 follow the same trends and similar abundances (for the same input parameters) as in Cuppen *et al* (2009) (see lower panel of their Figure 3). This is also expected. The upper panels show the H atom low-density case that was not discussed in Cuppen *et al* (2009). A further extension is realized by inclusion of the five new reaction routes that are incorporated in our code and that aim at introducing glycolaldehyde and ethylene glycol formation in interstellar reaction schemes, following the experimental confirmation discussed in the previous section of this paper. Therefore, two additional curves are presented in panels a and c that show the evolution of the HC(O)CH$_2$OH and H$_2$C(OH)CH$_2$OH abundances, respectively.

Both abundances experience a clear growth, and the glycolaldehyde abundance correlates with the formaldehyde abundance, while the abundance of ethylene glycol correlates with the abundance of methanol. This is not surprising since both CH$_3$OH and H$_2$C(OH)CH$_2$OH are hydrogen saturated species while both H$_2$CO and HC(O)CH$_2$OH are not. The HC(O)CH$_2$OH/H$_2$CO ratio is kept within a 3-5 % range, while the H$_2$C(OH)CH$_2$OH/CH$_3$OH ratio is about 2-4 %. These relatively high values for HC(O)CH$_2$OH and H$_2$C(OH)CH$_2$OH formation are in fact of the same order as derived from the experiments shown in Figures 8.2 and 8.3. An exact comparison of the amounts of formed species requires a precise knowledge of ionization cross-sections for all desorbing species as well as their pumping efficiencies, and this information is not available. A rough estimation, however, can be given just by integrating the corresponding areas in the TPD curves. By comparing the QMS TPD areas for all four species, HC(O)CH$_2$OH/H$_2$CO and H$_2$C(OH)CH$_2$OH/CH$_3$OH ratios are found in the range of 1-9% (depending on the m/z number used for comparison), covering the 3-5 and 2-4 % values mentioned above.

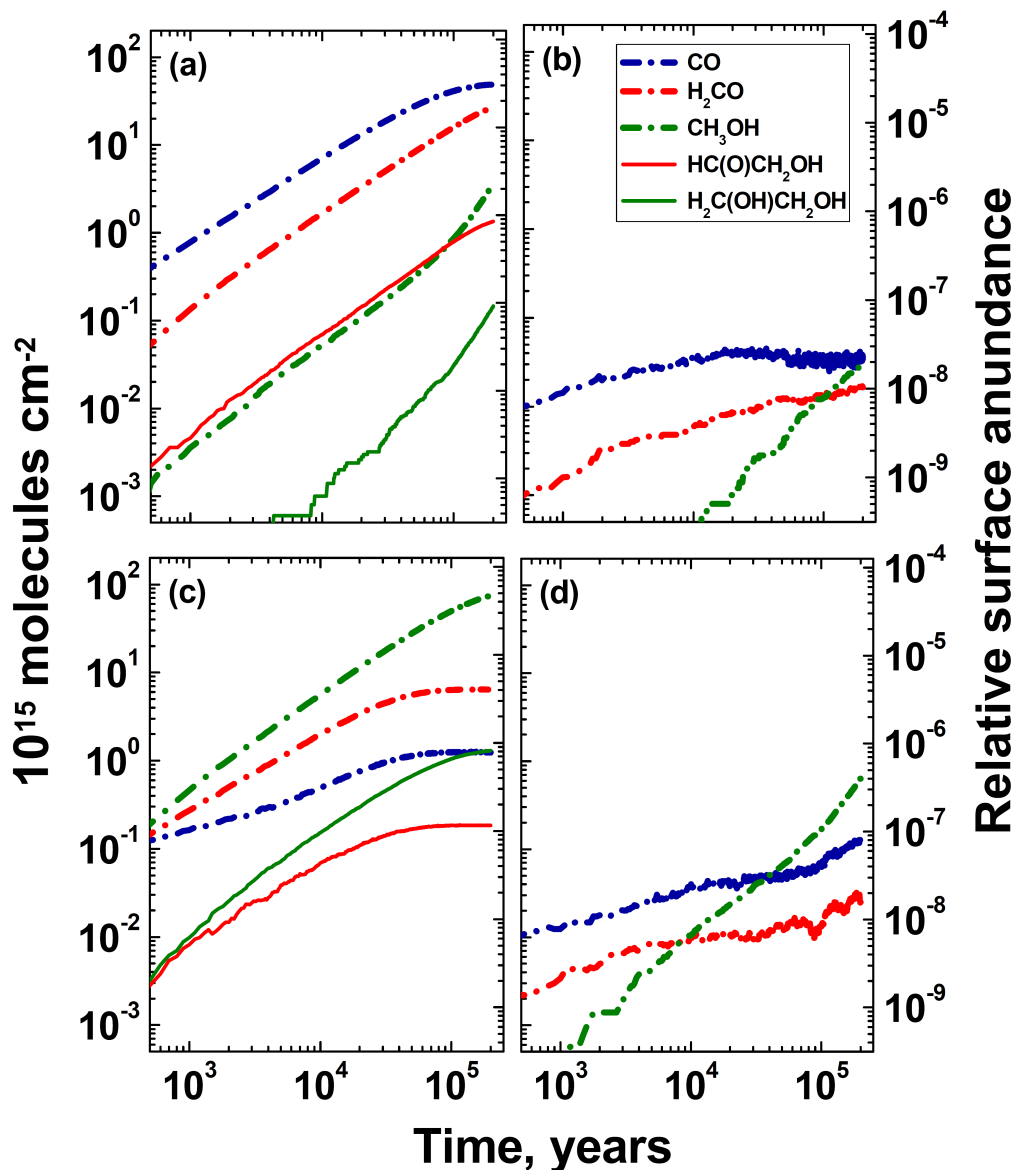**Figure 8.5.** CO, H_2CO, CH_3OH, $HC(O)CH_2OH$ and $H_2C(OH)CH_2OH$ build up as a function of time for n_H $= 1\cdot10^5$ cm^{-3}, $n_{grain} = 1\cdot10^{-12}\,n_H$ and $n(CO)_{initial} = 1\cdot10^{-4}\,n_H$. (a) T = 12 K and $n(H)$ = 1 cm^{-3} (b) T = 16.5 K and $n(H)$ = 1 cm^{-3} (c) T = 12 K and $n(H)$ = 10 cm^{-3} (d) T = 16.5 K and $n(H)$ = 10 cm^{-3}. The relative surface abundance is given with respect to n_H.

It should be noted that the new reaction channels introduced here, leading to the formation of $HC(O)CH_2OH$ and $H_2C(OH)CH_2OH$ do not affect the CO, H_2CO, and CH_3OH abundances and their dependencies, and, consequently, do not change previous conclusions from Cuppen *et al* (2009). This is mainly due to the low final amount of glycolaldehyde and

ethylene glycol formed in the simulations that lock only a few % of the originally available CO.

In Figure 8.6, the cross sections of the grown ice mantles are shown, similar to Cuppen *et al* (2009) (see their Figures 5 and 6). Correlations between the abundances of glycolaldehyde and formaldehyde and between the abundances of ethylene glycol and methanol find a further confirmation in these plots. Moreover, one can see that the distribution of $HC(O)CH_2OH$ (light green) among the cross-section of the ice mantle matches the H_2CO (orange) distribution, while $H_2C(OH)CH_2OH$ (dark green) correlates with the CH_3OH (red), further suggesting that these species are chemically linked.
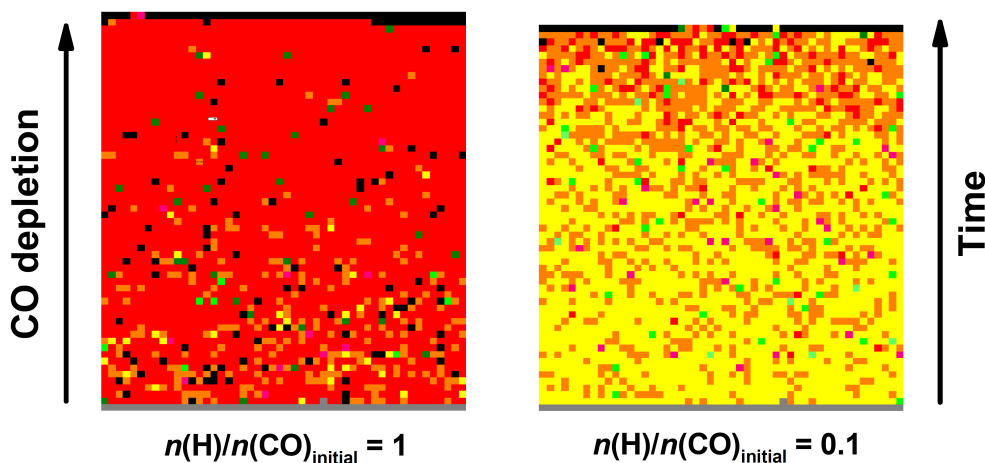
Figure 8.6. Schematic picture of the growth of the ice mantle after $2 \cdot 10^5$ years at $n_H = 1 \cdot 10^5 \, cm^{-3}$, $n_{grain} = 1 \cdot 10^{-12} n_H$ and $n(CO)_{initial} = 1 \cdot 10^{-4} n_H$ for 12 K grain temperature. Left panel $n(H) = 10 \, cm^{-3}$. Right panel $n(H) = 1 \, cm^{-3}$. Grain surface is indicated by brown colour, unoccupied cites by black, CO is yellow, H_2CO is orange, CH_3OH is red, $HC(O)CH_2OH$ is light green, and $H_2C(OH)CH_2OH$ is dark green. Magenta corresponds to all kinds of intermediate radicals.

As stated before, this combined experimental and theoretical study shows that formation of both glycolaldehyde and ethylene glycol may take place already in the prestellar stage well before energetic processing of the ice by the newly formed protostar will take place. The correlation between the abundances of $HC(O)CH_2OH$ and $H_2C(OH)CH_2O$ with those of formaldehyde and methanol, typically in ratios of the order of a few percent, is as expected. CH_3OH is a common component of interstellar ices, and its formation mainly proceeds through sequential surface hydrogenation of CO molecules during the CO-freeze-out stage. We therefore expect that the formation of both $HC(O)CH_2OH$ and $H_2C(OH)CH_2O$ proceeds during the same stage of the molecular cloud evolution as the formation of CH_3OH ice, but with substantially lower abundances.

It is hard to say more on how this relates to complex molecule formation during a later stage, upon energetic processing. UV photo-processing of interstellar ice analogues has been proposed as the way to form prebiotic species in space. Early experiments, pioneered by Hagen, Allamandola, and Greenberg (1979), revealed that such molecules form upon long term vacuum UV exposure of low temperature ices comprising a mixture of astronomically relevant constituents. This discovery has motivated many of the ice chemistry studies that were performed in the following decades, with two key papers published by Bernstein *et al.* (2002) and Munoz-Caro *et al.* (2002). In Öberg *et al.* (2009) the formation of larger complex species, including glycolaldehyde and ethylene glycol have been extensively described upon Lyman-α irradiation of pure methanol ice. In Table 6 of Öberg *et al.* (2009) a comparison is made for the abundance ratios of complex molecules in the gas phase detected towards a variety of astrophysical environments and the ratios found upon vacuum UV processing of a pure methanol ice.

It is not our intention to discriminate between H-atom addition and UV irradiation processes, or others, like electron bombarded ice as described by Arumainayagam et al. (2010), but to show that solid state reactions as these and studied in the laboratory offer a pathway for complex molecule formation in space. In this paper, this is discussed for the first time for sequential atom addition reactions. Glycolaldehyde has been successfully detected toward the low-mass protostar IRAS 16293-2422 (Jørgensen *et al.* 2012) with abundances of $6 \cdot 10^{-9}$ relative to H_2. This reported gas-phase abundance is well below the abundance of $HC(O)CH_2OH$ obtained in our simulations (see Figure 8.5) and therefore consistent with a scenario where it has been sublimated or non-thermally desorbed from the solid state. It is also worth comparing abundance ratios, specifically for species that are considered to be chemically linked (*i.e.*, $HC(O)CH_2OH/H_2CO$ and $H_2C(OH)CH_2OH/CH_3OH$). In a rough model one may assume that solid-state and gas-phase ratios should be comparable, although we stress that different desorption mechanisms – (non) thermal desorption, chemisorption, or even grain collisions – may have different efficiencies for different molecules, specifically over large time scales covering different evolutionary stages. However, as stated above, the goal here is to show that the numbers have the right order of magnitude. Observations toward the same source performed by Schöier *et al.* (2002) reported a gas-phase H_2CO abundance of $6 \cdot 10^{-8}$ and a solid-state abundance of $(1-4) \cdot 10^{-6}$ relative to H_2, yielding a gas-phase $HC(O)CH_2OH/H_2CO$ ratio of 10 %, comparable within the uncertainties to the 3-5 % value found in the simulations and (1-9)% concluded from the experiments. In a similar way, correlations between ethylene glycol and methanol abundances yield $H_2C(OH)CH_2OH/CH_3OH$ ratios of 2-4 % found in the simulations and (1-9)% in the experiments. Jørgensen *et al.* (2012) give a tentative assignment of $H_2C(OH)CH_2OH$ toward the low-mass protostar IRAS 16293-2422 with a relative abundance of ethylene glycol of 0.3-0.5 with respect to glycolaldehyde, *i.e.*, $(2-3) \cdot 10^{-9}$, while Schöier *et al.* (2002) for the

same source reported CH_3OH abundance of $3 \cdot 10^{-7}$. This results in a $H_2C(OH)CH_2OH/CH_3OH$ ratio of about 1%.

More observational data, specifically in the prestellar phase are needed to link the present hydrogenation laboratory data to solid state efficiencies in space. The important conclusion that stands is that atom addition reactions – in the past specifically proposed as important for the formation of smaller molecules, including H_2O and NH_3, also can contribute to molecular complexity in space, *i.e.*, far beyond methanol formation.

References

Anton R., Wiegner T., Naumann W., Liebmann M., Klein Chr., Bradley C., 2000, RSI, 71, 1177

Arumainayagam C. R., Lee H. L., Nelson R. B., Haines D. R, Gunawardane R. P., 2010, Surf. Sci. Rep., 65, 1

Beltrán M. T., Codella C., Viti S., Neri R., Cesaroni R., 2009, ApJL, 690, L93

Bernstein M. P., Dworkin J. P., Sandford S. A., Cooper G. W., Allamandola L. J., 2002, Nature, 416, 401

Bisschop S. E., Fuchs G. W., van Dishoeck E. F., Linnartz H., 2007, A&A, 474, 1061

Blagojevic V., Petrie S., Bohme D. K., 2003, MNRAS, 339, L7

Buckley & Giguère, 1967, Canadian Journal of Chemistry. 45, 397

Ceponkus J., Chin W., Chevalier M., Broquier M., Limongi A., Crépin C., 2010, JCP, 133, 094502

Charnley S. B., Rodgers S. D., 2005, Astrochemistry: Recent Successes and Current Challenges, Proceedings of the 231st Symposium of the International Astronomical Union held in Pacific Grove, 237

Charnley S. B., Rodgers S. D., Ehrenfreund P., 2001, A&A, 378, 1024

Congiu E., Fedoseev G., Ioppolo S., Dulieu F., Chaabouni H., Baouche S., Lemaire J. L., Laffon C., Parent P., Lamberts T., Cuppen H. M., Linnartz H., 2012a, ApJL, 750, L12

Cuppen H. M., van Dishoeck E. F., Herbst E., Tielens A. G. G. M., 2009, A&A, 508, 275

Duley W. W. & Williams D. A., 1984, Interstellar chemistry, ed. W. W. Duley & D. A. Williams

Faraday Discuss., 2014, 168, 287

Feierabend K. J., Zhu L., Talukdar R. K., Burkholder J. B., 2008, J. Phys. Chem. A, 112, 73

Fuchs G. W., Cuppen H. M., Ioppolo S., Bisschop S. E., Andersson S., van Dishoeck E. F., Linnartz H., 2009, A&A, 505, 629Galano A., Alvarez-Idaboy J. R., Ruiz-Santoyo M. E., Vivier-Bunge A., 2004, ChemPhysChem, 5, 1379

Garrod R.T., 2013, ApJ, 765, 60

Gerakines P. A., Schutte W. A., Ehrenfreund P., 1996, A&A, 312, 289

Goldsmith P. F. & Li D., 2005, ApJ, 622, 938

Hagen W., Allamandola L. J., Greenberg J. M., 1979, Astrophys. Space. Sci., 65, 215

Hidaka H., Kouchi A., Watanabe N., 2007, JCP, 126, 204707

Hiraoka K., Ohashi N., Kihara Y., Yamamoto K., Sato T., Yamashita A., 1994, Chem. Phys. Lett., 229, 408

Hollis J. M., Lovas F. J., Jewell P. R., 2000, ApJ, 540, L107

Hollis J. M., Lovas F. J., Jewell P. R., Coudert L. H., 2002, ApJ, 571, L59

Hudson R. L., Moore M. H., Cook A. M., 2005, .Adv. in Space Res., 36, 184

Ioppolo S., Fedoseev G., Lamberts T., Romanzin C., Linnartz H., 2013, RSI., 84, 073112

Jørgensen J. K., Favre C., Bisschop S. E., Bourke T. L., van Dishoeck E. F., Schmalzl M., 2012, ApJL, 757, L4

Kobayashi Y., Takahara H., Takahashi H., Higasi K., 1976, J. Mol. Struct., 32, 235

Maury A. J., Belloche A., André Ph., Maret S., Gueth F., Codella C., Cabrit S., Testi L., Bontemps S., 2014,

A&A, 563, L2

Muñoz Caro G. M., Meierhenrich U. J., Schutte W. A., Barbier B., Arcones Segovia A., Rosenbauer H., Thiemann W. H.-P., Brack A, Greenberg J. M., 2002, Nature, 416, 403

Munoz-Caro G. M., Meierhenrich U. J., Schutte W. A., 2002, Nature, 416, 403

Noble J. A., Theule P., Mispelaer F., Duvernay F., Danger G., Congiu E., Dulieu F., Chiavassa T., 2012, A&A, 543, A5

Öberg K. I., Garrod R. T., van Dishoeck E. F., Linnartz H., 2009, A&A, 504, 891

Schöier F. L., Jørgensen J. K., van Dishoeck E. F., Blake G. A., 2002, A&A, 390, 1001

Schutte W. A., Allamandola L. J., Sandford S. A., 1995, Adv. Space Res., 15, 401

Snyder L. E., Lovas F. J., Hollis J. M., Friedel D. N., Jewell P. R., Remijan A., Ilyushin V. V., Alekseev E. A., Dyubko S. F., 2005, ApJ, 619, 914

Tschersich K. G., 2000, J. Applied Phys., 87, 2565

Watanabe N., Kouchi A., 2002, ApJ, 571, L173

Watanabe N., Shiraki T., Kouchi A., 2003, ApJ, 588, L121

Woods P. M., Slater B., Raza Z., Viti S., Brown W. A., Burke D. J., 2013, ApJ, 777, 90

Zhitnikov R. A., Dmitriev Yu. A., 2002, A&A, 386, 1129

Atoom additie reacties in interstellair ijs:
Nieuwe routes richting moleculaire complexiteit in de ruimte

Introductie

Het interstellair medium (ISM) is een zeer ijle omgeving, bestaande uit gas, stof en ijs; het speelt echter wel een belangrijke rol in de evolutie van ons sterrenstelsel. Het gas (99% qua massa) en ijzige stof deeltjes (1%) zijn de overblijfselen van dode sterren en tegelijkertijd ook de bouwstenen van nieuwe sterren en planeten. Het gas bestaat vooral uit waterstof (H, 70%), helium (He, 28%) en slechts een klein deel bestaat uit zwaardere elementen, terwijl het stof voornamelijk is opgebouwd uit silicaat deeltjes en koolstofhoudend materiaal. Een goed begrip van de vele fysische en chemische processen die plaatsvinden in het ISM is nodig om de processen die uiteindelijk tot ster- en planeetvorming leiden te kunnen beschrijven. Momenteel is onomstotelijk vastgesteld dat er meer dan 180 verschillende moleculen in het ISM voorkomen. Ruim 50 van deze moleculen bestaan uit 6 of meer atomen en worden daarmee gezien als 'complexe' moleculen. Sommige worden in de gas fase gevormd, maar van andere moleculen, zoals water, koolstofdioxide, methanol, ammonia, mierenzuur en het grotere dimethylether, glycolaldehyde en etheenglycol wordt aangenomen dat deze in het ISM via oppervlakte reacties op ijzige stofdeeltjes ontstaan. Bij oppervlakte reacties spelen niet-energetische reacties tussen twee neutrale moleculen een belangrijke rol. De studie van dit soort reacties in het laboratorium is het onderwerp van dit proefschrift. Ze zijn vooral van belang tijdens een specifiek evolutionair stadium in de stervormingscyclus, het zogenaamde donkere wolk stadium, wanneer een jonge ster wordt gevormd, maar de ster nog niet geboren is. In dit stadium zijn de stofdeeltjes bedekt met een laagje ijs hetgeen een reservoir met moleculen oplevert. Niet-energetische processen geïnitieerd door 'bombardementen' van het ijzige stofdeeltje met vrije atomen, voornamelijk waterstof (H), maar ook deuterium (D), stikstof (N), zuurstof (O), stikstof (N) and koolstof (C), ontketenen een fascinerende vaste stof chemie die resulteert in de vorming van kleinere moleculen, zoals water, maar ook van COMs: complexe organische moleculen. Grootschalige astronomische waarnemingsprojecten bevestigen dat donkere interstellaire wolken een rijke chemie bezitten. Omdat het juist in deze regio's is waar nieuwe ster en planeten ontstaan, zijn laboratorium experimenten belangrijk, zodat wetenschappers in staat zijn de link te maken tussen interstellaire chemie en het ontstaan van organische moleculen, zoals die op aarde aanwezig zijn en hebben bijgedragen aan het ontstaan van het leven.

SURFRESIDE[2] (Hoofdstuk 2)

De vooruitgang in ultra-hoog vacuum cryogene oppervlakte technieken en de

beschikbaardheid van intense atoom bundels hebben ervoor gezorgd dat het sinds enkele jaren mogelijk is om atoom additie reacties in interstellair ijs analogen in detail te bestuderen. De meerderheid van de experimenten beschreven in dit proefschrift is uitgevoerd met SURFRESIDE[2] (SURFace Reaction Simulation Device – vrij vertaald Oppervlakte Reacties Simulatie Apparaat), een nieuwe ultrahoog vacuum (UHV) opstelling die volledig is gewijd aan het ondezoek van reacties in interstellair ijs. De opstelling is afgebeeld op de foto in figuur 1 en de experimentele details staan beschreven in hoofdstuk 2. De opstelling is ontworpen om atoom (H, D, N, O) en radicaal (OH, NH, NH_2) additie reacties in interstellaire ijs analogen te bestuderen bij zeer lage (astronomisch relevante) temperaturen, zo'n 13 K (ongeveer 260 graden onder nul). Het gebruik van een dubbele atoom bundel maakt het mogelijk dat een ijs wordt blootgesteld aan de gelijktijdige inwerking van verschillende soorten atomen en radicalen en dat zorgt ervoor dat het aantal mogelijk te bestuderen reactie routes aanzienlijk toeneemt. Een ander belangrijk kenmerk is de aanwezigheid van twee onafhankelijke moleculaire depositie bundels. Dit maakt het mogelijk om ijs te groeien onder verschillende co-depositie condities. Zo kan H_2O gebruikt worden om waterrijk polair ijs te simuleren, terwijl CO een apolair ijs nabootst. Als gevolg daarvan kan de invloed van polariteit op specifieke reacties en van interacties tussen de reactant en ijs componenten systematisch worden geverifieerd. Voor de diagnostiek worden infrarood spectroscopie – RAIRS - en massa spectrometrie - TPD QMS - gebruikt. Het is hiermee mogelijk het ijs *in situ* te onderzoeken.
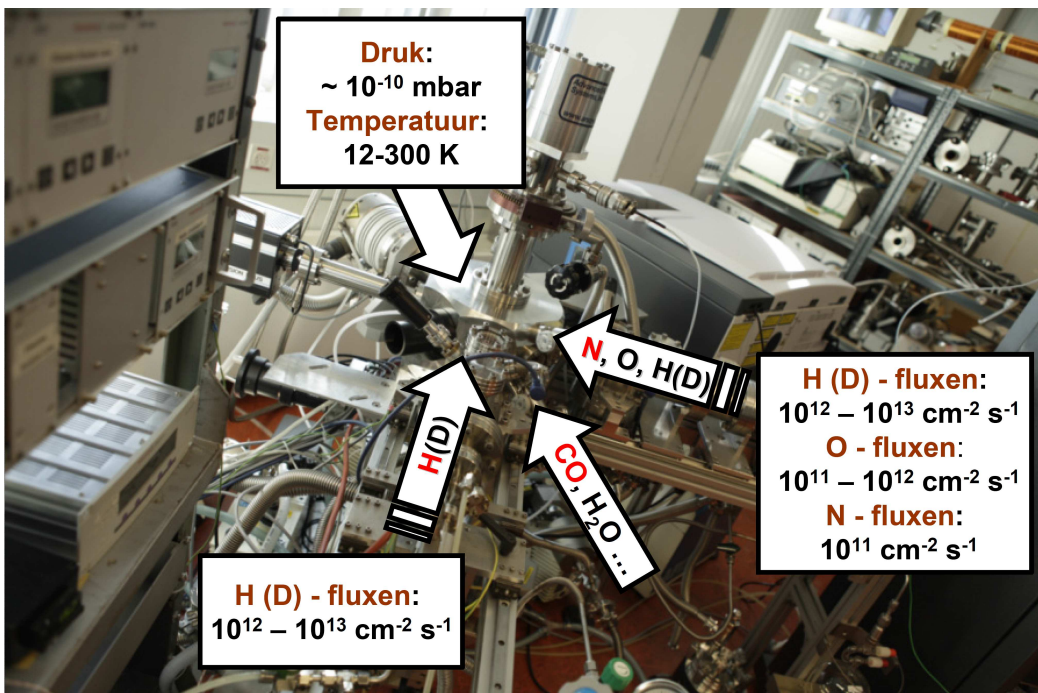
Figuur 1. SURFRESIDE[2]

De flux van H-, D-, N-, en O- atomen is kwantitatief gekarakteriseerd. Daardoor biedt SURFRESIDE[2] niet alleen de mogelijkheid om reactieschema's te visualiseren, maar ook de reacties die plaatsvinden te kwantificeren. H- en D- atoom fluxen zijn vastgesteld aan de hand van Quadrupool Massa Spectrometrie, een welbekende methode. De N- en O- atoom fluxen zijn indirect gekwantificeerd, door te kijken naar reacties waarvan de verwachte conversie efficiëntie gelijk is aan 1. De combinatie van ultrahoog vacuum (UHV~10^{-10} mbar) gekwantificeerde atoom fluxen, een nauwkeurige temperatuurscontrole (13-300 K), RAIRS en/of TPD QMS als detectiemethoden, maakt het mogelijk reacties in het ijs systematisch te bestuderen. Het uiteindelijke doel van dit onderzoek is om te begrijpen of, hoe en hoe effectief de vorming van COMs is. De resultaten daarvan kunnen direct worden vergeleken met astronomische waarnemingen of als input voor astrochemische simulaties die de donkere periode in het stervormingsproces nabootsen.

Voortbordurend op werk eerder verricht in Leiden, waarbij de nadruk lag op atoom additie reacties in cryogeen ijs (promotie werk van Dr. Bisschop en Dr. Ioppolo), richt het promotie onderzoek beschreven in dit proefschrift zich met name op vaste stof reacties waarbij stikstof (N) betrokken is of reacties die resulteren in grote COMs.

Een interstellair vaste stof stikstof chemie netwerk (Hoofdstuk 3, 4, 5 en 6)

Moleculen die stikstof bevatten zijn essentieel voor het leven op aarde. Het is echter een grote stap van de eenvoudige stikstofhoudende moleculen in interstellair ijs naar complexe organische moleculen van astrobiologisch belang, inclusief aminozuren. Tot nu toe was de vaste stof stikstof chemie aan ijs oppervlakken nauwelijks bestudeerd en met name de reacties tussen twee neutrale moleculen, d.w.z. zonder inwerking van energetische straling (UV licht of kosmische straling) is slecht begrepen. In de hoofdstukken 3-5 van dit proefschrift wordt de experimentele afleiding van een zeer compleet stikstof chemie netwerk beschreven waarbij stikstof oxides (NO, NO_2, N_2O) en H-, O- en N- atomen betrokken zijn.

De oppervlakte hydrogenatie van NO vindt zonder barriere plaats en leidt tot de vorming van hydroxylamine (NH_2OH) - een pre-biotisch molecuul dat tot dusver niet gedetecteerd is in de ruimte, maar waarvoor astrochemische modellen (beschreven in hoofdstuk 3) relatief hoge hoeveelheden voorspellen ($7 \cdot 10^{-9}$ i.v.t. H_2) tegen het einde van de levensduur van een donkere wolk. O- en N- atoom reacties met vast NO hebben ook een lage activerings energie, hetgeen resulteert in de vorming van NO_2 en N_2. Het gevolgde reactie pad is niet sterk afhankelijk van de ijsomgeving; vergelijkbare resultaten worden gevonden voor H_2O-rijk (polair) en CO-rijk (apolair) ijs. Vastgevroren NO_2 valt uiteen na botsing met een atoom en daarbij ontstaan stikstof oxides zoals NO, N_2O, en andere moleculen zoals HNO, NH_2OH en H_2O. Wanneer NO_2 gemengd wordt in een CO-rijk

(d.w.z. interstellair meer relevant) ijs, worden ook CO_2 en HCOOH geproduceerd. De stabiele (eind)producten van de samengevoegde reactienetwerken - NO+H/O/N en NO_2+H/O/N - zijn NH_2OH, H_2O, N_2 en N_2O.

In hoofdstuk 6 is dit reactienetwerk verder uitgebreid door experimenteel onderzoek van niet-energetische reacties die leiden tot de vorming van NH_3 en HNCO. Ammonia (NH_3) blijkt efficient te worden gevormd door drie sequentiële H-atoom addities aan N-atomen. Daarnaast laten we zien dat in een CO-rijk interstellair ijs analoog, de vorming van NH_3 wordt afgeremd door de vormnig van HNCO. De interactie van CO moleculen met NH radicalen - een van de tussenproducten tijdens de vorming van NH_3 - verstoort het reactie pad. Dit is een belangrijke experimentele conclusie. Allereerst laat het zien dat net zoals bij de hydrogenatie van O_2 en NO_2, reactieroutes niet onafhankelijk kunnen worden behandeld en dat mogelijke reacties van tussenproducten met omgevingsmoleculen mee in de overweging moeten worden genomen. Ten tweede is de vorming van HNCO door de interactie van NH met CO het eerste voorbeeld van een reactie waarbij een N-C binding wordt gevormd zonder tussenkomst van energetische processen zoals UV licht of kosmische straling. Deze route naar HNCO is een belangrijke stap om de astronomische waarneming van de zogenaamde XCN spectrale ijs band te verklaren: HNCO kan gemakkelijk converteren tot OCN^- via thermisch geinduceerde zuur-base reacties.

Een groot aantal verschillende reacties is bestudeerd in Hoofdstuk 3-6 en de efficiëntie van deze reactes is samengevat in Tabel 1.

Tabel 1. Efficientie van de belangrijkste oppervlakte reacties die zijn besproken in Hoofdstukken 3-6.

| Geen barriere	Kleine barriere	Barriere	Geen reactie
$NO + 3H \rightarrow NH_2OH$[b]	$NO + O_2 \rightarrow NO_2 + O$	$CO + H \rightarrow HCO$	$NO + H_2$
$NO + O \rightarrow NO_2$		$H_2CO + H \rightarrow CH_3O$	$NO + N_2$
$NO + N \rightarrow N_2 + O$		$(NO)_2 + O_2 \rightarrow (NO_2)_2$	$NO_2 + H_2$
$NO + NO \rightarrow (NO)_2$		$(NO_2)_2 + N \rightarrow N_2O + NO_2 + O$	$NO_2 + O_2$
$NO + NO_2 \rightarrow ONNO_2$		$NH + CO \rightarrow HNCO$	$NO_2 + N_2$
$NO_2 + H \rightarrow NO + OH$			$N_2O + H$
$NO_2 + O \rightarrow NO + O_2$			$N_2O + O$
$NO_2 + N$[a] $\rightarrow N_2O + O$			$N_2O + N$
$NO_2 + NO_2 \rightarrow (NO_2)_2$			
$N + 3H \rightarrow NH_3$[b]			

[a]Deze reactie heeft mogelijk een kleine barriere. [b]Drie opeenvolgende H-atoom addities.

Hoofdstuk 7 is hieraan gerelateerd door de efficiëntie te bespreken van reacties waarin deuterium een rol speelt, specifiek toegepast op NH_3 en resulterend in NH_2D, NHD_2 en ND_3.

HNCO and NH$_2$OH als een mogelijk startpunt voor de vorming van eenvoudige aminozuren (Hoofdstukken 3-6)

De aanwezigheid van HNCO, OCN$^-$ of NH$_2$OH in interstellair ijs in de protostellaire fase is belangrijk voor de astrobiologie. Gedurende deze fase wordt interstellair stof blootgesteld aan verschillende processen die energie leveren en daarmee reacties kunnen starten. Deze bestaan uit onder andere, temperatuurverhoging, UV straling of interactie met elektronen of ionen (kosmische straling). Deze processen kunnen de samenstelling van de ijs mantels drastisch veranderen. Met name in het geval van kosmische straling kan de energie die vrijkomt bij inslag leiden tot het uiteenvallen van honderden tot duizenden moleculaire bindingen langs het pad dat het ion volgt, resulterend in de vorming van reactieve fragmenten. Deze fragmenten kunnen recombineren en weer andere en complexere moleculen vormen. Uiteindelijk kan een complex polymeer gevormd worden dat hoge temperaturen kan weerstaan. Zoals te zien in het linker paneel van figuur 2 zijn HNCO moleculen onderdeel van de peptide bindingen [-(H)N-C(O)-] tussen elke set van twee aminozuren. Bovendien bevat het eenvoudigste aminozuur, polyglycine, niets dan HNCO en CH$_2$ fragmetten. Als OCN$^-$ inderdaad aanwezig is in het ijs (in plaats van HNCO), dan kunnen de anionen van aminozuren en anionische fragmenten daarvan ook gevormd worden.

Tijdens de vorming van de protoster kan een deel van het ijs sublimeren of niet-thermisch desorberen. Daarom is het belangrijk te weten uit welke componenten een ijs bestaat alvorens de energetische processen domineren. Dat geldt in het bijzonder voor hydroxylamine waarvan in dit onderzoek wordt aangetoond dat het efficient gevormd kan worden in de vaste stof via een niet-energetische route in de vroege stadia van stervorming. Tegelijkertijd kan NH$_2$OH ook gezien worden als startpunt in de synthese van eenvoudige aminozuren. Er wordt aangenomen dat hydroxylamine dat als het ware opgeslagen ligt in de ijs mantels aan het begin van de ineenstorting van de wolk, in een later stadium beschikbaar komt voor vervolg reacties. Dit geldt dan met name wanneer de protoster vormt en UV straling en thermische processen dominant worden (zie ook het rechter paneel van Figuur 2); het is goed mogelijk dat de synthese van aminozuren in een interstellaire omgeving begint met de desorptie van NH$_2$OH. De sleutel van het slagen van een dergelijk mechanisme ligt bij reacties tussen geprotoneerd hydroxylamine en carboxyl zuren. Ook al is het verloop van deze reacties aangetoond bij kamertemperatuur, dit is nog niet het geval voor astrochemisch relevante temperaturen.
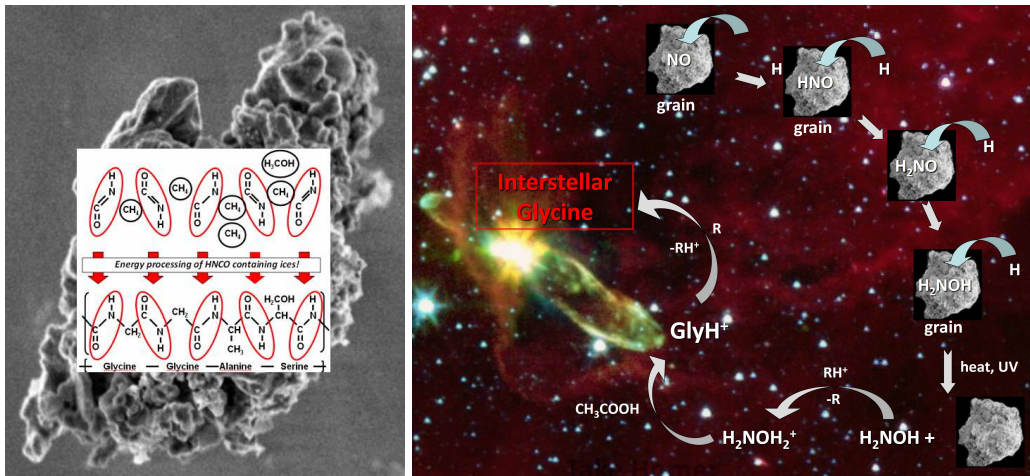
Figuur 2. Mogelijke vormingsroute van de simpelste aminozuren, zoals besproken in dit proefschift.

Eenvoudige suikers in interstellair ijs (Hoofdstuk 8)

In het afsluitende hoofdstuk van dit proefschrift worden de astrobiologische implicaties verder uitgebreid naar de eerste voorbeelden van de twee andere klassen prebiotische verbindingen - aldoses en polyolen. Glycolaldehyde ($HC(O)CH_2OH$) en etheenglycol ($H_2C(OH)CH_2OH$) zijn de kleinste moleculen binnen dit type verbindingen. Beide moleculen zijn onomstokelijk waargenomen in het ISM. Beide moleculen ontstaan door aan CO ijs waterstof atomen toe te voegen. Omdat CO een van de laatste moleculen is die vastvriezen in de ruimte, wordt verwacht dat ijs in koude donkere interstellaire wolken een CO-coating bezit. De vorming van glycolaldehdye en etheenglycol vindt gelijktijdig plaats met de vorming van de twee belangrijkste producten hydrogenatie producten van CO: H_2CO en CH_3OH. Hier wordt voor de eerste keer aangetoond, dat het reguliere hydrogenatie schema van CO ook leidt tot de vorming van zulke complexe moleculen. Een ronduit belangrijk punt binnen dit schema is de vorming van het koolstof skelet (C-C binding) door HCO + HCO recombinatie.

In hoofdstuk 8 wordt verder beschreven hoe deze experimentele resultaten kunnen worden geïmplementeerd in een astrochemisch model gebaseerd op een continue 'random walk' Monte-Carlo methode. Dit schept de mogelijkheid om uitgaande van de laboratorium data de microscopische stof-oppervlakte chemie te simuleren en te extrapoleren van typische laboratorium waarden tot tijdsschalen in het interstellaire medium. De methode houdt rekening met de locatie van individuele moleculen in het ijs en maakt het mogelijk om de hoeveelheid glycolaldehyde en etheen glycol in de vaste stof in compacte interstellaire wolken te voorspellen. Het is nu aan de astronomen om met behulp van waarnemingen deze resultaten verder te onderbouwen.

List of Publications

Astrochemistry (refereed):

- <u>Fedoseev G.</u>, Cuppen H. M., Ioppolo S., Lamberts T., Linnartz H., "*Experimental evidence for Glycolaldehyde and Ethylene Glycol formation by surface hydrogenation of CO molecules under dense molecular cloud conditions*", 2014, submitted to Mon. Not. R. Astron. Soc.

- <u>Fedoseev G.</u>, Ioppolo S., Linnartz H., "*Deuterium enrichment of ammonia produced by surface N+H/D addition reactions at low temperature*", 2014, Mon. Not. R. Astron. Soc., in press, article doi: 10.1093/mnras/stu1852

- <u>Fedoseev G.</u>, Ioppolo S., Zhao D., Lamberts T., Linnartz H., "*Low Temperature Surface Formation of NH_3 and HNCO: hydrogenation of nitrogen atoms in CO-rich interstellar ice analogues*", 2014, Mon. Not. R. Astron. Soc., in press, article doi: 10.1093/mnras/stu2028

- Lamberts T., Cuppen H.M., <u>Fedoseev G.</u>, Ioppolo S., Chuang K-J., Linnartz H., "*On the relevance of the H_2+O reaction pathway for the surface formation of interstellar water: A combined experimental and modeling study*"; 2014, Astron. Astrophys, article doi: 10.1051/0004-6361/201424252.

- Ioppolo S., <u>Fedoseev G.</u>, Minissale M., Congiu E., Dulieu F., Linnartz H., *"Solid state chemistry of nitrogen oxides - Part II: surface consumption of NO_2"*, 2014, Phys. Chem. Chem. Phys., 16, 8270.

- Minissale M., <u>Fedoseev G.</u>, Congiu E., Ioppolo S., Dulieu F., Linnartz H., "*Solid state chemistry of nitrogen oxides - Part I: surface consumption of NO*", 2014, Phys. Chem. Chem. Phys., 16, 8257.

- Ioppolo S., <u>Fedoseev G.</u>, Lamberts T., Romanzin C., Linnartz H., "*SURFRESIDE^2: An ultrahigh vacuum system for the investigation of surface routes of interstellar interest*", 2013, Rev. Sci. Instrum., 84, 073112.

- <u>Fedoseev G.</u>, Ioppolo S., Lamberts T., Zhen J.F., Cuppen H.M., Linnartz H., "*Efficient surface formation route of interstellar hydroxylamine through NO hydrogenation. II. The multilayer regime in interstellar relevant ices*", 2012, J. Chem. Phys., 137, 4714.

- Congiu E., <u>Fedoseev G.</u>, Ioppolo S., Dulieu F., Chaabouni H., Baouche S., Lemaire J. L., Laffon C., Parent P., Lamberts T., Cuppen H. M., Linnartz H., "*NO ice hydrogenation: A solid pathway to NH_2OH formation in space*", 2012, Astrophys. J. Lett., 750, L12.

Conference proceedings:

- Linnartz H., Bossa J.-B., Bouwman J., Cuppen H. M., Cuylle S. H., van Dishoeck E. F., Fayolle E. C., <u>Fedoseev G.</u>, Fuchs G., Ioppolo S., Isokoski K., Lamberts T., Öberg K. I., Romanzin C., Tenenbaum E., Zhen J., "*Solid state pathways towards nolecular complexity in space*", in Proc. IAU Symposium No. 280, The Molecular Universe, Toledo/Spain, 2011.

Plasma chemistry and physics (refereed):

- Korolenko V. A., Zagoskin A. I., Kozlov K. V., Nikitina T. A., <u>Fedoseev G. S.</u>, Samoilovich V. G., "*Plasma diagnostics of barrier-torch discharge in argon flow in a capillary by cross-correlation spectroscopy*", 2012, Moscow University Chemistry Bulletin, 67, 1.

- Kloc P., Wagner H.-E., Trunec D., Navratil Z., <u>Fedoseev G.</u>, "*Investigation of dielectric barrier discharge in Ar and Ar/NH$_3$ mixture using cross-correlation spectroscopy*", 2010, J. Phys. D: Appl. Phys., 43, 345205.

- <u>Fedoseev G. S.</u>, Kozlov K. V., Rode S. V., Wagner H.-E., "*Optical emission spectroscopy of a chemically active dielectric barrier discharge plasma in mixtures of argon and nitrogen*", 2010, Design and Technologies, 17, 122-126 (**in Russian**).

- <u>Fedoseev G. S.</u>, Kozlov K. V., Rode S. V., Wagner H.-E., "*Radiation kinetics of microdischarges in mixtures of argon and nitrogen at atmospheric pressure*", 2010, Design and Technologies, 17, 117-121 (**in Russian**).

Conference proceedings:

- Bogaczyk M., <u>Fedoseev G.</u>, Wild R., Wagner H.-E., "*Investigation of barrier discharges in He/N$_2$ mixtures by cross-correlation spectroscopy and surface charge measurements*"*,* in Proc. 12th International Symposium on High Pressure Low Temperature Plasma Chemistry (HAKONE XII), Trenčianske Teplice/Slovakia, 2010.

- Kozlov K. V., <u>Fedoseev G. S.,</u> Wagner H.-E.,"*Spatio-temporally resolved spectroscopic diagnostics of the filamentary and diffuse modes of barrier discharges in Ar/N$_2$ mixtures at atmospheric pressure*", in Proc. XVIII International Conference on Gas Discharges and Their Applications (GD 2010). Greifswald/Germany, 2010.

- Kozlov K. V., Odic E., Tatarenko P. A., Dodet B., <u>Fedoseev G. S.</u>, Kirkpatrick M. J., Samoilovich V. G., Ganciu M., "*Kinetics and chemical reactivity of barrier discharges in humid argon*", in Proc. 10th Int. Symp. on High Pressure Low Temperature Plasma Chemistry (HAKONE X), Saga/Japan, 2006.

Curriculum Vitae

I was born in 1985 in Kharkov, in the former Soviet Union. My parents were students at the Kharkov Institute for Radioelectronics and sometimes I was brought to the institute, where I spent my time with other students while my parents were passing exams, thus I can consider it to be the first place that systematically participated in my education.

Upon completion of their studies my parents (and therefore me) first moved to Krasniy Luch, Luhansk, where they were distributed on a factory (electric transformers) which bears the same name as the town. However my parents unsubscribed from this appointment and moved to Orel in 1987 where they joined the Research and Production Association "Autograph" (design and prototyping of pencil graph plotters) and in 1988 we finally settled in Bryansk where my Father was appointed to the Bryansk Plant of Manufacturing Equipment. In Bryansk I attended both elementary (№64) and secondary (№64, Bryansk Municipal Luceum №1) schools.

I never intended to link my life so deeply with the Natural Sciences, however, the excellent education available in school made it - if not the favorite choice - but at least the one of the least resistance. After completing my secondary education I entered the Institute of Chemistry of M.V. Lomonosov Moscow State University (MSU), where I obtained my specialist degree at the Department of Physical Chemistry under the supervision of Assoc. Prof. Dr. K. V. Kozlov, with a thesis devoted to the spatially resolved spectroscopic diagnostics of barrier discharges in humid argon by cross-correlation spectroscopy. During my study at MSU I actively learned Chinese and as a result I was granted with the China Government Scholarship and spent one year of my studies in China at Dalian Polytechnic University. This so far was the richest period of my life from which I keep harvesting new impressions and thoughts even after so many years have passed.

After my graduation from MSU (2008), I joined the Department of Material Science of Moscow State University of Design and Technology as a PhD student under the supervision of Assoc. Prof. Dr. K.V. Kozlov and Prof. Dr. S.V. Rode. During this time I greatly benefited from the DAAD (German Academic Exchange Service) program and spent six months in the Institute of Physics, University of Greifswald, under the supervision of Privatdozent Dr. H.-E. Wagner and Assoc. Prof. Dr. K.V. Kozlov. There I continued to work on plasma diagnostics of barrier discharges at atmospheric pressure by cross-correlation spectroscopy. This work resulted in the publication of several papers and conference proceedings.

Since October 2010, I am a PhD student in the Raymond and Beverly Sackler Laboratory for Astrophysics under the supervision of Prof. Dr. H. V. J. Linnartz, Dr. S. Ioppolo, and Dr. H. M. Cuppen. My position was part of a large EU programme (LASSIE) fully devoted to laboratory studies of solid state astrochemistry. Over these four years,

together with another PhD student, T. Lamberts, I worked on the construction, calibration and application of SURFRESIDE^2, an ultra-high vacuum (UHV) system for the investigation of non-energetic surface reactions of interstellar relevant molecules. The use of this system has already led to the publication of nine articles I (co)authored and I hope it will provide many more for students who will decide to link their scientific life with laboratory astrophysics. Seven of these publications are presented here and comprise the body of this thesis.

another, and I'm sure Fabrizio, for example, will agree with me on this point.

These four years in a foreign country would not have been as pleasant and fruitful without so many people around me. I would wish first of all to make a special thanks: for the people who granted me with the endless hospitality in their own country: Thanja, Daniel, Niels; and for the people who were always willing to make even the gloomiest day happy for me: Junfeng, Emanuele, and Sarah; for the people who have never been in the Observatory but were always willing to talk with me in my mother tongue even from far far away: Aleksandr Babkin, Maria Zamiralova, Kristina Chernozemtseva; and for Vladimir Danilov and Vladimir Sushkov, they will probably be surprised to find themselves in this list, but those tea-breaks we had long ago I always missed and remembered with pleasure over here.

And of course at the end we always return to the origins. Therefore I would wish to tell about my Parents, this not only because I know that their love is a feeling that exists outside of the category of time and it is something that will just always be. But also because of Taras Bulba's words (a story written by Nikolai Vasilievich Gogol): 'I gave you life I will also kill you' (a winged words depicting the superiority of a Father's rights over those of the son). This PhD would have never happened without my parents permission. My last thanks belongs to my nephews: Sasha, Maksim, Sergey, Matvey, Lera, Katya and Kirill they will be able to read this text only after many years passed from now on and, therefore, these final thanks although belong to the past are ironically and willingly addressed to the future.

Propositions
Accompanying the thesis
Atom addition reactions in interstellar ice

1. The construction of a solid state astrochemical nitrogen network involving nitrogen oxides (NO, NO_2, N_2O) and H- ,O- , and N- atoms has only become possible by using two independent atom beam lines. (Chapters 2-6)

2. Reactions in interstellar ices involving intermediate radicals and their surrounding molecules are more important than previously thought. (Chapter 5, 6 and 8)

3. A higher sticking probability of D- over H-atoms impacting onto an icy grain surface may result in deuterium enrichment of newly formed species. (Chapter 7)

4. The simplest representatives of polyols and aldoses can be formed in dark molecular clouds just by surface CO hydrogenation. (Chapter 8)

5. The molecule containing the four most abundant chemical elements in space and of proteins - HNCO - can be formed on the surface of interstellar grains starting from the basic constituents of molecular clouds *without* any external energetic processing. (Chapter 6)

6. A critical scientist should not only look for observations that prove a proposed theory correct, but rather systematically disprove also all other possible interpretations.

7. The way citation indices are handled shows similarities with Marxism-Leninism ideas on expressing quality through quantity.

8. Astronomical time-scale is the most challenging condition to simulate in the lab.

9. Only real deadlines work, unless you can lie to yourself truly well.

10. The XXI century we are living in is not at all similar to "the World of the Noon" described by Arkady and Boris Strugatsky in their sci-fi novels.

11. The realization of human dreams of space exploration has moved from the real World to the virtual one of 3D cinema and video-games industry.

12. Putting hard restrictions on the content of propositions ultimately may diminish their meaning.

Gleb Fedoseev
Leiden, November 2014